



**HAL**  
open science

# Synergy of 3D and 2D Perovskites for Durable, Efficient Solar Cells and Beyond

Isaac Metcalf, Siraj Sidhik, Hao Zhang, Ayush Agrawal, Jessica Persaud, Jin Hou, Jacky Even, Aditya Mohite

► **To cite this version:**

Isaac Metcalf, Siraj Sidhik, Hao Zhang, Ayush Agrawal, Jessica Persaud, et al.. Synergy of 3D and 2D Perovskites for Durable, Efficient Solar Cells and Beyond. *Chemical Reviews*, 2023, 123 (15), pp.9565-9652. 10.1021/acs.chemrev.3c00214 . hal-04160913

**HAL Id: hal-04160913**

**<https://hal.science/hal-04160913v1>**

Submitted on 8 Sep 2023

**HAL** is a multi-disciplinary open access archive for the deposit and dissemination of scientific research documents, whether they are published or not. The documents may come from teaching and research institutions in France or abroad, or from public or private research centers.

L'archive ouverte pluridisciplinaire **HAL**, est destinée au dépôt et à la diffusion de documents scientifiques de niveau recherche, publiés ou non, émanant des établissements d'enseignement et de recherche français ou étrangers, des laboratoires publics ou privés.



Distributed under a Creative Commons Attribution - NonCommercial 4.0 International License

# Synergy of 3D and 2D perovskites for durable, efficient solar cells and beyond

Isaac Metcalf<sup>1</sup>, Siraj Sidhik<sup>1</sup>, Hao Zhang<sup>2,3</sup>, Ayush Agrawal<sup>2</sup>, Jessica Persaud<sup>2</sup>, Jin Hou<sup>1</sup>, Jacky Even<sup>4</sup> and Aditya D Mohite<sup>2,3\*</sup>

<sup>1</sup>Department of Materials Science and NanoEngineering, Rice University, Houston, Texas 77005, USA.

<sup>2</sup>Department of Chemical and Biomolecular Engineering, Rice University, Houston, Texas 77005, USA.

<sup>3</sup>Applied Physics Graduate Program, Smalley-Curl Institute, Rice University, Houston, TX, 77005, USA.

<sup>4</sup>Univ Rennes, INSA Rennes, CNRS, Institut FOTON - UMR 6082, 35708 Rennes, France.

\*Correspondence: [adm4@rice.edu](mailto:adm4@rice.edu)

## Abstract:

Three-dimensional (3D) organic-inorganic lead halide perovskites have emerged in the past few years as a promising material for low-cost, high-efficiency optoelectronic devices. Spurred by this recent interest, several subclasses of halide perovskites such as two-dimensional (2D) halide perovskites have begun to play a significant role in advancing the fundamental understanding of structural, chemical, and physical properties of halide perovskites, which are technologically relevant. While the chemistry of these 2D materials is similar to that of the 3D halide perovskites, their layered structure with a hybrid organic-inorganic interface induces new emergent properties that can significantly or sometimes subtly be important. Synergistic properties can be realized in systems that combine different materials exhibiting different dimensionalities by exploiting their intrinsic compatibility. In many cases, the weaknesses of each material can be alleviated in hetero architectures. For example, 3D-2D can demonstrate novel behavior that neither material would be capable of separately. This review describes how the structural differences between 3D halide perovskites and 2D halide perovskites give rise to their disparate materials properties, discusses strategies for realizing mixed-dimensional systems of various architectures through solution-processing techniques, and presents a comprehensive outlook at the use of 3D-2D systems in solar cells. Finally, we investigate applications of 3D-2D systems beyond photovoltaics, and offer our perspective on mixed-dimensional perovskite systems as semiconductor materials with unrivaled tunability, efficiency and technologically relevant durability.

## Table of Contents

### 1. Introduction

#### Part 1: Individual Properties of 3D and 2D halide perovskites

### 2. Structural Properties of 3D and 2D Halide Perovskites

#### 2.1. The structure of 3D halide perovskites

#### 2.2. From 3D to 2D: Reduced dimensionality while maintaining corner-sharing octahedra

#### 2.3. From 2D to quasi-2D: Introducing n-value

### 3. Optoelectronic properties of 3D and 2D Halide Perovskites

#### 3.1. Semiconductor properties of 3D halide perovskites

#### 3.2. Semiconductor properties of 2D halide perovskites

### 4. Stability of 3D and 2D halide perovskites

#### 4.1. Issues with 3D halide perovskite stability

#### 4.2. Improved stability with 2D halide perovskites

## Part 2: Combining 3D and 2D Halide Perovskites

5. Doping 3D halide perovskite with 2D halide perovskite
  - 5.1. Long chain monoammonium cations
  - 5.2. Zwitterion type spacer cations (bifunctional spacer cations)
  - 5.3. Cyclic or aromatic ring monoammonium spacer cations
  - 5.4. Long chain diammonium spacer cations
  - 5.5. ACI-type spacer cations
6. Capping 3D halide perovskites with 2D halide perovskites
  - 6.1. Processing methods for capped 3D-2D halide perovskites
  - 6.2. Orientation of 2D halide perovskite on 3D halide perovskite
  - 6.3. Dimensional (n-value) control of 2D halide perovskite layer on 3D halide perovskite
  - 6.4. Thickness control of 2D halide perovskite layer on 3D halide perovskite
  - 6.5. Heterojunction sharpness
7. Synergistic applications of mixed 3D-2D halide perovskites
  - 7.1. Two-dimensional halide perovskites as selective contacts
  - 7.2. 3D-2D halide perovskites for Light emitting diodes
  - 7.3. 3D-2D halide perovskites for Photodetectors
  - 7.4. 3D-2D halide perovskites in lasing applications
8. Conclusions
  - 8.1. Future work for 3D-2D stacks
  - 8.2. Future work for 3D-2D composites

## **1. Introduction**

The projected economic, environmental, and humanitarian costs of climate change have prompted an urgent call for rapid and sustained decarbonization of all aspects of human activity. With the recognition that electricity generation is among the easiest sectors to decarbonize, most road maps for deep decarbonization suggest the immediate replacement of fossil fuel generating capacity with renewables and long-duration energy storage and the simultaneous electrification of as many high-emissions sectors, such as transportation and industry, as possible. As a result, global renewable electricity generation capacity must increase from 3.1TW in 2021 to 7.1TW by 2030, and between 2030 and 2050 an additional 630GW of solar photovoltaic capacity alone must be installed every year.<sup>1-3</sup> While the building of renewable energy generating capacity must begin immediately to avoid intractably destructive climate change, it must also continue for decades in order to create the infrastructure needed for a sustainable future, justifying both the rapid manufacture of silicon solar cells and continued research into lower-cost near- and medium-term solar technology.

Halide perovskite solar cells are perhaps the most promising emerging solar technology for near-term deployment, having reached efficiencies exceeding silicon solar cells for single junction devices using completely recyclable materials and manufacturing processes with near ambient temperatures, thus making them potentially much cheaper than silicon.<sup>4</sup> Moreover, H-silicon tandem architectures are challenging at the lab-scale the champion tandem solar cells based on ultra-high-cost III-V semiconductor heterostructures.<sup>5</sup> However, these highest-efficiency halide perovskite cells use a 3D halide perovskite absorber layer that is susceptible to degradation by environmental stressors and device operation. Stability has also held 3D perovskites back in a variety of other potential optoelectronics applications including LEDs, lasing, and photodetection.

Lower-dimensional quasi-2D halide perovskites, having a wider bandgap than 3D perovskites, also have shown success as solar cells, LEDs, lasers, and photodetectors. With a layered architecture created by splitting the 3D perovskite lattice with hydrophobic spacer cations, 2D halide perovskites show significantly improved stability

compared to their 3D counterparts. However, devices made with these absorbers trail 3D halide perovskite cells in terms of efficiency. Unfortunately, the same structural properties that imbue 2D halide perovskites with better stability are responsible for their lower solar cell performance. For a real-world solar cell, it is mandatory that both high stability and high efficiency are realized in the same device.

However, there need not be a trade-off between stability and efficiency in halide perovskite photovoltaics. In fact, 3D halide perovskites and 2D halide perovskites are extremely compatible materials that can be incorporated together into a single device in a variety of architectures. Combining 3D and 2D halide perovskites in one solar cell can achieve the stability of the 2D without sacrificing the efficiency of the 3D. Additionally, through the passivation of defects, grain boundaries, and interfaces, 3D-2D halide perovskite devices can exhibit superior stability and efficiency than their constituent materials alone. Recent developments in materials processing leading to a better control of the 2D-3D heterostructures are now also opening novel opportunities for device optimization and innovative multilayered device architectures. While 3D-2D halide perovskites still lag behind the figures of merit required for commercialization, we see a clear path towards reaching those parameters that wouldn't be possible in a single-phase system. Such developments initiated in the context of solar cells will foster further progress for myriad other optoelectronic applications based on halide perovskite semiconductors, in particular for light emission and photodetection.

This review explores the structures, optoelectronic properties, and stabilities of 3D and 2D halide perovskites, investigating the structural explanations for their materials properties. We then discuss incorporation mechanisms to realize 3D-2D halide perovskite devices with both doped and capped architectures. We review the performance of 3D-2D halide perovskites with various architectures reported in literature and discuss what approaches have shown the most success. Finally, we discuss future avenues for advanced semiconducting devices using 3D-2D architectures. While several excellent reviews and perspectives have been published on the properties of 3D and 2D

perovskites alone, the recent focus on mixed-dimensional perovskites deserves its own exploration. To that end, the purpose of this review is to summarize the state of the field for 3D-2D halide perovskites, and to serve as a handbook for future investigation of mixed-phase halide perovskites as this area of research grows in popularity for photovoltaics and other optoelectronic device technologies.

## List of terms

### Structures and Architectures

(3D) halide perovskite: A crystal with perovskite structure and stoichiometry  $A^+B^{2+}X_{-3}^-$ , where  $X^-$  is a halide

2D halide perovskite: A layered quasi-2D halide perovskite

3D-2D: Any system that incorporates both 3D and 2D halide perovskites

3D-2D composite: A mixture of 3D and 2D halide perovskites, e.g., deposited together from a single precursor solution

3D-2D or 3D/2D Stack: A heterostructure of 2D halide perovskite deposited on top of 3D halide perovskite, with the 2D halide perovskite sufficiently thick for its semiconductor properties to be relevant

Bilayer: a stack with a 3D-2D interface of sharpness on the order of the surface roughness

Abrupt: (of an interface) as sharp as the surface roughness

Graded: (of an interface) less sharp than the surface roughness, having a gradient in chemical composition (e.g., n-value) from that of the bottom layer to that of the top layer

Capping layer: A heterostructure of 2D halide perovskite deposited on top of 3D halide perovskite, with the 2D halide perovskite too thin for its semiconductor properties to be relevant or only serving to passivate surface defect states at the interface

RP: Ruddlesden Popper phase 2D halide perovskite with stoichiometry  $A'^{2+}_2A^+_{n-1}B^{2+}_nX^-_{-3n+1}$

DJ: Dion-Jacobson phase 2D halide perovskite with stoichiometry  $A'^{2+}A^+_{n-1}B^{2+}_nX^-_{-3n+1}$

ACI: Alternating-cation phase 2D halide perovskite with stoichiometry  $A'^+A^+_nB^{2+}_nX^-_{-3n+1}$

n, or n-value: The thickness of a 2D halide perovskite's inorganic layer as defined by the



number of  $\text{PbI}_6$  octahedra in the out-of-plane direction

$A' n=x$ : The 2D phase commonly formed by  $A'$  with  $n$ -value of  $x$ . Unless redefined in the text, assume an A-site of MA, B-site of Pb, and X-site of I. e.g.,  $\text{BA}_n$   $n=3$ :  $\text{BA}_2\text{MA}_2\text{Pb}_3\text{I}_{10}$

$n$ -i-p/regular architecture: ETL between substrate and perovskite, HTL between perovskite and top contact

$p$ -i-n/inverted architecture: HTL between substrate and perovskite, ETL between perovskite and top contact

### Device Layers

CTL: Charge transport layer

ETL: Electron transport layer

HTL: Hole transport layer

### Chemicals

MA: Methylammonium

FA: Formamidinium

BA: Butylammonium

PEA: Phenylethylammonium, or Phenethylammonium

3AMP: 3-(aminomethyl)piperidinium

4AMP: 4-(aminomethyl)piperidinium

GA: Guanidinium

Spiro-OMeTAD: 2,2',7,7'-tetrakis(N,N-di-*p*-methoxyphenyl-amine)9,9'-spirobifluorene

PEDOT:PSS: poly(3,4-ethylenedioxythiophene) polystyrene sulfonate

PCBM: [6,6] phenyl- $\text{C}_{61}$ -butyric acid methyl ester

PTAA: Poly(triaryl amine)

MeO-2PACZ: [2-(3,6-Dimethoxy-9H-carbazol-9-yl)ethyl]phosphonic Acid

BCP: Bathocuproine

DMF: N,N-Dimethylformamide

DMSO: Dimethyl sulfoxide

IPA: Isopropanol

MeCN: Acetonitrile

ITO: Indium Tin Oxide

FTO: Fluorine-doped Tin Oxide

(Abbreviations used for less common molecules will be defined in the text)

### Characterization Techniques

XRD: X-Ray Diffraction

GIWAXS: Grazing-Incidence Wide-Angle X-Ray Scattering

PL: Photoluminescence

PLQY: Photoluminescence quantum yield

AFM: Atomic Force Microscopy

SEM: Scanning Electron Microscopy

ToF-SIMS: Time-of-Flight Secondary Ion Mass Spectroscopy

TR: Transient Reflectance

TA: Transient Absorption

XPS: X-Ray Photoelectron Spectroscopy

DFT: Density Functional Theory

UPS: Ultraviolet Photoelectron Spectroscopy

### Physics terms

HOMO: Highest-energy occupied molecular orbital

LUMO: Lowest-energy unoccupied molecular orbital

VBM: Valence Band Maximum, highest-energy occupied electron state below the bandgap

CBM: Conduction Band Minimum, lowest-energy unoccupied electron state above the bandgap

SOC: Spin-orbital coupling

STE: self-trapped exciton

EEA: exciton-exciton annihilation

### Device Parameters

$J_{\text{sc}}$ : Short-Circuit Current

$V_{\text{oc}}$ : Open-Circuit Voltage

FF: Fill Factor

PCE: Power Conversion Efficiency

J-V curve: Current density - Voltage curve

MPP Tracking: Maximum Power Point Tracking, measure device efficiency over time while applying the voltage which gives the maximum power output.

The voltage is dynamically updated to maintain the maximum power point as device conditions change.

$T_x$  (e.g.,  $T_{80}$ ): Degradation time at which  $x\%$  (e.g., 80%) of initial PCE remains

### Measurement conditions

RT: Room temperature,  $\sim 25^\circ\text{C}$

RH: Relative humidity

1-sun: AM1.5G solar spectrum

Ambient air: laboratory atmosphere (outside of a glovebox or another artificial atmosphere)

Inert:  $\text{N}_2$  or Ar atmosphere

# Part 1: Individual properties of 3D and 2D Halide Perovskites

## 2. Structural Properties of 3D and 2D halide perovskites

### 2.1. The crystallographic structure of 3D halide perovskites

Halide perovskites are a class of ionic crystals with stoichiometry  $A^+B^{2+}X_3^-$ , where X is a halogen, B is usually a heavy group-IV metal such as Sn or Pb, and A is either an organic or inorganic monovalent cation. The broader perovskite crystallographic structure supports other ionic materials including oxides with different charge combinations (e.g.,  $A^{2+}B^{4+}O^{2-}_3$ ) but these materials are less useful as semiconductors for optoelectronics and will not be discussed here. In the ideal (cubic) perovskite structure, the  $B^{2+}$  and  $X^-$  ions form a lattice of corner-sharing  $BX_6$  octahedra with B-sites in the center of each octahedron and X-sites at the corners. Eight neighboring octahedra define the cuboctahedral A-site (**Figure 1a**).<sup>6</sup> The semiconducting properties of halide perovskites derive from the s/p orbital overlap of the B and X ions in the 3D sublattice of octahedra, with the A-site stabilizing the structure and maintaining the crystal's charge neutrality.<sup>7</sup> A lower-symmetry lattice of corner-sharing  $BX_6$  octahedra obtained from the reference cubic perovskite structure by lattice distortion is also defined as a perovskite by extension.

If the A-site cation is too small to fill the cuboctahedral site, the  $BX_6$  octahedra will undergo cooperative in- and out-of-plane tilts to reduce the volume of the A-site, distorting the lattice from cubic to tetragonal or orthorhombic.<sup>8</sup> The Goldschmidt tolerance factor ( $t$ ) is a geometric factor of the three ionic radii which can be used to predict the stability and degree of octahedral distortion in a perovskite system:  $t = (r_A + r_X) / \sqrt{2}(r_B + r_X)$ .<sup>9,10</sup> The factor can be derived from the geometry of the perovskite structure, and is defined such that for  $t=1$  hard spheres of A, B, and X would touch without intersecting to form a cubic unit cell. For  $t=1$  the structure is perfectly cubic, with a Pb-I-Pb bond angle of  $180^\circ$  between corner-sharing octahedra. If  $0.8 < t < 1$  the octahedral tilt lowers the Pb-I-Pb angles and yields a lower-symmetry lattice, either tetragonal or orthorhombic (**Figure 1b**). For  $t < 0.8$  the required distortion will be too severe, and the

perovskite structure does not form. Likewise, for  $t > 1$  the cuboctahedral site cannot accommodate the A cation and a nonperovskite phase will be the stable phase. However, for ion combinations at the edge of the acceptable range at room temperature (e.g.,  $CsPbI_3$ ), the perovskite phase can form at higher temperatures and persist as a metastable phase when cooled.<sup>8,11</sup> The octahedral factor  $\mu = r_B / r_X > 0.41$  is another geometric factor which predicts the stability of the B-X octahedra in the perovskite structure.<sup>11</sup> For  $\mu=0.41$  hard spheres of X coordinating the same B-site would touch each other without overlapping, and for  $\mu < 0.41$  they begin to overlap. **Table 1** lists tolerance factors for possible combinations of common A-, B-, and X-site ions and comments on which have been synthesized with a perovskite structure.

The most well-studied halide perovskite is  $MAPbI_3$  (MA=methylammonium). With  $t \sim 0.912$ ,  $MAPbI_3$  is very close to an ideal perovskite, forming a tetragonal phase at room temperature.<sup>12,13</sup> The MA cation has the most suitable effective radius of any organic or inorganic monovalent cation for a phase-stable lead iodide perovskite, but chemical stability issues associated with MA have motivated the use of less suitably-sized but more chemically stable cations for halide perovskites such as  $FAPbI_3$  (FA=formamidinium,  $t \sim 0.987$ ) and  $CsPbI_3$  ( $t \sim 0.851$ ). At room temperature the stable form of  $FAPbI_3$  is a hexagonal nonperovskite structure (the  $\delta$ - phase).<sup>8</sup> The  $PbI_6$  octahedra still form but join into a 1D face-sharing network with a Pb-I-Pb bond angle below  $100^\circ$ , and as a result the phase is not optically active (**Figure 1c**). The cubic perovskite phase of  $FAPbI_3$  becomes stable for  $T \sim 150^\circ C$ .  $CsPbI_3$  also adopts a nonperovskite  $\delta$ - phase at room temperature, with the  $PbI_6$  octahedra forming a 1D edge-sharing network (**Figure 1d**).<sup>14</sup> Heated past  $360^\circ C$   $CsPbI_3$  converts into the cubic  $\alpha$ - phase; upon cooling from  $360^\circ C$  it moves through three perovskite phases: first the tetragonal  $\beta$ - phase ( $260^\circ C$ ), then the orthorhombic  $\gamma$ - phase ( $175^\circ C$ ).<sup>15</sup> The substitution of iodine atoms with bromine atoms leads to an increase in the tolerance factors, which would be expected to stabilize  $CsPbBr_3$  and destabilize

FAPbBr<sub>3</sub>. However, neither FAPbBr<sub>3</sub><sup>16</sup> nor CsPbBr<sub>3</sub><sup>14</sup> exhibit the structural instabilities from high temperature cubic phases toward non-perovskite yellow phases of their iodides. The increased tolerance factor also causes MAPbBr<sub>3</sub> to adopt an undistorted cubic phase at room temperature.<sup>13</sup>

In order to realize a chemically-stable perovskite phase at room temperature, the A-site is often an alloy of FA-Cs<sup>10</sup> or FA-MA-Cs<sup>17</sup> to give an

effective cation radius for a near-ideal tolerance factor (**Figure 1e**). While the B-site<sup>18</sup> and X-site<sup>19</sup> can also be alloyed, this changes the bandgap of the halide perovskite; the A-site, decoupled from the crystal's electronic structure, can be alloyed without significantly altering its semiconductor properties. Triple-cation A-site mixtures including FA<sub>0.8</sub>MA<sub>0.15</sub>Cs<sub>0.05</sub> have become the state of the art for 3D halide perovskite photovoltaics.

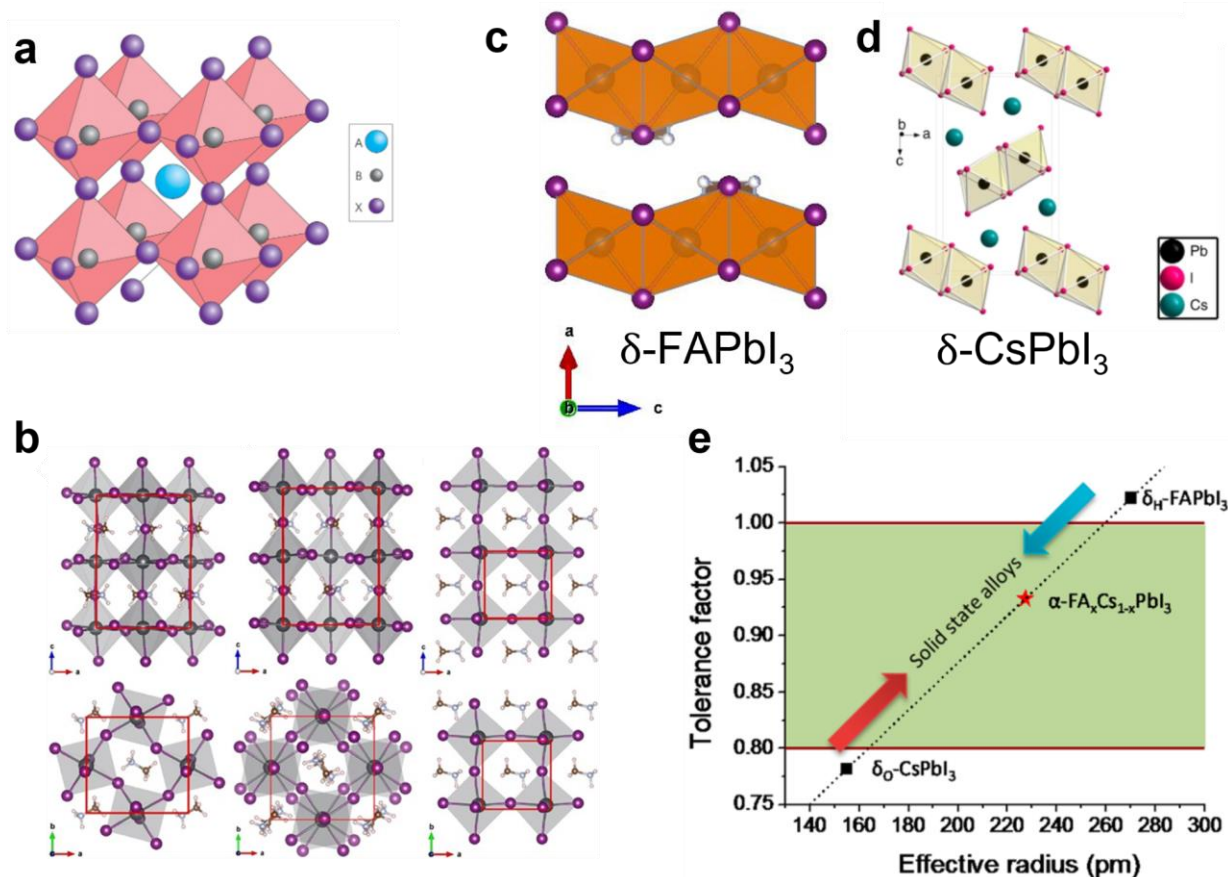


**Figure 1: The structures and tolerance factor of 3D perovskites.** a) Cubic perovskite crystal structure. Reproduced with permission from ref.<sup>20</sup> Copyright 2014 Springer Nature. b) Comparison between Orthorhombic (left), tetragonal (middle), and cubic (right) phases of 3D halide perovskite. Reproduced with permission from ref.<sup>21</sup> Copyright 2016 Wiley-VCH. c) Delta phases of FAPbI<sub>3</sub> perovskites, created using crystallographic data from ref.<sup>22</sup> d) Delta phases of CsPbI<sub>3</sub> perovskites. Reproduced with permission from ref.<sup>23</sup> Copyright 2018 Springer Nature. e) Tolerance factor tuning with Cs-FA alloys. Reproduced with permission from ref.<sup>10</sup> Copyright 2015 American Chemical Society.

**Table 1: Reported ABX<sub>3</sub> Perovskites**

| A              | B              | X           | $t^{12,24}$ | Reported / Not Reported | Ref |    |
|----------------|----------------|-------------|-------------|-------------------------|-----|----|
| MA<br>(217 pm) | Pb<br>(119 pm) | F (128.5pm) | 0.987       | Not reported            | 25  |    |
|                |                | Cl (181 pm) | 0.938       | Reported                |     |    |
|                |                | Br (196 pm) | 0.927       | Reported                |     | 26 |
|                |                | I (220 pm)  | 0.912       | Reported                | 13  | 8  |
|                | Sn<br>(115 pm) | F           | 1.003       | Not reported            |     |    |
|                |                | Cl          | 0.951       | Reported                | 27  | 28 |
|                |                | Br          | 0.939       | Reported                |     | 28 |
|                |                | I           | 0.922       | Reported                | 28  | 8  |
| FA<br>(253 pm) | Pb             | F           | 1.09        | Not reported            |     |    |
|                |                | Cl          | 1.023       | Reported                | 29  |    |
|                |                | Br          | 1.008       | Reported                |     | 26 |
|                |                | I           | 0.987       | Reported                | 30  | 8  |
|                | Sn             | F           | 1.108       | Not reported            |     |    |
|                |                | Cl          | 1.037       | Not reported            | 31  | 32 |
|                |                | Br          | 1.021       | Reported                | 33  |    |
|                |                | I           | 0.998       | Reported                | 34  | 8  |
| Cs<br>(188 pm) | Pb             | F           | 0.904       | Reported                | 35  |    |
|                |                | Cl          | 0.87        | Reported                | 36  |    |
|                |                | Br          | 0.862       | Reported                | 37  | 26 |
|                |                | I           | 0.851       | Reported                | 38  |    |
|                | Sn             | F           | 0.919       | Not reported            | 39  |    |
|                |                | Cl          | 0.881       | Reported                | 27  | 40 |
|                |                | Br          | 0.873       | Reported                | 41  |    |
|                |                | I           | 0.861       | Reported                | 42  |    |

## 2.2. From 3D to 2D: Reduced dimensionality while maintaining corner sharing octahedra

Assigning an “effective radius” to molecular A-site cations is a simplification which neglects the cation’s shape and charge distribution. For specific classes of high-aspect-ratio A-site cations, quasi-perovskite structures can be stabilized, which show reduced dimensionality but maintain the 3D structure’s corner-sharing  $\text{PbI}_6$  octahedra and therefore remain photoactive. Linear ammonium or diammonium “spacer” cations can sit in what used to be the cuboctahedral A-site cage, breaking it in half and separating the  $\text{PbI}_6$  octahedral network into disconnected layers.

The  $\langle 100 \rangle$ ,  $\langle 110 \rangle$ , and  $\langle 111 \rangle$  layered halide perovskite series along with a few more atypical halide perovskite networks are known.<sup>43</sup> The  $\langle 100 \rangle$  layered halide perovskites are the most extensively studied<sup>44–46</sup>. The dimensionality of their electronic structure is considered to be equal to 2, sharing strong similarities with strongly confined classical semiconductor quantum wells and other 2D materials (vide infra).

Among  $\langle 100 \rangle$  layered halide perovskites, monolayered Ruddlesden-Popper (RP) 2D halide perovskites were the first to be synthesized and studied in detail.<sup>47–49</sup> They have the stoichiometry  $\text{A}^{+2}\text{B}^{2+}\text{X}^{-4}$ , with  $\text{A}'$  a linear spacer monocation. RP  $\text{A}'$  cations have an ammonium group which sits within the half-cuboctahedral site and a long, typically nonpolar group which extends perpendicular to the Pb-I plane (e.g., butylammonium,  $\text{BA}^+$ ). This breaks the lattice into strongly ionic monolayers of corner-sharing  $\text{PbI}_6$  octahedra (inorganic layer) separated by two linear  $\text{A}'$  cations (organic layer) in a region presenting a smaller dielectric constant. The  $\text{A}'$  cations of neighboring layers face each other, holding the layers together via van der Waals interactions between their nonpolar groups. A reference RP crystallographic structure can be defined for which adjacent layers exactly present a  $(\frac{1}{2}, \frac{1}{2})$  unit-cell offset in the 2D plane, although actual structures may exhibit slight deviations from this ideal offset<sup>50</sup> (**Figure 2a**).

Dion-Jacobson (DJ) 2D halide perovskites, which were discovered more recently,<sup>51</sup> have the stoichiometry  $\text{A}'^{2+}\text{B}^{2+}\text{X}^{-4}$ , with  $\text{A}'$  a linear dication terminated on either end by ammonium groups (e.g.,

1,4-butanediammonium,  $\text{BDA}^{2+}$ ). The DJ structure is similar to RP except that the organic layer is composed of one  $\text{A}'$  cation with an ammonium group sitting in the A-site of both Inorganic layers it connects. As a result the DJ structure has little unit-cell offset between layers, and a reference DJ crystallographic structure with no offset can be defined.<sup>50</sup> DJ halide perovskites generally have stronger interlayer bonding than RP halide perovskites. They tend to show a larger (near  $180^\circ$ ) axial (out-of-plane) Pb-I-Pb bond angle and a smaller ( $155^\circ$ - $165^\circ$ ) equatorial (in-plane) Pb-I-Pb bond angle compared to RP halide perovskites, which have more consistent bond angles between  $165^\circ$  and  $172^\circ$ , although the distortion varies for both phases depending on the chemistry (**Figure 2b**).<sup>47,51</sup>

A third class of 2D halide perovskite, alternating cation (ACI), has stoichiometry  $\text{A}'^+\text{A}^+\text{B}^{2+}\text{X}^{-4}$ , where  $\text{A}$  is a 3D halide perovskite A-cation and  $\text{A}'$  is a larger cation.<sup>52</sup> The  $\text{A}'$  cation in the ACI structure lacks the high aspect ratio of RP and DJ  $\text{A}'$  cations and is usually only slightly too large to fit in the 3D cuboctahedral site (e.g., Guanidinium). The structure is once again broken into planar sheets, this time separated by alternating rows of A-cations and  $\text{A}'$ -cations. The ideal ACI structure has a  $(\frac{1}{2}, 0)$  unit cell offset in the 2D plane between layers.<sup>50</sup> ACI halide perovskites show Pb-I-Pb bond angles which are large (near  $180^\circ$ ) in one in-plane direction and small (near  $160^\circ$ ) in the other, with intermediate ( $165^\circ$ - $167^\circ$ ) axial bond angles (**Figure 2c**).<sup>52</sup>

There should be a size requirement for an organic spacer to form a 2D halide perovskite, albeit undetermined in some cases. For linear RP monoammonium cations, the longest chain reported is octadecyl ammonium (18 carbons)<sup>53</sup> and the smallest is methylhydrazinium.<sup>54</sup> For cyclic cations, the diameter of the ring has to be smaller than  $\text{BX}_6$  octahedron (6.3 Å) to be fit into the 2D structure. Generally, a ring size of three to six carbons is required to form 2D halide perovskite, while larger rings facilitate the formation of 1D halide perovskite.<sup>55,56</sup> Each of the three types of  $\langle 100 \rangle$  2D perovskites has different size requirements as determined by the materials’ structure. In the case of ACI-type 2D perovskites, the  $\text{A}'$ -site must be smaller and has less room for structural variability than in either RP or DJ phases.

For interested readers, *The 2D Halide Perovskite Rulebook* by Li et al. provides an excellent comprehensive review of reported 2D halide perovskites.<sup>57</sup>

### 2.3. From 2D to quasi-2D: Introducing n-value

2D halide perovskites with an inorganic layer a single sheet of  $\text{PbI}_6$  octahedra thick, like those discussed above, are said to have an n-value of 1. The inorganic layer thickness can be increased if 3D A-site cations are incorporated to fill the new unbroken cuboctahedral sites between eight neighboring octahedra. This broadens the RP, DJ, and ACI materials classes to include “quasi-2D” structures of the form  $\text{A}'^{2+}_2\text{A}^{+}_{n-1}\text{B}^{2+}_n\text{X}^{-}_{3n+1}$  (RP)<sup>58–60</sup>,  $\text{A}'^{2+}\text{A}^{+}_{n-1}\text{B}^{2+}_n\text{X}^{-}_{3n+1}$  (DJ)<sup>51</sup>, and  $\text{A}'^+\text{A}^{+}_n\text{B}^{2+}_n\text{X}^{-}_{3n+1}$  (ACI)<sup>52</sup>, where n corresponds structurally to the number of octahedra of the inorganic layer in the out-of-plane direction. From an electronic viewpoint, the n-value is directly connected to the structure’s quantum well thickness. The 3D halide perovskite structure can be conceptualized as the limit of this quasi-2D structure out to  $n=\infty$ , and n-values between 1 and  $\infty$  are expected to provide a tuning of the materials properties between those of an n1 2D and a pure 3D halide perovskite (**Figure 2d**).

In reality, pure quasi-2D halide perovskites with arbitrary n-value out to  $n=\infty$  cannot be physically realized. Usually, above a threshold n-value that varies depending on the structure and chemistry but can be as low as  $n=1$  and is practically limited to  $n=6-7$ , the system will form a mixture of 3D and lower-n 2D phases instead of a higher single n-value. **Table 2** lists A'-site cations which can form 2D halide perovskites with  $n>2$ , for which crystallographic data has been reported from single crystal diffraction. We note that this is not a comprehensive list of known 2D halide perovskites with  $n>2$ , as there have been several other reports of novel high-n 2D halide perovskites that did not include crystallographic data.<sup>61–64</sup> An effective average  $\langle n \rangle$  value is sometimes defined for mixed-n-value systems, although this terminology can be misleading given the differences in materials properties between a pure single-n-value system and an effective  $\langle n \rangle$  value system. It has been shown experimentally that for pure systems with n up to 5, the halide perovskite electronic properties are still

characteristic of 2D materials, which justifies the use of the quasi-2D terminology for pure systems. For mixed systems where  $\langle n \rangle$  reaches much higher values, the effective electronic dimensionality can be questioned. There are two factors determining the highest n ( $n_{\text{max}}$ ) of pure quasi-2D halide perovskites: thermodynamics and strain energy accumulation resulting from internal lattice mismatch.<sup>65</sup>

From a thermodynamics perspective, generally the enthalpy of formation ( $\Delta H$ ) is used to determine whether a pure quasi-2D material such as  $\text{BA}_2\text{MA}_{n-1}\text{Pb}_n\text{I}_{3n+1}$  (BA=butylammonium) is favorable or not with respect to a mixture of classical binary precursors such as MAI, BAI and  $\text{PbI}_2$  in solution based synthesis (calculated using enthalpy of solvation).<sup>66</sup> The assumption that the entropy of formation ( $\Delta S$ ) in the system is never positive is based on the highly ordered quantum well structure of the quasi-2D halide perovskite. Therefore, as  $\Delta G = \Delta H - T\Delta S$ , to obtain the negative  $\Delta G$ ,  $\Delta H$  has to be negative. For example, for BA MA 2D halide perovskites,  $\Delta H$  is negative for  $n=1$  to  $n=5$  and becomes positive for  $n=6$  and  $n=7$ .<sup>66</sup> These compositions were also found to be unstable with respect to the decomposition into the 3D halide perovskite  $\text{MAPbI}_3$ , and the BAI and  $\text{PbI}_2$  precursors. As a result, the highest n of BA MA 2D halide perovskite for a stable pure phase is  $n=5$ . However, the structural parameters for  $n=6$  and  $n=7$  were indeed successfully obtained from the analyses of diffraction patterns at the price of ignoring small contributions coming from minor phases<sup>66</sup>.

A complementary approach consists in trying to understand the origin of the internal energy accumulated in a quasi-2D lattice such as  $\text{BA}_2\text{MA}_{n-1}\text{Pb}_n\text{I}_{3n+1}$  from a mechanical perspective. For that purpose a quasi-2D system is envisioned as a composite formed by alternating  $n=1$  and bulk-like 3D layers, assembled through coherent interfaces<sup>67</sup> (**Figure 2e**). This concept is central for the analysis of the formation of heterostructures between different materials in the field of classical semiconductors. A  $n=1$  bulk 2D halide perovskite with an in-plane lattice parameter very different from the one of a targeted 3D bulk halide perovskite will most likely not form coherent interfaces in quasi-2D compounds, because the internal strain energy scales roughly as the square of the lattice mismatch between the two

bulk materials. As an example,  $\text{BA}_2\text{PbI}_4$  and  $\text{MAPbI}_3$  have an in-plane lattice mismatch on the order of 1%, which is usually considered in the field of classical semiconductors as an upper limit for the formation of heterostructures. However, the accumulation of strain energy in  $\text{BA}_2\text{MA}_{n-1}\text{Pb}_n\text{I}_{3n+1}$  is reduced by the flexibility of the BA cation<sup>67</sup>. Phenethylammonium (PEA) offers a counterexample, with  $(\text{PEA})_2(\text{MA})_{n-1}\text{Pb}_n\text{I}_{3n+1}$  having an in-plane lattice parameter very close to  $(\text{BA})_2(\text{MA})_{n-1}\text{Pb}_n\text{I}_{3n+1}$  but a maximum n-value of only 3 due to a lack of flexibility compared to BA (**Table 2**) (BA is a linear alkane, while PEA is an aromatic molecule). The relaxation of interface strain accumulated by lattice mismatch in a quasi-2D lattice also takes advantage of a specific feature of halide perovskite semiconductors. Strain relaxation only occurs in classical semiconductors through bond stretching or compression, but the energy cost is

lowered in halide perovskites by the tilting of the surface octahedra (octahedra that are bonded with the A' cations) and the elongation of the octahedron cage. Since the A' cations move together with the surface octahedra, the structure flexibility of organic cations will determine the extent of the relaxation. On the other hand, the stress is also a function of the size of the A site cation, as more stress will be built up as the size of A site cation increases.

The organic cations in 2D halide perovskite can relax the Goldschmidt tolerance factor, enabling larger A site cation incorporation into the  $\text{PbI}_6$  cage. For example, guanidinium ( $\text{GA}^+$ ), and dimethylammonium ( $\text{DMA}^+$ ) (**Figure 2f**) were too large to be incorporated into the  $\text{PbI}_6$  cage in 3D lead-iodide halide perovskites but could be fit into the cage in RP 2D halide perovskites with a BA spacer cation.<sup>68</sup>



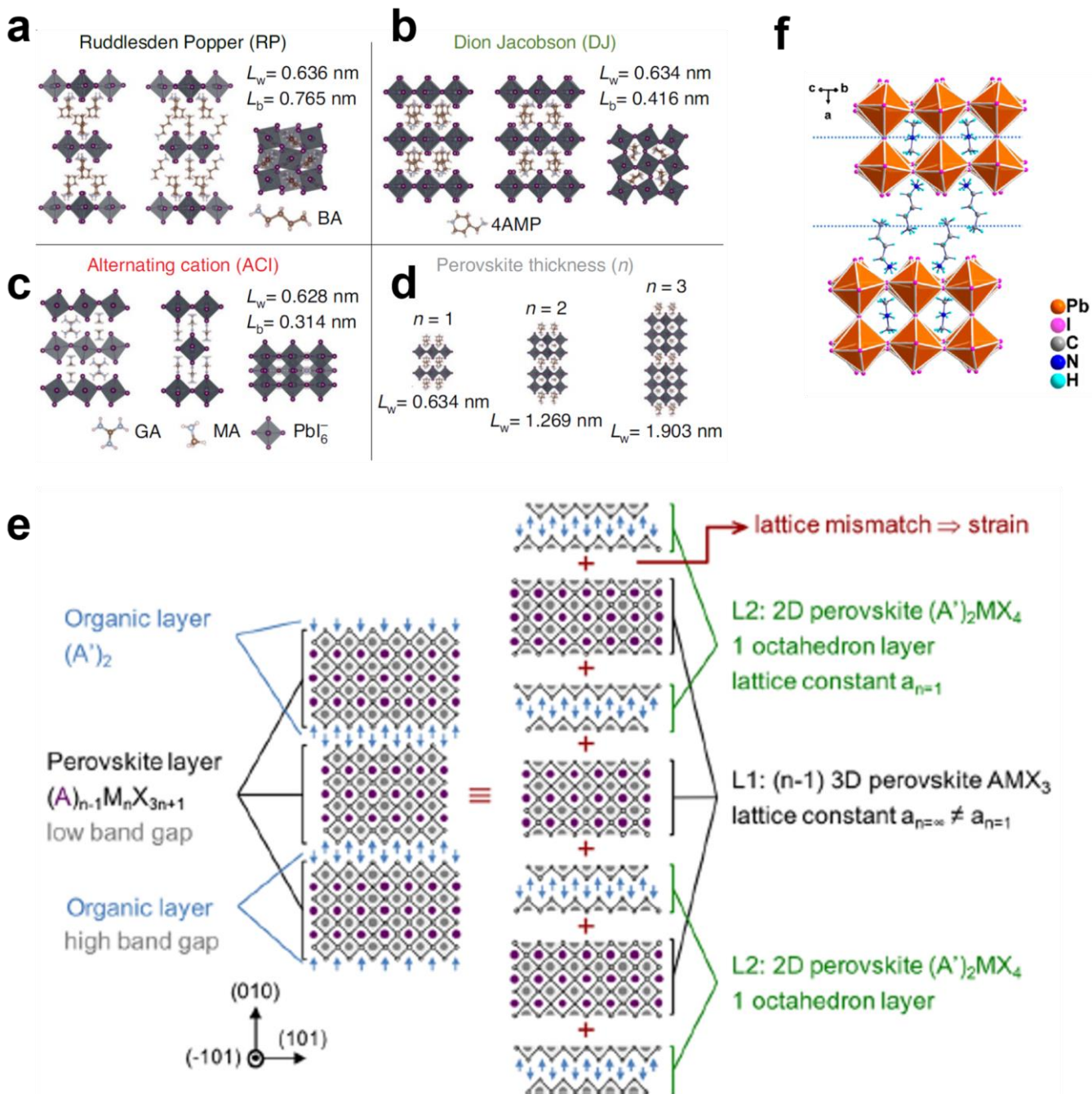


**Figure 2: The structures of 2D perovskites.** a-c) 3 types of 2D halide perovskite, which are (a) Ruddlesden Popper (RP), (b) Dion Jacobson (DJ) and (c) Alternating cation (ACI),  $n=1$ . d) RP structures for different perovskite thicknesses ( $n=1, 2, 3$ ), which corresponds to the number of octahedra along the stacking direction in the perovskite layers (Ranging from  $n = 1$  2D halide perovskite to 3D halide perovskite ( $n \rightarrow \infty$ )). (a-d) Reproduced with permission from ref.<sup>50</sup> Copyright 2020 Springer Nature. e) Schematic illustration of the lattice mismatch concept. 2D halide perovskite of  $n$  larger than 2 is regarded as L1/L2 with L1 the 3D ( $n = \infty$ ) bulk material, e.g.,  $\text{MAPbI}_3$ , and L2, a  $n = 1$  compound, e.g.,  $(\text{BA})_2\text{PbI}_4$ . Reproduced with permission from ref.<sup>67</sup> Copyright 2018 American Chemical Society. f) The structures of  $(\text{BA})_2(\text{DMA})\text{Pb}_2\text{I}_7$ , where DMA is a large A cation (geometric Goldschmidt tolerance factor is relaxed). Reproduced with permission from ref.<sup>68</sup> Copyright 2020 American Chemical Society.

**Table 2: Highest reported  $n$ -value for 2D halide perovskites that form  $n > 2$ . Only phases with published crystallographic data are collected.**



| Phase | A'                               | A                                   | B  | X  | max n | Ref |    |
|-------|----------------------------------|-------------------------------------|----|----|-------|-----|----|
| RP    | Ethylammonium (EA <sup>+</sup> ) | MA                                  | Pb | Br | 3     | 69  |    |
|       |                                  | EA                                  | Pb | Br | 3     | 70  |    |
|       |                                  |                                     |    | Cl | 3     | 71  | 70 |
|       | Propylammonium                   | MA                                  | Pb | I  | 4     | 72  |    |
|       | Butylammonium                    | MA                                  | Pb | I  | 7     | 66  |    |
|       |                                  |                                     |    | Br | 3     | 73  |    |
|       |                                  |                                     | Sn | I  | 3     | 74  |    |
|       |                                  |                                     |    | Br | 3     | 75  | 73 |
|       |                                  | EA                                  | Pb | I  | 3     | 76  | 77 |
|       |                                  | Cs                                  | Pb | Br | 3     | 78  |    |
|       | Pentylammonium                   | MA                                  | Pb | I  | 6     | 79  |    |
|       | Hexylammonium                    | MA                                  | Pb | I  | 4     | 80  | 81 |
|       | Allylammonium                    | MA                                  | Pb | I  | 3     | 82  |    |
|       |                                  | EA                                  | Pb | Br | 3     | 83  |    |
|       | Phenylmethylammonium             | MA                                  | Pb | I  | 3     | 61  |    |
|       | Phenylethylammonium              | MA                                  | Pb | I  | 3     | 49  |    |
|       | Benzylammonium                   | MA                                  | Pb | I  | 3     | 61  |    |
|       | 3-phenyl-2-propenammonium        | MA <sub>0.5</sub> FA <sub>0.5</sub> | Pb | I  | 3     | 84  |    |
|       | Isoamylammonium                  | MA                                  | Pb | Cl | 3     | 85  |    |
|       | Isoamylammonium                  | EA                                  | Pb | Br | 3     | 86  |    |
|       | 4-bromobutylammonium             | EA                                  | Pb | Br | 3     | 87  |    |
|       | 4-iodobutylammonium              | MA                                  | Pb | I  | 3     | 88  |    |
|       | 2-iodopropylammonium             | MA                                  | Pb | I  | 3     | 82  |    |
|       | 4-fluorophenylethylammonium      | MA                                  | Pb | I  | 3     | 89  |    |
|       | 2-thiophenemethylammonium        | MA                                  | Pb | I  | 3     | 90  |    |
|       | 4-Aminomethyl-1-                 | EA                                  | Pb | Br | 3     | 91  |    |

|     |                             |    |    |   |   |    |  |
|-----|-----------------------------|----|----|---|---|----|--|
|     | cyclohexanecarboxylate      |    |    |   |   |    |  |
| DJ  | 1,4-butanediammonium        | MA | Pb | I | 3 | 92 |  |
|     |                             | FA | Sn | I | 3 | 93 |  |
|     | 1,6-hexanediammonium        | MA | Pb | I | 3 | 92 |  |
|     | 1,7-heptanediammonium       | MA | Pb | I | 3 | 92 |  |
|     | 1,8-octanediammonium        | MA | Pb | I | 4 | 92 |  |
|     | 1,9-nonanediammonium        | MA | Pb | I | 4 | 92 |  |
|     | 3-(aminomethyl)piperidinium | MA | Pb | I | 4 | 51 |  |
|     | 4-(aminomethyl)piperidinium | MA | Pb | I | 7 | 94 |  |
|     | 3-(aminomethyl)pyridinium   | MA | Pb | I | 4 | 95 |  |
|     | 4-(aminomethyl)pyridinium   | MA | Pb | I | 4 | 95 |  |
|     | m-phenylenediammonium       | MA | Pb | I | 3 | 96 |  |
| ACI | Guanidinium                 | MA | Pb | I | 3 | 52 |  |
|     | Protonated thiourea         | MA | Pb | I | 3 | 97 |  |

### 3. Optoelectronic properties of 3D and 2D halide perovskites

#### 3.1. Semiconductor properties of 3D halide perovskites

##### 3.1.1. From structure to optoelectronic properties: The physical basis for 3D halide perovskites' bandgap

Many of the remarkable optoelectronic properties of ABX<sub>3</sub> halide perovskites which are not present in other halides are derived from the electronic configuration of the B-site cations and the corner-sharing BX<sub>6</sub> sublattice of the crystal structure<sup>98, 32, 99, 100</sup>. The B-site of a halide perovskite is conventionally a 2+ cation with an ns<sup>2</sup> configuration. In the case of the Pb<sup>2+</sup> cation, the electronic configuration is [Xe] 6s<sup>2</sup> 4f<sup>14</sup> 5d<sup>10</sup>, with the 6s states fully occupied and sitting below the halogen's filled p-orbital. As a result, the valence band maximum (VBM, highest-energy occupied electron state below the bandgap) of APbI<sub>3</sub> is formed from the antibonding molecular orbitals of the Pb 6s - I 5p states, whereas in most common semiconductor

materials the VBM would be composed of bonding molecular orbitals (**Figure 3a-c**).<sup>32</sup> This antibonding character of the VBM contributes significantly to halide perovskites' defect tolerance, which will be expanded upon later.<sup>101, 102</sup> The conduction band minimum (CBM, lowest-energy unoccupied electron state above the bandgap) of a halide perovskite is an antibonding molecular orbital of the B-site p- and X-site s-states, and is comprised mainly of the np atomic orbitals of the B-site. Group theory analysis reveals that the space group symmetry of the crystal prevents B-site and X-site p-state hybridization at the R-point where the VBM and CBM sit, which reduces the X-site character of the CBM.<sup>100</sup> As a result the VBM is more strongly influenced than the CBM by lattice distortions which change bond angles and distances.<sup>32</sup>

The X-site p-orbitals contributing to the VBM are directional, with two lobes of electron density pointing in opposite directions. By a stroke of good

luck, the B-X sublattice of a cubic halide perovskite crystal happens to be a 3D network of corner-sharing  $BX_6$  octahedra with X sites at the corners and B sites at the centers, such that each X-site's occupied p-orbital points directly towards both B-sites the anion is coordinated with. The valence band therefore has an exceptional degree of orbital overlap and the electronic structure takes on a delocalized character.<sup>98,103</sup> Extended electronic states dominate over localized states and the electronic dispersions display a direct bandgap with an allowed optical transition between twice degenerated conduction and valence bands with low and similar effective masses. In other words, it is an almost ideal situation for optoelectronic applications not even encountered in a III-V semiconductor such as GaAs.<sup>104</sup> Moreover, contrary to the initial expectations, it was shown that the binding energy of the exciton is small, leading to easy ionization at temperatures for device operations<sup>105,106</sup>, and the crystal thus demonstrates free-carrier rather than excitonic charge behavior with low effective masses. The ultimate limitations of the carrier mobilities, by comparison to classical semiconductors such as GaAs or Si, come not from unfavorable electronic band structures but from the softness of the lattice and the low-energy vibrational density of states which promotes charge carrier scattering<sup>107</sup>.

Lower-symmetry (tetragonal and orthorhombic) halide perovskite phases relax strain by distorting the network of  $BX_6$  octahedra. The octahedral sublattice distorts by reducing the B-X-B bond angle from the maximum value of  $180^\circ$  (cubic), which reduces the p-orbital overlap, reduces the covalency, and widens the bandgap.<sup>108,109</sup> For A-sites too large or too small for the octahedral sublattice to accommodate them, the structure breaks into a lower-dimensional network of edge- (e.g.,  $CsPbI_3$   $\delta$ -phase) or face- (e.g.,  $FAPbI_3$   $\delta$ -phase) sharing  $BX_6$  octahedra, for which the network of overlapping p-orbitals is lost. In these structures the delocalized character disappears, the bandgap widens, and the lattice no longer accommodates free-carrier charge transport. While A-site orbitals do not meaningfully contribute to the band structure, sitting far below the VBM, the A-site still is a crucial

contributor to the optoelectronic properties of 3D halide perovskites by stabilizing the corner-sharing  $BX_6$  sublattice.

Depending on the Pb-I-Pb bond angle,  $APbI_3$  halide perovskites vary in bandgap from 1.45-1.48eV (cubic  $FAPbI_3$ ) to 1.67-1.73eV (orthorhombic  $CsPbI_3$ ).<sup>8,109-111</sup> A 1.45eV bandgap is just slightly larger than the ideal bandgap for a solar cell according to the Shockley-Queisser limit, which is why most of the highest-performing 3D halide perovskite solar cells use a  $FAPbI_3$  or majority- $FAPbI_3$  absorber. In the general  $ABX_3$  structure increasing A-site radius can either decrease bandgap due to reduced octahedral distortions or increase bandgap due to lattice expansion (**Figure 3f**). Replacing Pb with Sn directly impacts the atomic orbitals comprising the VBM and CBM and lowers the bandgap, from 1.52eV for  $MAPbI_3$  to 1.30eV for  $MASnI_3$ <sup>8,112</sup> (**Figure 3e**). Replacing I with Br likewise influences the atomic orbital comprising the VBM and widens the bandgap to 2.34eV<sup>113</sup> (**Figure 3d**). Alloys of I/Br at the X-site can yield bandgaps intermediate between  $MAPbI_3$  and  $MABrI_3$  with a near-linear concentration dependence<sup>19</sup> (**Figure 3i**); however, Pb/Sn alloys at the B-site show a nonlinear, non-monotonic concentration dependence (**Figure 3h**), with  $MASn_{0.5}Pb_{0.5}I_3$  having a bandgap below 1.2eV.<sup>18</sup> This bowing behavior is common for  $APb_xSn_{1-x}X_3$  halide perovskites and appears to emerge from the competing influences of expansive lattice strain (bandgap-widening) and increasing Pb-I-Pb angle (bandgap-narrowing) as tolerance factor increases,<sup>108,114</sup> which also explains why the bandgaps of  $(FA_{1-x}Cs_x)PbI_3$  and  $(FA_{1-x}Cs_x)SnI_3$  show respectively positive and negative x-dependence (**Figure 3g**).<sup>108</sup> The bandgaps of selected halide perovskites are shown in **Table 3**.

Bandgap tunability through the alloying of A, B, and X sites unlocks new applications for perovskite absorbers. In the case of solar cells, lead iodide-based perovskites which incorporate Br or Sn can serve as wide-bandgap or narrow-bandgap layers in tandem solar cells, respectively, with bandgaps tuned to maximize the power conversion efficiency (PCE) of the full device.

**Table 3: Reported bandgaps of common halide perovskites.**  
Multiple values are given where reports conflict.

| A  | B                                   | X                                    | Bandgap | Ref  | Bandgap | Ref  | Bandgap | Ref  |     |
|--|-------------------------------------|--------------------------------------|---------|------|---------|------|---------|------|-----|
| MA   | Pb                                  | Cl                                   | 3.06    | 115  |         |      |         |      |     |
|  |                                     | Br                                   | 2.25    | 115  |         |      |         |      |     |
|  |                                     | Br <sub>0.5</sub> I <sub>0.5</sub>   | 1.8     | 19   |         |      |         |      |     |
|  | Pb <sub>0.5</sub> Sn <sub>0.5</sub> | I                                    | 1.61    | 115  | 1.55    | 18   |         |      |     |
|  |                                     | I                                    | 1.17    | 18   |         |      |         |      |     |
|  |                                     | Sn                                   | Cl      | 3.46 | 116     | 3.61 | 117     | 3.69 | 118 |
|  |                                     |                                      | Br      | 2.15 | 118     | 2.25 | 119     |      |     |
| I  | 1.3                                 |                                      | 18      | 1.3  | 112     | 1.15 | 120     |      |     |
| FA   | Pb                                  | Br                                   | 2.15    | 30   | 2.13    | 121  |         |      |     |
|  |                                     | Br <sub>0.5</sub> I <sub>0.5</sub>   | 1.62    | 122  |         |      |         |      |     |
|  |                                     | I                                    | 1.41    | 30   | 1.45    | 110  | 1.48    | 111  |     |
|  | Pb <sub>0.5</sub> Sn <sub>0.5</sub> | I                                    | 1.28    | 123  |         |      |         |      |     |
|  | Sn                                  | I                                    | 1.41    | 124  | 1.4     | 120  |         |      |     |
| Cs   | Pb                                  | Cl                                   | 3       | 125  | 2.85    | 126  | 2.86    | 127  |     |
|  |                                     | Br                                   | 2.4     | 125  | 2.23    | 126  | 2.24    | 127  |     |
|  |                                     | I                                    | 1.67    | 8    | 1.73    | 109  |         |      |     |
|  | Sn                                  | Cl                                   | 2.97    | 128  | 2.98    | 129  | 2.9     | 130  |     |
|  |                                     | Br                                   | 1.92    | 119  |         |      |         |      |     |
|  |                                     | I                                    | 1.3     | 42   | 1.3     | 8    |         |      |     |
| FA <sub>0.85</sub> Cs <sub>0.15</sub>                    | Pb                                  | I                                    | 1.52    | 10   |         |      |         |      |     |
| FA <sub>0.79</sub> MA <sub>0.16</sub> Cs <sub>0.05</sub> | Pb                                  | I <sub>0.83</sub> Br <sub>0.17</sub> | 1.6     | 17   |         |      |         |      |     |
| FA <sub>0.7</sub> MA <sub>0.3</sub>                      | Pb <sub>0.5</sub> Sn <sub>0.5</sub> | I                                    | 1.26    | 131  |         |      |         |      |     |
| FA <sub>0.85</sub> MA <sub>0.15</sub>                    | Pb                                  | I <sub>0.85</sub> Br <sub>0.15</sub> | 1.55    | 132  |         |      |         |      |     |

### 3.1.2. The origin of defect tolerance in 3D halide perovskites

halide perovskites appear to have high tolerance to point defects. This is unusual for halides which tend to exhibit high defect concentrations. High defect tolerance in a semiconductor has three possible explanations: a low defect density (either because of high defect formation energy or lattice self-healing), defect states being shallow or resonant

with band states, and defect states with low capture cross sections.<sup>133</sup> All these properties seem to coexist in halide perovskites to an extent.<sup>133–138</sup> Single crystals of halide perovskites have been reported with defect densities  $<10^{12}\text{cm}^{-3}$ ,<sup>139</sup> which is impressive even for inorganic semiconductors<sup>140</sup>; films of halide perovskites appear to have several orders of magnitude higher defect densities, although the reliable measurement of defects in films

is difficult.<sup>139</sup> Direct measurement of defect concentration or defect behavior is difficult not only for halide perovskites but for semiconductors in general, with experimental methods open to misinterpretation.<sup>135</sup> As such it has been difficult to disentangle the relative contribution of these three explanations for defect tolerance, or to quantify the relationship between defect density and performance in halide perovskites.

The defect tolerance of halide perovskites is at least in part derived from the antibonding character of the VBM, a result of the  $ns^2$  electronic configuration of the B-site cation<sup>98,135</sup>. With a VBM above the constituent atomic orbitals of both the X and B site ions, any defect states which would be expected to fall near or between these atomic orbitals (e.g., B-site vacancies) would be near or below the VBM, whereas with a VBM comprised of bonding states and a CBM of antibonding states the same defect levels may sit in the middle of the bandgap (**Figure 4b**). This design principle further suggests that a CBM composed of bonding states would grant additional defect tolerance.<sup>102,141</sup> Fortunately, the large energy difference between the Pb 6p and I 5p orbitals gives MAPbI<sub>3</sub>'s antibonding CBM almost entirely Pb 6p character and keeps it from being pushed up in energy such that donor defects become trap states<sup>98</sup>.

The ABX<sub>3</sub> halide perovskite structure has 12 possible intrinsic point defects: A-, B-, and X-site vacancies, A, B, and X interstitials, and the six possible substitutions between these three ions. In the case of MAPbI<sub>3</sub>, defects with low formation energy include I<sub>i</sub>, MA<sub>Pb</sub>, V<sub>MA</sub>, V<sub>Pb</sub>, MA<sub>i</sub>, Pb<sub>MA</sub>, and V<sub>i</sub>. It appears that these defects all form states at most 50meV into the bandgap, close to either the VBM or CBM.<sup>142</sup> Defect states with deeper levels such as I<sub>MA</sub>, I<sub>Pb</sub>, Pb<sub>i</sub>, and Pb<sub>i</sub> seem to have higher formation energy and low population in MAPbI<sub>3</sub> films at room temperature<sup>134,142,143</sup> (**Figure 4a**).

The halogen vacancy is of particular interest, being a common deep-level defect (F-center) in ionic halide crystals and even in some other  $ns^2$  halides. The strength of the interaction between the two B cations which bond to the vacancy site determines the position of the defect level. In the case of MAPbI<sub>3</sub>, the size of the A-site, along with Coulomb repulsion, gives a large Pb-Pb distance which minimizes this

interaction. The corner-sharing octahedral network in which only two B cations coordinate each X site also reduces the hybridization of cation p-orbitals at the vacancy<sup>98</sup>.

The recognition that  $ns^2$  cations are responsible for halide perovskite defect tolerance can help guide the search for future optoelectronic materials. Pb<sup>2+</sup>, Sn<sup>2+</sup>, Ge<sup>2+</sup>, Sb<sup>3+</sup>, and Te<sup>4+</sup> all adopt the  $ns^2$  configuration and may be promising candidates for semiconductors, although the  $ns^2$  orbital must be close enough in energy to the anion p-orbital to push the antibonding VBM above the level of cation vacancy states.<sup>102</sup>

Besides their shallow defect levels, halide perovskites are granted additional defect tolerance thanks to screening of electrostatic potentials by their high static dielectric constant of ~22, as well as by dynamical lattice screening through various ionic displacement or reorientation processes occurring across a wide frequency range, as is apparent in halide perovskites' complex dielectric permittivity spectra (**Figure 4c**).<sup>144</sup> Dynamic lattice effects will be discussed further below.

Related to the dynamic processes which contribute to dielectric screening, halide perovskite crystals also exhibit dynamic self-healing through ion migration and the re-forming of localized degradation products. Self-healing after humidity- or light-induced degradation will be discussed further in the context of halide perovskite stability below. In the context of defect tolerance, the possibility of dynamic defect formation and annihilation either through diffusion or through lattice reformation creates an upper limit to the possible defect concentration in the crystal bulk and limits the effect such defects can have on charges, as proposed by Rakita et al.<sup>145</sup> halide perovskites' low activation energy for ion hopping, discussed further below, allows for the diffusion of defects to surfaces on the time scale of seconds to hr. Further, dynamic lattice restructuring in halide perovskites can create and destroy local defects on timescales short enough that charges do not experience such defects as different from the lattice itself, which also allows for the screening of extrinsic or non-dynamic trap states by dynamic defects. Rakita et al. identify two key properties which a semiconductor should possess to exhibit such self-healing: a low formation energy with high entropic

stabilization which allows for the local dynamical breaking and reforming of the lattice, and a low activation energy for ion diffusion which allows for defect migration to surfaces within seconds. As will be discussed later, this dynamic lattice limits the degree to which halide perovskites can be doped, which explains why halide perovskites are almost always used as intrinsic semiconductors within devices.

Defect tolerance in halide perovskites also extends to A-, B-, and X-site alloying. Intuitively, a mixed-ion perovskite should show worse carrier

mobility and higher nonradiative recombination than a pure system because of the introduction of local lattice strain. However, both mixed-cation and mixed-anion perovskites have in fact shown suppressed nonradiative recombination and enhanced charge transport compared to their pure counterparts.<sup>105,146,147</sup> The dynamic lattices of halide perovskites affords tolerance towards local strain, and such strain can actually help suppress collective lattice dynamics which hinder charge transport.<sup>105</sup>

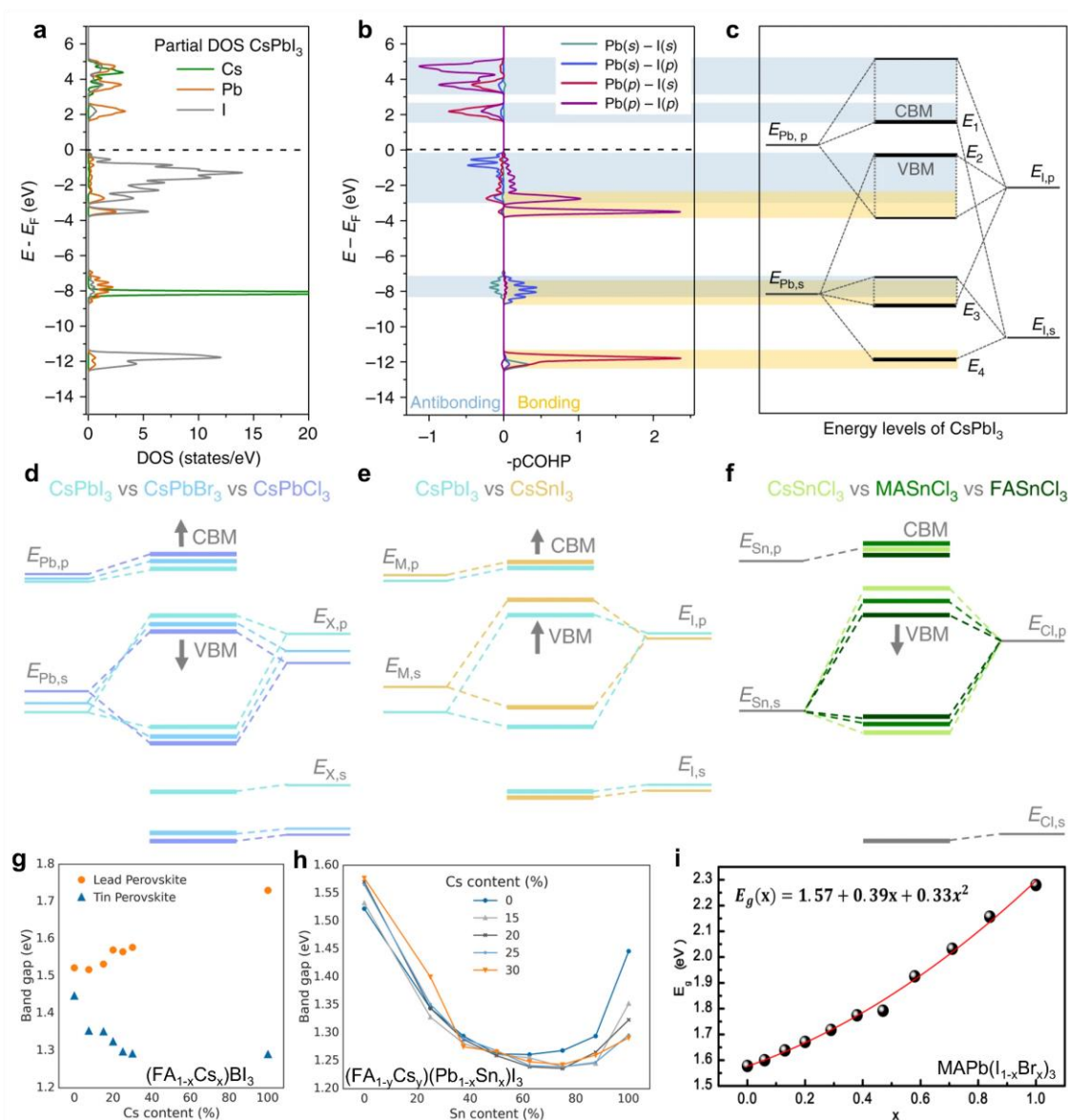


**Figure 3: Bandgap of 3D perovskites.** a) CsPbI<sub>3</sub> partial density of states for Cs, Pb, and I atoms. b) CsPbI<sub>3</sub> Crystal Orbital Hamiltonian Population analysis showing bonding (positive) and antibonding (negative) character. c) Schematic energy level diagram for CsPbI<sub>3</sub>. d) Influence of X-site on energy level diagram for CsPbX<sub>3</sub> series. e) Influence of B-site on energy level diagram for CsBi<sub>3</sub> series. f) Influence of A-site on energy level diagram for ASnCl<sub>3</sub> series, showing non-intuitive bandgap increase with cation size. This increase is a result of lattice expansion with larger tolerance factor in MASnCl<sub>3</sub> and FASnCl<sub>3</sub>. The VBM is more affected than the CBM because of its greater B-X hybridization. (a-f) reproduced with permission from ref.<sup>32</sup> Copyright 2019 Springer Nature. g) Effect of Cs incorporation on bandgaps of (FA<sub>1-x</sub>Cs<sub>x</sub>)PbI<sub>3</sub> and (FA<sub>1-x</sub>Cs<sub>x</sub>)SnI<sub>3</sub>. Bandgap decreases with Cs for (FA<sub>1-x</sub>Cs<sub>x</sub>)SnI<sub>3</sub> as lattice contracts, and increases with Cs for (FA<sub>1-x</sub>Cs<sub>x</sub>)PbI<sub>3</sub> as octahedra distort. h) Effect of Sn incorporation on bandgaps of (FA<sub>1-y</sub>Cs<sub>y</sub>)(Pb<sub>1-x</sub>Sn<sub>x</sub>)I<sub>3</sub> showing non-monotonic x-dependence. Bowing effect decreases with y as (FA<sub>1-y</sub>Cs<sub>y</sub>)SnI<sub>3</sub> tolerance factor is reduced. (g-h) reproduced with permission from ref.<sup>108</sup> Copyright 2017 American Chemical Society. i) Effect of Br incorporation on bandgap of MAPb(I<sub>1-x</sub>Br<sub>x</sub>)<sub>3</sub> showing monotonic increase with x. Reproduced with permission from ref.<sup>19</sup> Copyright 2013 American Chemical Society.

### 3.1.3. Nonradiative recombination in 3D halide perovskites

The defect tolerance of 3D halide perovskites contributes to their low nonradiative recombination, as quantified by the open-circuit

voltage ( $V_{OC}$ ) deficit of halide perovskite solar cells<sup>20</sup>. When sunlight excites charges in a solar cell, it splits the quasi-Fermi levels of electrons and holes. The difference between these quasi-Fermi levels is the achievable  $V_{OC}$  for a solar cell. Any non-radiative recombination of electrons and holes reduces the quasi-Fermi level splitting, lowering achievable  $V_{OC}$ . The  $V_{OC}$  deficit  $E_g/q - V_{OC}$ , the difference between the bandgap voltage and  $V_{OC}$ , correlates with the halide perovskite's nonradiative recombination rate. State-of-the-art 3D halide perovskite devices have shown  $V_{OC}$  deficits as low as 0.4 compared to their Shockley-Queisser (SQ) minimum  $V_{OC}$  deficit of 0.27, much better than other solution-processed photovoltaics such as organic photovoltaics (OPV) or dye-sensitized solar cells (DSSC) but still worse than GaAs or GaInP<sup>143</sup> (**Figure 4d**).

It appears that nonradiative recombination can be suppressed in halide perovskites through the strong coupling between the soft lattice and free carriers, which is discussed further below. Dynamic lattice distortions around a carrier can minimize the effect of electric fields generated by trap states on the carrier and reduce those trap states' capture cross sections. Screening from the material's high static dielectric constant also has an effect.<sup>148</sup>

A once-popular explanation for the low recombination rates in 3D halide perovskites is the existence of a bulk Rashba effect. In noncentrosymmetric crystals, electrons can feel an effective magnetic field from spin-orbit coupling (SOC) which lifts electron spin degeneracy and creates an indirect bandgap, suppressing recombination. The heavy Pb and I ions in MAPbI<sub>3</sub> indeed show significant SOC, but whether or not MAPbI<sub>3</sub> is centrosymmetric has been a subject of debate. More recently it has appeared that MAPbI<sub>3</sub> is indeed centrosymmetric, and no static bulk Rashba effect exists<sup>149</sup> (**Figure 4e**). Moreover, depolarization fields strongly reduce the impact of bulk polarizations in halide perovskites, which do not belong to the category of hyperferroelectric materials<sup>150</sup>. There may be a dynamic Rashba effect due to inversion symmetry breaking from MA cation rotations, but recent work has suggested that this effect is not large enough to cause meaningful band splitting.<sup>149</sup> However, local polarization effects

should not be ignored, since any local symmetry breaking in such highly ionic materials shall lead to the creation of a local charge or dipole.

Although the effects of defects are suppressed in 3D halide perovskites, shallow trap states from charged defects are still a major contributor to nonradiative recombination. Defect states at grain boundaries and interfaces in particular seem to be detrimental to charge extraction. Many of the innovations made to push halide perovskite device efficiency higher have centered around reducing or passivating these defect states.



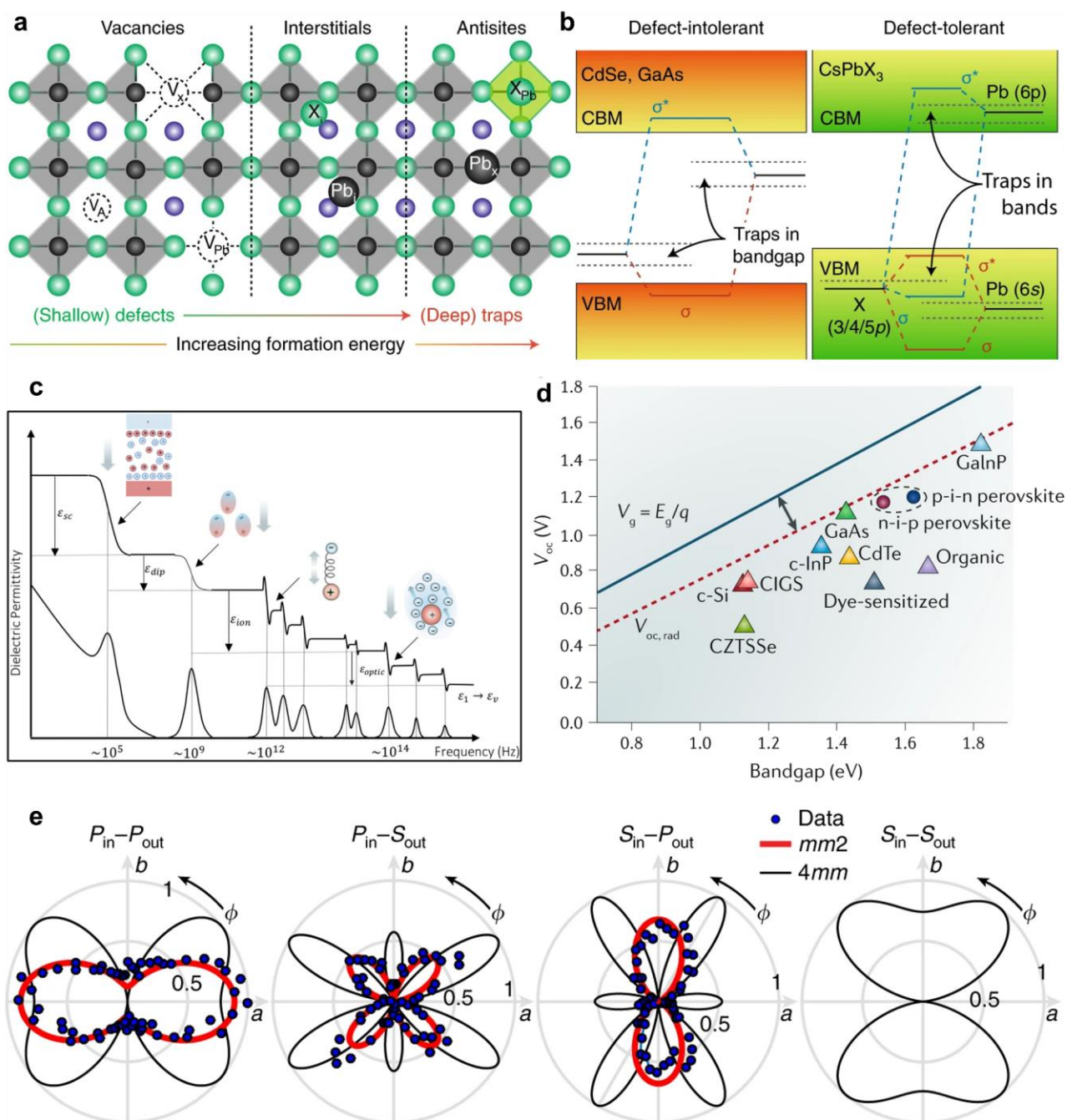


**Figure 4: Defect tolerance and nonradiative recombination in 3D perovskites.** a) Schematic of point defects found in  $ABX_3$  perovskites. Defects with low formation energies tend to be shallow, whereas deep-level defects usually have high formation energies. b) Schematic energy level diagram showing how the antibonding VBM and the CBM with majority Pb-character allow most  $MAPbI_3$  defect levels to fall outside of the bandgap, in contrast to inorganic semiconductors. (a-b) reproduced with permission from ref.<sup>151</sup> Copyright 2018 Springer Nature. c) Schematic permittivity spectrum of a perovskite showing the contributions of lattice dynamics and ion migration. Reproduced with permission from ref.<sup>144</sup> Copyright 2019 American Institute of Physics. d) Best-reported  $V_{oc}$  values for a variety of solar cell absorbers, plotted against absorber bandgap. The solid line shows the bandgap voltage, and the dashed line shows the maximum  $V_{oc}$  allowed by the Shockley-Queisser limit. Reproduced with permission from ref.<sup>143</sup> Copyright 2019 Springer Nature. e) Polar plots of  $MAPbI_3$  Second Harmonic Generation Rotational Anisotropy experiments for parallel (P) or perpendicular (S) incident (in) and outgoing (out) light. Data fits excellently with theory for the surface  $mm2$  point group of a centrosymmetric  $I4/mcm$  space group crystal, rather than the  $4mm$  point group of a noncentrosymmetric  $I4cm$  crystal. Reproduced with permission from ref.<sup>149</sup> Copyright 2018 Springer Nature.

### 3.1.4. Carrier transport in 3D halide perovskites

The high covalency afforded by the 3D network of overlapping Pb-I orbitals in halide perovskite crystals gives a delocalized electronic structure leading to a low exciton binding energy and free-carrier-like charge transport.<sup>98,105</sup> The exciton binding energy of MAPbI<sub>3</sub> is 16meV in the low temperature orthorhombic phase (**Figure 5a**), comparable to that of Si (15meV), and <10 meV in the room temperature tetragonal phase. This energy is well below the thermal energy  $k_B T$  at room temperature (about 25meV)<sup>105,106,152</sup>. As a result, excitons in MAPbI<sub>3</sub> are easily dissociated into free carriers at room temperature. The electron and hole effective masses appear to be comparable, with an exciton reduced effective mass  $m^* = (1/m_e + 1/m_h)^{-1}$  of  $0.104m_e$ <sup>106</sup>. The charge carrier mobility of 3D halide perovskites is on the order of tens of  $\text{cm}^2/(\text{Vs})$ , and the carrier diffusion length can range from 100s of nm in films to 100s of  $\mu\text{m}$  in single crystals<sup>153,154</sup>.

The soft lattice of 3D halide perovskites gives experimentally a low-energy density of optical vibrations that as a result have a high population at room temperature<sup>155</sup>, therefore promoting electron-lattice coupling which is much more pronounced than in inorganic semiconductors<sup>107</sup>. The high dielectric constants of 3D halide perovskites gives phonons a greater effect on local electric fields, enhancing coupling further.<sup>156</sup> It is often suggested that the strong electron-phonon interactions in halide perovskites could manifest in polaronic charge transport, whereby charge carriers couple to local lattice deformations which travel together as a quasiparticle<sup>157–160</sup>. While it appears that some form of local polaronic behavior is present in these materials<sup>161</sup> (**Figure 5b**), many materials properties including the temperature dependence of the carrier mobility are inconsistent with a polaron model<sup>156,162</sup> (**Figure 5c**). Indeed state of the art modeling of carrier mobilities clearly states that extended Fröhlich polaron mechanisms have a negligible effect.<sup>107</sup> A complementary picture of electron-phonon interactions is based on the dynamic disorder model, which aims at capturing the anharmonicity of 3D halide perovskites' lattice<sup>156</sup> (**Figure 5d**). It is indeed nowadays very often assumed that optical phonons have a protective

effect on charge carriers, with local lattice deformation leading to longer carrier lifetime. This effect is a double-edged sword, however, causing a decrease in carrier mobility. Most analyses nevertheless rely on idealized or weakly anharmonic phonon pictures that do not match the direct experimental observations of the lattice dynamics displaying overdamped and dispersionless optical branches<sup>155</sup>, as well as various low-frequency stochastic relaxational motions.<sup>163</sup> It is therefore urgently needed to propose theoretical treatments of lattice anharmonicity and electron-phonon coupling far beyond classical perturbative or self-consistent approaches. Using such approaches, a correct picture of the lattice dynamics can be recovered with a strong impact on the electronic properties including bandgap renormalization and smearing of both electronic and vibrational densities of states<sup>164</sup>.

It has been suggested that dynamic ordering of the  $ns^2$  lone pairs on B-site cations contributes to the high dielectric function and acts to protect charges in 3D halide perovskites<sup>148</sup>. The sp antibonding state comprising the halide perovskite's VBM is stabilized through hybridization between the B cation's s state (VBM) and p state (CBM), facilitated by the anion p state. With some p-character, the VBM state now shows an asymmetric electron density directed towards one of the B cation's coordination sites. This results in an inherent lattice instability that can manifest as dynamic B-cation off-center displacement. The flat-bottom potential of B-cation reorientation in 3D halide perovskites allows for dynamic local reorientation in the presence of free carriers, manifesting in a ferroelectric-like increase in the dielectric function in the THz regime and electron-lattice coupling which can reduce scattering.

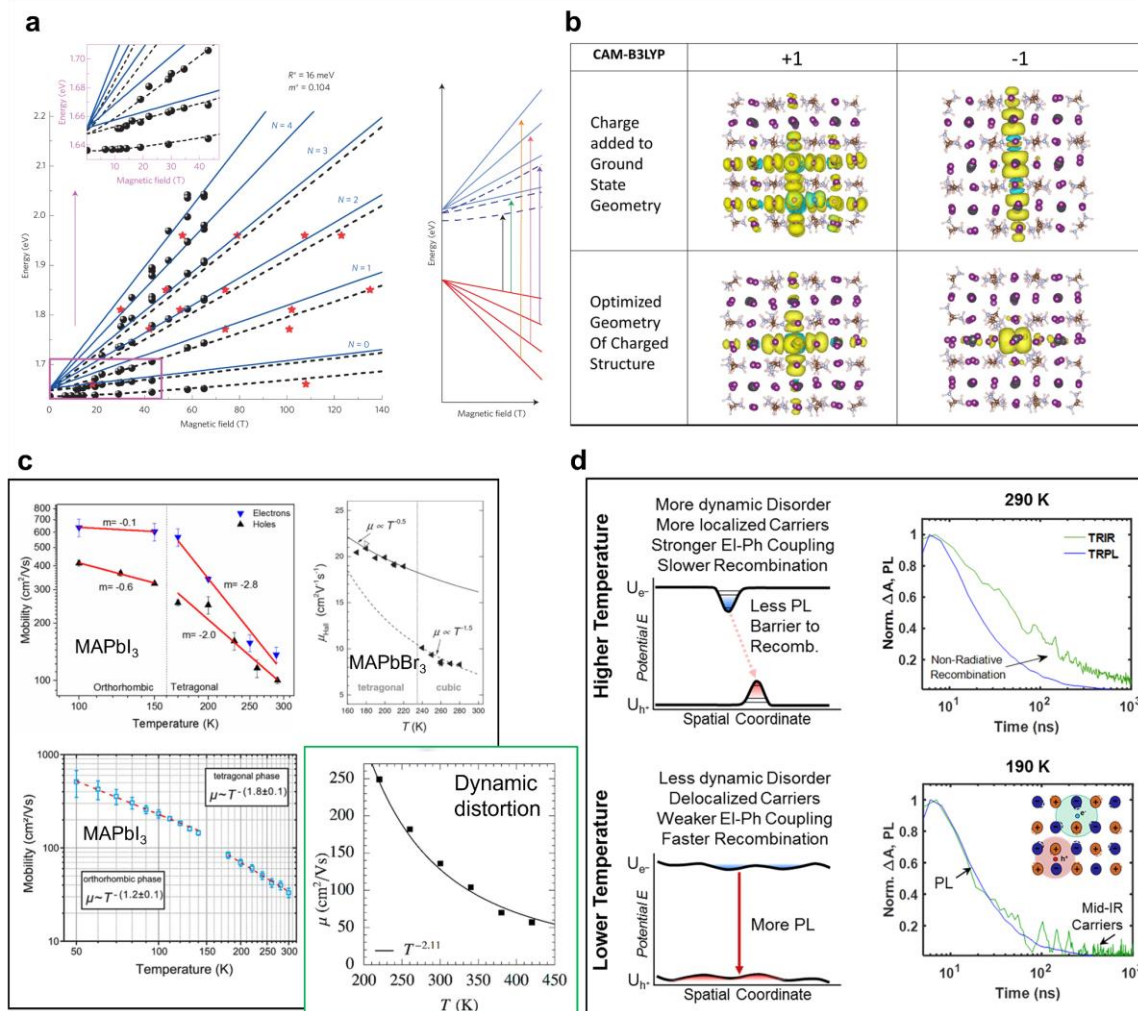


**Figure 5: Carrier transport in 3D perovskites.** a) Left: Magnetic field-dependence of low-temperature MAPbI<sub>3</sub> energy transitions, including free-carrier transitions (blue solid lines) are from long-pulse fixed-field measurements (black circles), and exciton transitions (black dashed lines) from fixed-energy fast-field-sweep measurements. An exciton binding energy of 16meV is calculated. Right: A schematic of free-carrier levels (solid lines) and excitonic levels (dashed lines), showing transitions. Reproduced with permission from ref.<sup>106</sup> Copyright 2015 Springer Nature. b) Calculated hole (left) and electron (right) spin density for neutral (top) and charged (bottom) CsPbI<sub>3</sub> cluster showing charge localization through lattice distortion. Reproduced with permission from ref.<sup>165</sup> Copyright 2016 American Chemical Society. c) Various measurements of temperature-dependent mobility for perovskites showing a  $T^{-\gamma}$  dependence for  $1.5 < \gamma < 3$  near room temperature. Top left: Time-of-flight measurements of MAPbI<sub>3</sub> single crystals, reproduced with permission from ref.<sup>166</sup> Copyright 2018 American Chemical Society. Top right: Hall measurements of MAPbBr<sub>3</sub> single crystals, reproduced with permission from ref.<sup>167</sup> Copyright 2016 Wiley-VCH. Bottom left: Optical measurements of MAPbI<sub>3</sub> thin films, reproduced with permission from ref.<sup>168</sup> Copyright 2019 American Chemical Society. Inset in green shows results of dynamic distortion model for MAPbI<sub>3</sub> predicting  $\gamma \sim 2.1$ , reproduced with permission from ref.<sup>169</sup> Fröhlich large polaron models predict  $\gamma \sim 0.5-1$ . Copyright 2018 American Chemical Society. (c) adapted with permission from ref.<sup>156</sup> Copyright 2021 American Chemical Society. d) Schematic of temperature dependence of recombination as explained by dynamic disorder model. Reproduced with permission from ref.<sup>170</sup> Copyright 2018 Elsevier.

### 3.1.5. Urbach Energy in 3D halide perovskites

The Urbach energy  $E_U$  of a solar cell's absorber layer is also correlated with its  $V_{OC}$  deficit (Figure 6b). 3D halide perovskites show Urbach

energies comparable to those of GaAs (7.5meV) and c-Si (12.5meV) as shown in Figure 6a-b, which is remarkable for such soft materials<sup>171</sup>. halide perovskite films have static Urbach energies (i.e.  $E_U$  at 0K) between 3.5 and 5meV,<sup>172,173</sup> lower

than the static  $E_U$  of GaAs, GAN, InP, or c-Si (**Figure 6c**).<sup>173</sup> At room temperature, halide perovskite films show  $E_U$  as low as 11meV (MAPbI<sub>3</sub>)<sup>174</sup> or 13meV (FAPbI<sub>3</sub>),<sup>175</sup> although some halide perovskites such as CsPbI<sub>3</sub> have  $E_U$  as high as 77meV.<sup>176</sup> Notably, halide perovskite films do not have significantly higher  $E_U$  than single crystals.<sup>171</sup> These small Urbach tails and steep absorption edges indicate a high degree of nanoscale crystallinity. Molecular dynamics

simulations have suggested that although halide perovskites show anharmonic nuclear dynamics and disorder at room temperature, MAPbI<sub>3</sub> and CsPbI<sub>3</sub> exhibit short-range disorder potentials within a bond length (**Figure 6d**). The correlation length of the disorder potential in these materials is comparable to that of Si and GaAs, which is possible because of dynamic displacements of primarily the X anion and indirectly from the A cation.<sup>177</sup>

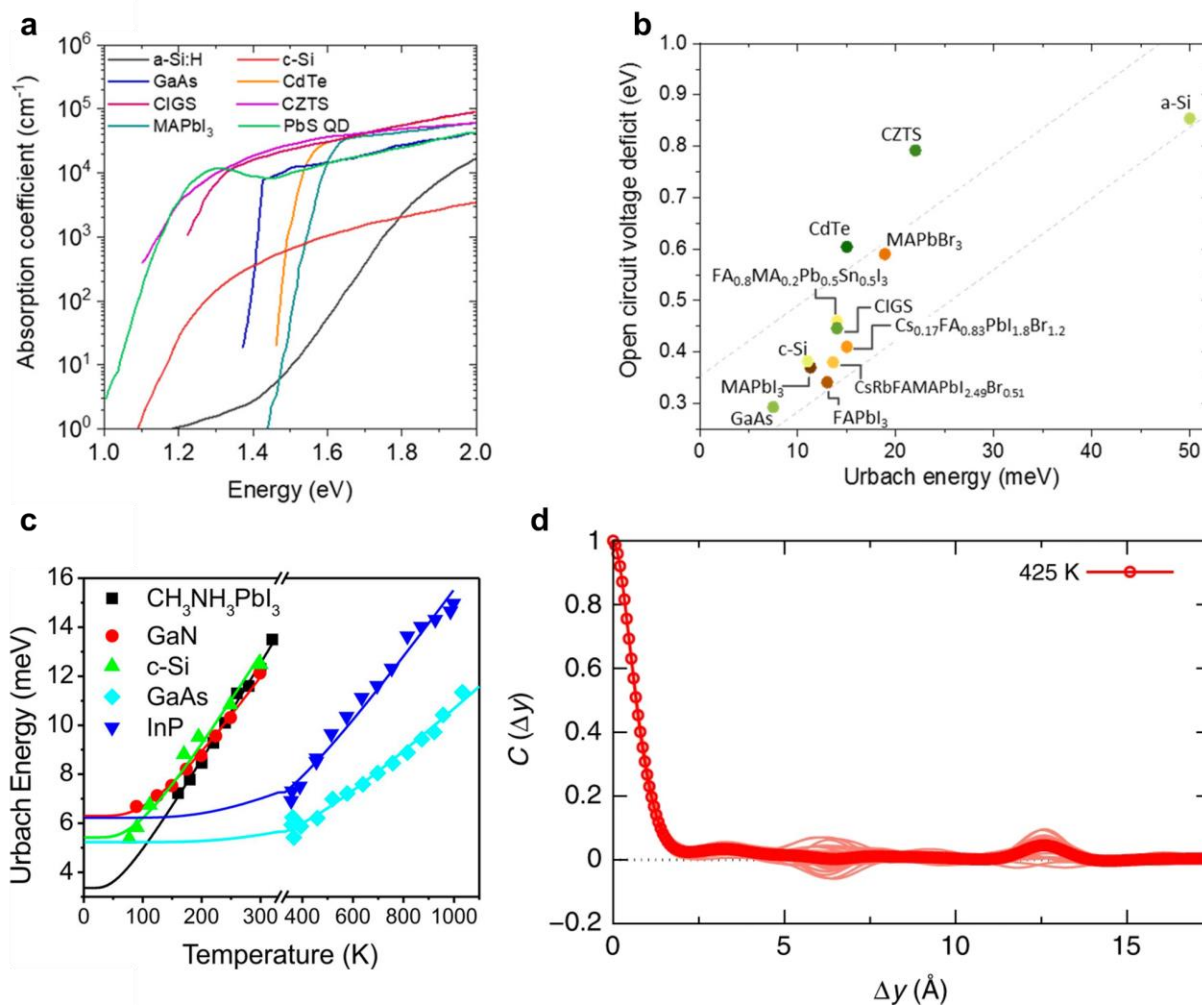


**Figure 6: Sharp optical absorption edge in 3D perovskites.** a) Comparison of absorption spectra for various photovoltaic absorbers showing excellent MAPbI<sub>3</sub> Urbach energy, reproduced with permission from ref.<sup>178</sup> Copyright 2017 American Chemical Society. b)  $V_{OC}$  deficit plotted against Urbach energy for a variety of perovskite and inorganic semiconductors, reproduced with permission from ref.<sup>172</sup> Copyright 2020 American Chemical Society. (a-b) reproduced with permission from ref.<sup>171</sup> Copyright 2022 American Chemical Society. c) Temperature-dependence of Urbach energy for a variety of semiconductors showing the extremely low static Urbach energy of MAPbI<sub>3</sub> (black). Reproduced with permission from ref.<sup>179</sup> Copyright 2019 American Chemical Society. d) Autocorrelation function of the disorder potential of MAPbI<sub>3</sub> at 425K calculated using molecular dynamics (MD). Thick curve is the average of snapshots along force-field MD trajectory (thin curves). Reproduced with permission from ref.<sup>177</sup> Copyright 2019 Springer Nature.



### 3.1.6. Solution processability of 3D halide perovskites

Because of their ionic nature, their soft lattice, and their low lattice energy, halide perovskites have the distinct advantage over inorganic semiconductors of being solution processable.<sup>180–187</sup> High-quality halide perovskite films can be prepared by dissolving precursor AX and BX<sub>2</sub> salts in a mixture of polar aprotic solvents such as 4:1 DMF:DMSO, precipitating the halide perovskite phase with an antisolvent, and annealing (**Figure 7a-d**). In this case DMF acts as a solute and DMSO as a Lewis base to complex with the precursor salts in solution. In the case of MAPbI<sub>3</sub>, IR Spectroscopy shows a decrease in stretching frequency for the S=O bond of DMSO upon incorporation of PbI<sub>2</sub> and MAI+PbI<sub>2</sub> powders, confirming the formation of PbI<sub>2</sub>·DMSO and MAI·PbI<sub>2</sub>·DMSO adducts.<sup>187</sup> This MAI·PbI<sub>2</sub>·DMSO adduct phase corresponds to the white film seen for MAPbI<sub>3</sub> before annealing. By exploiting the volatility of DMSO in this adduct, annealing of the film can remove the DMSO and leave a dense film of MAPbI<sub>3</sub> (**Figure 7f**). Films of MAI·PbI<sub>2</sub>·DMSO adducts are precipitated during spin-coating by dripping an antisolvent that is miscible with the precursor solvent but does not dissolve the halide perovskite precursors (e.g., Toluene)<sup>186</sup>. For FAPbI<sub>3</sub>, DMSO is sometimes fully or partially replaced with a more suitable Lewis base such as NMP<sup>188</sup> or thiourea.<sup>189</sup> A two-step deposition method can also be employed, whereby FAI is deposited on top of a PbI<sub>2</sub>·DMSO film to form FAPbI<sub>3</sub> through FAI-DMSO intramolecular exchange.<sup>190</sup> As with MAPbI<sub>3</sub>, each of these FAPbI<sub>3</sub>-adduct films can then be annealed to drive off the Lewis base and leave compact FAPbI<sub>3</sub> films, with the caveat that the halide perovskite must be heated to 150°C to form the high-temperature black phase. Thermodynamically stable halide perovskite phases such as MAPbI<sub>3</sub> are usually processed at temperatures below 100°C, and pinhole-free films can even be achieved at room temperature through solvent engineering<sup>185</sup> (**Figure 7e**). Solution-based processing also allows for the easy incorporation of additives (e.g., for defect passivation or to control film growth kinetics) or the alloying of A-, B-, or X-site ions through the mixing of their salts.<sup>18,19,191</sup>

Scaling up of perovskite devices is another requirement for commercialization, since the conventional spin-coating film deposition techniques are limited to devices  $\leq 1\text{cm}^2$  compared to a  $>800\text{cm}^2$  commercial module.<sup>192</sup> Fortunately, a variety of techniques have been demonstrated for forming high-quality large-area halide perovskite films, including blade coating, slot-die coating, spray coating, and electrodeposition.<sup>193</sup> It is important to note that each of these techniques place different constraints on the solvents, antisolvents, and deposition steps possible for film formation, depending on factors including solvent evaporation rate.<sup>192</sup> Moreover, solution processing offers opportunities for low-cost, high-throughput manufacturing compared to the conventional high-temperature crystal growth and wafer processing used for inorganic solar cells.<sup>4</sup> Low-temperature solution processing may also one day enable a roll-to-roll manufacturing process on flexible substrates which promises high-throughput mass production.<sup>193,194</sup> For interested readers, the review article *Scalable fabrication and coating methods for perovskite solar cells and solar modules* by Park and Zhu provides an excellent introduction to large-area perovskite deposition technologies and considerations for their use.<sup>192</sup>

However, it is important to note that not only the halide perovskite layer but every layer in the device stack must be processable via low-cost techniques to realize cheap devices, and in particular must be low-temperature processable for flexible substrates.<sup>195</sup> Conventional perovskite solar cells use an intrinsic (undoped, “i”) halide perovskite layer sandwiched between an n-doped electron transport layer (ETL, “n”) and a p-doped hole transport layer (HTL, “p”). So-called “regular” (n-i-p) perovskite device architectures place the ETL between the substrate/bottom contact and the perovskite, and place the HTL between the perovskite and the top contact. Common ETLs for regular-architecture devices are metal oxides such as TiO<sub>2</sub> and SnO<sub>2</sub>, which generally have high processing temperatures. These considerations have motivated research on inverted (p-i-n) halide perovskite devices, with a hole-collecting substrate and electron-collecting top contact, because of the reduced temperatures required for processing the substrate HTL in an

inverted device stack compared to mesoporous TiO<sub>2</sub> for a regular stack.<sup>196</sup> High processing temperatures

for transport layers also limit the possibilities for two-terminal tandem devices.<sup>197</sup>

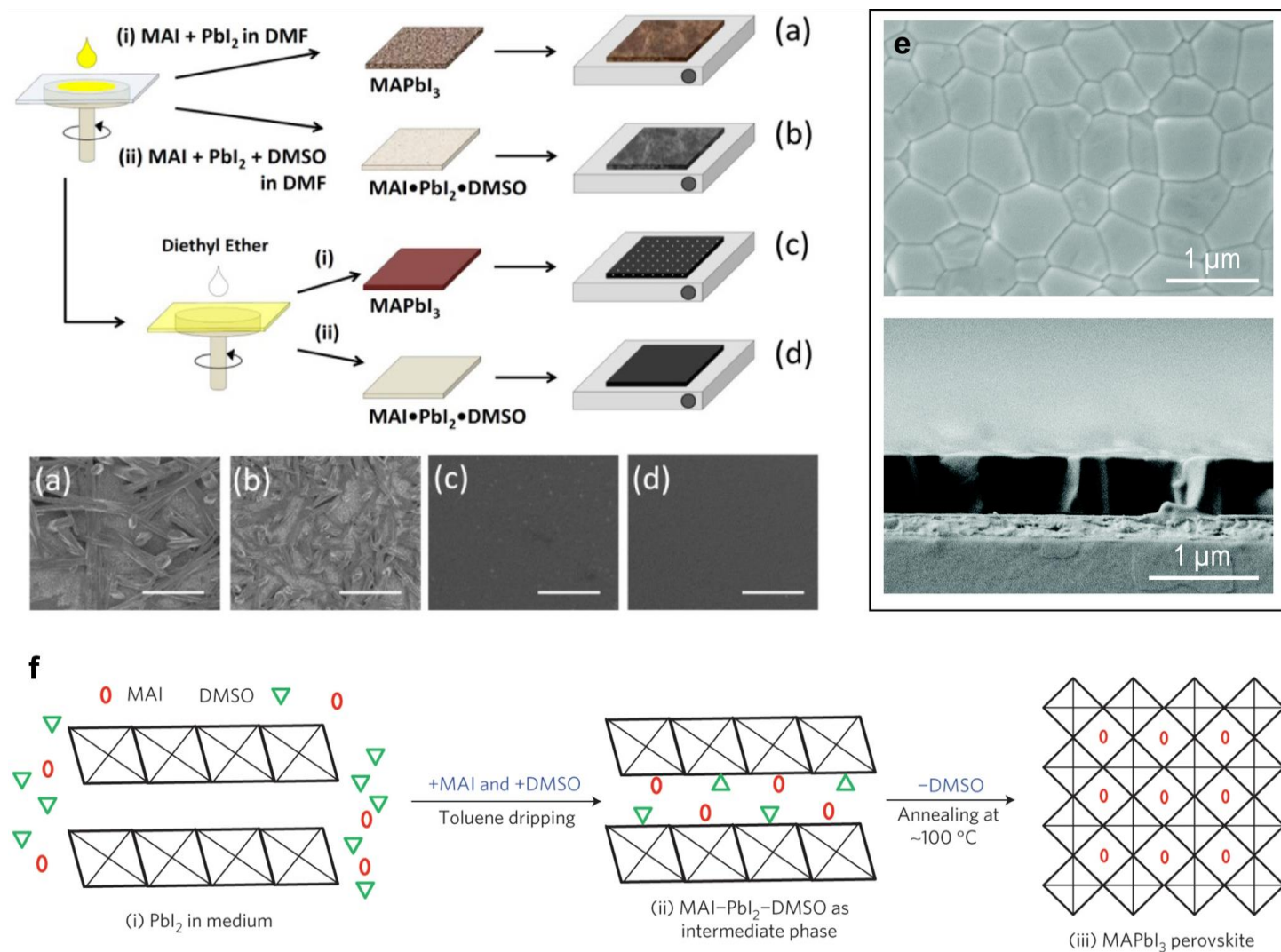


**Figure 7: Solution processing of 3D perovskites.** (a-d) Schematic of film deposition pathways for MAPbI<sub>3</sub> and their resulting microstructures. The use of a Lewis base (DMSO) and an antisolvent (Diethyl Ether) gives compact, high-quality MAPbI<sub>3</sub> films as in (d). (a-d) reproduced with permission from ref.<sup>187</sup> Copyright 2015 American Chemical Society. (e) SEM images of highly crystalline and pinhole-free MAPb(I<sub>1-x</sub>Cl<sub>x</sub>)<sub>3</sub> film grown at room temperature through the formation of a metastable intermediate 2D phase. Reproduced with permission from ref.<sup>185</sup> Copyright 2020 Royal Society of Chemistry. (f) Schematic showing the formation of an MAI·PbI<sub>2</sub>·DMSO adduct complex as an intermediate phase for perovskite crystal growth. Reproduced with permission from ref.<sup>186</sup> Copyright 2014 Springer Nature.

### 3.1.7. Ionic mobility in 3D halide perovskites and resistance to extrinsic electrical doping

The soft lattice of 3D halide perovskites allows for significant ionic mobility in the crystal. DFT simulations of MAPbI<sub>3</sub> disagree on the precise activation energies for ion diffusion but agree that I<sup>-</sup> is the most mobile species, hopping along the edges of PbI<sub>6</sub> octahedra. In comparison, MA<sup>+</sup> is less mobile,

hopping through the face of the cuboctahedral site, and Pb<sup>2+</sup> is the least mobile, hopping diagonally across the cuboctahedral face<sup>198,199</sup> (Figure 8a). Ionic mobility is a significant contributing factor to the significant current-voltage hysteresis observed in 3D halide perovskite solar cells which will be expanded upon in section IV. Reports on the temperature-dependence of conductivity in MAPbI<sub>3</sub> have found a

clear transition in slope around room temperature which suggests a switch in the principal charge-carriers from electrons (low-T) to ions (high-T)<sup>200,201</sup> (**Figure 8b**). These measurements confirmed that at room temperature MAPbI<sub>3</sub> is effectively a mixed ionic-electronic conductor.

Related to halide perovskites' ionic mobility is their resistance to be extrinsically electronically doped<sup>202</sup>. Although many impurities are expected to introduce shallow donor or acceptor states into the lattice, charge compensation by mobile ions and intrinsic defects limits the effect of introducing dopants. DFT simulations suggest that degenerate p-doping is possible in MAPbI<sub>3</sub> by substitution of Pb<sup>2+</sup> with Na<sup>+</sup> or K<sup>+</sup>, or substitution of I<sup>-</sup> with O<sup>2-</sup>, but that extrinsic n-doping cannot achieve a higher concentration than what is possible with intrinsic doping in MAPbI<sub>3</sub>.

As many intrinsic defects are shallow donors or acceptors, some degree of control over the Fermi level can be achieved by controlling the concentration of intrinsic defects. By tuning the I:Pb ratio in MAPbI<sub>3</sub>, the ratio between the crystal's dominant donor defects (MA<sub>i</sub>, Pb-rich conditions) and acceptor defects (V<sub>Pb</sub>, Pb-poor conditions) can be controlled to raise or lower the Fermi level<sup>203</sup> (**Figure 8c**). However, most studies have found an intrinsic carrier density cap of <10<sup>14</sup> for MAPbI<sub>3</sub><sup>202</sup>. Charge transfer doping between a halide perovskite and a p-doped or n-doped substrate has been observed to dictate the Fermi level deep into the halide perovskite layer, indicating a low density of intrinsic carriers<sup>202,204,205</sup> (**Figure 8d**).

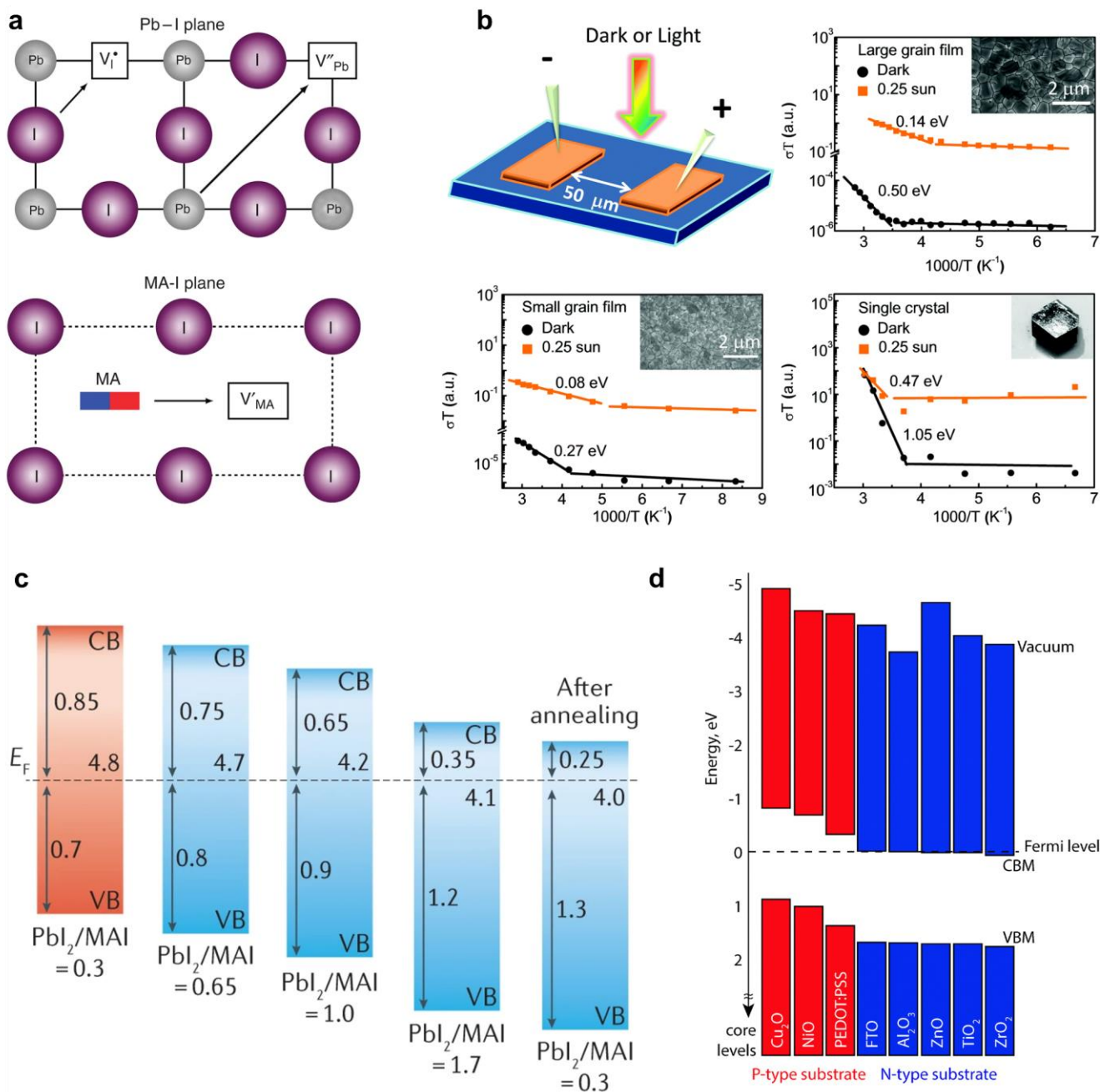


**Figure 8: Ionic mobility and doping in 3D perovskites.** a) Vacancy-mediated ion migration pathways for I (along octahedral edges), Pb (diagonally across cuboctahedral faces), and MA (through cuboctahedral faces). Reproduced with permission from ref.<sup>199</sup> Copyright 2015 Springer Nature. b) Temperature dependent conductivity of MAPbI<sub>3</sub> large-grain film (top right), small-grain film (bottom left), and single crystal (bottom right). Top left: schematic of experimental setup. Ion migration is seen in all samples as the change in slope of  $\ln(\sigma T)$  vs  $T^{-1}$  at high temperatures. Ion migration is suppressed in single crystals compared to small-grain films and in dark compared to light conditions. Reproduced with permission from ref.<sup>200</sup> Copyright 2016 Springer Nature. c) Influence of Pbl<sub>2</sub>:MAI precursor ratio on Fermi level in MAPbI<sub>3</sub> films showing p-doping by  $V_{Pb}$  and n-doping by  $V_{MA}$ . Reproduced with permission from ref.<sup>203</sup> Copyright 2014 American Institute of Physics. d) Influence of substrate on Fermi level of MAPbI<sub>3</sub> showing significant charge transfer doping, which implies a low intrinsic carrier density. Reproduced with permission from ref.<sup>205</sup> Copyright 2014 Royal Society of Chemistry.



### 3.1.8. Bulk ferroelectricity in 3D halide perovskites

There are several factors which complicate the measurement of ferroelectricity in 3D halide perovskites. First, their  $< 2\text{eV}$  bandgaps are low enough that applying a strong electric field generates a significant unwanted leakage current which obscures the measurement of polarization domain reorientation.<sup>206</sup> Second, their dynamic lattices allow mobile ions to move in response to an intrinsic or applied field, adding to leakage current and introducing hysteresis that can be misinterpreted as ferroelectricity.<sup>206,207</sup> As a result, whether or not  $\text{MAPbI}_3$  is ferroelectric has been a point of debate for years within the halide perovskite community.<sup>206,208–210</sup> Several studies have reported a ferroelectric response in the tetragonal phase of  $\text{MAPbI}_3$  (stable below  $57^\circ\text{C}$ ) which decreased in the cubic phase (above  $57^\circ\text{C}$ ). Poling with a  $16\text{kV/cm}$  field was shown to orient polarization domains within tetragonal  $\text{MAPbI}_3$ , which could persist for weeks<sup>208</sup>. Integration of the imaginary component of the dielectric function of tetragonal  $\text{MAPbI}_3$  over applied bias reveals an unmistakable hysteresis loop, which is strong evidence for ferroelectricity (**Figure 9a**). However, these results contradict experimental and simulation results, which contend that  $\text{MAPbI}_3$  is centrosymmetric and therefore non-ferroelectric.<sup>149</sup> Nonetheless, it appears that  $\text{MAPbI}_3$  can indeed be ferroelectric in its tetragonal phase at low temperature.

Other perovskite phases such as  $\text{MAPbBr}_3$  have been definitively proven to not be ferroelectric.<sup>211</sup>  $\text{MAPbBr}_3$  was found to create an electric current in response to surface heating, which could be an indicator of pyroelectricity and a non-centrosymmetric structure; however, this current was electrode-dependent and decreased with repeated cycling, suggesting that it was actually related to the detrapping of charges from the crystal and that the structure is in fact centrosymmetric (**Figure 9b**). On the other hand, nanocrystals of  $\text{FAPbBr}_3$  do show ferroelectricity, and have been successfully employed in piezoelectric devices.<sup>212</sup>

Many crystals which contain  $ns^2$  cations such as  $\text{Pb}^{2+}$  have shown 2nd-order Jann-Teller

distortion, which manifests a displacive ferroelectric effect; however, oxide perovskites that demonstrate this effect all have a tolerance factor above 1, which facilitates the required B-site distortion<sup>148</sup>. In that case, an A-site cation larger than FA would be required to expect bulk ferroelectricity, but such a cation would be unstable in the 3D halide perovskite structure. It seems that the B cation displacement potential for most 3D halide perovskites is a flat bottom well rather than the double-well characteristic of ferroelectric behavior. A-site molecular reorientation could in theory also lead to a long-range lattice polarization, but in the  $\text{MAPbI}_3$  ground state the MA cations are antipolar, resulting in no net dipole moment. At room temperature MA cations appear fully disordered, which would also preclude ferroelectricity.<sup>213</sup> Depolarization fields are also expected to strongly counteract the creation of a spontaneous polarization at the macroscopic scale, and 3D halide perovskites do not belong to the class of hyperferroelectric materials.<sup>150</sup>

It has been proposed that many of the reports of ferroelectricity in halide perovskites are in fact observations of ferroelastic effects - that is, the creation of a spontaneous strain distribution rather than a spontaneous net dipole moment.<sup>144,213</sup> For example, the apparently ferroelectric domains in  $\text{MAPbI}_3$  observed via piezoresponse force microscopy (PFM) may in fact be ferroelastic domains of alternating crystal orientation. It was shown directly from a combined inelastic neutron and Brillouin scattering study that the unusual softening of the shear modulus  $C_{44}$  in  $\text{FAPbBr}_3$  just below RT is typically related to the proximity of a ferroelastic transition, which, in this case, remains incipient at the macroscopic level<sup>138</sup> (**Figure 9c**). It means nevertheless that any local lattice perturbation or stoichiometry deviation may stabilize ferroelastic strain in such a compound. If 3D halide perovskites exhibit some local polarization or spontaneous strain effects, it seems unlikely that these features meaningfully affect the charge transport properties of the crystal or device performance.

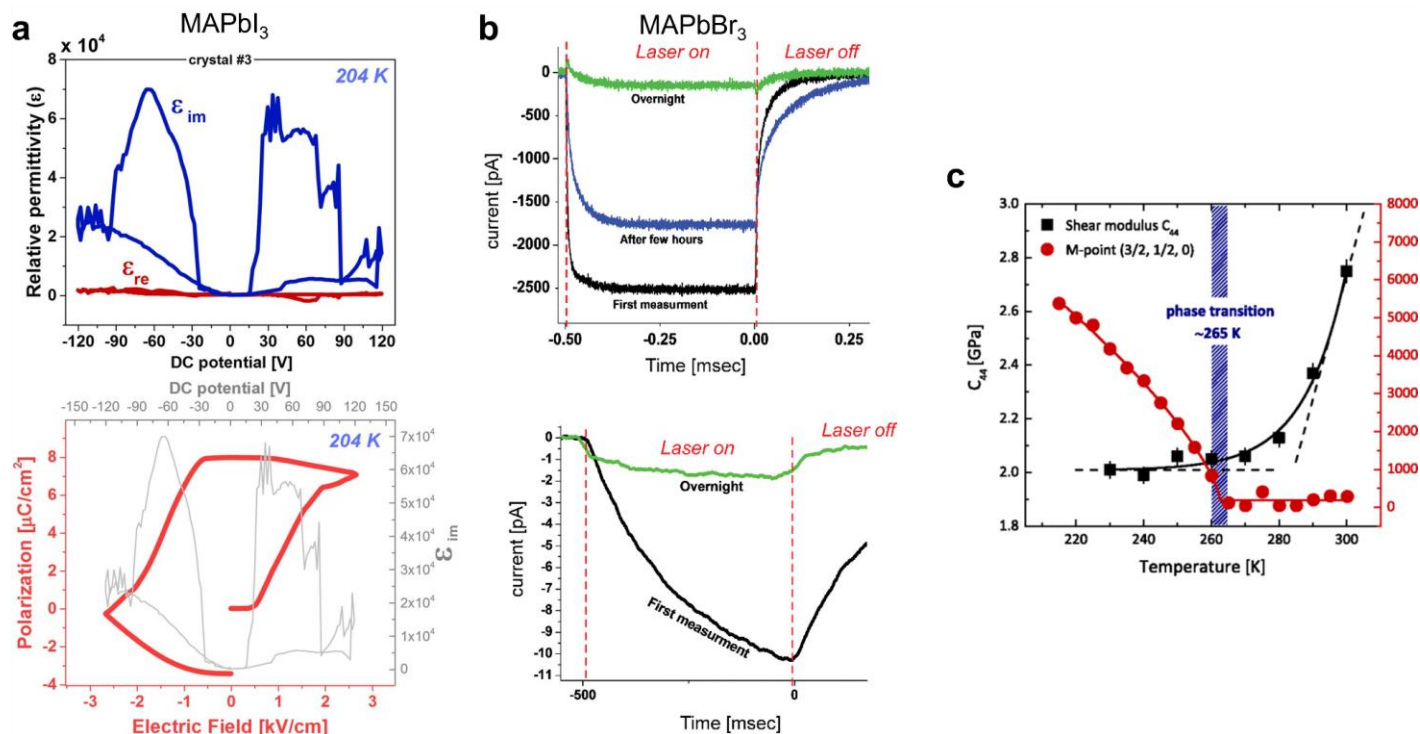


**Figure 9: Ferroelectricity of 3D perovskites.** a) Dielectric function of a tetragonal MAPbI<sub>3</sub> single crystal at 204K (top) and integration of the dominant imaginary component over the bias field to reveal a polarization-electric field (P-E) hysteresis loop (bottom), which is strong evidence for ferroelectricity. Reproduced with permission from ref.<sup>206</sup> Copyright 2017 National Academy of Sciences. b) Electric current generated in response to IR illumination in a cubic MAPbBr<sub>3</sub> single crystal for Au electrodes (top) and Pb electrodes (bottom). A current response to surface heating could be indicative of pyroelectricity, which is a prerequisite for ferroelectricity. However, the electrode-dependent current response and the decay of the response across cycles from the first measurement (black) to the last (green) suggests that the current is actually from trapped charges, and no pyroelectric effect is evident. This forbids Cubic MAPbBr<sub>3</sub> from being ferroelectric. Reproduced with permission from ref.<sup>211</sup> Copyright 2016 American Institute of Physics. c) Temperature-dependence of the C<sub>44</sub> shear modulus (black) and Bragg M point intensity (red) for FAPbBr<sub>3</sub> showing a ferroelastic phase transition at ~265K. Reproduced with permission from ref.<sup>138</sup> Copyright 2018 American Physical Society.

### 3.1.9. Best-performing 3D halide perovskite devices

In recent years the record efficiency of 3D halide perovskite solar cells has exceeded that of polycrystalline Si and is now approaching monocrystalline Si.<sup>5</sup> **Figure 10a** shows the record halide perovskite and halide perovskite-Si tandem efficiency over time. In general the “regular” n-i-p device architecture outperforms the “inverted” p-i-n architecture, although p-i-n devices have nearly caught up with n-i-p devices recently<sup>214,215</sup>. **Tables 4 and 5** list n-i-p and p-i-n 3D halide perovskite solar cells with efficiency exceeding 24%.

As of February 2023 the highest efficiency verified by NREL for an n-i-p halide perovskite solar cell is 25.7%.<sup>5,216</sup> Almost all reported devices with efficiency over 24% (of which there were only a

handful as of January 2023) shared the same general architecture: an FTO bottom contact, a SnO<sub>2</sub> or TiO<sub>2</sub> ETL, a FAPbI<sub>3</sub> or majority-FAPbI<sub>3</sub> absorber layer, a spiro-OMeTAD HTL, and an Au top contact.<sup>217–224</sup> The innovation of each of these devices, which allowed for such excellent efficiency varied in each case, but usually involved a combination of passivation of interfaces and grain boundaries, improvement of transport layer energy alignment and carrier transport, passivation or reduction of intrinsic trap states, and improved crystallinity. Notably, many aspects of these high-performing devices are either difficult to scale (e.g., the Spiro HTL) or prohibitively expensive for commercial devices (e.g., the Au top contact). The J-

V curve and cell architecture of a characteristic high-efficiency n-i-p device are shown in **Figure 10c**.

The p-i-n architecture seems much more promising than n-i-p in terms of scalability, but p-i-n efficiency is still lagging slightly behind<sup>215</sup>. The highest-efficiency p-i-n halide perovskite solar cell reported as of February 2023 had a 25.35% efficiency (certified 24.05%)<sup>225</sup>, with cell architecture and J-V curve shown in **Figure 10d**; the highest certified efficiency stands at 24.3%.<sup>226</sup> There have been only ~10 reported p-i-n devices with PCE>24%, and only two above 25%.<sup>225-233</sup> These cells also shared a majority-FAPbI<sub>3</sub> absorber layer, but there was more variance in charge transport layer choice between them. NiO<sub>x</sub> and MeO-2PACZ are both popular bottom HTLs for high-efficiency p-i-n cells, and the top ETL is usually C<sub>60</sub> or PCBM. Usually, a buffer layer is added between the halide perovskite and ETL layer.

Interestingly, when compared in terms of cumulative number of publications instead of time, halide perovskite solar cell efficiency has increased at about the same rate as that of Si, CIGSe, and CdTe, showing about a 5% increase in PCE per factor of 10 increase in publications<sup>234</sup> (**Figure 10b**). This logarithmic increase suggests that improving the last few percentage points towards halide perovskites' thermodynamic limit of efficiency may be a difficult task. Fortunately, the efficiency of halide perovskite solar cells taken alone is already sufficient to compete with established solar cell technologies. However, the new and critical challenge is to improve the scalability and stability of halide perovskite cells.<sup>4</sup>

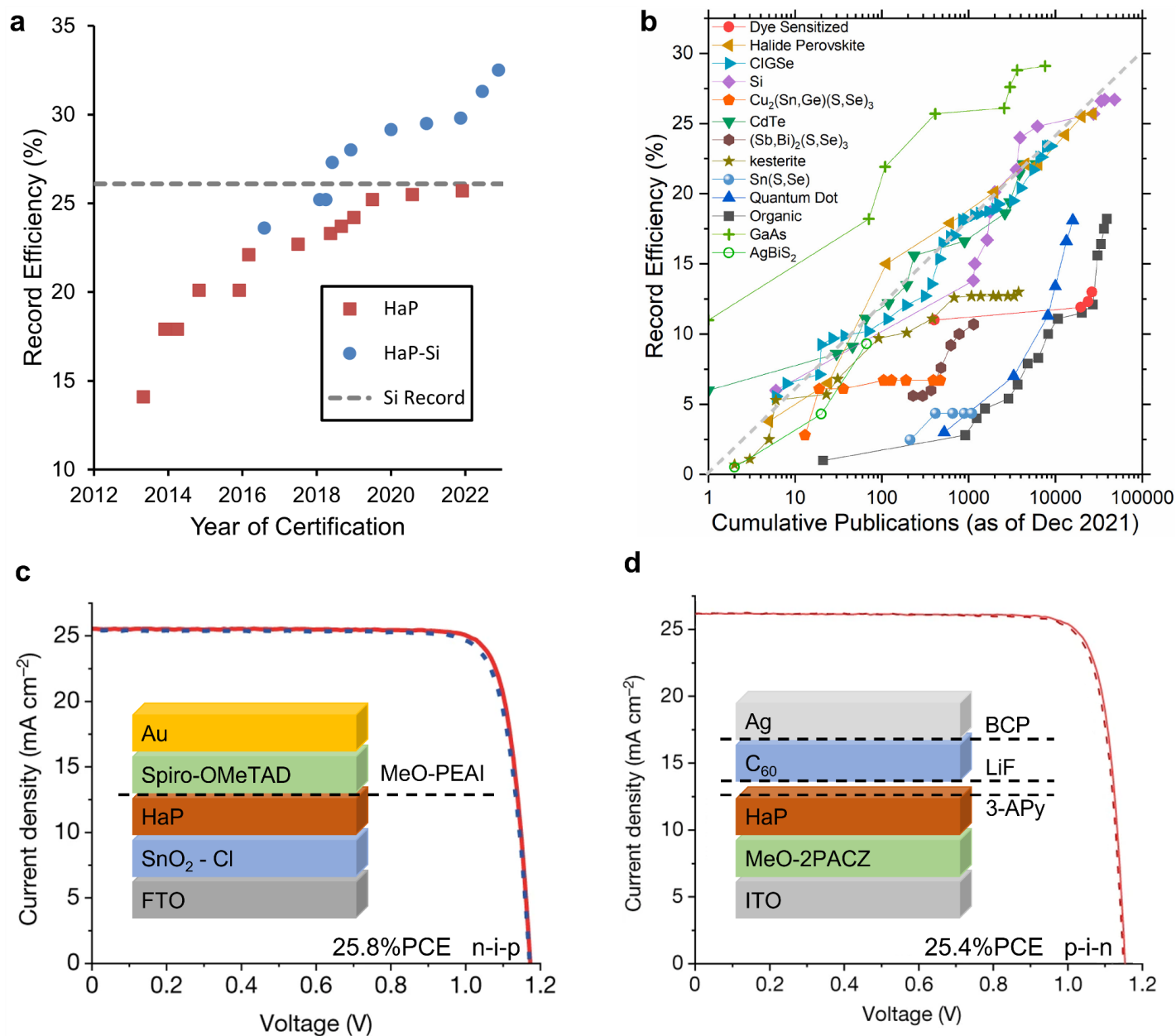


**Figure 10: State-of-the-art 3D perovskite solar cells.** a) Record efficiency for perovskite and perovskite-Si tandem solar cells over time. Record Si solar cell efficiency is shown by the dashed line. Data from ref.<sup>5</sup> This plot is courtesy of the National Renewable Energy Laboratory, Golden, CO. b) Record efficiency for a variety of solar cell materials plotted against cumulative publications. A trend of ~5% PCE increase for every 10x publications is shared by a variety of materials including perovskites. Reproduced with permission from ref.<sup>234</sup> Copyright 2023 Elsevier. c) A characteristic high-efficiency n-i-p 3D perovskite device J-V curve with 25.8% PCE. Inset shows device architecture: FTO – Cl-treated SnO<sub>2</sub> – FAPbI<sub>3</sub>-MDACl<sub>2</sub> perovskite – MeO-PEAI passivation layer (MeO-PEA = 4-methoxy-phenethylammonium) – Spiro-OMeTAD – Au. Reproduced with permission from ref.<sup>219</sup> Copyright 2021 Springer Nature. d) A characteristic high-efficiency p-i-n 3D perovskite device J-V curve with 25.4% PCE. Inset shows device architecture: ITO – MeO-2PACZ – (Rb<sub>0.05</sub>Cs<sub>0.05</sub>MA<sub>0.05</sub>FA<sub>0.85</sub>)Pb(I<sub>0.95</sub>Br<sub>0.05</sub>)<sub>3</sub> perovskite – 3-(aminomethyl)pyridine passivation layer – LiF passivation layer – C<sub>60</sub> – BCP passivation layer – Ag. Reproduced with permission from ref.<sup>225</sup> Copyright 2022 Springer Nature.

**Table 4: Reported n-i-p halide perovskite devices with PCE>24.5%. 1-sun illumination stability and shelf stability are also reported. Devices incorporating 2D halide perovskites are highlighted**

| Year | Efficiency   |               |       | 1-sun illumination, MPP tracking, inert atmosphere |                                 |                           | Shelf stability, ambient air |                                 |                   |       | Ref |
|------|--------------|---------------|-------|--|---------------------------------|---------------------------|------------------------------|---------------------------------|-------------------|-------|-----|
|      | Reported PCE | Certified PCE | Notes | Stability  | Stability scaled to 1000 hr (%) | Notes                     | Stability                    | Stability scaled to 90 days (%) | Relative Humidity | Notes |     |
| 2023 | 26.08        | 25.73         |       | 88% after 600 hr                                   | 80                              | Encapsulated, in air      |                              |                                 |                   |       | 216 |
|      | 25.64        | 25.06         |       |  |                                 |                           |                              |                                 |                   |       | 235 |
|      | 24.5         |               |       | 82.2% after 350 hr                                 | 49                              |                           | 94.5% after 1680 hr          | 93                              | 30%               |       | 236 |
| 2022 | 25.7         | 25.4          |       | ~85% after 350 hr                                  | 57                              |                           | 80% after 1000 hr            | 57                              | 20%               |       | 224 |
|      | 25.01        | 24.6          |       | ~80% after 500 hr                                  | 60                              |                           |                              |                                 |                   |       | 237 |
|      | 25.05        | 24.39         |       | 91% after 1000 hr                                  | 91                              |                           |                              |                                 |                   |       | 238 |
|      | 24.95        | 24.17         |       | 81% after 1000 hr                                  | 81                              | 55C                       |                              |                                 |                   |       | 239 |
|      | 25.14        |               |       | 93% after 400 hr                                   | 83                              |                           | 90% after 1800 hr            | 88                              | 40%               |       | 240 |
|      | 24.5         |               |       | 99% after 2000 hr                                  | 100                             | Encapsulated, in air, 55C |                              |                                 |                   |       | 241 |
| 2021 |              | 25.7          |       |  |                                 |                           |                              |                                 |                   |       | 242 |
|      | 25.8         | 25.5          |       | ~90% after 500 hr                                  | 80                              |                           |                              |                                 |                   |       | 243 |
|      | 25.6         | 25.2          |       | 85% after 450 hr                                   | 67                              |                           | 90% after 1000 hr            | 78                              | 20%               |       | 218 |

|      |       |       |                     |                       |    |              |                        |    |      |                                   |     |
|------|-------|-------|---------------------|-----------------------|----|--------------|------------------------|----|------|-----------------------------------|-----|
|      |       | 25.2  |                     | ~80% after<br>500 hr  | 60 |              |                        |    |      |                                   | 217 |
|      | 25.28 | 24.68 |                     |                       |    |              |                        |    |      |                                   | 244 |
|      |       | 24.59 | 24.35<br>stabilized | >98% after<br>1620 hr | 99 | Encapsulated | 97.3% after<br>1083 hr | 95 | 85%  | Changed HTL for<br>test, 20.6%PCE | 221 |
|      | 24.7  |       |                     | 90% after<br>1000 hr  | 90 |              | 73% after<br>740 hr    | 21 | >85% |                                   | 245 |
|      | 24.6  |       |                     |                       |    |              | 99% after<br>2000 hr   | 98 | 85%  | No HTAB,<br>21%PCE                | 246 |
| 2020 |       | 25.5  |                     |                       |    |              |                        |    |      |                                   | 247 |
|      |       | 25.5  |                     |                       |    |              |                        |    |      |                                   | 248 |
|      | 24.82 | 24.64 |                     |                       |    |              | 87% over<br>500 hr     | 44 | 50%  |                                   | 222 |
|      | 25.17 | 24.37 |                     | 90% after<br>400 hr   | 75 |              |                        |    |      |                                   | 223 |
| 2019 |       | 25.2  |                     |                       |    |              |                        |    |      | 249                               |     |

Accepted manuscript

**Table 5: Reported p-i-n halide perovskite devices with PCE>24%. 1-sun illumination stability and shelf stability are also reported. Devices incorporating 2D halide perovskites are highlighted**

| Year | Efficiency   |               |                     | 1-sun illumination, MPP tracking, inert atmosphere |                                 |                         | Shelf stability, ambient air |                                 |                   |       | Ref |
|------|--------------|---------------|---------------------|--|---------------------------------|-------------------------|------------------------------|---------------------------------|-------------------|-------|-----|
|      | Reported PCE | Certified PCE | Notes               | Stability  | Stability scaled to 1000 hr (%) | Notes                   | Stability                    | Stability scaled to 90 days (%) | Relative Humidity | Notes |     |
| 2023 | 24.6         | 24.2          |                     | 96% after 1000 hr                                  | 96                              |                         |                              |                                 |                   |       | 233 |
|      | 24.3         | 24.2          |                     | ~120% after 1100 hr                                | 118                             |                         |                              |                                 |                   |       | 232 |
|      | 24.48        | 23.2          |                     | 82% after 1000 hr                                  | 82                              |                         | 96% after 1000 hr            | 91                              | 30%               |       | 231 |
|      | 24.12        |               |                     |  |                                 |                         | 95% after 1200 hr            | 91                              | 55%               |       | 230 |
| 2022 | 25           | 24.3          |                     | 98% after 1500 hr                                  | 99                              |                         | 98% after 2000 hr            | 98                              | 45%               |       | 226 |
|      | 25.35        | 24.05         |                     | 87% after 2428 hr                                  | 95                              |                         |                              |                                 |                   |       | 225 |
|      | 24.3         | 23.5          |                     | 90.5% after 1000 hr                                | 91                              | 55C                     |                              |                                 |                   |       | 228 |
|      | 24.27        | 23.4          | perovskite/BHJ cell | 90% after 1000 hr                                  | 90                              |                         | 85% after 1000 hr            | 68                              | 55%               |       | 227 |
|      | 24.3         |               |                     | 95% after 500 hr                                   | 90                              | Encapsulated, 20.5% PCE |                              |                                 |                   |       | 229 |

| Table 6: Charge carrier mobilities for 3D halide perovskites |  |  |   |     |
|--|--|--|---|-----|
| Year   | Compound   | Charge carrier mobility (cm <sup>2</sup> V <sup>-1</sup> s <sup>-1</sup> ) | Approach  | Ref |
| 1995   | MASnI <sub>3</sub>                                   | 50 (Hall mobility)   | Hall effect measurement   | 250 |
| 2013z  | MASnI <sub>3</sub>                                   | 2320 (Hall electron mobility)  |   | 8   |
|  | CsSnI <sub>3</sub>                                   | 536 (Hall electron mobility)   |   |     |
|  | FASnI <sub>3</sub>                                   | 103 (Hall electron mobility)   |   |     |
|  | MASn <sub>0.5</sub> Pb <sub>0.5</sub> I <sub>3</sub> | 270 (Hall electron mobility)   |   |     |
|  | MAPbI <sub>3</sub>                                   | 66 (Hall electron mobility)  |   |     |
| 2016   | MAPbI <sub>3</sub>                                   | 197  | far infrared spectroscopy, estimated by electron-LO phonon coupling | 251 |
|  | MAPbBr <sub>3</sub>                                  | 158  |   |     |
|  | MAPbCl <sub>3</sub>                                  | 58   |   |     |
| 2013   | MAPbI <sub>3-x</sub> Cl <sub>x</sub> (thin film)     | 11.6   | THz spectroscopy  | 252 |
|  | MAPbI <sub>3</sub> (thin film)                       | 8  |   |     |
| 2015   | MAPbI <sub>3</sub> (single crystals)                 | 164 (hole mobility)  | SCLC measurements   | 154 |

| Table 7: Charge carrier mobilities for 2D halide perovskites |   |  |   |     |
|--|---|--|---|-----|
| Year   | Compound  | Charge carrier mobility (cm <sup>2</sup> V <sup>-1</sup> s <sup>-1</sup> ) | Approach                                    | Ref |
| 1999   | PEA <sub>2</sub> SnI <sub>4</sub>   | 0.62   | field effect transistors                    | 253 |
| 2016   | PEA <sub>2</sub> SnI <sub>4</sub>   | 15 (hole mobility)   | field effect transistors                    | 254 |
| 2016   | mixed MA-PEA 2D halide perovskites  | 1 - 25 (from PEA <sub>2</sub> PbI <sub>4</sub> to MAPbI <sub>3</sub> )     | optical pump THz probe spectroscopy         | 255 |
| 2017   | (n-BA) <sub>2</sub> (MA) <sub>3</sub> Pb <sub>4</sub> I <sub>13</sub>           | 1.88   | optical pump THz probe spectroscopy         | 256 |
|  | (iso-BA) <sub>2</sub> (MA) <sub>3</sub> Pb <sub>4</sub> I <sub>13</sub>         | 0.38   |   |     |
| 2016   | (BA) <sub>2</sub> (MA) <sub>3</sub> Pb <sub>4</sub> I <sub>13</sub>             | 10 <sup>-2</sup> (in solar cell)   | linearly increasing voltage (CELIV)         | 257 |
| 2017   | (BA) <sub>2</sub> (MA) <sub>n-1</sub> Pb <sub>n</sub> I <sub>3n+1</sub> (n=1-5) | 10 <sup>-1</sup> - 10 <sup>0</sup>   | Time-resolved microwave conductivity (TRMC) | 258 |
| 2018   | (BA) <sub>2</sub> (MA) <sub>n-1</sub> Pb <sub>n</sub> I <sub>3n+1</sub> (n=1-4) | 10 <sup>-2</sup> - 10 <sup>-1</sup> (yield-mobility product)               | Time-resolved microwave conductivity (TRMC) | 259 |
| 2019   | (PEA) <sub>2</sub> PbI <sub>4</sub>   | 10 <sup>-2</sup> - 10 <sup>-1</sup> (in-plane)                             | Time-resolved microwave conductivity (TRMC) | 260 |
|  |   | 10 <sup>-3</sup> - 10 <sup>-2</sup> (out-of-                               |   |     |



|      |   |  |  |     |
|------|---|--|--|-----|
|      |   | plane)   |  |     |
|      | (F-PEA) <sub>2</sub> PbI <sub>4</sub>   | 10 <sup>-2</sup> - 10 <sup>-1</sup> (in-plane)         |  |     |
|      |   | 5 x 10 <sup>-3</sup> - 10 <sup>-2</sup> (out-of-plane) |  |     |
| 2018 | mixed MA-ALA 2D halide perovskites <n=10>   | 1.1  | Photoluminescence Quenching Experiments, then use diffusion length and Einstein relation | 261 |
|      | mixed MA-PEA 2D halide perovskites <n=10>   | 5.7 x 10 <sup>-1</sup>                                 |  |     |
|      | mixed MA-BTA 2D halide perovskites <n=10>   | 8.9 x 10 <sup>-2</sup>                                 |  |     |
| 2001 | (C <sub>6</sub> H <sub>4</sub> FC <sub>2</sub> H <sub>4</sub> NH <sub>3</sub> ) <sub>2</sub> SnI <sub>4</sub> (m=2-4) | 0.2-0.6 (m=4-2)  | field effect transistors   | 262 |
| 2017 | (PEA) <sub>2</sub> PbI <sub>4</sub>   | 26 (hole)  | field effect transistors   | 263 |

**Table 8: exciton effective mass and binding energy for 3D halide perovskites**

|                       | Year | Compound  | Binding energy (meV) | Effective mass (m <sub>0</sub> ) | Approach   | Ref |
|-----------------------|------|---|----------------------|----------------------------------|--|-----|
| 3D halide perovskites | 2015 | MAPbI <sub>3</sub>                                      | 16                   | 0.104                            | High-field magneto optical absorption spectroscopy | 106 |
|                       | 2016 | FAPbI <sub>3</sub> (tetragonal phase)                   | 10                   | 0.095                            | Magneto optical spectroscopy                       | 264 |
|                       |      | MAPbI <sub>3-x</sub> Cl <sub>x</sub> (tetragonal phase) | 10                   | 0.105                            |  |     |
|                       |      | MAPbI <sub>3</sub> (tetragonal phase)                   | 12                   | 0.104                            |  |     |
|                       |      | FAPbBr <sub>3</sub> (tetragonal phase)                  | 24                   | 0.13                             |  |     |

**Table 9: exciton effective mass and binding energy for 2D halide perovskites**

| Year | Compound   | Binding energy (meV) | Effective mass (m <sub>0</sub> ) | Approach | Ref                                     |     |
|------|--|----------------------|----------------------------------|----------|---|-----|
| 2018 | (BA) <sub>2</sub> (MA) <sub>n-1</sub> Pb <sub>n</sub> I <sub>3n+1</sub> (n=1-5)  | n=1                  | 470                              | 0.221    | Magneto optical absorption spectroscopy | 65  |
|      |  | n=2                  | 250                              | 0.217    |   |     |
|      |  | n=3                  | 180                              | 0.201    |   |     |
|      |  | n=4                  | 160                              | 0.196    |   |     |
|      |  | n=5                  | 125                              | 0.186    |   |     |
| 2005 | (C <sub>6</sub> H <sub>13</sub> NH <sub>3</sub> ) <sub>2</sub> (MA) <sub>n-1</sub> Pb <sub>n</sub> I <sub>3n+1</sub> (n = 1 - 4) | n=1                  | 361                              |          | Optical absorption spectroscopy         | 265 |
| 2003 |  | n=2                  | 260                              |          | Optical and electrical                  | 266 |

|      |  |     |     |      |   |     |
|------|--|-----|-----|------|---|-----|
|      |  | n=3 | 150 |      | absorption spectroscopy                         |     |
|      |  | n=4 | 100 |      |   |     |
| 1996 | $(C_9H_{19}NH_3)_2(MA)_{n-1}PbI_{3n+1}$<br>(n = 1 - 4) | n=1 | 388 |      | Optical absorption spectra                      | 267 |
|      |  | n=2 | 181 |      |   |     |
|      |  | n=3 | 96  |      |   |     |
|      |  | n=4 | 60  |      |   |     |
| 1998 | $(PEA)_2(MA)_{n-1}PbI_{3n+1}$<br>(n = 1 - 4)           | n=1 | 220 |      | Transmission spectroscopy                       | 268 |
| 1991 |  | n=1 | 220 | 0.09 | Optical absorption spectra                      | 58  |
|      |  | n=2 | 170 |      |   |     |
| 2019 |  | n=3 | 125 |      | Estimated from exciton scaling law              | 269 |
|      | n=4  | 100 |     |      |   |     |
| 1991 | $(C_{10}H_{21}NH_3)_2PbI_4$                            | n=1 | 320 | 0.09 | Optical absorption spectra                      | 58  |
| 1989 | $(C_{10}H_{21}NH_3)_2PbI_4$                            | n=1 | 370 |      | Reflection, luminescence and absorption spectra | 46  |
| 2009 | $(FC_6H_4C_2H_4NH_3)_2PbI_4$                           | n=1 | 540 | 0.12 | Temperature dependence PL spectroscopy          | 270 |
| 1990 | $(C_mH_{2m+1}NH_3)PbI_4$<br>(m=4, 6, 12)               | n=1 | 300 |      | Optical absorption spectroscopy                 | 271 |
| 2000 | $[H_3N(CH_2)_6NH_3]PbI_4$                              | n=1 | 153 |      | Optical absorption spectroscopy                 | 272 |
|      | $[H_3N(CH_2)_6NH_3]PbBr_4$                             |     | 166 |      |   |     |
|      | $[H_3N(CH_2)_6NH_3]PbCl_4$                             |     | 205 |      |   |     |

**Table 10: carrier diffusion length for 2D halide perovskites**

| Year | Compound                                | Exciton diffusion constant (cm <sup>2</sup> s <sup>-1</sup> ) | Approach                                       | Ref |
|------|---|---|--|-----|
| 2020 | $(BA)_2(MA)_{n-1}PbI_{3n+1}$<br>(n=3)   | 0.18  | Transient absorption with pumping front & back | 273 |
| 2020 | $(PEA)_2PbI_4$                          | 0.192   | Transient photoluminescence microscopy         | 274 |
| 2020 | $(BA)_2(MA)_{n-1}PbI_{3n+1}$<br>(n=1-5) | 0.06 - 0.34   | Transient absorption microscopy                | 275 |

## 3.2. Semiconductor properties of 2D halide perovskites

### 3.2.1. The origin of 2D halide perovskites' wider bandgap and optical spectrum

The optoelectronic properties of 2D halide perovskites, like those of 3D, arise from the corner-sharing  $\text{PbI}_6$  octahedra.<sup>43,50</sup> The VBM and CBM have the same atomic orbital character as in 3D halide perovskites, as shown in **Figure 11a**. However, quantum confinement raises 2D halide perovskites' bandgap substantially, as the organic spacer layers present a barrier to out-of-plane electron motion. 2D halide perovskites can be considered as superlattices of quantum wells similar to classical semiconductors,<sup>276</sup> with the important exception that their electronic structure cannot be understood on the basis of transverse effective mass models, since the halide perovskite well and the organic barrier strongly differ in nature.<sup>277</sup> Quantum confinement effects are rather revealed by DFT calculations, including the existence of  $n$  sub-bands in both the conduction and valence bands when the quantum thickness is tuned.<sup>43</sup> For RP 2D halide perovskites, the band structure shows in most cases a close to flat dispersion along the stacking axis indicating minimal coupling (**Figure 11b**), since the interlayer distances between halide perovskite quantum wells are large even for small alkylammonium chains such as BA in the barrier; for DJ and ACI 2D halide perovskites interlayer coupling can be enhanced by shorter interlayer distances, but the transverse effective masses along the stacking axes remain so far much larger than the in-plane effective masses.<sup>50</sup>

2D halide perovskites exhibit unique photo-physics properties compared with their 3D counterparts, resulting from a reduced dimensionality, and strongly bound electron-hole pairs (excitons) at room temperature. The steady-state optical absorption and photoluminescence spectra of 2D halide perovskites exhibit strong excitonic resonances at room temperature, as a result of the strong Coulomb interactions and large exciton binding energies of 2D halide perovskites (0.1-0.5eV) in layered QW like materials.<sup>65</sup> The absorption coefficient of 2D halide perovskites is typically a few  $10^5 \text{ cm}^{-1}$  at exciton ground states, which is one order of magnitude higher than 3D

halide perovskites, making 2D halide perovskites efficient absorbers in this spectral region. Such high absorption coefficient in 2D systems results from the quantum and dielectric confinement in 2D systems, leading to a large oscillator strength of excitons at ground state (**Figure 11c**).

The steady-state optical absorption and PL spectra of typical RP 2D halide perovskites series ( $\text{BA}_2\text{MA}_{n-1}\text{Pb}_n\text{I}_{3n+1}$ ) are listed in **Figure 11d-e**<sup>278</sup>. Both PL and optical absorption spectra show monotonous decrease in exciton energy and bandgap, with  $n$ -value increase from 1 to 5. Such behavior is expected from the decrease of quantum and dielectric confinement with increasing inorganic layer thickness, resulting in lower continuum bandgap and exciton binding energy. The most remarkable evidence of the dielectric confinement effect similarly to other 2D materials<sup>279</sup>, is the deviation of  $nS$  exciton resonances from 2D Rydberg series. It has been analyzed in detail as a function of  $n$  up to  $n=5$  in  $\text{BA}_2\text{MA}_{n-1}\text{Pb}_n\text{I}_{3n+1}$  RP phases by combining magneto-optical spectroscopy and theoretical analyses<sup>65</sup>.

Structural differences between the three types of 2D halide perovskite result in subtly different bandgaps. The ACI 2D halide perovskite  $\text{GAMA}_n\text{Pb}_n\text{I}_{3n+1}$  has a bandgap of 2.27eV for  $n=1$  and 1.73eV for  $n=3$ .<sup>52</sup> The RP halide perovskite  $\text{BA}_2\text{MA}_{n-1}\text{Pb}_n\text{I}_{3n+1}$  has a bandgap of 2.43eV for  $n=1$  and 2.03eV for  $n=3$ , wider than ACI because of the longer interlayer distance and increased octahedral distortion<sup>47</sup>. The DJ halide perovskite  $(3\text{AMP})(\text{MA})_{n-1}\text{Pb}_n\text{I}_{3n+1}$  (3AMP = 3-(aminomethyl) piperidinium) has a bandgap of 2.23eV for  $n=1$  and 1.92eV for  $n=3$ , lower than RP because of DJ's lower axial octahedral distortion and the destabilizing effect of interlayer I-I interactions on the VBM.<sup>51</sup> Bandgaps for a selection of 2D halide perovskites are given in Table 5.

Furthermore, as a result of the layered structure, a strong anisotropic optical response is observed in terms of the dielectric function of these materials, leading to the formation of excitons with anisotropic absorption in 2D halide perovskite systems<sup>280-284</sup>.

The emission bandwidth of 2D halide perovskites is highly variable on the intrinsic

structural disorder, and strength of electron-phonon coupling. For example, Photoluminescence of lead-based 2D halide perovskite shows narrow exciton emission bandwidths with low Stokes shift, which allow for the design of tunable-color narrowband emitters<sup>278</sup>. On the other hand, strong electron-phonon coupling in 2D halide perovskites results in structural deformation and charge localization leading to the formation of self-trapped excitons and broadband emissions, which has promising applications in white-light emission.<sup>285</sup>

Another important feature related to the optical properties of 2D halide perovskites is the emission from low-energy states located at the edges of the perovskite layers, first evidenced for  $n>2$  in  $\text{BA}_2\text{MA}_{n-1}\text{Pb}_n\text{I}_{3n+1}$  RP phases<sup>278</sup>, as demonstrated in **Figure 11f**. They have been attributed to intrinsic strain relaxation by localized octahedra promoting electron and hole separation<sup>67</sup>, but may be enhanced by external effects such as the

presence of moisture.<sup>286</sup> Their existence is fundamental for exciton dissociation and proper operation of solar cells based on 2D halide perovskites.<sup>287</sup> However, they may have detrimental effects for solar cell operation leading to a limitation of the open-circuit voltage. In the case of LEDs based on multilayered  $\text{BA}_2\text{MA}_{n-1}\text{Pb}_n\text{I}_{3n+1}$  RP phases<sup>278</sup>, this effect limits the external quantum efficiency (EQE) despite the injection of very large electrical current and excellent device stability<sup>288</sup>. Since the pioneering work by Blancon et al. in 2017, low-energy edge state emission has been observed in many other 2D halide perovskites including bromide ones<sup>289</sup>.

For interested readers, the article *Semiconductor physics of organic–inorganic 2D halide perovskites* by Blancon et al. provides a more detailed review of the optoelectronic properties of 2D halide perovskites.<sup>50</sup>

**Table 11: Bandgaps of common RP 2D halide perovskites**

| A'            | A  | B  | X   | n    | Bandgap     | Ref  |    |
|---------------|----|----|-----|------|-------------|------|----|
| Butylammonium |    | Pb | I   | 1    | 2.43        | 47   |    |
|               | MA |    |     | 2    | 2.17        |      |    |
|               |    |    |     | 3    | 2.03        |      |    |
|               |    |    |     | 5    | 1.83        | 66   |    |
|               |    |    |     | 7    | 1.74        |      |    |
|               |    |    | Br  | 1    | 2.99        | 290  |    |
|               | 3  |    |     | 2.4  | 73          |      |    |
|               | Cl | 1  | 3.7 | 291  |             |      |    |
|               |    |    | Sn  | I    | 1           | 1.83 | 63 |
|               | MA | 2  |     |      | 1.64        |      |    |
|               |    | 3  |     |      | 1.5         |      |    |
|               |    | 5  |     |      | 1.37        |      |    |
|               |    | Br |     | 1    | 2.28 (calc) | 292  |    |
| MA            | 3  |    |     | 2.22 | 75          |      |    |
| FA            | Pb | I  |     | 2    | 2.18        | 68   |    |

|                      |    |    |   |   |      |     |
|----------------------|----|----|---|---|------|-----|
|                      | GA | Pb | I | 2 | 2.2  |     |
| Hexylammonium        | MA | Pb | I | 2 | 2.16 | 79  |
|                      |    |    |   | 3 | 2.01 |     |
| Phenyl-ethylammonium |    | Pb | I | 1 | 2.57 | 293 |
|                      | MA |    |   | 3 | 2.1  | 49  |

| Table 12: Bandgaps of common DJ and ACI 2D halide perovskites |                              |    |    |   |      |         |     |
|---|------------------------------|----|----|---|------|---------|-----|
| Phase   | A'                           | A  | B  | X | n    | Bandgap | Ref |
| DJ  | 4-(aminomethyl) piperidinium |    | Pb | I | 1    | 2.38    | 51  |
|   |                              | MA |    |   | 2    | 2.17    |     |
|   |                              |    |    |   | 3    | 1.99    |     |
|   |                              | 4  |    |   | 1.89 |         |     |
|   | 3-(aminomethyl) piperidinium |    | Pb | I | 1    | 2.23    |     |
|   |                              | MA |    |   | 2    | 2.02    |     |
|   |                              |    |    |   | 3    | 1.92    |     |
|   |                              | 4  |    |   | 1.87 |         |     |
|   | 1,7-heptanediammonium        |    | Pb | I | 1    | 2.43    | 92  |
|   |                              | MA |    |   | 3    | 2       |     |
|   | 1,9-nonanediammonium         |    | Pb | I | 1    | 2.43    |     |
|   |                              | MA |    |   | 3    | 2.02    |     |
| ACI   | Guanidinium                  | MA | Pb | I | 1    | 2.27    | 52  |
|   |                              |    |    |   | 2    | 1.99    |     |
|   |                              |    |    |   | 3    | 1.73    |     |
|   | Protonated thiourea          | MA | Pb | I | 1    | 2.11    | 97  |
|   |                              |    |    |   | 2    | 1.97    |     |
|   |                              |    |    |   | 3    | 1.81    |     |

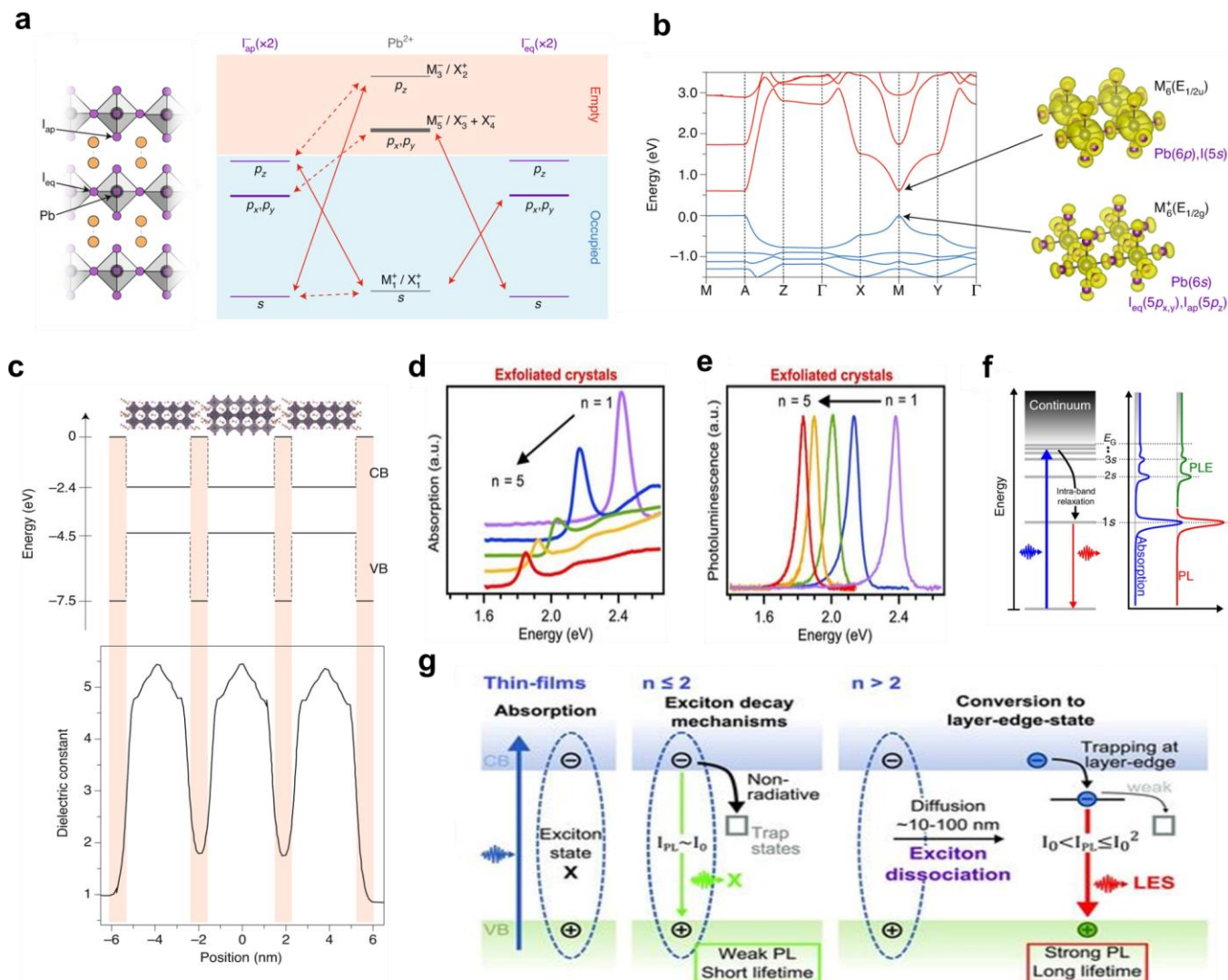


**Figure 11: The origin of 2D halide perovskites' wider bandgap and optical spectrum.** a) Hybridizations of atomic orbitals for the electronic states at the band edges in 2D halide perovskites ( $\text{Cs}_2\text{PbI}_4$ ), without SOC. The VBM is formed by antibonding orbitals of Pb 6s - I 5p, and CBM by Pb - p and I - s states, the same characteristics as in 3D halide perovskites. b) Band structure of the  $\text{Cs}_2\text{PbI}_4$  calculated by DFT including SOC. c) Energy level alignment (top) and dielectric constant profile (bottom) along the stacking direction in the 2D halide perovskites. (a-c) Reproduced with permission from ref.<sup>50</sup> Copyright 2020 Springer Nature. d) Absorption and e) PL spectra for exfoliated crystals of 2D halide perovskites  $(\text{BA})_2(\text{MA})_{n-1}\text{Pb}_n\text{I}_{3n+1}$  with  $n=1-5$ , respectively. (d-e) Reproduced with permission from ref.<sup>278</sup> Copyright 2017 American Association for the Advancement of Science. f) Schematics of the Rydberg series of the exciton ground state (1s) and excited exciton states (2s, 3s, etc.). Reproduced with permission from ref.<sup>65</sup> Copyright 2018 Springer-Nature. g) Illustration of exciton diffusion and recombination dynamics in 2D halide perovskites after photo-excitation. Reproduced with permission from ref.<sup>278</sup> Copyright 2017 American Association for the Advancement of Science.

### 3.2.2. Defect tolerance in 2D halide perovskites

2D halide perovskites appear to share the defect tolerance of 3D halide perovskites afforded by the antibonding VBM of their band structure, at least to an extent.<sup>294</sup> However, quantum confinement and higher exciton binding energy in 2D halide perovskites increases exciton trapping. Below-bandgap exciton trap states can be detected using the transient absorption spectra, as shown for example in **Figure 12a** for  $\text{BA}_2\text{MA}_{n-1}\text{Pb}_n\text{I}_{3n+1}$  ( $n=1$ ). The density of traps increases with decreasing  $n$ -value, estimated from the relative magnitudes of peak bleaching from trap states (normalized to the 1s exciton bleaching signal).<sup>295</sup> 2D halide perovskites can also form self-trapped excitons from exciton-phonon interactions as a result of their lowered

deformation energy compared to 3D halide perovskites (**Figure 12b**).<sup>285,295–297</sup> This may account for the below-gap and white-light emission seen in 2D halide perovskites that are not present in 3D, as shown in **Figure 12c** for  $(\text{N-MEDA})[\text{PbBr}_4]$  ( $\text{N-MEDA}=\text{N}^1\text{-methylene-1,2-diammonium}$ ).<sup>298</sup>

Computational evidence also suggests that shallow defects in 3D halide perovskites may be deeper in 2D halide perovskites as a result of their lowered VBM and raised CBM due to quantum confinement (**Figure 12d**).<sup>299</sup> On the other hand, 2D halide perovskites have been shown to have higher defect formation energies than 3D halide perovskites (**Figure 12e**).<sup>300–302</sup> This may be a result of the higher lattice formation enthalpy of 2D halide perovskites and will be expanded upon below.

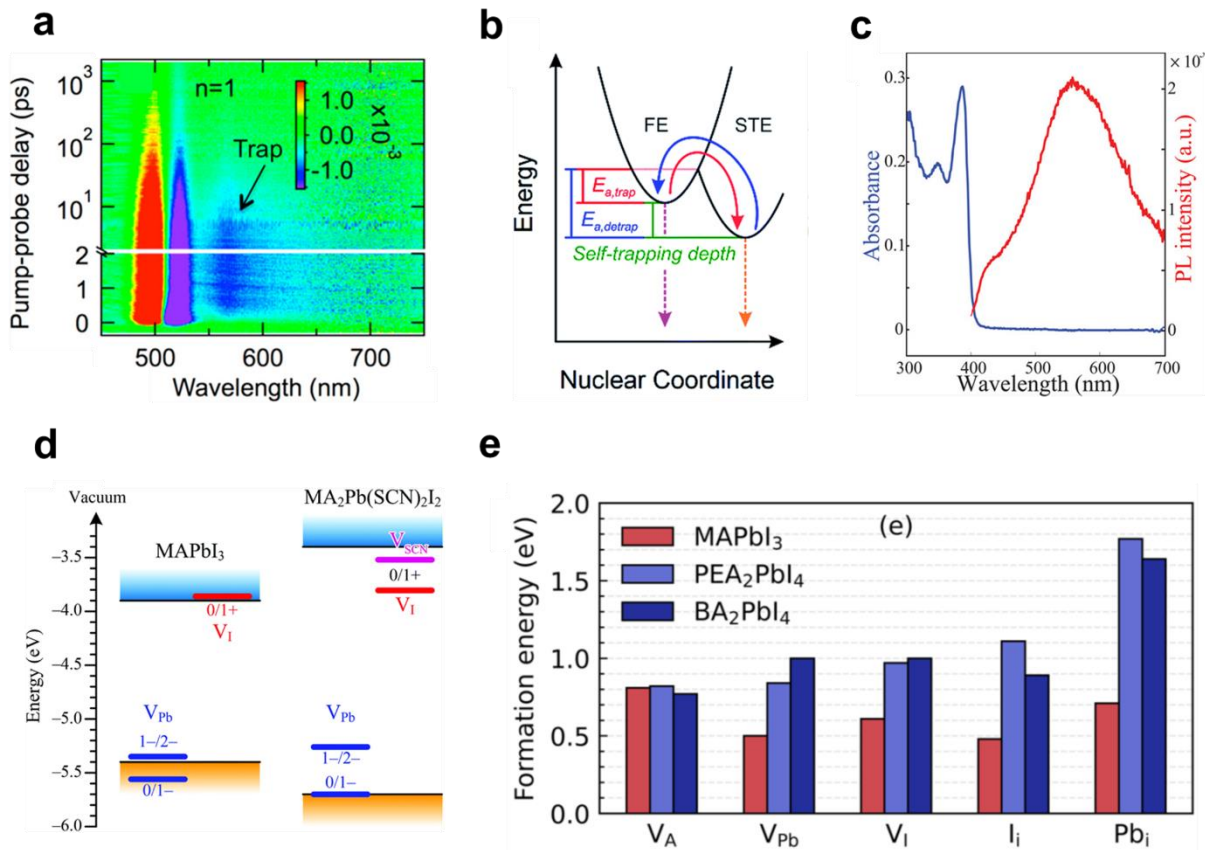


**Figure 12: Defect tolerance in 2D perovskites.** a) Pseudo color representations of TA spectra of  $\text{BA}_2\text{PbI}_4$  with 350nm excitation. A bleaching centered below the bandgap is attributed to the excitonic trap states. Reproduced with permission from ref.<sup>295</sup> Copyright 2015 American Chemical Society. b) Schematics of self-trapped excitons (STE). Red and blue arrows indicate trapping and detrapping, respectively. Reproduced with permission from ref.<sup>285</sup> Copyright 2017 Royal Society of Chemistry. c) PL and Absorbance spectra of  $(\text{N-MEDA})\text{PbBr}_4$ , showing white-light emission due to STEs. Reproduced with permission from ref.<sup>298</sup> Copyright 2016 American Chemical Society. d) Energy alignments of CBM and VBMs of  $\text{MAPbI}_3$  and  $\text{MA}_2\text{Pb}(\text{SCN})_2\text{I}_2$  as



well as the defect transition levels, with respect to the vacuum levels. Reproduced with permission from ref.<sup>299</sup> Copyright 2016 Royal Society of Chemistry. e) Calculated defect formation energies of MAPbI<sub>3</sub>, PEA<sub>2</sub>PbI<sub>4</sub>, and BAPbI<sub>4</sub>, at intrinsic Fermi level. Reproduced with permission from ref.<sup>303</sup> Copyright 2022 arXiv.

### 3.2.3. Nonradiative recombination in 2D halide perovskites

Like other lower-dimensional materials, layered 2D halide perovskites suffer from non-radiative losses of carriers, especially with high fluence of carrier injection. The emergence of the loss mechanism originated from the enhanced many-body interactions, such as Auger effect and exciton-exciton annihilation (EEA). Compared with 3D systems, rapid rates of EEA and Auger recombination are generally expected in 2D halide perovskites, since the reduced dimensionality and large exciton binding energies enhance the electron-hole interactions, giving more probability of many body effects in confined systems.<sup>304,305</sup> Specifically, the Auger recombination describes a three-body interaction, where an electron and hole non-radiatively gives up their energy to another electron into the conduction band, resulting in a fast carrier recombination rate scaling with the cube of carrier population. Analogously, the EEA process describes a two-particle interaction, where kinetic energy is transferred from a recombined exciton to another exciton, giving a second order bimolecular carrier recombination. Both recombination losses are non-radioactive and therefore results in a roll-off of photoluminescence quantum yield (PLQY) at higher fluence and limits the efficient harvesting of carriers in a device (**Figure 13a**).<sup>306</sup>

The rates of Auger and EEA can be extracted from time-resolved photoluminescence or transient absorption spectroscopies, based on the kinetics equation of the carriers. However, the assignment of the kinetics of recombination can be sometimes nontrivial, since additional carrier dynamics (such as trap-assisted recombination, and bimolecular free-carrier recombination) may be convoluted.<sup>269,275,307</sup>

There have been a few studies on the EEA and Auger recombination in 2D halide perovskites based on time-resolved spectroscopy. Delport et al. have studied PEA<sub>2</sub>MA<sub>n-1</sub>Pb<sub>n</sub>I<sub>3n+1</sub> halide perovskites and demonstrated EEA rates on the order of 10<sup>-4</sup> cm<sup>2</sup>/s, one order of magnitude lower than the typical values in monolayer TMDs.<sup>269</sup> At high fluence, EEA rates start to dominate in the carrier recombination and show weak n-dependence (**Figure 13b**). Chen et al. reports a decrease of biomolecular and third-order kinetics as n-value increases in 2D halide perovskite series.<sup>307</sup> Milot et al. reported the bimolecular and Auger rate for mixed PEA and MAPbI<sub>3</sub> thin films, showing fastest recombination rate with 67% PEA (<n>=2) content (**Figure 13c**).<sup>255</sup> Deng et al. utilized transient absorption microscopy to visualize both the spatial and temporal evolution of the exciton dynamics, revealing a large exciton diffusion constant and decreasing annihilation rate with increasing n value.<sup>275</sup> Till this day, there is still not a general consensus on the n-value dependence on EEA and Auger rates in 2D halide perovskites, and more fundamental questions of the EEA and Auger recombination, as well as their interplay with carrier transport, and dependence with organic spacers, and structural distortion are still not well understood.

To reduce the unwanted non-radiative recombination rates, several methods have been proposed to lower the nonlinear process in 2D halide perovskites, including compositional engineering to increase the recombination centers in 2D systems, structural engineering, and tailoring the dielectric confinement by reducing the e-h overlap.<sup>269,308</sup> These methods aim to manipulate the dielectric screening by the organic layers, which brings down the exciton binding energy.

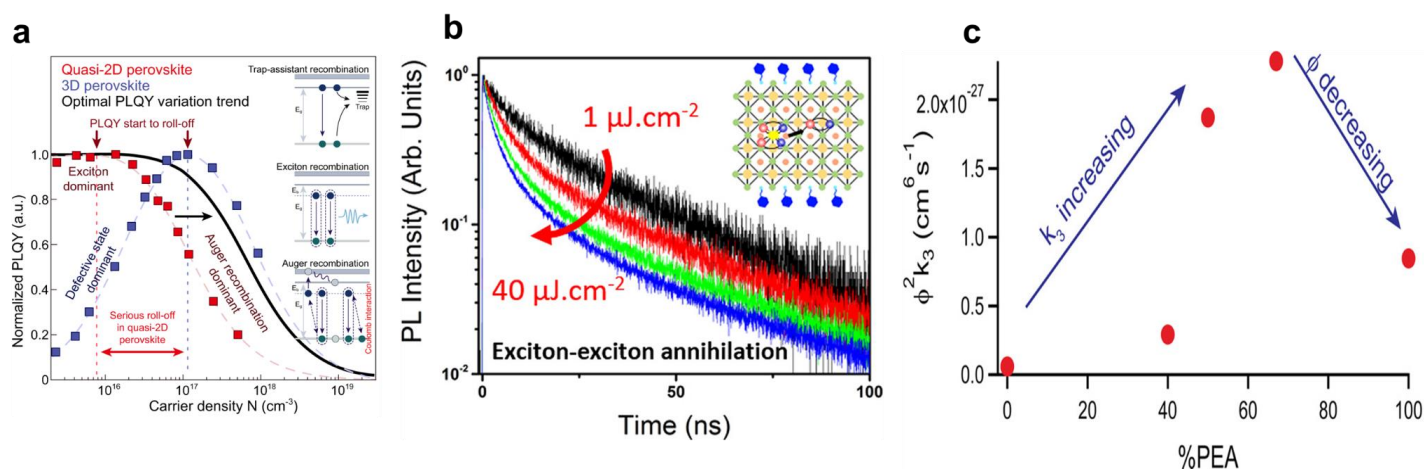


**Figure 13: Nonradiative recombination in 2D halide perovskites.** a) PLQYs of 2D halide perovskite (red) and 3D halide perovskite films (blue) as a function of carrier density; the curves indicate serious Auger recombination takes place in 2D halide perovskites compared to the 3D ones, leading to rapid PLQY declining at lower threshold. Reproduced with permission from ref.<sup>306</sup> Copyright 2021 Springer Nature. b) Evolution of PL decays in 2D halide perovskites as a function of excitation intensity, showing Exciton-Exciton annihilation is the dominant recombination path in high-density regime. Reproduced with permission from ref.<sup>269</sup> Copyright 2019 American Chemical Society. c) Effective Auger rate constant ( $\phi^2 k_3$ ) in PEA-MA lead iodide thin films as a function of PEA concentration, extracted from fits to traces of optical pump terahertz probe spectroscopy. The recombination rates show increase with PEA concentration and then decreasing for 100% PEA film, which is attributed to the tradeoff between increase of electric density of states and increased quantum confinement. Reproduced with permission from ref.<sup>255</sup> Copyright 2016 American Chemical Society.

### 3.2.4. Carrier transport of 2D halide perovskites

Despite being a good light absorber with high absorption coefficient at exciton resonance, 2D halide perovskites suffer from reduced PCE in photovoltaic devices ( $\sim 19\%$  so far) compared to their 3D system<sup>309</sup>. This is partially due to the inferior charge transport properties in the multiple quantum well-like system, forming stable excitons leading to an inefficient charge separation and collection. The typical values of mobility are of the order of  $10^{-2} - 10 \text{ cm}^2 \text{ Vs}^{-1}$  (see **Table 5**) variable on specific techniques, approximately one order of magnitude lower than the mobilities in 3DPKs, as well as other 2D materials such as TMDs and inorganic MQWs.<sup>50</sup>

The low charge mobilities are mainly governed by the electron-phonon scattering mechanisms in 2D halide perovskites, as demonstrated by temperature-dependent microwave conductivity measurements in  $\text{BA}_2\text{MA}_{n-1}\text{Pb}_{n+1}$  systems,<sup>258</sup> however deviation from the electron-phonon scattering model has been observed with

increasing n-value approaching 3D (**Figure 14a**). This suggests the transport behavior in 2D halide perovskites is approaching their 3D analogue with increasing numbers of inorganic layers, and that the dynamic disorder greatly affects the local crystal structure and subsequently the charge mobility.<sup>170,258</sup> Additionally, strong electron phonon coupling in 2D halide perovskites results in small polarons or immobilized self-trapped states, strong local lattice distortion and hinders the efficient band-edge transport to hopping-like transport between trapping sites,<sup>157,310</sup> while on the other hand favors the broadband emission towards the applications of white-light LEDs.<sup>285</sup> However, the specific types of phonons involved in the electron-phonon scatterings 2D halide perovskites, and the subsequent effects on the charge mobilities are still in debate.

Besides the free-carrier transport in 2D halide perovskites, diffusion and dissociation of excitons are the key mechanisms determining the charge separation. Typical reported diffusion constants are  $10^{-2} - 10^{-1} \text{ cm}^2 \text{ s}^{-1}$ , listed in **Table 7**. An illustration

summarizing typical exciton dynamics and transport is shown in **Figure 14b**. Photogenerated charge carriers typically go through thermalization and subsequent cooling process, which typically occurs at sub-ps to ps time scale. Exciton and charge dynamics dominate the energy transfer on the 1~100ps. Excitons can diffuse to the crystal surfaces over 100ps, where dissociation to free carriers occurs. Rapid and efficient exciton dissociations have been reported in hot-cast RPP films with  $n > 2$ , where the exciton transport mechanisms are dominated by the diffusion to low-energy edge states leading to subsequent dissociation.<sup>273,278</sup> The transfer kinetics from excitons to the edge states, is explicitly characterized using transient absorption spectroscopies with both front and back pump excitation (**Figure 14c-f**), which demonstrates the transport of excitons to the surface edge states via a diffusive process, and the dissociation at surface electronic states driving the charge separation.<sup>273</sup>

Here, we have listed the key factors and bottlenecks that greatly affect the charge carrier transport in 2D halide perovskites and methods to enhance the transport properties for device optimization.

#### **a) Quantum-well structure**

The presence of quantum and dielectric confinement in QWs of 2D halide perovskites resulting in high exciton binding energies exceeding  $k_B T$ , making the dissociation process of photo-generated excitations difficult. Besides, the presence of QWs reduces the carrier diffusion lengths and gives more probability of non-radiative recombination.<sup>274</sup> Overall, increasing the number of perovskite layers in each QW ( $n$  number) increases the fraction of free carriers, which favors the charge separation, however at the consequence of more trap density and less controlled phase purity<sup>255,258,258</sup>. For example, Herz et al. have studied the charge transport properties of the  $PEA_2MAPb_nI_{3n+1}$  system (PEA=2-phenylethylammonium), and demonstrated a maximum mobility with 50% PEA concentration, suggesting a balance between the reduced excitonic system (less  $\langle n \rangle$  value), and increasing density of trap states (higher  $\langle n \rangle$  value) (**Figure 14g**).<sup>255</sup> Gé lvez-Rueda et al. demonstrated enhanced carrier mobility with increasing  $n$ -value, consisting with

lowering of hole effective mass from DFT calculations.<sup>258</sup> Researchers have demonstrated organic cations with high dielectric constants, which reduces the exciton binding energy and promotes the exciton dissociation and transfer of the carriers<sup>310,311</sup>. Besides the exciton transport in quantum wells, exciton dissociation to lower energy states at the edge of perovskite layers have been investigated to be an efficient pathway for 2D halide perovskites with higher  $n$ -value, where diffused excitons efficiently dissociate into free carriers leading to efficient transfer of charge carriers<sup>273,276</sup>.

#### **b) Organic cations**

While organic spacers have greatly limited the out-of-plane mobility of 2D halide perovskites, the carrier transport behavior can be improved by rational design of organic cations, including the ligand lengths, polarity, aromatic moiety, dielectric constant, and divalent spacers. Many studies have focused on exploring short-chain ligands which increase out-of-plane carrier transport.<sup>312,313</sup> For example, Ren et al. demonstrate MTEA molecules enable a sulfur-sulfur interaction at the organic tails, resulting in efficient charge transport.<sup>312</sup> Increasing the dipole moment of organic cations, such as fluorinated spacers, has been found to facilitate the charge separation with polarized crystal lattice, which in turn enhances the carrier transport, as displayed for one example in **Figure 14h**.<sup>260,314-316</sup> Additionally, studies on  $n=1$  halide perovskite have demonstrated increase of out-of-plane conductivity by orders of magnitude, by using the aromatic organics (perylene and pyrene) with proper energy matching with the inorganic layers and enhanced intermolecular hydrogen bonding and super molecular  $\pi$ -stacking.<sup>317</sup> Additionally, 2D halide perovskites with Dion-Jacobson phase with single layer of divalent organics have shorten the interlayer spacing and can lead to more efficient carrier transport than the RP phase.<sup>318</sup> Furthermore, it has been suggested that the distortion of the crystal lattice, including the Pb-I bond lengths and Pb-I-Pb bond angle can greatly affect the charge transport properties in 2D halide perovskites<sup>319</sup>. Many researchers have proposed the introduction of various organic cations, which tailors the structural distortions and bond-angle of Pb-I-Pb in different

ways, resulting in overlap of the orbitals in favor of the electron transport.<sup>320,321</sup>

**c) quality control of the thin film: orientation, thickness, and phase purity**

Besides the intrinsic factors of the 2D halide perovskite crystals, the thin film quality of these are the crucial factors of efficient charge collection. Researchers have explored a variety of methods to control the crystal vertical orientation, film thickness, and single pure phase distribution. Tsai et al. have developed a hot-casting technique to form high-single crystalline films with preferred vertical orientation.<sup>257</sup> Zhao et al. reported the solvent vapor deposition for deposition  $\text{PEA}_2\text{MA}_4\text{Pb}_5\text{I}_{16}$  film resulting in enhanced carrier mobility<sup>322</sup>. Sidhik et al. have observed the presence of memory seeds in the

crystal solvent and develop a new method with pure phase and high crystallinity.<sup>323</sup> Tsai et al. have demonstrated the optimizing the thin film thickness is crucial in the design of 2D halide perovskite-based photovoltaics, where a significant drop in PCE have been revealed with film thickness beyond the depletion region (200-300nm), limited by the exciton diffusion lengths.<sup>287</sup> As suggested in **Figure 14i-j**, thin absorbers result in inefficient photoabsorption despite high internal electrical field assisting the charge collection; Thick absorbers on the other hand, lead to weak internal field to extract carriers from energy barriers. They have shown that the dominant photocurrent collection is related to the electric field assisted electron-hole pair separation and transport across potential barriers.

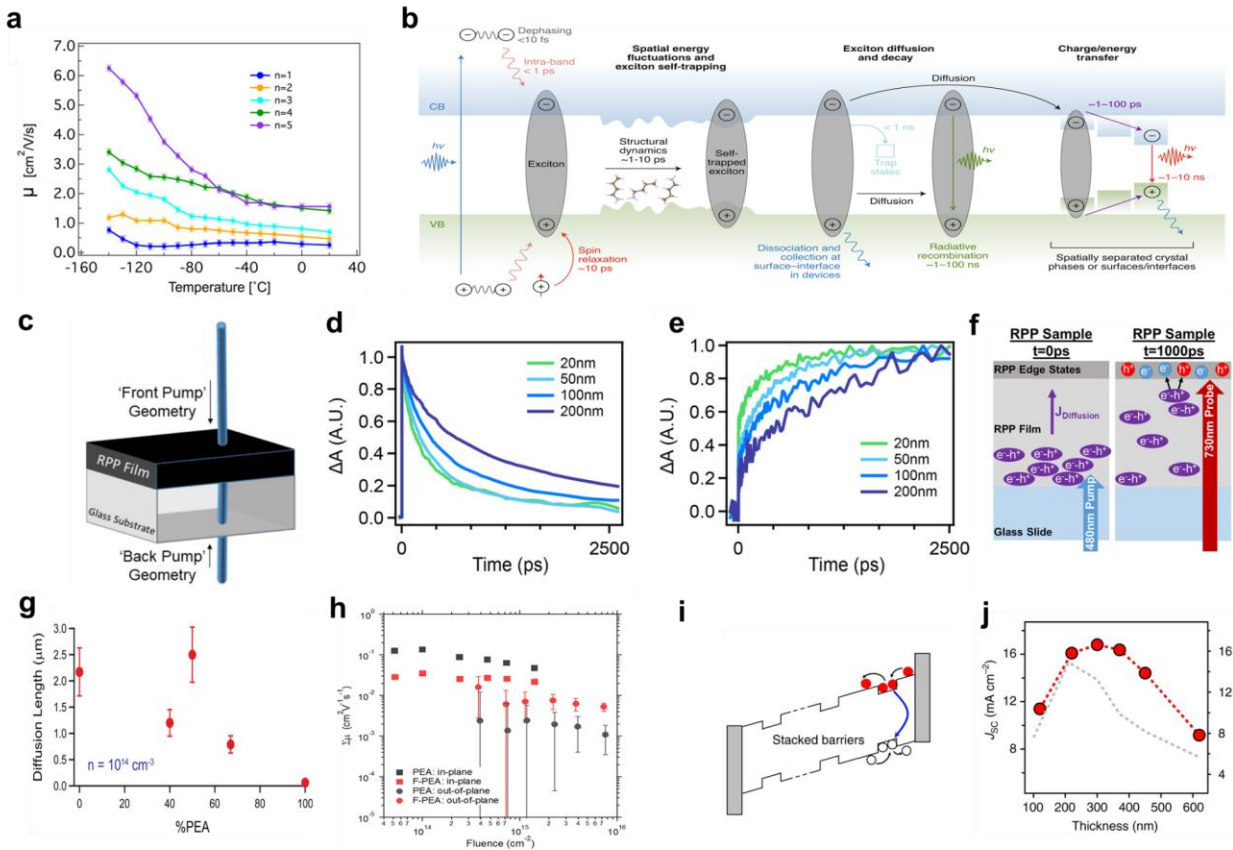


**Figure 14: Carrier transport of 2D perovskites.** a) Carrier mobility of  $(\text{BA})_2(\text{MA})_{n-1}\text{Pb}_n\text{I}_{3n+1}$  at different temperatures. Reproduced with permission from ref.<sup>258</sup> Copyright 2017 American Chemical Society. b) Schematic illustration of exciton dynamics and transport for 2D halide perovskites. Reproduced with permission from ref.<sup>50</sup> Copyright 2020 Springer Nature. c) Schematics of TA spectroscopy with front and back pumping geometry. d) Kinetics of excitonic feature at back pump geometry for various thickness, under excitation of 480nm with  $4 \times 10^{11}$  photons /cm<sup>2</sup>. e) Corresponding rising kinetics of edge state for different thickness. f) Illustration of the charge distribution and transport at back pump geometry. Excitons are created near the bottom of the glass slide and diffuse onto the surfaces where high density of edge states are present,

leading to efficient exciton dissociation at surface. (c-f) Reproduced with permission from ref.<sup>273</sup> Copyright 2020 American Chemical Society. g) Charge carrier diffusion lengths as a function of PEA content for PEA-MA perovskites. Reproduced with permission from ref.<sup>255</sup> Copyright 2016 American Chemical Society. h) TRMC comparison of out-of-plane and in-plan transport for n=1 2D halide perovskites, showing enhanced transport with fluorination. Reproduced with permission from ref.<sup>260</sup> Copyright 2019 American Chemical Society. i) Schematic model showing potential wells in a stacked structure where carriers are prevented from escaping. j) Thickness dependence of  $J_{sc}$  in a device, showing optimal thickness of 200~300nm. (i-j) Reproduced with permission from ref.<sup>287</sup> Copyright 2018 Springer Nature.

### 3.2.5. Urbach energy in 2D halide perovskites

Studies on single-phase 2D halide perovskites have reported typical Urbach energies ranging from 18-35meV at room temperature,<sup>324-326</sup> which are comparable with the typical Urbach tails of 13-15meV in the 3D halide perovskite MAPbI<sub>3</sub> thin films<sup>327,328</sup>. These studies also suggest that the sharpness of the Urbach tail can be greatly impacted by careful material design, such as the homogeneity of the energy landscape, and better control of phase purity and degree of structural disorder<sup>325</sup>.

Besides the static contribution of Urbach energy resulting from intrinsic disorder, temperature-dependent Urbach energies tails are also reported in 2D halide perovskites, as a result of dynamic band energy disorder that is influenced by the vibrational states of the lattice.<sup>324</sup> For instance, Zhang et al. reported Urbach energies of PEAPbI<sub>4</sub> (n=1) film, which gives 20meV at 80K and 35meV at room temperature. Analysis of the Urbach energies based on the Urbach-Martinessen formula reveals a coupling with optical phonons with average energy of 30meV, consistent with the PL broadening as a function of temperature.

### 3.2.6. Solution-processability of 2D halide perovskites

The prerequisite to fabricate a highly efficient halide perovskite solar cell is to obtain crystalline and compact thin films. The traditional solution processing of the halide perovskite film evolves from the precursor solution to the wet film, and finally a solid film on annealing. The crystallization process of halide perovskites follows the classical nucleation and growth theories, which usually starts from the precursor solution. It is very important to optimize this crystallization process to control the nucleation, and growth rate, hence obtaining a high-quality film.

As a result, an in-depth understanding of fundamental mechanisms involved in the crystal nucleation and growth process is required for the optimization of the crystallization kinetics.

In the 2D halide perovskites, the crystalline orientation is very important for efficient charge carrier transport towards the selective contacts. The anisotropy in the charge transport observed in the 2D halide perovskite thin films is not only related to the multiple quantum well nature but also to the inhomogeneous crystal orientation within the crystal structure.<sup>257</sup> There are generally three different types of orientations observed in the two-dimensional halide perovskites namely, vertical, horizontal, and mixed orientation(**Figure 15a**).<sup>329</sup> In a parallel orientation, the inorganic layers are aligned parallel to the substrate which is otherwise referred to as the in-plane orientation. 2D halide perovskites with n<3 are generally aligned parallel to the substrate due to its low formation energy, limiting the charge transport across the layers.<sup>329</sup> In case of vertical orientation, the inorganic layers are aligned perpendicular to the substrate referred as the out-of-plane orientation which is perfect for the charge carrier transport and extraction to the selective contacts. However, the mixed orientation corresponds to the crystallites aligned in random direction inside a thin film. The insulating nature of the organic layers leads to a preferred charge transport along the inorganic layers, while the transport along the spacer layer is hindered. It was reported that the parallel orientation of the 2D halide perovskite thin films can be converted to the mixed orientation by a sequential method, where some of the grains are vertically oriented which increases the performance of the 2D halide perovskite solar cells<sup>330</sup>. There are three important characteristics of a 2D halide perovskite thin film; the n-layer thickness distribution, crystalline orientation, and crystallinity which determines the optoelectronic

properties. The huge diversity in precursor composition which includes different spacer cations, deposition technique, and use of different solvent composition has complicated the crystallization mechanism in the 2D halide perovskite thin films. As a result, there is no generalized technique to fabricate homogenous, oriented, and crystalline 2D halide perovskite thin films which calls for an in depth understanding of the nucleation and the growth mechanism which is a guide for the progress of 2D halide perovskite solar cells or other devices.

In contrast to the 3D halide perovskite, the crystallization of 2D halide perovskites starts at the air-liquid interface where 3D-like inorganic octahedra are formed first, which results in a downward oriented growth as the solvent escapes (**Figure 15b**). Due to the poor solubility of lead iodide, there is an uncontrolled and rapid formation of the PbI<sub>2</sub>-solvent complexes at the air-liquid interface and within the liquid, which results in the formation of 2D halide perovskites with heterogeneous orientation. As a result, a better control of the nucleation process by controlling the growth and the number of PbI<sub>2</sub>-solvent complexes will help in controlling the orientation of the 2D halide perovskite thin films. Tremendous effort which includes solvent engineering, additive engineering, and hot casting technique developed by our group has helped in attaining a out-of-plane oriented 2D halide perovskite thin films from the air-liquid interface<sup>257,331,332</sup>.

Chen et al., studied the crystallization process of the 2D halide perovskite thin films, by starting from a wet solution to the solvent dried final film.<sup>333</sup> They proposed that the difference in solubility of lead iodide, and different organic cations results in heterogenous distribution of the quantum well or n-layer thicknesses within the 2D halide perovskite film. The PbI<sub>2</sub>-solvent complex forms first at the air-liquid interface. Following this, due to the difference in solubility and the steric hindrance of different organic cations, the smaller organic cation (MA or FA) goes and attaches first to the PbI<sub>2</sub>-solvent complex forming a 3D halide perovskite like structures at the top surface which acts as a template for the downward growth of the 2D halide perovskite crystals. The consumption of the small organic cation is accompanied by the coordination with the bulky organic cations resulting in the formation of larger

quantum well or n-value thicknesses at the top air-liquid interface. Thenceforth, there is an increase in concentration of the larger organic spacer cation compared to the small cations promoting the formation of a lower n-phase 2D halide perovskites at the bottom of the film. Therefore, the final film comprises of a mixture of low n-value, larger n-value, and 3D-like halide perovskite crystal structures in a single thin film. Truhlar et al., proposed that the surface tension of solution is the primary reason for the difference in the crystal growth rate on the surface of the liquid and the substrate.<sup>334</sup> Further, Li et al., proposed to slow down the crystallization process to increase the reaction time of the larger organic cations with the PbI<sub>2</sub>-solvent complexes, which has shown to improve the quality of the 2D halide perovskite thin film with much ordered crystal orientation, and reduced phase heterogeneity.<sup>335</sup>

Hence, we can identify the two important prerequisites to obtain a high-quality 2D halide perovskite thin film used for high-efficiency halide perovskite solar cells; 1. Homogenous distribution of the quantum well crystal structures, or n-phases, and 2. ordered out-of-the-plane or vertical crystal lattice orientation. As a result, a tremendous amount of effort has been put forward to obtain these properties in a 2D halide perovskite thin film through different processing strategies.

### **Solution based thin-film processing strategies**

The most attractive part of the 3D halide perovskite materials is their easy solution processability to obtain high quality thin films. However, the solution processed 2D halide perovskite thin film has issues concerning the phase heterogeneity, and crystal orientation. Quintero et al., identified three different 2D halide perovskite thin film properties which can affect the performance of the PV devices<sup>336</sup>, 1. QW orientational disorder and the presence of horizontal wells, particularly of low-n phases acting as source of resistive losses in the device limiting the fill factor, 2. The varying distribution in the bandgap of the 2D halide perovskite films leads to photovoltage losses in the PV devices. The presence of low-n phase is expected to increase the bandgap and hence the open-circuit voltage, but the open-circuit voltage is identical for most 2D halide perovskite devices. This voltage loss can be attributed to the polydispersity of

the quantum well structures. Also, the presence of these low- $n$  phases creates traps for charge carriers due to the type-II band alignment of thin wells, an effect which also leads to the losses in short-circuit current density. 3. The presence of low  $n$  phases reduces the probability of generating charge carriers due to the decreased absorbance of films. The reason of which might be the reduced density of the halide perovskite in the thin films when compared to the proportion of organic spacers. This issue can be resolved by increasing the thickness of the film and reducing the length of the organic spacers. As a result, it becomes imperative to understand and improve the fabrication methods of the 2D halide perovskite thin films. Several works have shown that retarding the crystal growth, rapid nucleation or seed-assisted growth are conducive to obtain a high quality 2D halide perovskite thin film. The methods that are generally used for fabricating the 2D halide perovskite films are hot casting, vacuum method, antisolvent, and post annealing method etc.

**Hot-casting method:** The room temperature processing of 2D halide perovskite thin films results in a random orientation, whereas the hot casting approach where the hot precursor solution is spin casted on a hot substrate has realized dominant vertical orientation of the 2D halide perovskite crystals (**Figure 15c**). In 2016, Tsai et al. fabricated a high-quality 2D  $\text{BA}_2\text{MA}_3\text{Pb}_4\text{I}_{13}$  ( $n=4$ ) halide perovskite film with single crystal like characteristics using the hot-casting approach, where the halide perovskite solution kept at 70 C was immediately spin-coated on a hot substrate (150 C) to obtain a preferential out-of-the-plane orientation.<sup>257</sup> They utilized the grazing incidence wide angle scattering (GIWAXS) measurements to explore the crystallinity and orientation of the as grown films. Sharp Bragg spots were obtained for films fabricated using the hot casting approach indicating high crystallinity and better orientation, whereas the film fabricated by normal spin coating process showed wide concentric rings indicative of lack of preferential orientation and inferior crystallinity. Currently, the hot casting approach is widely used for various 2D halide perovskite materials. Looking into the mechanism, the pre-heated substrate accelerates the nucleation process from the intermediate sol-gel complex to the

2D halide perovskite phase, which initiates from the solution-substrate interface instead of the air-liquid interface. Some of the concerns regarding this technique stems from the experimental repeatability, which includes difficulty in precise control over the temperature, upscaling of the technique, and sudden variation in the temperature leading to undesirable strain and cracks arising due to the difference in the thermal expansion coefficient of the glass and the halide perovskite film.

**Post-annealing strategy:** The post-annealing technique was initially used in the 3D halide perovskite films to reduce the number of grain boundaries by increasing the grain size achieved by Ostwald ripening. However, this strategy has been shown to modify the phase distribution and crystalline orientation of the 2D halide perovskite thin films to attain more order in the crystal structure. Zheng et al., demonstrated a slow post annealing (SPA) technique where the fabricated  $(\text{BA})_2(\text{MA})_3\text{Pb}_4\text{I}_{13}$  RP halide perovskite film was annealed at a temperature of 60 C for 2.5 days. They observed a reorganization in the phase distribution of the 2D halide perovskite films achieving a gradual increase in the QW thickness in the perpendicular direction which helps in efficient charge carrier extraction and reduced surface recombination. The devices fabricated by the SPA technique achieved a power conversion efficiency of 17.3% with enhanced shelf life stability.<sup>337</sup>

Thenceforth, some modifications were made to the post annealing treatment where the annealing process was carried out in a solvent-vapor environment, which will basically plasticize the thin film, and lead to the reorientation of the crystallite domains (**Figure 15d**). Loo et al., used isopropanol as the processing solvent, where the 2D  $\text{PEA}_2\text{MA}_4\text{Pb}_5\text{I}_{16}$  RP halide perovskite film was annealed for several hours to attain vertical orientation without compromising the phase of the obtained film. Similar strategy was utilized in a DJ based halide perovskite  $(\text{BDA})(\text{Cs}_{0.1}\text{FA}_{0.9})_4\text{Pb}_5\text{I}_{16}$  ( $\text{BDA} = 1,4\text{-butanediamonium}$ ), which provided an efficiency of 18.2%<sup>322</sup>. In addition to the modification observed in the crystalline orientation, the solvent vapor also helps in improving the crystalline quality of the 2D halide perovskite films not only on the



surface but also within the bulk depending on the penetration depth of the solvent vapor which is directly proportional to the amount of time used for annealing. Despite of all these advantages, there are some major concerns that the extended annealing times would affect the compositional stability of the 2D halide perovskite film due to the volatility of the organic components resulting in the formation of ionic defects within the bulk and on the surface, deteriorating the solar cell performance and the stability of the device.

**Antisolvent technique:** The antisolvent approach evolved from the field of 3D halide perovskites was used for growing highly crystalline, uniform, and compact film by selectively washing away the high boiling point solvent to obtain uniform crystallization.<sup>189</sup> The most common solvents used for fabricating the halide perovskite films include the polar protic solvents; dimethylformamide, dimethyl sulfoxide, N-methylpyrrolidone, and gamma-butyrolactone, all of which have high boiling points greater than 150°C. As a result, uniform evaporation of these solvents at lower temperature of 100°C (used for fabricating the halide perovskite thin films) is difficult, which leads to a retarded nucleation, and random crystallization forming a non-uniform and less crystalline film. To counter this, the researchers developed an antisolvent process to produce high quality films. The antisolvents used include nonpolar solvents like diethyl ether, chlorobenzene, anisole, and toluene etc., which is having a huge polarity difference with the polar protic solvents used for the film fabrication. Due to this difference, these antisolvents get mixed with the main solvent without interacting with the solute hence rapidly washing away the solvent forming a supersaturated precursor mix which acts as a driving force for the crystallization process. The antisolvent approach was mainly used in the Dion Jacobson 2D halide perovskites considering its close similarity with the 3D halide perovskite which shows a stronger Lewis acid-base interaction between the main solvent and the halide perovskites<sup>51,338</sup>. Xie et al. showed that the introduction of the antisolvent chlorobenzene in the precursor solution improves the morphology and the crystalline quality of thin films.<sup>339</sup> They found that it is achieved by accelerating the nucleation of 2D

(BA)<sub>2</sub>(MA)<sub>3</sub>Pb<sub>4</sub>I<sub>13</sub> halide perovskite leading to a compact, pinhole free, and highly crystalline film. However, the major drawback is the experimental reproducibility, which requires a precise control in the location at which the antisolvent is dropped, the time of antisolvent dropping, the amount of antisolvent used, and the height from the substrate from where the antisolvent is dropped. Any slight variation from these optimized conditions has serious impacts on the final crystalline quality and the morphology of the thin film obtained. Hence, the upscaling of the antisolvent process turns out to be difficult. In addition, the amount of antisolvent used is large in quantity, which would increase the fabrication cost, and also most of these antisolvents are toxic organic compound which happens to be harmful for the environment and difficult to handle for human beings. Despite of all these shortcomings the antisolvent approach still continues to be a convenient, and significant method for use in the lab scale.

**Phase-selective strategy:** A key challenge in the field of 2D halide perovskites is to develop a technique to synthesize phase-pure 2D halide perovskite, which dominantly comprises of single QW thicknesses. The classical approaches, which we discussed previously forms halide perovskite layer thickness intermediate between the 2D halide perovskite n=1 and the 3D halide perovskite. It usually goes through an intermediate sol gel complex between the precursor and the solvent which is the main reason for the heterogeneous phase distribution in 2D halide perovskite thin films. Liang et al., used a molten salt n-butylammonium acetate, instead of the traditional spacer salt n-butylammonium iodide, to obtain a single QW thickness of BA<sub>2</sub>MA<sub>n-1</sub>Pb<sub>n</sub>I<sub>3n+1</sub> (n=1-5).<sup>340</sup> The n-butylammonium acetate forms a gel-like intermediate phase that is uniformly distributed throughout the halide perovskite framework, allowing phase-pure quantum well films to be produced with vertically aligned grains. These quantum wells have a single well width and are highly efficient, achieving a power conversion efficiency of 16.25% and an open voltage of 1.31 V. Furthermore, the solar cells show excellent stability, with less than 10% efficiency degradation after exposure to high humidity, high temperature, or continuous light for extended periods of time. Further, Sidhik et al., reported a phase-

selective synthesis method which involves a pre-crystallization step of 2D halide perovskite crystalline powders followed by single-step solution processing, to produce 2D halide perovskite thin-films principally formed from perovskite layers with a single QW layer thickness (or  $n$ -value), with high crystallinity and desired orientation suitable for fabricating optoelectronic devices (**Figure 15e**).<sup>323</sup> Comprehensive characterization revealed the exact

nature of 2D halide perovskite film formation where the growth is dominated by the nucleation of 100-200 nm homogeneous  $n$ -value seeds, which has characteristics similar to the parent crystal dissolved. The phase-selective method showed solar cells with an efficiency of 17.1% with a high open-circuit voltage of 1.22 V and an enhanced operational stability of  $T_{98} > 800$  h under continuous illumination without any external heat management

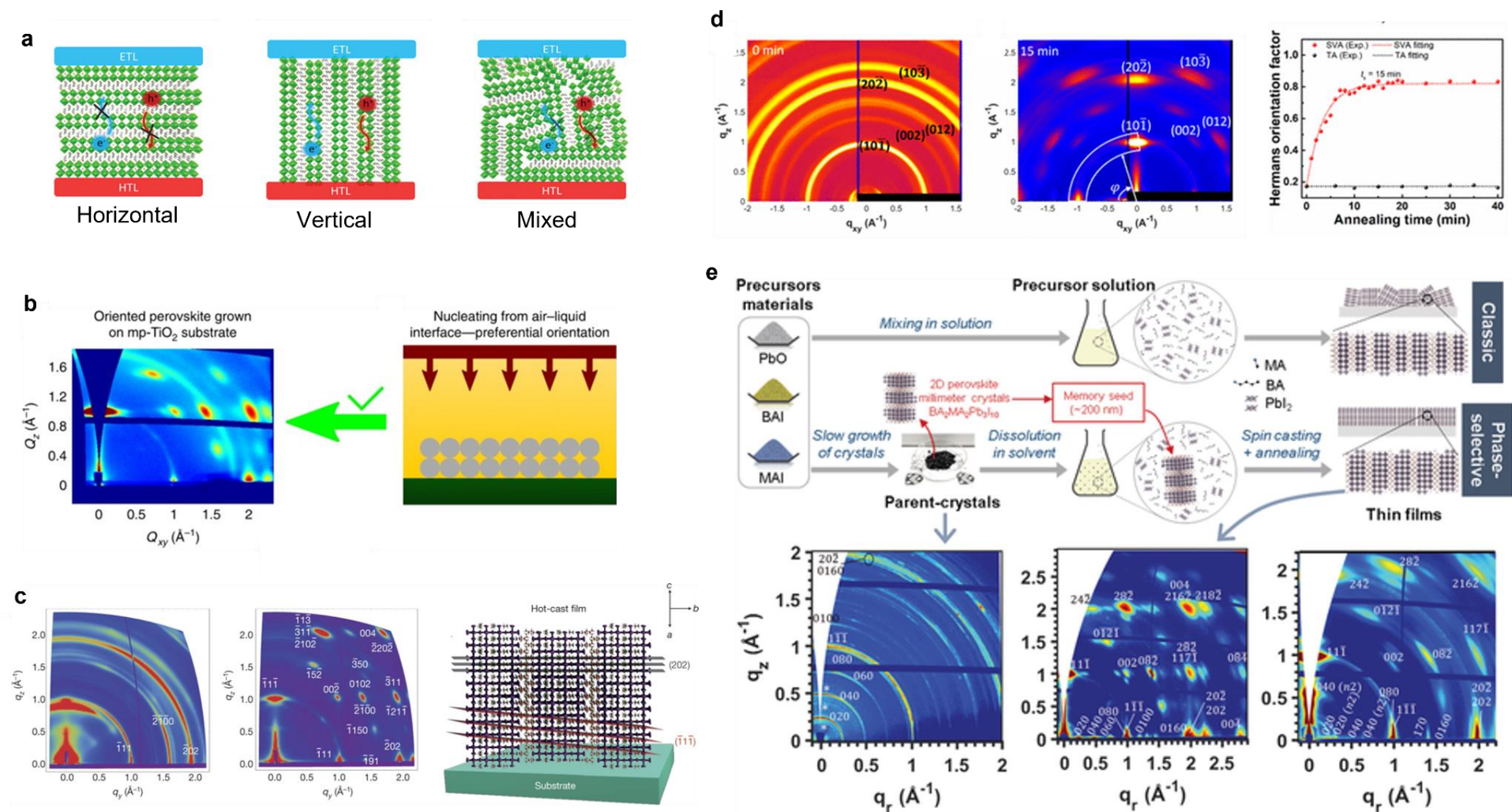


**Figure 15: Solution processing of 2D halide perovskites.** a) Schematic showing the difference in charge transport for horizontal (left), vertical (middle) and mixed (right) orientation of a 2D halide perovskite film. Reproduced with permission from ref.<sup>329</sup> Copyright 2021 Wiley-VCH. b) A schematic showing how 2D halide perovskites nucleate from the air-liquid interface in contrast to 3D halide perovskites (right) and a GIWAXS pattern of an oriented 2D film demonstrating that despite this nucleation behavior growing oriented 2D perovskite films is possible. Reproduced with permission from ref.<sup>333</sup> Copyright 2018 Springer Nature. c) GIWAXS patterns of room-temperature-cast (left) and hot-cast (middle) films of BA<sub>2</sub>MA<sub>3</sub>Pb<sub>4</sub>I<sub>13</sub> films showing formation of oriented film with hot-casting, and a schematic representation of (101) orientation with the (202) and (-11-1) planes labeled (right). Reproduced with permission from ref.<sup>257</sup> Copyright 2016 Springer Nature. d) GIWAXS patterns of PEA<sub>2</sub>MA<sub>4</sub>Pb<sub>5</sub>I<sub>16</sub> perovskite films before (left) and after (right) solvent vapor annealing treatment, and device PCE as a function of Hermans orientation factor (right). Reproduced with permission from ref.<sup>322</sup> Copyright 2020 American Chemical Society. e) (top) Schematic showing the phase purity and orientation

2D halide perovskite films for classic solution method (from precursor salts) and phase selective method (from single crystals). (bottom) GIWAXS patterns for phase-pure crystal powder (left), phase-selective film (middle), and classically-processed film (right). Reproduced with permission from ref.<sup>323</sup> Copyright 2021 Wiley-VCH.

Accepted manuscript

### 3.2.7. Ionic mobility in 2D halide perovskites and potential for electrical doping

2D halide perovskites show reduced ionic mobility compared to 3D halide perovskites. In the out-of-plane direction this can intuitively be explained by the A' cation acting as an energetic barrier to ion hopping<sup>57</sup>. What's more interesting is that in-plane ionic mobility is suppressed as well, apparently as a result of a higher vacancy formation energy for  $V_I$  and  $V_{MA}$  and therefore a lower vacancy concentration.<sup>341-343</sup> Several studies have compared the temperature dependence of conductivity in 3D and 2D halide perovskites and found that while 3D halide perovskites show a distinct transition from electronic to ionic-dominated charge transport at high temperatures, 2D halide perovskite conductivity remains electronic across the temperature region<sup>341,342</sup>. This is true both in dark conditions and under 1-sun illumination (**Figure 16a**).

As should be expected, halide mobility has been shown to increase with  $\langle n \rangle$ -value<sup>344</sup>. **Figure 16b** shows the activation energy for iodine ion diffusion across a mechanically-paired  $PEA_2MA_{n-1}Pb_nI_{3n+1}$  -  $PEA_2MA_{n-1}Pb_nBr_{3n+1}$  interface for varying  $\langle n \rangle$ -value. PEA n1 films show an  $E_a$  of 71.5kJ/mol compared to 66.9kJ/mol for  $\langle n \rangle=6$  and 57.8kJ/mol for  $\langle n \rangle=10$ . The spacer cation also influences ionic mobility, with bulky  $\pi$ -conjugated cations

suppressing mobility compared to linear cations and longer-chain linear cations suppressing mobility compared to shorter ones.<sup>345,346</sup> **Figure 16c** shows the rate of ion diffusion across a mechanically paired  $A'_2MAPb_2I_7$  -  $A'_2MAPb_2Br_7$  interface for A' = BA or HA (hexylammonium), as measured by the shift in excitonic absorption peak for the iodide film. HA, with a carbon backbone two units longer than BA, shows an  $E_a$  14kJ/mol greater.<sup>346</sup>

Another result of 2D halide perovskites' higher defect formation energy is their suppressed self-doping compared to 3D halide perovskites. The self-doping concentration in single crystals of  $PEA_2MA_{n-1}Pb_nI_{3n+1}$  for  $n=1-3$  was found to be more than three orders of magnitude lower than in  $MAPbI_3$ ,<sup>302</sup> as seen from sheet resistance measurements (**Figure 16d**). Low self-doping concentrations could suppress the screening of extrinsic electronic dopants seen in 3D halide perovskites.<sup>202</sup> Combined with 2D halide perovskites' suppressed ion migration, this suggests that electronically doped homojunctions or heterojunctions of 2D halide perovskites may be more feasible than with 3D halide perovskites. More research needs to be done on the performance and stability of doped 2D-2D and 2D-3D junctions, which could in theory be used to realize 2D halide perovskite transport layers in devices

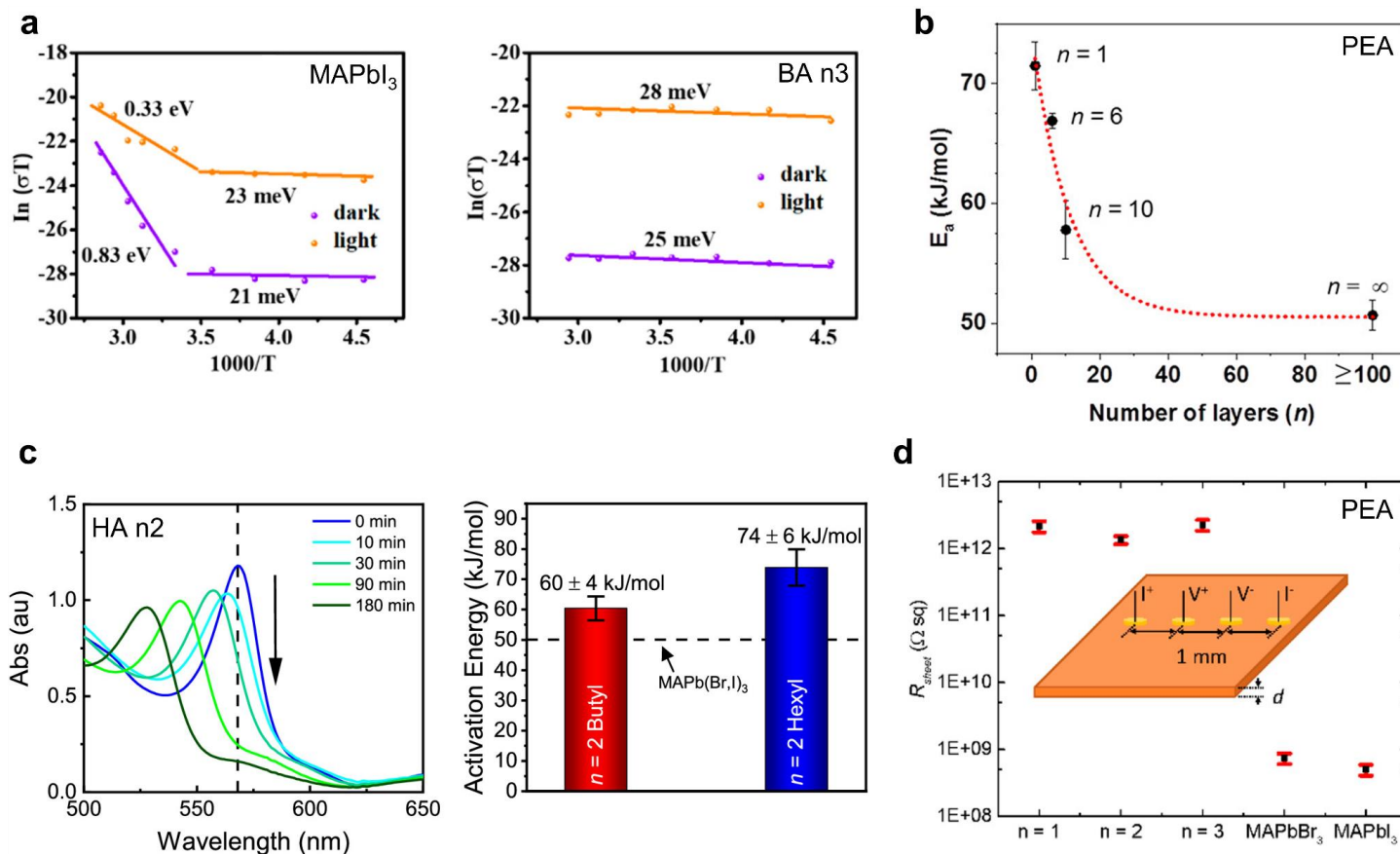


**Figure 16: Ion migration in 2D perovskites.** a) Temperature-dependent conductivity of single crystals of MAPbI<sub>3</sub> (left) and BA<sub>2</sub>MA<sub>2</sub>Pb<sub>3</sub>I<sub>10</sub> (right) showing high-temperature transition to ionic-dominated conductivity in 3D halide perovskites but no such ionic conductivity regime in 2D halide perovskites. Reproduced with permission from ref.<sup>342</sup> Copyright 2018 American Chemical Society. b) Activation energy for iodine ion diffusion across a mechanically-paired PEA<sub>2</sub>MA<sub>n-1</sub>Pb<sub>n</sub>I<sub>3n+1</sub> - PEA<sub>2</sub>MA<sub>n-1</sub>Pb<sub>n</sub>Br<sub>3n+1</sub> interface for varying  $\langle n \rangle$ -value.  $E_a$  is determined by the rate of change in the PEA<sub>2</sub>MA<sub>n-1</sub>Pb<sub>n</sub>Br<sub>3n+1</sub> film's absorption spectrum. The  $E_a$  for 3D  $n=\infty$  was taken with permission from ref.<sup>347</sup> Copyright 2020 American Chemical Society. Reproduced with permission from ref.<sup>344</sup> Copyright 2019 American Chemical Society. c) Absorption spectrum over time for a film of HA<sub>2</sub>MAPb<sub>2</sub>I<sub>7</sub> (HA=hexylammonium) mechanically paired with a film of HA<sub>2</sub>MAPb<sub>2</sub>Br<sub>7</sub> at 100°C (left) showing a bandgap shift with Br diffusion, and calculated activation energy for Br ion diffusion for BA vs HA A'-site cation (right) found by repeating this experiment at a variety of temperatures and fitting the rate of excitonic peak shift. Reproduced with permission from ref.<sup>346</sup> Copyright 2020 American Chemical Society. d) Sheet resistance of single crystals of PEA<sub>2</sub>MA<sub>n-1</sub>Pb<sub>n</sub>I<sub>3n+1</sub> ( $n=1-3$ ) using the four-point probe method shown in the inset. The thickness  $d$  is  $<10\mu\text{m}$  for 2D samples and  $200\mu\text{m}$  for 3D samples. The high sheet resistance for 2D samples suggests a low intrinsic carrier concentration. Reproduced with permission from ref.<sup>302</sup> Copyright 2017 American Chemical Society.

### 3.2.8. Bulk ferroelectricity in 2D halide perovskites

Compared to 3D halide perovskites, ferroelectricity in 2D halide perovskites is much more common and moreover can be engineered to an extent through the choice of A'-site and A-site cations. A'-site cations that are reorientable with a dipole moment perpendicular to their rotation axis (i.e., the stacking axis) can in some cases form polarization domains of the same orientation,

exhibiting an order-disorder ferroelectric-paraelectric phase transition, although this is not guaranteed. For example, BZA<sub>2</sub>PbCl<sub>4</sub> (BZA = benzylammonium) exhibits a ferroelectric phase transition through spacer cation alignment,<sup>348</sup> but BZAPbI<sub>4</sub> does not.<sup>349</sup> The 2D structure also permits larger A-site cations ( $t>1$ ) and a greater degree of B-site distortion, which can unlock a displacive ferroelectric effect through the preferential orientation of the B-site  $ns^2$  electron pair and off-center displacement of the B-site cation

within its octahedral cage.<sup>148</sup> This effect can explain the ferroelectric and antiferroelectric phases shown in 2D halide perovskites with oversized A-site cations such as  $\text{BA}_2\text{EA}_2\text{Pb}_3\text{I}_{10}$  (EA = ethylammonium),<sup>77</sup> and  $\text{EA}_4\text{Pb}_3\text{I}_{10}$ <sup>350</sup> and may explain why  $\text{BZAPbI}_4$  is not ferroelectric while  $\text{BZA}_2\text{PbCl}_4$  is.<sup>148</sup>

The ideal (undistorted) reference RP and DJ structures for bulk 2D halide perovskites correspond to the  $D_{4h}$  point group<sup>50,100</sup>. High temperature centrosymmetric crystal phases of 2D hybrid halide perovskites further exhibit an in-plane cell doubling via antiferrodistorsive tilts of the octahedra. Additional polar lattice distortions in relation with polar space groups can be very often proposed depending on the number of Bragg reflections considered in the refinement of the crystallographic structure. But as pointed out by some authors, such assignment can be ambiguous because of the dynamic disorder present in most of the halide perovskites<sup>52</sup>.

A better way to gauge the existence of a ferroelectric phase is to rely on experimental techniques dedicated to the direct characterization of the electrical polarization and to observe a phase transition from a ferroelectric to a paraelectric phase at a well-defined Curie temperature, and a polarization hysteresis. An example is provided by the 2D halide perovskite  $\text{BZA}_2\text{PbCl}_4$ , which crystallizes in a  $\text{Cmca}$  centrosymmetric phase at high temperature and undergoes a ferroelectric phase transition at  $T=438\text{K}$  to a  $\text{Cmc}21$  non-centrosymmetric structure<sup>348,351</sup> (**Figure 17**). It shall be pointed out that in most cases reported so far, the polar axis is perpendicular to the stacking which leads to an incomplete Rashba effect with a partial in-plane spinor splitting<sup>352</sup>. In recent years, a number of well-documented examples have been reported, mostly involving 2D bromide halide perovskites. Interestingly, ferroelectricity can be sometimes observed for  $n=2$  or  $n=3$  materials,<sup>73,78,353–355</sup> while the  $n=1$  phase remains non-polar.<sup>285</sup>

Another type of lattice distortion can be induced by using chiral molecules in the barrier. These distortions are not necessarily related to a loss of centrosymmetry and a polar lattice.<sup>356</sup> Transfer of chirality to the halide perovskite lattice is expected, with a modification of the electronic properties close to the bandgap and various specific

optoelectronic properties, such as circular dichroism or circular polarized light emission.<sup>357–363</sup>



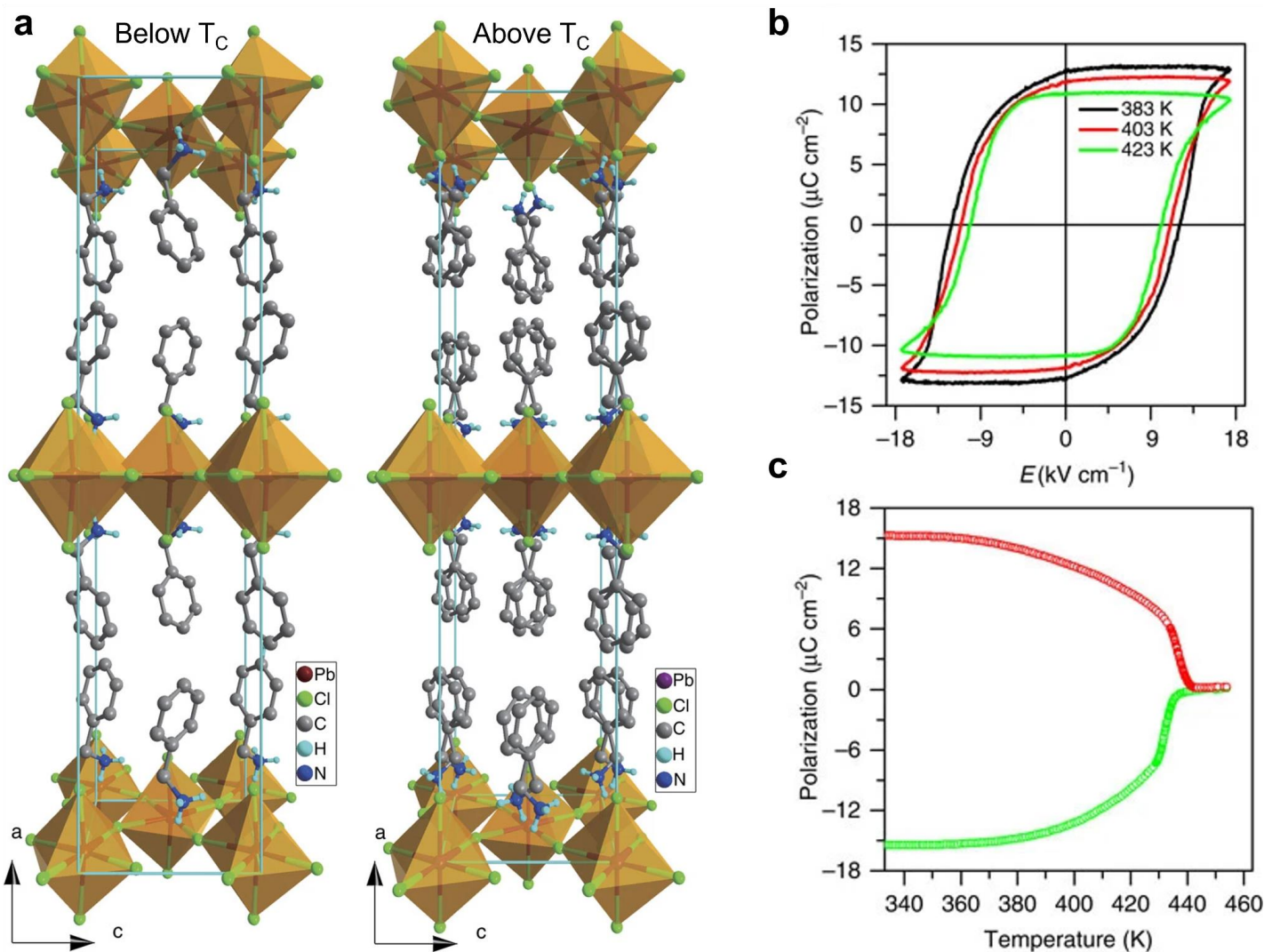


**Figure 17: Ferroelectricity in 2D perovskite BZA<sub>2</sub>PbCl<sub>4</sub> (BZA=benzylammonium).** a) Structure of BZA<sub>2</sub>PbCl<sub>4</sub> below (left) and above (right) its Curie temperature of 438K showing preferential rotational alignment of the BZA cations at low temperature, giving rise to a non-centrosymmetric crystal structure. b) Polarization-Electric field (PE) hysteresis loops for BZA<sub>2</sub>PbCl<sub>4</sub> showing a saturation polarization of ~13μC cm<sup>-2</sup>, among the highest values reported for a molecular ferroelectric. c) Temperature-dependence of BZA<sub>2</sub>PbCl<sub>4</sub> polarization as determined by pyroelectric response, showing the paraelectric-ferroelectric phase transition at 438K. (a-c) Reproduced with permission from ref.<sup>348</sup> Copyright 2015 Springer Nature.

### 3.2.9. Photodoping of 2D halide perovskites/light-induced lattice dynamics

In the semiconductors, photo-generated carriers release their energy to lattice, which eventually loses their energy as heat via lattice vibrations, and therefore perturbs the crystal lattice. For 2D halide perovskites, despite intensive studies on electron-phonon coupling, and carrier dynamics, only a few studies have been focused directly on the lattice dynamics. This is partially due to the structural complexity in 2D halide perovskites. Studies based on ultrafast spectroscopy and diffraction techniques

have revealed a variety of lattice dynamics, such as polaronic carrier-lattice coupling<sup>364</sup>, exciton-polarons<sup>365,366</sup>, coherent optical and acoustic phonons<sup>364,367-369</sup>, and specific movements involving octahedral twisting and tilt.

#### a) Polaronic lattice response

Thouin et al. have observed polaronic characters of excitons in n=1 PEA 2D halide perovskites, where the exciton states are coherently coupled at low temperatures (T<100K) and low excitation densities to low-frequency optical vibrational modes. These coherent vibrational modes

involve motions of the lead iodide layers (octahedral tilt and twisting), leading to specific lattice reorganizations.<sup>364</sup> Kandada & Silva attribute their observations to the formation of ‘exciton polaron’ quasiparticles to describe the exciton-lattice interaction dynamics via polaronic effects, in 2D halide perovskites<sup>365</sup>.

#### **b) Coherent coupling to lattice vibrations**

Similarly, Guo et al. reported oscillation of electronic bandgaps induced by coherent lattice vibrations via optical phonons by non-resonance infrared pumping, which is attributed to the antiphase octahedral rotations at ultrafast time scales<sup>367</sup>. Quan et al. studied the vibration relaxation in Bromide 2D halide perovskites, which suggests dynamic lattice disorder via phonon dephasing. Such vibrational relaxation rate and their temperature dependence can be tailored by the choice of flexible alkyl- or aromatic spacer cations<sup>369</sup>.

#### **c) Relaxation of lattice distortion via octahedral tilt**

Cuthriell et al. studied the non-equilibrium lattice response of BA and PEA n=1 halide perovskites and reveals a suppressing linewidth narrowing in both transient X-rays and photoluminescent spectra at ~1ns time scales, suggesting a transient ordering of distorted octahedra (**Figure 18 a,b**)<sup>370</sup>. Interestingly, Zhang et al. has reported lattice dynamics beyond mott density, and revealed an ultrafast relaxation of the lattice distortion at very short time, via reduced in-lane octahedral tilting (relaxation of antiferro-distortions) in DJ-type 2D halide perovskites (**Figure 18 c-e**)<sup>371</sup>. Such strong carrier-lattice interactions are initiated by dense electron-hole plasma beyond mott

density. Furthermore, such response is observed to be absent in RP-type 2D halide perovskites, where less in-plane distortion is present in the intrinsic structure. These behaviors suggest the interactions between the carrier gas and lattice are tailored by the rigidity of the spacer cations and the intrinsic distortion of the crystal structure.

#### **d) Long-time dynamics: lattice response upon light soaking**

Apart from the role of octahedral tilting in the short-time light-induced lattice dynamics, the lattice parameter contractions have also been reported at long-time scale. Specifically, Li et al. investigated the light-soaking effect of 2D halide perovskites and observed interlayer contraction in in-plane and out-of-plane directions (**Figure 18 f-h**), which leads to an increase in power conversion efficiency in DJ based 2D-halide perovskite solar cells.<sup>372</sup> The work showed that by illuminating solar light onto a 4AMP based DJ phase 2D halide perovskite (4AMP = 4-(aminomethyl)piperidinium), we can modulate the pre-existing interlayer iodine---iodine interactions and increase carrier mobilities in the out-of-plane (across the organic spacer cation) direction by a factor of 3. We further find that this enhancement of the transport properties only occurs in 2D halide perovskite have compact spacer cation such as 4AMP and GA molecules and where the stacking of the inorganic octahedra slabs are directly on top of each other in either one or both planar directions. Similar experimental and theoretical studies have also indicated that the DJ phase halide perovskite exhibits longer carrier lifetime and higher transport mobilities compared to the “softer” RP phase.

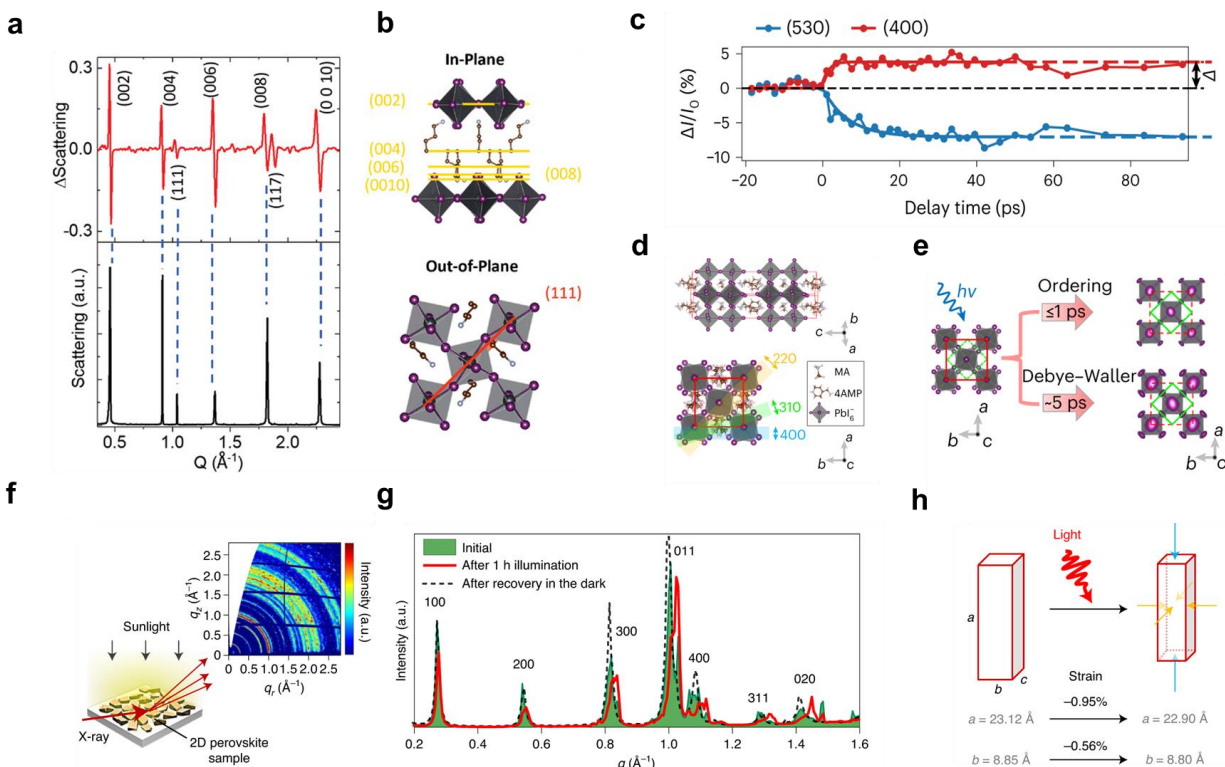


**Figure 18: Photodoping and light-induced lattice dynamics in 2D halide perovskites.** a) Static (black) and transient (red) XRD patterns of RP 2D halide perovskites BAPbI<sub>4</sub> at 1ns and 22 $\mu$ J/cm<sup>2</sup>. The positive and negative differential signals in the transient pattern indicate peak shifting towards lower Q. This behavior is attributed to the increase of out-of-plane Pb-I-Pb bond angles, which gives rise to red shifting and narrowing of PL over time. b) Demonstration of In-plane and out-of-plane Bragg peaks of interest. (a-b) Reproduced with permission from ref.<sup>370</sup> Copyright 2022 Wiley-VCH. c) Time traces of Bragg peaks (400) (530) in 2D halide perovskites (4AMP)(MA)Pb<sub>2</sub>I<sub>7</sub> single crystal, revealing in-plane lattice dynamics with light excitation. d) Crystal structure of (4AMP)(MA)Pb<sub>2</sub>I<sub>7</sub> viewed at [110] and [001] directions, showing intrinsic in-plane octahedral rotations. e) Schematic illustration of the lattice dynamics in DJ 2D halide perovskites, showing light-induced reduction of octahedral tilt, and thermally activated atomic displacement from Debye-Waller effect. (c-e) Reproduced with permission from ref.<sup>371</sup> Copyright 2023 Springer Nature. f) Schematic illustration of in-situ GIWAXS experiment and powder diffraction pattern of 2D halide perovskites. g) Angular-integrated diffraction spectra before and after sun light illumination, and after sample resting in the dark. h) Overview of the light-induced lattice contraction in 2D halide perovskites. (f-h) Reproduced with permission from ref.<sup>371</sup> Copyright 2022 Springer Nature.

### 3.2.10. Best-performing 2D halide perovskite devices

Partially because of its higher exciton binding energy and reduced carrier mobility and partially because of a diminished focus in the halide perovskite community on 2D halide perovskite devices, 2D solar cell efficiency trails behind that of 3D. Exciton binding energy is reduced, and carrier mobility is increased as a 2D halide perovskite's n-value increases, and as a result increasing the n-value of 2D halide perovskites is a major goal in the halide perovskite community. As of February 2023

the highest-efficiency low- $n$ -value “quasi-2D” halide perovskite solar cell used an ACI absorber layer of GAMA<sub>5</sub>Pb<sub>5</sub>I<sub>16</sub> (GA  $\langle n \rangle = 5$ ) in an n-i-p architecture with a TiO<sub>2</sub> ETL and a Spiro-OMeTAD HTL, and achieved an excellent PCE of 22.3%.<sup>373</sup> The J-V curve and device architecture for this cell is shown in **Figure 19a**. However, treating such devices as quasi-2D may be inaccurate, as the diffraction pattern (**Figure 19b**) and absorption spectrum (**Figure 19c**) of the GA  $\langle n \rangle = 5$  film in fact showed a mixture of 3D MAPbI<sub>3</sub> and 2D GA  $n = 1-3$ . The label of “quasi-2D” for mixed 3D-2D systems

grown using the stoichiometric ratio of precursor salts for a certain  $n$ -value may not accurately capture the materials properties of such systems, which have complex microstructures and significant regions of majority-3D phase. The language used to describe phase-pure ( $n$ ) and mixed-phase ( $\langle n \rangle$ ) systems is often interchangeable in the perovskite community, but their materials and device properties are vastly different, suggesting an urgent need to refine the language and make the distinction clear as phase-purity becomes more realizable in 2D films. As will be discussed below, both pure-phase and mixed-phase systems show great promise for high-performance halide perovskite devices, and both deserve significant further exploration.

One reason for the prevalence of mixed 2D or mixed 2D-3D in reports of 2D halide perovskite films and devices is the difficulty of depositing phase-pure 2D films, as discussed above. As a result, relatively

few papers exist which demonstrate phase-pure high- $n$  2D devices. The best-performing solar cell using a majority-“phase-pure” 2D halide perovskite absorber was reported by our group in 2022 at 18.3%.<sup>372</sup> High phase-purity (4AMP)MA<sub>2</sub>Pb<sub>3</sub>I<sub>10</sub> (DJ  $n=3$ ) was used as the absorber layer of an inverted solar cell with a PEDOT:PSS HTL, a PCBM ETL, and an Al top contact. The device efficiency was seen to improve by 2.7% after 10 minutes light exposure, which was attributed to light-induced interlayer contraction reducing the height and width of the organic layer’s potential barrier. **Figure 19d** shows the J-V curve and device architecture for the phase-pure DJ cell. The GIWAXS pattern for the DJ film in **Figure 19e** confirms the phase-purity, with no 2D peaks besides the  $n_3$  peaks observable. As these results suggest, the potential barrier of the organic layer is a persistent hindrance to the realization of high efficiency 2D devices

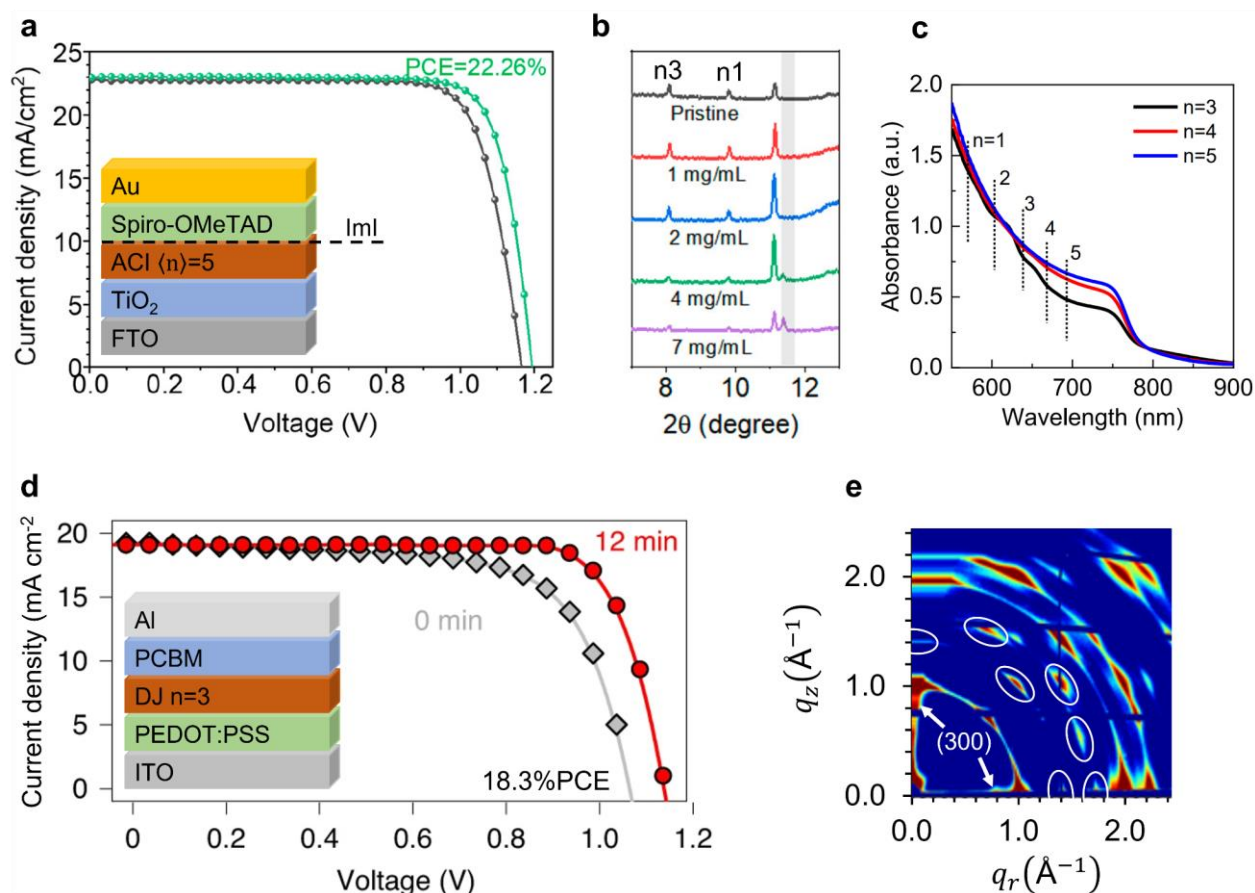


**Figure 19: State-of-the-art 2D perovskite solar cells.** a) Record-efficiency “quasi-2D” perovskite device J-V curve with 22.3% PCE. Inset shows device architecture: FTO – TiO<sub>2</sub> – (GA)(MA)<sub>5</sub>Pb<sub>5</sub>I<sub>16</sub> ( $\langle n \rangle = 5$ ) – lml passivation layer – Spiro-OMeTAD – Au. b) Low-angle XRD of  $\langle n \rangle = 5$  film showing mixed-phase  $n=3$ ,  $n=1$ , and 3D with and without lml additive. c) Absorption spectra of  $\langle n \rangle = 3, 4, 5$  films showing lower- $n$  phases for  $\langle n \rangle = 3$ , large 3D absorption edges for all samples. (a-c) reproduced with permission from ref.<sup>373</sup> Copyright 2022

American Chemical Society. d) Record-efficiency “phase-pure” 2D perovskite device J-V curve with 18.3% PCE after 12 min light soaking. Inset shows device architecture: ITO – PEDOT-PSS – (4AMP)(MA)<sub>2</sub>Pb<sub>3</sub>I<sub>10</sub> (n=3) – PCBM – Al. e) GIWAXS pattern of n=3 device film showing diffraction peaks of 4AMP n=3 including the low-angle (300) peak at q~0.8, with no other observable phases. Other peaks below q=2 which can be definitively assigned to n3 are circled in white. 3D diffraction peaks overlap with n3 peaks at q~1 and q~2 and so those peaks cannot definitively be assigned to n3. (d-e) reproduced with permission from ref.<sup>372</sup> Copyright 2022 Springer Nature.



## 4. Stability of 3D and 2D halide perovskites

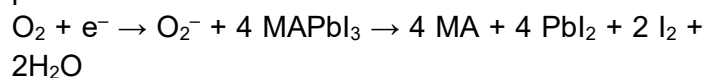
### 4.1. Issues with 3D halide perovskite stability

While the device performance of 3D halide perovskites is comparable to that of inorganic semiconductors, their stability is far worse. 3D halide perovskites are vulnerable to degradation via O<sub>2</sub>, water, elevated temperatures, bias, and light, as well as reactions with other layers in a device stack. The A, B, and X sites in 3D halide perovskites are all low-valence, high-radius ions, giving the crystal low lattice energy and higher instability against environmental stressors.<sup>374</sup> Ammonium groups in A-site cations are especially vulnerable to attack by reactive molecules such as O<sub>2</sub> and H<sub>2</sub>O.<sup>375</sup> Unfortunately, the stability of 3D halide perovskites does not share the same tolerance to defects as its device performance does; there is evidence that halide perovskite degradation is mediated by defects, which need to be almost entirely passivated to stabilize devices.<sup>142</sup>

The degradation route of 3D halide perovskites changes depending on their chemistry; in particular, different A-sites give rise to distinct degradation pathways depending on the relative contributions of phase instability and chemical instability.<sup>376,377</sup> However, both MAPbI<sub>3</sub>, which is found in a tetragonal perovskite black phase at RT but is chemically unstable, and FAPbI<sub>3</sub> and CsPbI<sub>3</sub>, which are more chemically stable but show structural reconstructions toward non-perovskite phases, degrade too quickly to be useful in a commercial device. Alloying the A-site can improve chemical stability significantly and preserve a perovskite lattice as will be discussed below. It has further merits, since the compositions of these alloys can be tuned to stabilize a cubic perovskite phase at RT. MAPbI<sub>3</sub> is indeed usually found in a perovskite tetragonal phase at RT, with a perovskite tetragonal to cubic structural instability slightly above RT. Domain walls between tetragonal domains and crystal twinning are among the possible additional consequences in the tetragonal phase.<sup>377</sup> Moreover, CsPbI<sub>3</sub> has an optical bandgap too high for PV in its high temperature cubic perovskite black phase. But the bandgap is not reduced but increased in the metastable black phase at RT, due to orthorhombic lattice distortions.<sup>376</sup>

#### 4.1.1. Chemical instability of MAPbI<sub>3</sub>

Degradation of MAPbI<sub>3</sub> proceeds through the deprotonation of the MA cation, which can then leave the crystal as a gas.<sup>375,378,379</sup> In air under light illumination MAPbI<sub>3</sub> degrades via photooxidation, which begins with the adsorption and diffusion of O<sub>2</sub> molecules through V<sub>I</sub> sites as shown in **Figure 20a**.<sup>380</sup> Photooxidation is a common degradation mechanism for all solar cell materials,<sup>381</sup> but it results in much more rapid degradation in halide perovskites than in Si. Particularly in the case of halide perovskites, light illumination causes lattice distortions which increase the concentration of iodide vacancies and the ionic mobility, increasing the adsorption and diffusion rates for O<sub>2</sub>.<sup>200,382</sup> It has also been suggested that I<sup>-</sup> in the lattice can reduce its radius by oxidizing to neutral iodine in the presence of photogenerated holes, increasing [V<sub>I</sub>].<sup>382</sup> Adsorbed O<sub>2</sub> creates a state near the CBM which can capture a photoelectron, forming the free radical O<sub>2</sub><sup>-</sup>. This reactive species then takes a proton from MA, destroying the perovskite structure in the process<sup>375,378,381</sup>:



In the absence of O<sub>2</sub>, a less reactive electron acceptor such as CO<sub>2</sub> can attack the halide perovskite via the same route<sup>378</sup>. In a dark O<sub>2</sub>-rich environment MAPbI<sub>3</sub> remains metastable since oxygen is unable to penetrate past the surface of the film.<sup>383</sup> Likewise, if charges are extracted quickly from the halide perovskite, e.g., during solar cell operation, photooxidation is suppressed compared to at V<sub>OC</sub>.<sup>384</sup>

Heat also has a degrading effect on MAPbI<sub>3</sub> halide perovskites. After holding MAPbI<sub>3</sub> at 100°C for 20 minutes in vacuum, Kim et. al. observed the creation of an intermediate degradation phase associated with the decomposition of MAPbI<sub>3</sub> into CH<sub>3</sub>I, NH<sub>3</sub>, and PbI<sub>2</sub>.<sup>385</sup> This phase was also seen at 80°C after >1 hr. Other studies have similarly found elevated temperatures as low as 85°C can also cause the MA<sup>+</sup> cation to deprotonate or decompose into NH<sub>3</sub> and CH<sub>3</sub>I.<sup>386,387</sup>

MAPbI<sub>3</sub> is very sensitive to humidity as even a small concentration of H<sub>2</sub>O molecules can accelerate the photooxidation process. Superoxide radicals can react with complexed H<sub>2</sub>O to form

hydroxide ( $\text{OH}^-$ ), which deprotonates MA more aggressively than  $\text{O}_2^-$ .<sup>375</sup> This changes the rate-limiting reaction of the degradation process and consequently accelerates the degradation kinetics significantly. As  $\text{H}_2\text{O}$  is one degradation product of anhydrous photooxidation, it can build up in a film even in a dry environment and accelerate degradation after enough has accumulated.<sup>383</sup> In humid environments  $\text{H}_2\text{O}$  will also complex with  $\text{MAPbI}_3$ , forming a monohydrate phase  $\text{MAPbI}_3 \cdot \text{H}_2\text{O}$  of edge sharing  $\text{PbI}_6$  octahedra<sup>388</sup> or a dihydrate phase  $\text{MA}_4\text{PbI}_6 \cdot 2\text{H}_2\text{O}$  of disconnected octahedra along with  $\text{PbI}_2$ .<sup>389</sup> The hydration reaction is reversible if reacted species can be prevented from leaving the crystal, but because the hydrate destroys the perovskite structure the film microstructure does not recover upon drying<sup>389</sup>. Both  $\text{MA}^+$  and  $\text{I}^-$  can escape the lattice through water-mediated reactions,  $\text{MA}^+$  by deprotonating and volatilizing and  $\text{I}^-$  by taking the  $\text{MA}^+$  proton and dissolving in  $\text{H}_2\text{O}$  as  $\text{HI}$ , which leaves  $\text{PbI}_2$ .<sup>390,391</sup>

#### 4.1.2. Phase instability of $\text{FAPbI}_3$ and $\text{CsPbI}_3$

The FA cation has much better chemical stability than MA as a result of its lower acidity, its increased mass, and its smaller dipole moment.<sup>392,393</sup> As a result,  $\text{FAPbI}_3$  shows significantly improved thermal stability compared to  $\text{MAPbI}_3$  in inert atmosphere. Whereas films of  $\text{MAPbI}_3$  were found to decompose within 20 hr at  $90^\circ\text{C}$  in  $\text{N}_2$ , thermal decomposition was substantially suppressed in  $\text{FAPbI}_3$  films under the same conditions.<sup>394</sup> However,  $\text{FAPbI}_3$  does still degrade at high temperatures, its diffraction pattern showing a notable increase in  $\text{PbI}_2$  after annealing for as little as 500s at  $170^\circ\text{C}$ .<sup>395</sup> The Cs cation is even more chemically stable than FA since it is not volatile and cannot be deprotonated.<sup>396</sup>

Unfortunately, the extreme tolerance factors of  $\text{FAPbI}_3$  and  $\text{CsPbI}_3$  introduce a new degradation pathway through reconstructive phase transformations. The cubic  $\alpha$ - phase of  $\text{FAPbI}_3$  and the orthorhombic  $\gamma$ - phase of  $\text{CsPbI}_3$  are metastable at room temperature, with the stable phases for both being their nonperovskite  $\delta$ - phases.<sup>8</sup>  $\gamma$ - $\text{CsPbI}_3$  showed a complete transformation to  $\delta$ - $\text{CsPbI}_3$  after annealing at  $90^\circ\text{C}$  in  $\text{N}_2$ .<sup>394</sup> The presence of water can catalyze the phase transformation of both

materials, with  $\text{FAPbI}_3$  degrading severely after 30 days in 15%RH and within 2 hr at 90%RH<sup>10</sup>. Light can also accelerate the phase transition: the absorbance of  $\text{FAPbI}_3$  films showed a 75% decrease after 16 hr of 1-sun illumination at 50%RH<sup>397</sup>. The phase transformation of these materials is in theory reversible through annealing above  $150^\circ\text{C}$  ( $\text{FAPbI}_3$ ) or  $320^\circ\text{C}$  ( $\text{CsPbI}_3$ )<sup>132,398</sup>, although annealing devices at temperatures that high would damage other organic layers and interfaces.

As lattice reconstruction is a consequence of extreme tolerance factor, it can be suppressed by tuning the tolerance factor through A-site alloying. The popular mixed-A-cation halide perovskite  $\text{FA}_{0.85}\text{Cs}_{0.15}\text{PbI}_3$  maintains the intrinsic heat stability of  $\text{FAPbI}_3$  but is significantly more tolerant to humidity because the lowered effective tolerance factor makes the black phase more thermodynamically stable at room temperature<sup>10</sup>. **Figure 20b** shows the calculated formation energy difference between the  $\text{FAPbI}_3$  and  $\text{CsPbI}_3$   $\delta$ -phases and the  $(\text{FA}_{1-x}\text{Cs}_x)\text{PbI}_3$   $\alpha$ -phase as a function of Cs concentration  $x$ . There is a minimum energy difference at the point where the  $\delta$ -FA and  $\delta$ -Cs curves intersect (around  $x \sim 0.15$ ), which explains the higher structural stability of the  $\text{FA}_{0.85}\text{Cs}_{0.15}\text{PbI}_3$  halide perovskite. Triple-cation recipes such as  $\text{FA}_{0.79}\text{MA}_{0.16}\text{Cs}_{0.05}\text{Pb}(\text{I}_{0.83}\text{Br}_{0.17})_3$  also show high stability even with the inclusion of MA<sup>17</sup>. Part of the improvement can be attributed to better crystallinity as a result of slower film growth kinetics in mixed-cation, mixed-anion systems, which is seen both for films and single crystals<sup>17,399</sup>.

However, mixed A-site halide perovskites do eventually degrade.  $\text{FA}_{.85}\text{Cs}_{.15}\text{PbI}_3$  is stable under humidity or light alone, but when both humidity and light are present it degrades into the  $\delta$ - phases of  $\text{FAPbI}_3$  and  $\text{CsPbI}_3$ , and into  $\text{PbI}_2$ <sup>400</sup>. At longer time scales the FA deprotonates or degrades, forming additional  $\text{PbI}_2$ . In an  $\text{N}_2$  atmosphere  $\text{FA}_{.85}\text{Cs}_{.15}\text{PbI}_3$  cells showed a moderate loss in efficiency after 600 hr at  $85^\circ\text{C}$  and a significant 47.7% PCE loss after 600 hr of 1-sun illumination at MPP (maximum power point), with the performance loss under light being caused by phase segregation and the formation of a current-blocking Cs  $\delta$ - phase<sup>401</sup>. Mixed FA-MA-Cs films have been shown to degrade in two stages at elevated temperatures ( $112$ - $181^\circ\text{C}$ ), quickly at first



by deprotonation of MA and then more slowly by deprotonation of FA<sup>402</sup>.

#### 4.1.3. Phase segregation in mixed systems

When a halide perovskite application requires a wider bandgap, a common practice is to alloy the X-site with a lighter halide ion, e.g., MAPb(I<sub>1-x</sub>Br<sub>x</sub>)<sub>3</sub><sup>19</sup>. Because the X anion is a mobile species in a halide perovskite crystal, a halide perovskite with an alloyed X-site is susceptible to phase segregation, particularly under illumination<sup>403–411</sup>. Because a mixed iodide-bromide halide perovskite's bandgap decreases as iodide concentration increases, localized I-rich regions in a non-uniform film have the effect of lowering the quasi-fermi level splitting and reducing the  $V_{OC}$ , leading to a decrease in device performance.<sup>403,404</sup> **Figure 20c** shows the shift in PL spectra of MAPb(I<sub>0.5</sub>Br<sub>0.5</sub>)<sub>3</sub> and FA<sub>0.83</sub>Cs<sub>0.17</sub>Pb(Br<sub>0.4</sub>I<sub>0.6</sub>)<sub>3</sub> under constant illumination. The spectra redshift as iodide and bromide phase-segregate and charges are shuttled into low-bandgap iodide regions. Notably, this process is significantly slower in the FA-Cs film which has a higher activation energy for halide diffusion.<sup>407</sup>

Several mechanisms have been proposed for light-induced halide demixing. A polaron picture of halide segregation suggests that illumination generates carriers that couple to the lattice, generating local strain, which lowers the halide diffusion barrier and facilitates demixing.<sup>405</sup> Another model suggests that the lowered bandgap of an iodide-rich phase (particularly a raised VBM) provides a free energy driving force for iodide segregation.<sup>403</sup> Light-induced halide segregation in MAPb(I<sub>1-x</sub>Br<sub>x</sub>)<sub>3</sub> has been shown to be intrinsic for  $x > 0.5$  and strain-induced for  $x < 0.5$ .<sup>406</sup> For films, this means that halide segregation occurs preferentially at grain boundaries and charged trap states as areas of localized strain. Improving film crystallinity<sup>407</sup>, reducing trap density,<sup>408–410</sup> relaxing strain,<sup>406</sup> reducing the carrier diffusion length,<sup>403</sup> and suppressing electron-phonon coupling<sup>405</sup> all appear to suppress halide segregation. Halide segregation is at least mostly reversible in an inert atmosphere or with perfect encapsulation, with films remixing in the absence of light, but the generation of additional trap states makes the process irreversible in air.<sup>410</sup>

Mixed A-site cations are less prone to demixing than mixed X-site halides. In fact, an alloyed A-site has been shown to decrease the rate of halide segregation compared to films with a pure A-site.<sup>408</sup> This effect may be due to reduced charge-lattice coupling in mixed A-site systems<sup>405</sup> or to the improved crystallinity of their films<sup>407</sup>. However, phase segregation is still an issue in mixed-cation systems. Phase segregation into  $\delta$ - phases is the primary degradation pathway for FA-Cs halide perovskites, although the formation of the  $\delta$ - phase breaks the halide perovskite structure completely unlike in the case of halide demixing<sup>400,401</sup>. Nanoscale A-site heterogeneity created during film formation in the mixed-cation system FA<sub>0.83</sub>Cs<sub>0.17</sub>PbI<sub>3</sub> has also been shown to induce larger-scale phase segregation during device operation.<sup>412</sup>

#### 4.1.4. Solar cell device-level stability and the effect of bias

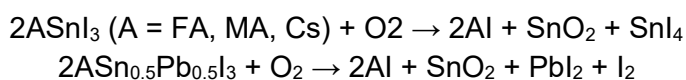
The mobility of ions and defects (both intrinsic and extrinsic) in 3D halide perovskites causes additional stability issues when a halide perovskite layer is assembled into a full device stack.<sup>142,413–415</sup> Adding an internal electric field across the halide perovskite layer induces the movement of halide ions. As a result a concentration gradient forms with X-site vacancies near the HTL and a halide-rich layer near the ETL.<sup>414</sup> This electric field can either be generated by an external bias or by quasi-Fermi level splitting under light illumination.<sup>415</sup> Dark current measurements of MAPbI<sub>3</sub> at a fixed voltage showed a decay and saturation of current on the time scale of seconds, which was attributed to ion migration.<sup>415</sup> As shown in **Figure 20d**, biasing a MAPbI<sub>3</sub> cell in the dark before measurement at voltages  $> 8V$  was shown to cause an efficiency loss dominated by a decrease in the short-circuit current ( $J_{SC}$ ), suggesting that an iodide vacancy layer could be blocking hole extraction to the HTL. Cells biased at 1V or 1.2V, then left in dark conditions for a week without bias completely and partially recovered, respectively, as a thermodynamic equilibrium ion concentration was re-established. It was suggested that open-circuit device degradation observed under light could be partially attributed to the 1V of forward bias established across the halide perovskite solar cell rather than to the light itself.

Besides bias effects, halide perovskites in a device stack can react with the other layers, especially at the degrading conditions of solar cell operation. Metal oxide charge transport layers (CTLs) such as  $\text{TiO}_2$ <sup>416</sup> and to a lesser extent  $\text{SnO}_2$ <sup>417</sup> are known to generate superoxides upon exposure to UV light, which can degrade the halide perovskite layer, and  $\text{Li}^+$  has been shown to diffuse from a Spiro-OMeTAD HTL into the halide perovskite layer<sup>418</sup>. Furthermore, a top metal contact in a device can diffuse through the top CTL into the halide perovskite layer to react with the halide or reduce the B cation,<sup>419,420</sup> or mobile reactive species can diffuse through the CTL and corrode the metal.<sup>421,422</sup> These reactions can be suppressed through electrode and CTL materials selection,<sup>423,424</sup> through the passivation of interfaces,<sup>419,420,425</sup> and by reducing ionic mobility within the halide perovskite.<sup>426</sup>

#### 4.1.5. B-site oxidation in Sn and Pb-Sn halide perovskites

The alloying or replacement of Pb with Sn at the B-site in 3D halide perovskites introduces a new aggressive degradation mechanism through the oxidation of  $\text{Sn}^{2+}$  to  $\text{Sn}^{4+}$ .<sup>8,427,428</sup> The  $5s^2$  valence electrons of Sn are significantly more active than the  $6s^2$  electrons of Pb and as a result Sn will oxidize to  $\text{Sn}^{4+}$  much more readily than Pb<sup>429</sup>. Sn oxidation occurs in the presence of  $\text{O}_2$  leading to the formation of Sn vacancies with energy level close to the VBM, which results in high p-type doping<sup>112,430</sup>. Excessive p-doping reduces carrier diffusion lengths and increases nonradiative recombination which deteriorates device performance. Sn-based halide perovskite absorber layers can also react with CTLs, for example being degraded by 4-tert butylpyridine or acetonitrile during deposition of Spiro-OMeTAD.<sup>431</sup>

Regardless of A-site, the degradation of  $\text{SnI}_3$ -based halide perovskites proceeds through the oxidation of Sn to form  $\text{SnO}_2$  and  $\text{SnI}_4$ .<sup>432</sup>  $\text{SnI}_4$  then evolves into  $\text{I}_2$ , which aggressively oxidizes the halide perovskite further, accelerating degradation.<sup>433</sup> It has been suggested that the presence of Pb in the B-site, for example in  $\text{APb}_{0.5}\text{Sn}_{0.5}\text{I}_3$ , can qualitatively change the degradation pathway and suppress  $\text{SnI}_4$  formation:<sup>432</sup>



As a result, incorporation of Pb can improve device stability faster than would be expected from a pure stoichiometric argument.<sup>432</sup>

$\text{Sn}^{2+} \rightarrow \text{Sn}^{4+}$  oxidation is reduced in  $\text{FASnI}_3$  compared to  $\text{MASnI}_3$  because of the higher  $V_{\text{Sn}}$  formation energy,<sup>434</sup> which is a result of the reduced Sn 5s - I 5p antibonding coupling in  $\text{FASnI}_3$  due to the larger FA cation increasing the Sn-I bond length.<sup>435</sup> This slower oxidation is demonstrated in **Figure 20e**, which compares PL spectra of  $\text{MASnI}_3$  and  $\text{FASnI}_3$  over 60 min in air.<sup>434</sup> Incorporating some amount of the larger molecule GA at the A-site can realize significant additional stabilization.<sup>436</sup> Oxidation can be additionally suppressed by the incorporation of reducing agents such as  $\text{SnX}_2$  (X = F, Cl, Br, I, SCN),<sup>428</sup> metallic Sn,<sup>437,438</sup> or other additives.<sup>427,428</sup> The low solubility of  $\text{SnX}_2$  compounds also causes them to precipitate early during solution processing and act as nucleation sites for homogeneous growth<sup>439</sup>. From a device architecture perspective, stability can be improved by extracting holes as efficiently as possible, for example by employing an inverted architecture where charges are generated near the HTL,<sup>427</sup> or by improving hole extraction and transport of the HTL.<sup>440</sup>

#### 4.1.6. 3D halide perovskite self-healing

An interesting aspect of halide perovskite degradation is that to an extent both single crystals and films of the materials are self-healing. Partial recovery of the perovskite phase in films or device performance in solar cells has been shown once halide perovskites are removed from degrading conditions, in particular from humid to dry atmosphere<sup>389,441–444</sup> and from illuminated or biased conditions to dark, unbiased conditions.<sup>445–455</sup>

In humid conditions halide perovskites degrade in several stages, some but not all of which are reversible<sup>389</sup>. The  $\text{MAPbI}_3$  halide perovskite phase will reversibly transform to a 1D monohydrate phase  $\text{MAPbI}_3 \cdot \text{H}_2\text{O}$  (which maintains the perovskite stoichiometry) upon exposure to low  $\text{H}_2\text{O}$  concentrations.<sup>389,441,443</sup> If the device is removed from humidity while only the monohydrate phase has been formed, it can recover. Additional  $\text{H}_2\text{O}$  will result in the formation of the 0D dihydrate phase  $\text{MA}_4\text{PbI}_6 \cdot 2\text{H}_2\text{O}$  and the precipitation of excess  $\text{PbI}_2$ . This reaction is also reversible in theory but

segregation of  $\text{PbI}_2$  and collapse of the microstructure makes it easier for volatile MAI to escape which renders the process irreversible.<sup>389,443</sup> Preventing the release of degradation products can improve the self-healing capability of  $\text{MAPbI}_3$  in humid conditions<sup>442</sup>. The dihydrate phase will decompose irreversibly with additional  $\text{H}_2\text{O}$  as MAI is dissolved and removed from the crystal<sup>389</sup>.

halide perovskites also self-heal when moved from light to dark conditions. The phase segregation of illuminated mixed-halide films,<sup>454,455</sup> the defect concentration gradient formed from light-induced bias across a device,<sup>451</sup> and the higher defect density in illuminated films<sup>382,445</sup> will each revert to the thermodynamic equilibrium state of uniform distribution when the driving force of light is removed. Nie et al. found that illumination of  $\text{MAPbI}_3$  led to the formation of light-induced metastable trap states, which self-healed after less than one minute in dark conditions.<sup>445</sup> Self-healing from light-induced degradation has been observed not only in devices but also in single crystals of  $\text{FAPbBr}_3$ ,  $\text{MAPbBr}_3$ , and  $\text{CsPbBr}_3$ <sup>453</sup>, with  $\text{FAPbBr}_3$  healing the fastest (**Figure 20f**); the authors attributed this recovery to the localization of degradation products. Some (but not all) light-induced decomposition reactions have also been shown to be reversible in devices with the requirement that degradation products stay within the device<sup>449</sup>.

As degradation progresses, self-healing effects can diminish or even reverse. Khenkin et al. found that light-dark cycling of  $\text{FA}_{0.79}\text{MA}_{0.16}\text{Cs}_{0.05}\text{Pb}(\text{I}_{0.83}\text{Br}_{0.17})_3$  devices initially showed complete PCE recovery in dark, but after 50% PCE degradation  $J_{\text{SC}}$  and FF would rapidly decrease when the light was turned off and increase when the light was turned on<sup>447</sup>. The authors attributed this behavior to multiple coexisting processes within the device: the formation of new defect states under light and disappearance under dark as in ref.<sup>445</sup> at the early stages of degradation, and the detrapping and resultant activation of interfacial defect states under dark that were filled by photocarriers under light at longer degradation times. Light-induced recovery through the passivation of defect states was also seen after degradation of halide perovskite devices under UV light.<sup>448</sup>

The self-healing effect in 3D halide perovskites can be enhanced with additives. 2D halide perovskites in particular can improve 3D halide perovskites' ability to self-heal as will be discussed later, but a similar improvement in  $\text{MAPbI}_3$  self-healing after humidity-induced degradation has been realized with a polyethylene glycol (PEG) scaffold.<sup>442</sup>  $\text{MAPbI}_3$  films which incorporated PEG saw a near-complete recovery in device performance after 60s exposure to water vapor and 45s in dry air. The proposed mechanism of this improvement was strong bonding between MAI and PEG, which retained degradation products in the vicinity of the degraded halide perovskite grain such that the perovskite phase could reform when water was removed. These promising results suggest that halide perovskite stability can be significantly enhanced through additive or architecture engineering to localize degradation products.

Notably, although halide perovskites are notoriously environmentally unstable compared to inorganic semiconductors, self-healing allows them to perform remarkably well in applications where damage is inevitable regardless of intrinsic material stability, for example as radiation detectors.<sup>456,457</sup> Halide perovskites have been shown to withstand proton doses several orders of magnitude higher than crystalline Si, and self-heal after radiation is stopped.<sup>457</sup> Conventional semiconductors receive their intrinsic stability from their rigid lattices with high bond energy but they are less forgiving towards the defect states which form when those bonds are broken. In contrast, halide perovskites' combination of intrinsic defect tolerance and self-healing is perfect for high-radiation applications.

Since self-healing is a characteristic not shared by conventional Si or III-V semiconductors, conventional accelerated degradation tests developed for these inorganic materials are not designed to measure its effects on device lifetime. This has prompted a call for the adoption of new halide perovskite-specific degradation tests, in particular tests to approximate the effects of day-night cycling on devices<sup>458,459</sup>. It has been proposed that a more complete understanding of self-healing in halide perovskites under operating conditions could be used to extend device lifetimes by intermittently taking devices offline to recover<sup>460</sup>.

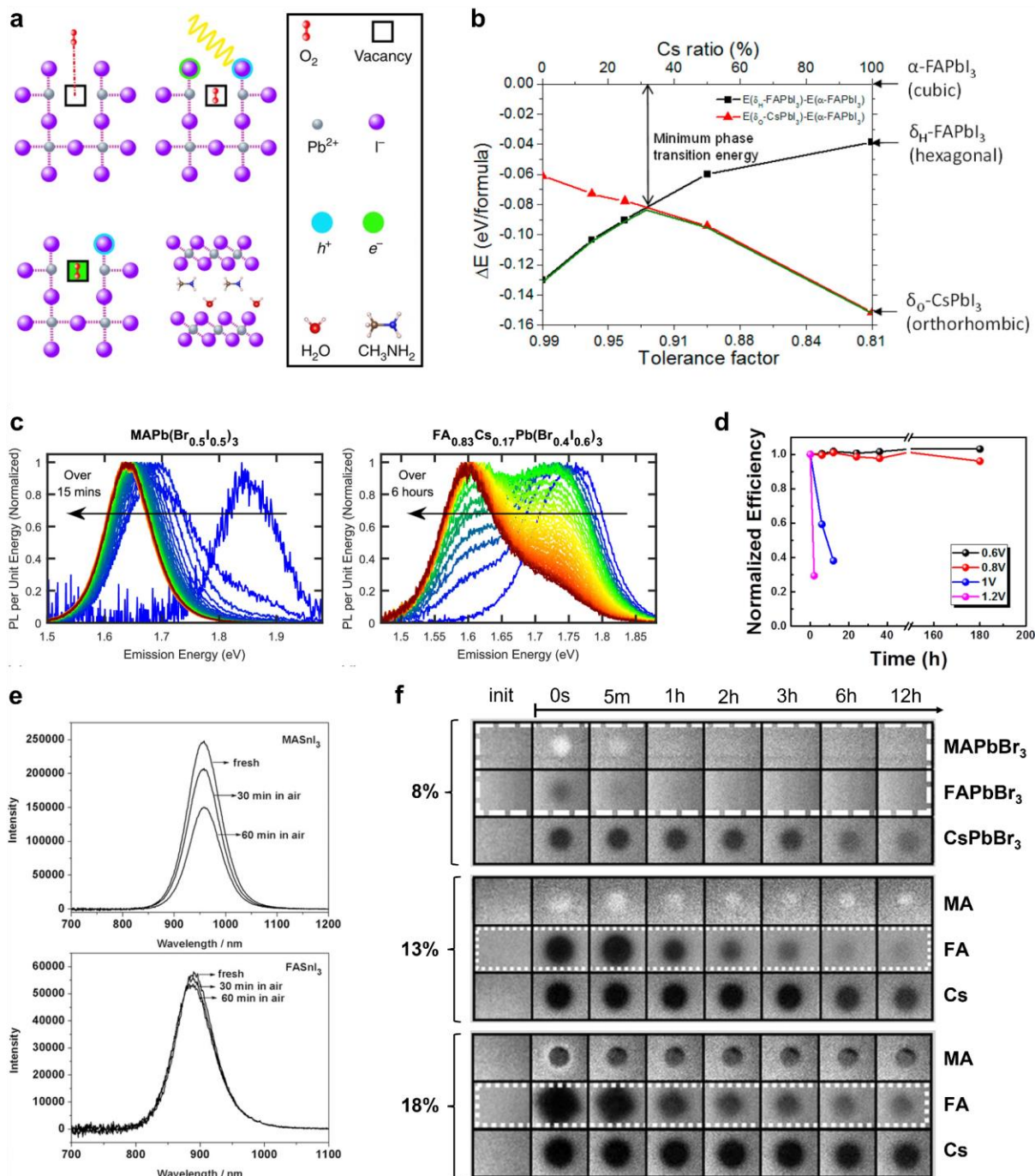


**Figure 20: Stability of 3D perovskites.** a) Schematic of MAPbI<sub>3</sub> photooxidation. Top left: O<sub>2</sub> adsorbs at an iodide vacancy. Top right: illumination generates e<sup>-</sup>-h<sup>+</sup> pairs. Bottom left: O<sub>2</sub> takes a photoelectron to form O<sub>2</sub><sup>-</sup> superoxide radical. Bottom right: O<sub>2</sub><sup>-</sup> reacts with MAPbI<sub>3</sub> to form PbI<sub>2</sub>, I<sub>2</sub>, MA, and H<sub>2</sub>O. Reproduced with permission from ref.<sup>380</sup> Copyright 2017 Springer Nature. b) Calculated formation energy difference between α-phase and FAPbI<sub>3</sub>/CsPbI<sub>3</sub> δ-phases in (FA<sub>1-x</sub>Cs<sub>x</sub>)PbI<sub>3</sub> as a function of x (top horizontal axis) or tolerance factor (bottom horizontal axis). The crossing point for the two curves at x~0.15 gives the concentration of minimum energy difference for either δ-phase and is predicted to be the most stable composition. Reproduced with permission from ref.<sup>10</sup> Copyright 2015 American Chemical Society. c) PL spectra of MAPb(I<sub>0.5</sub>Br<sub>0.5</sub>)<sub>3</sub> (left) and FA<sub>0.83</sub>Cs<sub>0.17</sub>Pb(Br<sub>0.4</sub>I<sub>0.6</sub>)<sub>3</sub> measured over time with constant light exposure. Both perovskites' emission peaks redshift as iodide and bromide phase-segregate and charges are shuttled into low-bandgap iodide regions. The process is slower for the FA-Cs film because of the larger barrier to halide diffusion. Reproduced with permission from ref.<sup>407</sup> Copyright 2021 American Chemical Society. d) Normalized PCE for a MAPbI<sub>3</sub> solar cell held at various biases in dark conditions. Applied voltages over 1V lead to rapid degradation of device performance, suggesting that photodegradation at V<sub>OC</sub> is partially due to the built-in field. Reproduced with

permission from ref.<sup>415</sup> Copyright 2016 American Chemical Society. e) PL spectra of  $\text{MASnI}_3$  (top) and  $\text{FASnI}_3$  (bottom) films over 60 min in air, demonstrating the suppression of  $\text{Sn}^{4+}$  formation in  $\text{FASnI}_3$ . PL intensity falls by ~40% in  $\text{MASnI}_3$  and by ~10% in  $\text{FASnI}_3$  as  $\text{Sn}^{4+}$  is created and nonradiative recombination increases. Reproduced with permission from ref.<sup>434</sup> Copyright 2016 Wiley-VCH. f) PL imaging before and after bleaching  $\text{APbBr}_3$  single crystals (A=MA, FA, Cs) with two-photon microscope at 8% (top), 13% (middle), and 18% (bottom) laser power, and recovery over 12 hr in dark. 0s marks the time immediately after 100 bleaching iterations. The degrading beam is focused 50  $\mu\text{m}$  within the crystal bulk. All crystals recover partially at all three laser intensities, but the rate of healing decreases at higher intensities.  $\text{FAPbI}_3$  shows the fastest recovery and  $\text{CsPbI}_3$  the slowest recovery in all cases. Reproduced with permission from ref.<sup>453</sup> Copyright 2018 Wiley-VCH.

#### 4.1.7. Current state-of-the-art 3D stability

A variety of methods have been developed to improve the stability of 3D halide perovskites, many of which seek to reduce or passivate defects within a film. Additives can be introduced to passivate charged defects at grain boundaries, simultaneously suppressing oxygen adsorption and halide segregation.<sup>461</sup> Improving the crystallinity of the film, for example through precursor solution engineering, will also suppress degradation. Likewise, enhancing the hydrophobicity of the halide perovskite film with additives can also improve stability. Ammonium salts (e.g.,  $\text{MACl}$ <sup>462</sup>), Lewis acids (e.g.,  $\text{C60-PEG}$ <sup>463</sup>), Lewis bases (e.g.,  $\text{PMMA}$ <sup>464</sup>), and ionic liquids (e.g., 1-alkyl-4-amino-1,2,4-triazolium<sup>465</sup>) have all been shown to improve 3D device stability through some combination of these three processes when introduced into the precursor solution or the antisolvent. As will be discussed extensively below, the incorporation of 2D halide perovskites as a dopant or capping layer can also significantly improve stability for partially the same reasons.

Besides defects, interfaces within a device are also principal origins of degradation. The stability of halide perovskite solar cells can be enhanced by passivating the halide perovskite-HTL and halide perovskite-ETL heterojunctions.<sup>466</sup> Since charge accumulation at interfaces can accelerate degradation reactions, improving band alignment at these heterojunctions can also increase stability.<sup>467,468</sup> Some CTLs are themselves prone to degradation, most notoriously Spiro-OMeTAD, which is known to degrade under heat, light, oxygen, and moisture, particularly when doped.<sup>469-472</sup> The environmental stability of not only the halide perovskite but every layer in the device must also be ensured. Ion migration also needs to be suppressed, both within the perovskite layer to avoid defect

accumulation at interfaces<sup>199</sup> and between layers to avoid reactions between CTLs or contacts.<sup>418,423</sup>

Encapsulation of halide perovskite devices can significantly enhance their stability in harsh environmental conditions.<sup>473</sup> Encapsulated devices have retained >95% of their initial PCE after 1000 hr at 85°C/85%RH, 2000 hr of outdoor testing, and 5 hr submerged in water. Encapsulation not only prevents the ingress of  $\text{O}_2$  and  $\text{H}_2\text{O}$ , but also prevents the outgassing of volatile halide perovskite degradation products which allows for self-healing when the degrading condition is removed.<sup>449</sup>

Unlike solar cell efficiency, which is a relatively unambiguous figure of merit, stability is much more difficult to quantify. The stability of any solar cell will depend on its environment, and unfortunately a standardized set of environmental and device conditions for degradation tests has not been adopted by the halide perovskite community. As a result, it is difficult to make one-to-one comparisons of device stability across publications and groups. For example, many reports will measure photostability in inert atmosphere with the justification that it effectively simulates the atmosphere seen by an encapsulated device (e.g.<sup>224</sup>); other reports will directly measure photostability of encapsulated cells in ambient air (e.g.<sup>229</sup>), and still others will measure photostability at elevated temperatures (e.g.<sup>474</sup>). Likewise, different reports measure air-stability in elevated (e.g.,<sup>221</sup>), ambient (e.g.,<sup>224</sup>), or reduced (e.g.<sup>475</sup>) humidity conditions, or measure shelf-stability in the dark in inert atmosphere (e.g.,<sup>237</sup>). Elevated temperature tests have also been reported in air (e.g.,<sup>235</sup>) or in  $\text{N}_2$  (e.g.<sup>236</sup>). When devices are encapsulated the encapsulation procedure is also not standardized across papers, and not all encapsulation is equally effective.<sup>473</sup> In order to better understand the present

and future state-of-the-art for halide perovskite stability the field must adopt a standardized and easily replicable set of degradation conditions. Recent progress has been made towards this goal, e.g., through the 2020 consensus statement for stability assessment which advocates for the use of modified International Summit on Organic Photovoltaic Stability (ISOS) testing protocols.<sup>458</sup> However, this statement has not been universally adopted and it is still unclear which testing procedures are the most relevant to predicting device lifetime under real world operating conditions.

Even when degradation tests are standardized, testing apparatus may introduce different conditions from what have been reported. For example, different sources for above-bandgap light can emit subtly different spectra which can influence a device's degradation rate, particularly for differences in the UV range.<sup>458</sup> It is therefore necessary to standardize not only the testing conditions but also the apparatus used to achieve those conditions. However, in the case of light soaking which apparatus should become the standard is unclear, since various light sources present a trade-off between accuracy to the solar spectrum (e.g., Xenon bulbs which can emit UV radiation) and lab-scale feasibility (e.g., LED lamps which are cheaper, last longer, and use less energy).<sup>476</sup> A possible compromise could be to measure in-operando stability under 1-sun visible (e.g. LED-generated) light with MPP tracking and separately measure stability under UV light alone with a standardized UV lamp.

A common degradation condition which is fairly repeatable is continuous 1-sun illumination in inert atmosphere with MPP tracking (ISOS-L-11).<sup>458</sup> If it is assumed that device encapsulation can achieve a perfect barrier to air and water this measurement has practical utility. The best devices as of 2023 retain >90% and up to 100% of their initial PCE after 1000 hr (~42 days) in this condition,<sup>477,478</sup> this 1000 hr mark has become somewhat of a key milestone in the field. "Shelf-stability" in ambient air without light (ISOS-D-1<sup>458</sup>) is another commonly-reported metric. In this case variations in the %RH of ambient air between laboratories and over the course of a measurement could introduce discrepancies in reported stability. However, tests such as this in

atmospheres containing both O<sub>2</sub> and H<sub>2</sub>O are important considering the various halide perovskite degradation pathways, which involve these molecules. The best devices retain >90% of their initial PCE after 90 days (2160 hr) in ambient conditions without encapsulation.<sup>479,480</sup> The photostability in N<sub>2</sub> and shelf stability in air are given in **Tables 4 and 5** for example high-efficiency devices over 24%PCE, where reported. To better compare between reports, the stability values given have also been projected to 1000 hr (photostability) or 90 days (ambient stability) assuming a constant degradation rate.

Along with ISOS protocols, it has become clear that light plays a key role in perovskite solar cell degradation more-so than in inorganic photovoltaics, which tend to lose performance due to the failure of module components besides the absorber layer itself.<sup>481</sup> As has been discussed above, light activates many degradation processes in halide perovskite films, and temperature accelerates these processes. We therefore suggest, as Boyd et al. do in their excellent review of perovskite degradation,<sup>476</sup> that light-soaking degradation tests in inert atmosphere be performed under a combination of concentrated sunlight (e.g., 5-suns) and elevated temperature (e.g., 85°C). The adoption of this testing standard should be done simultaneous with rigorous investigation by the halide perovskite community of how degradation rate in common perovskite devices scales with light intensity and temperature. In addition, the ability of each perovskite device to self-heal in dark conditions should be quantified through cyclic testing with standardized cycle rates and rest periods, which can likewise be performed with concentrated sunlight.

#### **4.2. Improved stability with 2D halide perovskites**

Compared to 3D halide perovskites with the same A-site cation, 2D halide perovskites demonstrate improved stability against heat, light, oxygen, and water. This was the main breakthrough brought by the 2016 seminal paper of Tsai et al., besides an over 2.5-times increase in then-reported efficiency for 2D halide perovskite solar cells.<sup>257</sup> However, 2D halide perovskites are still susceptible to degradation in operating conditions and more

effort is needed to improve their stability towards what is required for commercialization.

#### **4.2.1. Comparing the stability of RP, DJ, and ACI 2D halide perovskites**

While few rigorous studies on the degradation pathways of various 2D halide perovskites exist and the vast majority of 2D devices have been mixed 2D-3D films, the stability of reported devices suggests that in a device architecture DJ and ACI halide perovskites are more stable than RP halide perovskites<sup>482,483</sup>. This is often explained as being due to the stronger interlayer bonding in ACI and especially in DJ halide perovskites, compared to the RP structure for which layers are held together by the van der Waals forces between spacer molecules. The shorter interlayer distance in DJ and ACI structures may also have a stabilizing effect. Interestingly, bare films (not incorporated into devices) of RP halide perovskites have been shown to be more stable than bare films of DJ halide perovskites<sup>482</sup>, which may be due to the difference in formation energy between the two phases: RP halide perovskites have a negative formation energy larger than that of the 3D phase giving higher thermodynamic stability<sup>484,485</sup>, whereas DJ halide perovskites have a positive formation enthalpy making them metastable<sup>79</sup>. This suggests that interlayer bond strength and formation energy compete to respectively stabilize and destabilize the DJ phase relative to the RP phase, and that which effect is more important depends on the environmental conditions. Moreover, the rate at which reactive species can penetrate the crystal structure, the rate of degradation in the presence of those species, and the ease with which degradation products can leave the structure will each depend not only on the intrinsic stability of the structure but also on the microstructure, the device architecture, and the particular external conditions. More work needs to be done to elucidate the differences in degradation mechanism and degradation rate for the various 2D halide perovskite structures.

#### **4.2.2. Mechanistic rationale for 2D halide perovskites improved stability**

The improved stability of 2D halide perovskites comes from a combination of the

hydrophobic spacer cations<sup>329,482,486–488</sup> and the suppressed ion mobility<sup>341,342,344</sup> and reduced vacancy density<sup>302,303</sup> in the 2D phase. These materials properties result not only in better bulk stability, but also can enable a self-passivating degradation mechanism via disproportionation at surfaces as will be discussed later<sup>482,489–492</sup>. For some 2D halide perovskites, a higher thermodynamic stability additionally suppresses degradation<sup>484,485</sup>.

2D halide perovskites are more stable in humid environments than 3D halide perovskites.<sup>80,257,493</sup> This is at least partially due to the hydrophobicity of the A'-site cations.<sup>487</sup> The bulky spacer cation introduced into the 2D lattice can suppress the ingress of water molecules into the inorganic layer, slowing water-mediated deprotonation of the A-site cation in MAPbI<sub>3</sub><sup>329</sup> and the water-mediated  $\alpha \rightarrow \delta$  phase transition in FAPbI<sub>3</sub>.<sup>494</sup>

As has been discussed above, 2D halide perovskites show a reduced density of X-site and A-site vacancies and a reduced ion mobility compared to 3D halide perovskites.<sup>302,303,341,342,344</sup> This suppresses the several degradation pathways which are facilitated by vacancies or mobile halides. Lower vacancy density reduces the rate at which O<sub>2</sub> and H<sub>2</sub>O enters the lattice, as these molecules have a high affinity for point defects.<sup>495</sup> Light-induced halide segregation in mixed-halide 2D halide perovskites is also suppressed by the reduced [V<sub>X</sub>], although it does still occur.<sup>345,482,496–498</sup> It should be noted that halide segregation may be suppressed not only due to a reduction in defect concentration, but also because of a preferred I-Br distribution and a smaller band-gap change between the iodide and bromide phases in 2D halide perovskites.<sup>496</sup> Bias-induced halide migration and J-V hysteresis are also both suppressed in 2D halide perovskite devices.<sup>257,323,499</sup>

Part of the reason why 3D halide perovskites degrade so quickly, especially in the presence of water, is the low formation energy of the 3D structure. In RP 2D halide perovskites, introducing an A' cation into the lattice also introduces a significant van der Waals force between layers which has the effect of increasing the formation energy of the crystal.<sup>485</sup> This is another possible explanation for the improved stability of RP 2D halide perovskites. However, it



should be noted that MA-based DJ 2D halide perovskites have no such van der Waals interactions and in fact show a positive enthalpy of formation, suggesting that they are in fact metastable phases;<sup>79</sup> in spite of this, and while DJ films may indeed be less air-stable than RP films, DJ halide perovskite devices outperform RP devices in terms of stability.<sup>482,493</sup> This suggests that formation energy is not a sufficient explanation by itself for the improved stability of 2D phases.

#### **4.2.3. Novel degradation pathways in 2D halide perovskites**

Despite their improved stability, 2D halide perovskites do still degrade under environmental stressors. However, humidity-induced degradation of RP 2D halide perovskites proceeds via disproportionation at surfaces whereby a lower- $n$ -value 2D halide perovskite is formed along with 3D halide perovskite (or its degradation products)<sup>482,489–492</sup>. Forming lower  $n$ -values as a degradation product has the effect of increasing the  $A'$  cation concentration at surfaces exposed to humidity, which slows further water ingress. As a result, RP 2D halide perovskites are to an extent self-passivating.

The nature of the disproportionation reaction is still controversial and may be dependent on spacer cation chemistry. For RP halide perovskites with a BA  $A'$ -cation, studies have reported the formation of a mixed-lower- $n$  film (e.g.,  $n_3 \rightarrow n_2+n_1$ )<sup>489,491</sup>. Some reports on RP halide perovskites with a PEA cation suggest they behave similarly<sup>492</sup>, whereas others see the direct formation of  $n_1$  with no intermediate  $n$ -value appearing<sup>490</sup>. In DJ halide perovskites a hydrate complex has been shown to form on the surface of films exposed to humid air which can be transformed back to the DJ phase with annealing<sup>500</sup>.

The wider bandgap and the chemistry of the  $A'$  site can cause novel reactions in 2D halide perovskites which are absent in the 3D phase. In particular, a redox reaction between  $Pb^{2+}$  and the  $A'$  cation can reduce  $Pb^{2+}$  to  $Pb^0$  and oxidize the  $A'$  amine group to an imine<sup>501,502</sup>. This reaction proceeds through the formation of a  $Pb^{2+}$ -amide complex followed by a sequence of light-assisted proton-transfer reactions, and requires the  $A'$  cation to possess a  $\beta$ -C-H bond (e.g., butylammonium)<sup>501</sup>.

An interesting consequence of this degradation process is that, since it increases with decreasing  $n$ -value at the same time as 3D degradation processes are suppressed, it can lead to a non-monotonic  $n$ -value dependence of stability where an  $n>1$  RP is more stable than either its  $n_1$  or 3D phase in certain environments<sup>502</sup>.

The 2D structure informs the crystal surfaces along which degradation occurs. Mechanically exfoliated nanoflakes of the well-known 2D halide perovskite  $PEA_2PbI_4$  were used to investigate 2D halide perovskite intrinsic photostability.<sup>503</sup> Under resonant photoexcitation,  $PEA_2PbI_4$  degrades to  $PbI_2$  in a process initiated most aggressively at the crystal edges (in-plane) and secondarily from the surface (out-of-plane). This is in contrast to the layer-by-layer degradation observed in plate-like  $MAPbI_3$  crystals.<sup>504</sup> The surface degradation was explained by the observed lengthening of Pb-I bonds along the out-of-plane direction in  $PEA_2PbI_4$ , making those bonds more vulnerable to cleavage. Edge degradation was explained by outgassing of volatile organic degradation products being initiated at the edges, because of the more efficient mass transfer in the in-plane compared to out-of-plane direction. It was shown that encapsulation could efficiently suppress both degradation pathways.

Recent work by our group has shown a light-induced lattice contraction in the out-of-plane direction for DJ and ACI halide perovskites, which was not observed for RP halide perovskites or 3D halide perovskites.<sup>372</sup> When exposed to constant light illumination, DJ and ACI halide perovskites exhibited interlayer contraction over tens of minutes, which was reversible when light was removed. While our report did not observe or comment on degradation, modulation of bond lengths and introduction of compressive strain could change the activation energies for degradation reactions and the diffusion of degradation products for DJ and ACI halide perovskites under light. The effect of light-induced lattice contraction on stability warrants further investigation.

#### **4.2.4. Stability of 2D halide perovskites compared to 3D halide perovskites**

It was demonstrated experimentally that 2D RP phases  $BA_2MA_{n-1}Pb_{n+1}I_{3n+1}$  for  $n<5$  are

thermodynamically more stable than their 3D counterpart MAPbI<sub>3</sub><sup>66</sup> (**Figure 21a**). The enthalpy of formation ( $\Delta H_f$ ) of BA n=5 was found to be -20.47kJ/mol, compared to +34.5kJ/mol for MAPbI<sub>3</sub>. Past n=5,  $\Delta H_f$  increased significantly (138.59kJ/mol for n=6, 242.06kJ/mol for n=7) indicating that higher-n structures were not thermodynamically stable. Interestingly, even-n-value phases were consistently found to have lower  $\Delta H_f$  than odd n-value phases, a result of the different crystal symmetries for even-n and odd-n RP halide perovskites.

Under humidity, 2D halide perovskites are consistently found to have slower degradation kinetics compared to 3D halide perovskites with the same A, B, and X chemistry. Ahmad et al. compared the stability of solar cells using MAPbI<sub>3</sub>, the 2D RP phase PA<sub>2</sub>MA<sub>3</sub>Pb<sub>4</sub>I<sub>13</sub> (PA=propylammonium), and the 2D DJ phase (PDA)(MA)<sub>3</sub>Pb<sub>4</sub>I<sub>13</sub> (PDA=propyldiammonium) as the absorber layer<sup>493</sup> (**Figure 21b**). Devices were degraded under four conditions: ambient air, 85°C in ambient air, 85°C/85%RH in ambient air, and 1-sun illumination in N<sub>2</sub>. For all conditions the DJ devices were significantly more stable than both the RP and the 3D devices, maintaining >90% of their initial PCE by the time both the MAPbI<sub>3</sub> and RP devices had fallen to below 50%PCE. The RP devices likewise outperformed the 3D devices in terms of stability, although the extent of the stability improvement varied between each measurement: RP showed the largest improvement over 3D for 1-sun illumination, and the smallest improvement for 85°C/85%RH.

Tsai et al. fabricated solar cell devices from the RP phase BA<sub>2</sub>MA<sub>3</sub>Pb<sub>4</sub>I<sub>13</sub> and compared them to MAPbI<sub>3</sub> solar cells<sup>257</sup> (**Figure 21c**). They found that unencapsulated RP devices showed significantly improved stability compared to MAPbI<sub>3</sub> under 1-sun illumination in ambient air. The RP devices also outperformed the 3D devices at 65%RH, albeit to a lesser extent, consistent with the results of Ahmad et al. Encapsulation further improved the performance of RP devices compared to encapsulated 3D devices, likely because of the protection from humidity.

Spanopoulos et al. synthesized crystals of the RP halide perovskite series BA<sub>2</sub>MA<sub>n-1</sub>Pb<sub>n</sub>I<sub>3n+1</sub>, PA<sub>2</sub>MA<sub>n-1</sub>Pb<sub>n</sub>I<sub>3n+1</sub> (PA=pentylammonium, n=1-5), and HA<sub>2</sub>MA<sub>n-1</sub>Pb<sub>n</sub>I<sub>3n+1</sub> (HA=hexylammonium, n=1-4), and used these crystals to make phase-pure thin films<sup>80</sup>.

Lengthening the spacer cation from BA to HA increased the water contact angle of the RP films from 68.9° to 78.3°, and all three RP halide perovskites showed a significantly higher contact angle than MAPbI<sub>3</sub> (37.5°) (**Figure 21d**). All 2D films were air-stable for at least 120 days in dark, whereas MAPbI<sub>3</sub> degraded much more rapidly. Interestingly, the authors found a strong substrate dependence of degradation rate; films on polycrystalline silicon substrates outperformed those on amorphous glass, which was attributed to improved film crystallinity when grown on crystalline substrates.

Udalova et al. investigated the photostability of films of the RP halide perovskites BA<sub>2</sub>MA<sub>n-1</sub>Pb<sub>n</sub>I<sub>3n+1</sub> (n=1-3) and MAPbI<sub>3</sub> in a controlled atmosphere<sup>502</sup>. In inert atmosphere ([O<sub>2</sub>]<10ppm), photostability to 100mW/cm<sup>2</sup> 450 nm light as measured by PL intensity was found to have a non-monotonic dependence on n-value: BA n=3 showed the best stability, n2 and MAPbI<sub>3</sub> had comparable stability, and n1 was actually the least stable (**Figure 21e**). The authors attributed this non-intuitive stability trend to competition between two competing degradation processes: the Pb<sup>2+</sup> → Pb<sup>0</sup> / I<sup>-</sup> → I<sup>0</sup> redox reaction facilitated by the wide bandgap of low-n halide perovskites (n=1), and the volatilization of MA<sup>+</sup> in high-n halide perovskites (3D). The n3 phase represented an intermediate case which the authors termed a “stability island”, for which both processes existed but were suppressed compared to the extremes of n1 and 3D.

Aharon et al. used bulk PL to compare the photostability and self-healing of single crystals of BA n=1, BA n=3, and MAPbI<sub>3</sub> halide perovskites<sup>505</sup> (**Figure 21f**). Under degradation by a high-flux laser and subsequent holding in ambient conditions, they found that the RP phases showed improved self-healing compared to MAPbI<sub>3</sub>. BA n=1 self-healed from both moderate and high laser flux after 1 hr in the dark, while BA n3 healed only from moderate laser flux over the same time. MAPbI<sub>3</sub> did not heal under either laser flux. The authors attributed the improved self-healing ability to the suppression of degradation product out-diffusion by the layered structure of the RP halide perovskites. The study also found the creation of a small amount of BA n4 upon photodamage of the BA n3 sample, which could be attributed to the photoreduction of Pb<sup>2+</sup> to

Pb<sup>0</sup> by the butylammonium cation. Other reports have also shown 2D halide perovskites to self-heal more effectively than 3D.<sup>506</sup>

2D Sn-based halide perovskites show better stability than their 3D counterparts. Cao et al. synthesized phase-pure crystals and films of BA<sub>2</sub>MA<sub>2</sub>Sn<sub>3</sub>I<sub>10</sub> and BA<sub>2</sub>MA<sub>3</sub>Sn<sub>4</sub>I<sub>13</sub>, and made 2D devices with a TiO<sub>2</sub> ETL and a PTAA HTL.<sup>63</sup> Phase-purity of the n=3 and n=4 films was achieved by dissolving pure crystals of the phases rather than their constituent iodide salts in a precursor solution. SnF<sub>2</sub> was also added to the precursor solutions along with triethylphosphine to slow precipitation during film formation. The n=4 device showed a maximum PCE of 2.53%. More importantly, encapsulated n=4 devices exhibited 93.2% efficiency retention after being left in air for one month and retained 42.2%PCE after four months; MASnI<sub>3</sub> devices degraded completely under the same conditions within one month (**Figure 21g**). The authors attributed the stability improvement to the hydrophobicity of the BA cation protecting the inorganic layers.

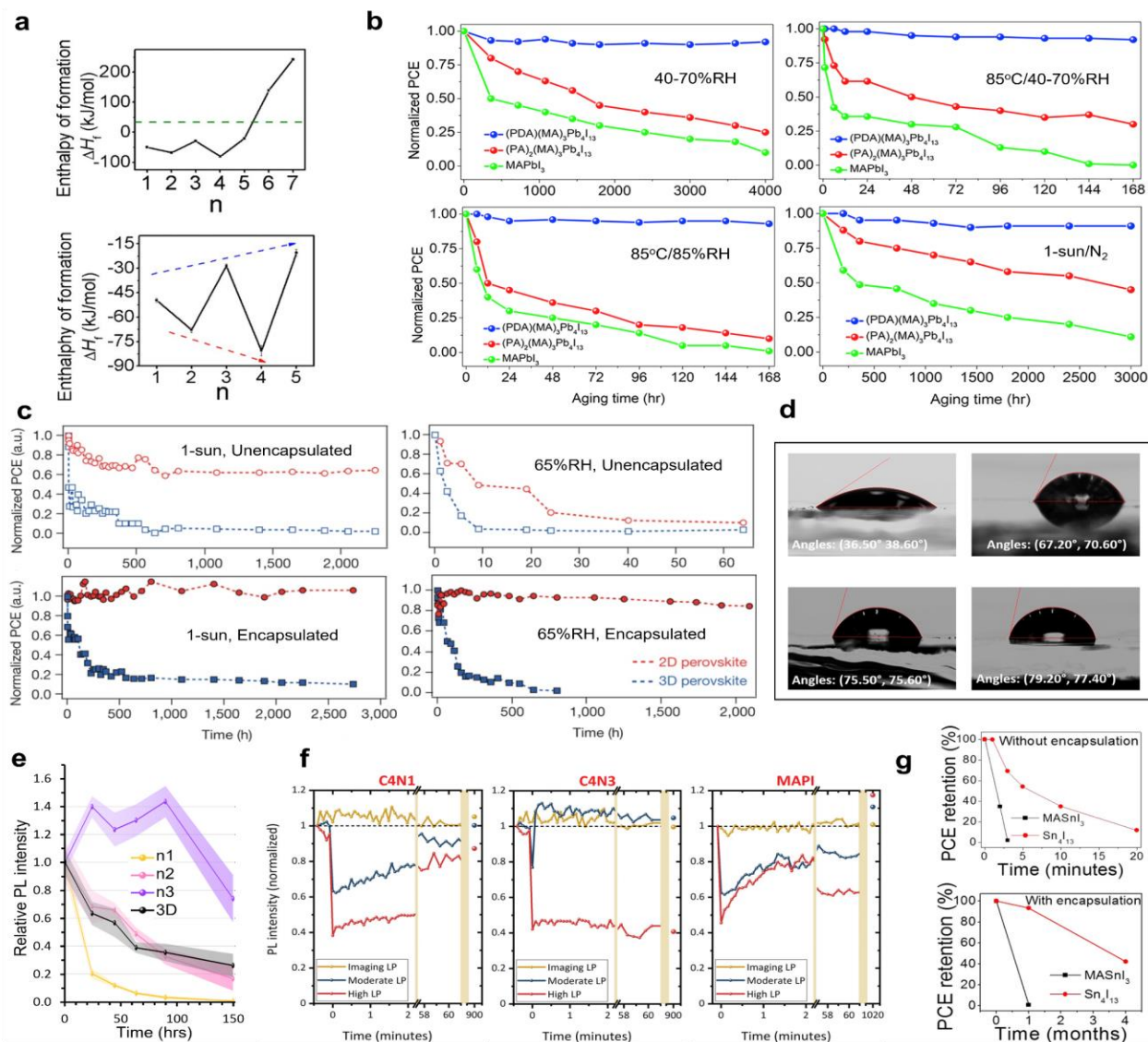


**Figure 21: Stability of 2D perovskites.** a) Top: Enthalpy of formation ( $\Delta H_f$ ) for 2D RP  $\text{BA}_2\text{MA}_{n-1}\text{Pb}_{n-1}\text{I}_{3n+1}$  ( $n=1-7$ ) showing step increase after  $n=5$ .  $\text{MAPbI}_3$   $\Delta H_f$  is shown in dashed green line. Bottom:  $\Delta H_f$  for  $n=1-5$  showing stabilization of even  $n$ -values. Reproduced with permission from ref.<sup>66</sup> Copyright 2018 National Academy of Sciences. b) Unencapsulated device PCE data over time for cells with absorber layers of DJ  $(\text{PDA})\text{MA}_3\text{Pb}_4\text{I}_{13}$  ( $\text{PDA}=1,3\text{-propanediammonium}$ ,  $\langle n \rangle=4$ , blue), RP  $(\text{PA})_2\text{MA}_3\text{Pb}_4\text{I}_{13}$  ( $\text{PA}=\text{propylammonium}$ ,  $\langle n \rangle=4$ , red), and 3D  $\text{MAPbI}_3$  (green) in four environments. Top left: ambient air, dark, 40-70%RH. Top right: ambient air, 85°C/40-70%RH. Bottom left: 85°C/85%RH. Bottom right: 1-sun illumination in inert atmosphere. The DJ device shows the best stability and the 3D device shows the worst stability under all conditions. Reproduced with permission from ref.<sup>493</sup> Copyright 2019 Elsevier. c) Unencapsulated (top) and encapsulated (bottom) device PCE data over time for RP  $(\text{BA})_2\text{MA}_2\text{Pb}_3\text{I}_{10}$  (red) and 3D  $\text{MAPbI}_3$  (blue) in two environmental conditions. Left: 1-sun illumination in inert atmosphere. Right: ambient air, 65%RH. Top: the unencapsulated RP device has better stability than the 3D device under both conditions. Bottom: encapsulation further improves the stability of the RP device relative to the 3D device. Reproduced with permission from ref.<sup>257</sup> Copyright 2016 Springer Nature. d) Water contact angle measurements for 3D  $\text{MAPbI}_3$  (top left) and the  $n=3$  RP structures  $(\text{A}')_2\text{MA}_2\text{Pb}_3\text{I}_{10}$  with  $\text{A}' = \text{BA}$  (top right), pentylammonium (PA, bottom left), and hexylammonium (HA, bottom right). Contact angle increases with spacer cation length. Reproduced with permission from ref.<sup>80</sup> Copyright 2019 American Chemical Society. e) PL intensity over time for films of RP  $(\text{BA})_2\text{MA}_{n-1}\text{Pb}_{n-1}\text{I}_{3n+1}$  ( $n=1-3$ ) and 3D  $\text{MAPbI}_3$  under continual irradiation by 450nm light in inert atmosphere. A nonmonotonic  $n$ -value dependence is observed with RP  $n=3$  showing better stability than both  $n=1$  and  $n=2$  and  $\text{MAPbI}_3$ . Reproduced with permission from ref.<sup>507</sup> Copyright 2021 American Chemical Society. f) PL intensity over time for single crystals of  $(\text{BA})_2\text{PbI}_4$  (left),  $(\text{BA})_2\text{MA}_2\text{Pb}_3\text{I}_{10}$  (center), and  $\text{MAPbI}_3$  (right) after a pulse of low (imaging, yellow), moderate (blue), and high (red) laser intensity. g) PCE retention (%) vs time for  $\text{MASnI}_3$  and  $\text{Sn}_4\text{I}_{13}$  with and without encapsulation.

irradiation. The RP films self-heal faster than 3D after moderate photodamage. For high photodamage the  $n=1$  crystal heals the fastest but the  $n=3$  crystal shows permanent photodamage. Reproduced with permission from ref.<sup>505</sup> Copyright 2022 Wiley-VCH. g) Unencapsulated (top) and encapsulated (bottom) device PCE data over time for RP (BA)<sub>2</sub>MA<sub>3</sub>Sn<sub>4</sub>I<sub>13</sub> (red) and 3D MASnI<sub>3</sub> (black) in ambient air. The RP device showed better air stability than the 3D device both with and without encapsulation. Reproduced with permission from ref.<sup>508</sup> Copyright 2017 American Chemical Society.

#### 4.2.5. Methods to improve 2D halide perovskite stability

Compared to the A-, B-, and X- sites of 3D halide perovskites for which there are only a handful of possible ion choices each, the A'-sites of 2D halide perovskites have a significantly larger assortment of molecular cations which they can accommodate. This opens up the possibility of functionalizing A'-site cations for improved stability. At the same time, the Goldschmidt tolerance factor governing allowed A-site cations is relaxed in the 2D structure, giving a larger design space for more stable A-site cations. As a result, the prospects for improving 2D halide perovskite stability are if anything more favorable than for 3D. On the other hand, the additional complexities in phase and microstructure control for solution-processed 2D halide perovskites and a reduced academic interest in 2D halide perovskites compared to 3D halide perovskites mean that improvements to 2D stability are comparatively understudied. Here we collect a few established principles for improving 2D halide perovskite stability which have been shown to apply regardless of  $n$ -value or phase.

##### **a) Strengthen interlayer interactions.**

Multiple reports have suggested that strengthening interlayer bonding can improve the stability of halide perovskite films and devices.<sup>312,493,509–516</sup> Strengthening interlayer interactions can be accomplished by functionalizing the A'-site of RP halide perovskites to increase interactions between interlayer cations.<sup>312,509</sup> For example, Ren et al. demonstrated an improvement in device stability upon replacement of BA<sup>+</sup> with the sulfur-containing 2-(Methylthio)ethylammonium (MTEA<sup>+</sup>).<sup>312</sup> The sulfur atom on MTEA<sup>+</sup> introduced a new S-S interaction in addition to the van der Waals force common to the RP structure, enhancing the overall interaction between spacer cations. As a result, MTEA  $n=5$  (BA  $n=5$ ) devices retained 85% PCE (40% PCE) after 1000 hr continuous

operation at MPP in N<sub>2</sub>. Furthermore, MTEA  $n=5$  films showed no degradation XRD peaks after 1512 hr in ambient air, whereas BA  $n=5$  films showed a noticeable Pbl<sub>2</sub> peak after the same time. MTEA films also showed suppressed degradation peaks compared to BA films after 375 hr at 85°C, after 36 hr at 85°C/85%RH in air, and after 96 hr at 150°C in N<sub>2</sub>. Zhang et al. found similar results from fluorination of PEA in Sn-based RP halide perovskite solar cells.<sup>509</sup>  $n=4$  Devices using 4-fluorophenethylammonium (FPEA<sup>+</sup>) as a spacer cation showed improved stability in inert atmosphere compared to PEA  $n=4$ , with FPEA maintaining 100% PCE after 180 hr whereas PEA fell to 0%PCE within 100 hr. The authors attributed this improvement to the electrostatic attraction between F atoms and adjacent phenyl rings, which stabilizes the 2D structure. Incorporation of F and other halides into the spacer cation has similarly been shown to improve stability by a variety of authors,<sup>510–512</sup> although some reports have found that this stabilization is not universal but is halide-dependent.<sup>512</sup> Fluorination has also been shown to improve structural rigidity and suppress phase transitions in  $n=1$  RP halide perovskites,<sup>513</sup> suggesting a stabilization of the 2D structure. Very recently, Yang et al. introduced the  $\pi$ -conjugated A' cation (9H-carbazol-9-yl)butyl-1-ammonium (CA<sup>+</sup>) which stabilized the RP structure through  $\pi$ - $\pi$  stacking. CA films showed no visible degradation over several minutes submerged in water, and unencapsulated CA devices retained 85% PCE after 2000 hr at 25°C/65%RH, better than 3AMP- and PEA-based devices and among the best high-humidity stabilities reported for halide perovskites.<sup>517</sup>

Interlayer interactions can also be strengthened by switching from an RP structure, where layers are held together through van der Waals interactions between monoammonium cations, to a DJ structure where a single diammonium cation bonds strongly to two successive inorganic layers.<sup>493,515</sup> Ahmad et al.<sup>493</sup> compared the efficiency

and stability of devices using MAPbI<sub>3</sub>, the RP halide perovskite PA<sub>2</sub>MA<sub>n-1</sub>Pb<sub>n</sub>I<sub>3n+1</sub> (PA=propylammonium, n=4), and the DJ halide perovskite (PDA)(MA)<sub>n-1</sub>Pb<sub>n</sub>I<sub>3n+1</sub> (PDA=1,3-propanediammonium, n=1-4) as the absorber layer. They found the PDA n=4 device significantly outperformed both MAPbI<sub>3</sub> and PA n=4 in terms of stability. Unencapsulated PDA n=4 (PA n=4) devices retained 95% PCE (25% PCE) after 4000 hr in ambient air, 95% PCE (50% PCE) after 3000 hr continuous light illumination, and 95%PCE (20%PCE) after 168 hr at 85°C/85%RH. The authors attributed the improved stability of the DJ phase to the hydrogen bonding between the diammonium cation and both interlayer slabs it bridges. Ma et al.<sup>515</sup> likewise found PDA n=4 to be more stable than BA<sub>2</sub>MA<sub>3</sub>Pb<sub>4</sub>I<sub>13</sub> (BA n=4). Encapsulated PDA n=4 (BA n=4) devices retained 90% PCE (40% PCE) after 1000 hr at RT/85%RH, and retained 100%PCE (0%PCE) after 100 hr at 70°C/85%RH. The authors once again attributed this improvement to strengthened interlayer interactions. Similar stability improvements have been observed for LEDs with DJ compared to RP emitters, attributed to an increased molecule dissociation energy in the DJ phase as a result of the bridging spacer cation.<sup>516</sup>

### **b) Increase the hydrophobicity of the A' cation.**

Enhancing the hydrophobicity of the spacer cation can improve the stability of 2D halide perovskite devices in humid and ambient environments. Hydrophobicity, like interlayer cation interaction, can be increased through fluorination of the spacer cation.<sup>64,89,514,518-521</sup> Slavney et al. found that fluorination of PEA can increase the hydrophobicity of the cation, leading to a significantly increased stability for phase-pure 4-fluorophenethylammonium (FPEA<sup>+</sup>) n=3 powder in humid air compared to phase-pure PEA n=3 powder.<sup>89</sup> Fluorination has also been demonstrated to increase hydrophobicity of the spacer cation and the 2D phase in DJ halide perovskites, for example by replacing 1,4-benzenedimethan ammonium (BDA<sup>2+</sup>) with 2,3,5,6-tetrafluoro-1,4-benzenedimethan ammonium (TFBDA<sup>2+</sup>).<sup>520</sup> Functionalization with oxygen can also improve hydrophobicity. For example, n=1 (MeO-PEA)<sub>2</sub>PbI<sub>4</sub> (MeO-PEA = 4-methoxyphenethylammonium)

showed enhanced water resistance compared to PEA in DFT simulations because of steric hindrance and repulsion between the oxygen and the H<sub>2</sub>O lone pair electrons; <n>=5 devices using MeO-PEA confirmed its air and humidity stability.<sup>521</sup> A combination of increased interlayer interactions and increased spacer cation hydrophobicity was shown to improve the air stability of the Sn-based 2D halide perovskite FSA<sub>2</sub>SnI<sub>4</sub> (FSA=2-(4-(3-fluoro)stilbenyl)ethan ammonium) compared to its nonfluorinated counterpart.<sup>514</sup> Other novel hydrophobic spacers have been explored, for example the polymeric ammonium cation polyethylenimine.<sup>64</sup>

### **c) Passivate defects and improve film quality.**

Similar to 3D halide perovskites, defect passivation and improvements in crystallinity can suppress defect-mediated degradation pathways in 2D halide perovskites and improve device stability.<sup>522-529</sup> Yukta et al. demonstrated an improvement in unencapsulated device stability both at RT/60%RH and at 85°C, as well as an increased water contact angle, for (NDA)(MA)<sub>3</sub>Pb<sub>4</sub>I<sub>13</sub> (NDA=1,5-diaminonaphthalene, n=4) treated with NH<sub>4</sub>SCN.<sup>522</sup> The improvement in stability was attributed to a reduced defect concentration and increased crystallinity as a result of the addition of NH<sub>4</sub>SCN, which regulates crystal growth and suppresses defects through the synergistic occupation of A-sites by NH<sub>4</sub><sup>+</sup> and X-sites by SCN<sup>-</sup>. NH<sub>4</sub>SCN has realized similar stability improvements in other reports.<sup>523</sup> Likewise, the crystallinity of the ACI halide perovskite GA<sub>3</sub>MA<sub>3</sub>Pb<sub>3</sub>I<sub>10</sub> (GA=guanadinium) was enhanced by the incorporation of MASCN and grain boundary defects were simultaneously passivated by the partial substitution of MA with PEA, improving stability in both ambient air and at 85°C in N<sub>2</sub> atmosphere.<sup>524</sup> Chen et al. observed that replacing either MAI with MACI or PEAI with PEACI in precursor solutions of PEA <n>=6 RP halide perovskite significantly improved crystallinity, reduced defect density, and enhanced device stability in inert atmosphere.<sup>525</sup> Other reports have also shown MACI to improve crystallinity and grain orientation.<sup>90,526</sup>

The A'-site itself can be engineered to improve film quality. Cheng et al. incorporated ammonium (AA<sup>+</sup>) into PEA  $n \geq 5$  halide perovskites to relax residual strain in the lattice.<sup>527</sup> They found that these mixed-A'-site RP halide perovskite films were more stable under air, humidity, heat, and light than films with a pure PEA A'-site, which they attributed to improved crystalline quality and suppressed defect concentration due to strain relaxation. A similar mixed-A'-site system (BA<sub>1-x</sub>NMA<sub>x</sub>)<sub>2</sub>MA<sub>3</sub>Pb<sub>4</sub>I<sub>13</sub> (NMA = 1-naphthalenemethylammonium) was investigated by Liu et al., who found that NMA incorporation increases the hydrogen bonding between the inorganic layer and the spacer cation ammonium group and improves grain size and orientation.<sup>528</sup> The reduction of defects and increased crystallinity improved the stability of 10%NMA devices in air compared to pure BA devices. Yao et al. likewise improved film crystallinity and as a result device stability in Cs-based RP halide perovskites by replacing phenylammonium (PA<sup>+</sup>) with phenylhydrazinium (PHA<sup>+</sup>) to strengthen the spacer cation - inorganic layer hydrogen bond.<sup>529</sup> Li et al. utilized 4-(2-Aminoethyl)pyridinium (4-AEP<sup>+</sup>) to simultaneously act as the spacer cation and modulate crystallization kinetics by complexing with Pb<sup>2+</sup>, improving crystallinity and stability relative to the nonfunctionalized PEA<sup>+</sup>.<sup>530</sup>

#### **d) Replace or alloy the A-site cation.**

Just as in 3D halide perovskites, partial or complete substitution of MA with another A-site can improve the stability of 2D halide perovskites.<sup>331,531-536</sup> Guo et al. used FA as the A-site in the DJ halide perovskite (BDA)(FA)<sub>2</sub>Pb<sub>3</sub>I<sub>10</sub> (BDA = 1,4-butanediammonium,  $n=3$ ).<sup>531</sup> Compared to (BDA)(MA)<sub>2</sub>Pb<sub>3</sub>I<sub>10</sub>, the unencapsulated FA-based device exhibited improved stability under continuous 1-sun illumination and under 65°C heating in inert atmosphere, and XRD revealed a slower degradation of FA-based films in humid air. The authors attributed this improvement to a reduced octahedral tilting in the FA-based crystal structures which they claimed indicates higher structural stability, and to a suppression of disproportionation in FA-based films in humid air. FA-based films also showed larger grains and improved vertical

orientation, which likely contributed to improved stability. Significant thermal stability improvements have been seen in (PDA)(FA)<sub>3</sub>Pb<sub>4</sub>I<sub>13</sub> compared to (PDA)(MA)<sub>3</sub>Pb<sub>4</sub>I<sub>13</sub>, attributed to the more heat-stable FA cation.<sup>532</sup> Unfortunately, although tolerance factor is relaxed in 2D halide perovskites,<sup>537</sup> computational and experimental evidence suggests that high- $n$  FA-based DJ halide perovskites are difficult to obtain because of high formation energies.<sup>538</sup> Developing a consistent method for phase-pure high- $n$  FA-based 2D halide perovskites could lead to a further improvement in 2D halide perovskite stability, and we see this as a key future research area.

Mixed A-site cations have also shown improved stability in 2D halide perovskites. Zhou et al.<sup>533</sup> and Zhang et al.<sup>331</sup> investigated the mixed-A-site RP halide perovskites BA<sub>2</sub>(MA<sub>0.8</sub>FA<sub>0.2</sub>)<sub>3</sub>Pb<sub>4</sub>I<sub>13</sub> and BA<sub>2</sub>(MA<sub>0.95</sub>Cs<sub>0.05</sub>)<sub>3</sub>Pb<sub>4</sub>I<sub>13</sub> respectively. Zhou et al. found near-identical stability but an improvement in PCE of BA<sub>2</sub>(MA<sub>0.8</sub>FA<sub>0.2</sub>)<sub>3</sub>Pb<sub>4</sub>I<sub>13</sub> compared to BA<sub>2</sub>MA<sub>3</sub>Pb<sub>4</sub>I<sub>13</sub>, while Zhang et al. showed improved humidity and heat stability for BA<sub>2</sub>(MA<sub>0.95</sub>Cs<sub>0.05</sub>)<sub>3</sub>Pb<sub>4</sub>I<sub>13</sub>. Motivated by these results, Jiang et al. demonstrated higher thermal stability in the triple-cation RP halide perovskite BA<sub>2</sub>(MA<sub>0.76</sub>FA<sub>0.19</sub>Cs<sub>0.05</sub>)<sub>3</sub>Pb<sub>4</sub>I<sub>13</sub> compared to either of the double-cation halide perovskites BA<sub>2</sub>(MA<sub>0.8</sub>FA<sub>0.2</sub>)<sub>3</sub>Pb<sub>4</sub>I<sub>13</sub> or BA<sub>2</sub>(MA<sub>0.95</sub>Cs<sub>0.05</sub>)<sub>3</sub>Pb<sub>4</sub>I<sub>13</sub>, which was attributed to an improved crystallinity and lower defect density.<sup>534</sup> Likewise, 10% FA incorporation in the DJ halide perovskite (PDA)(FA)<sub>x</sub>(MA)<sub>3-x</sub>Pb<sub>4</sub>I<sub>13</sub> (PDA=1,3-propanediammonium) was found to improve stability under humidity, heat, and light, attributed to improved crystallinity and the stronger FA-I hydrogen bond.<sup>535</sup> 5% Cs incorporation in (PDA)(Cs)<sub>x</sub>(MA)<sub>3-x</sub>Pb<sub>4</sub>I<sub>13</sub> also has been shown to improve stability.<sup>536</sup>

#### **e) Improve phase purity.**

Most of the reports mentioned so far in this section have involved mixed- $n$ -value films of 2D halide perovskites. Several reports by our group<sup>323,539</sup> and others<sup>288,340</sup> have indicated that phase-pure 2D halide perovskite films show improved stability compared to mixed phase films. Liang et al. demonstrated enhanced ambient, thermal, and light stability with phase-pure BA<sub>2</sub>MA<sub>3</sub>Pb<sub>4</sub>I<sub>13</sub> (BA  $n=4$ )



halide perovskite devices compared to mixed-phase  $\langle n \rangle = 4$  ones, and suggested that the degradation of mixed-phase devices began in regions of 3D halide perovskite within the film.<sup>340</sup> Likewise, our group demonstrated a significant enhancement in photostability in air for phase-pure  $\text{BA}_2\text{MA}_3\text{Pb}_4\text{I}_{13}$  devices compared to mixed-phase  $\langle n \rangle = 4$  devices.<sup>323</sup> This remains an underexplored aspect of 2D halide perovskite stability, principally because of the

difficulty of growing phase-pure 2D thin films. Recent work by our group has suggested a new solution processing technique via the dissolution of phase-pure 2D crystals to grow 2D films with significantly enhanced phase-purity.<sup>323</sup> We expect that as phase-pure 2D films become easily realizable the influence of phase distribution on all aspects of 2D halide perovskite behavior including stability will become more clear.

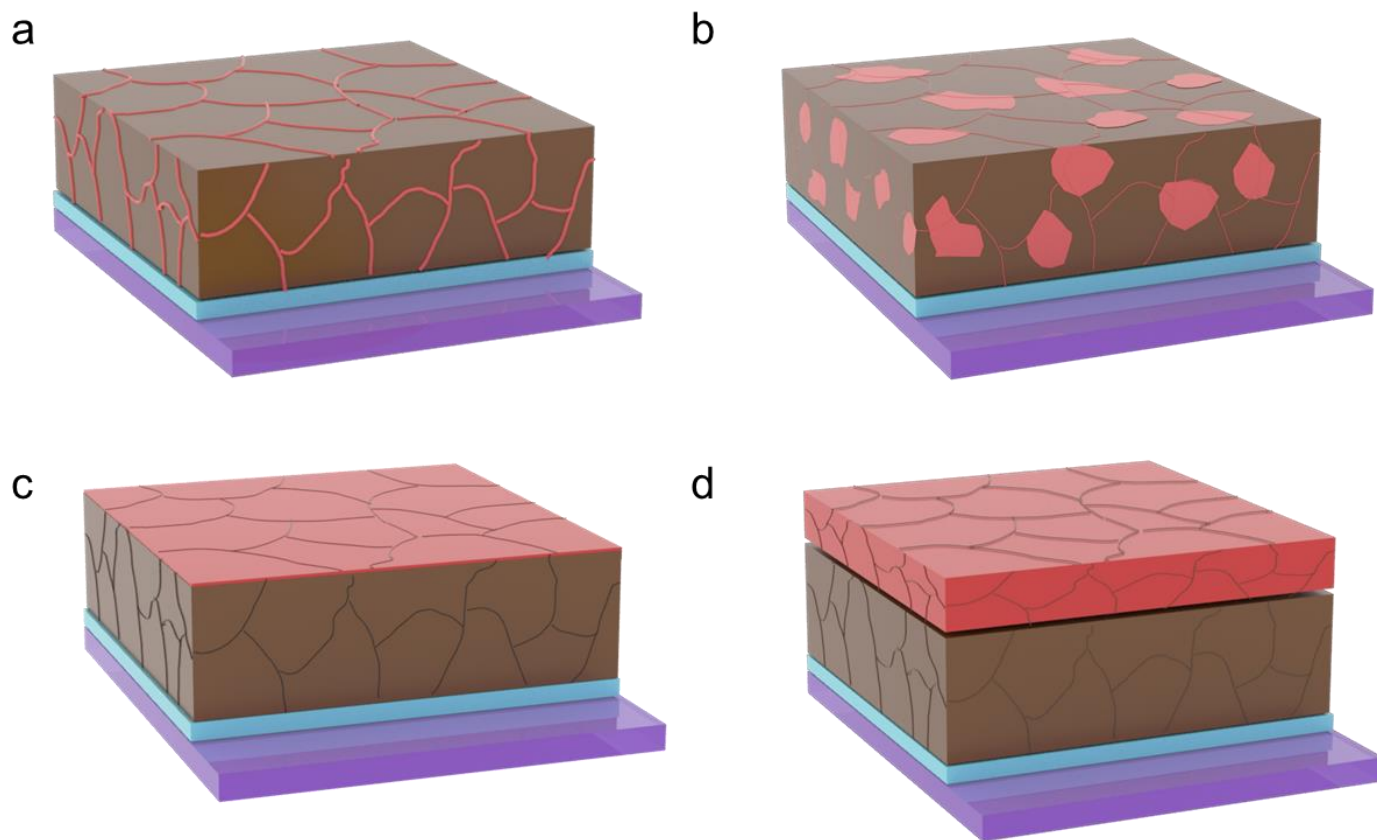


**Figure 22: Different types of 3D-2D halide perovskites.** a) 3D halide perovskite with 2D spacer cations incorporated into the grain boundaries. b) 3D-2D composite halide perovskite with quasi-2D structures intercalated into the 3D halide perovskite lattice. These quasi-2D structures can be present anywhere in the bulk. c) Thin 2D ( $n=1$ , thickness  $< 10\text{nm}$ ) halide perovskite layer on top of a 3D halide perovskite. d) 3D-2D halide perovskite bilayer stacks where 2D halide perovskite thickness  $> 30\text{nm}$

## **Part 2: Combining 3D and 2D halide perovskites**

While progress has been made with 2D halide perovskite solar cells, they still lag in terms of efficiency compared to their 3D counterparts due to their higher exciton binding energies, higher bandgaps, and inferior charge carrier dynamics. At the same time, 3D halide perovskites show worse stability than 2D halide perovskites due to their more hygroscopic chemistry, higher ion and defect mobility,

and poorer retention of degradation products. To address this issue, researchers have employed several strategies to combine the stability of 2D halide perovskite systems with the efficiency of 3D halide perovskites. There are two broad ways to synergistically integrate the stability of 2D halide perovskites (or their bulky organic cations) into the performance of 3D halide perovskites: 1) doping 2D

halide perovskites into 3D halide perovskite precursors, and 2) depositing 2D halide perovskites on top of 3D halide perovskites. In the former approach, 2D spacer cations are incorporated into the 3D precursor, either at the grain boundaries (**Figure 22a**) or by forming 3D-2D composite halide perovskites (**Figure 22b**). In the latter case, post-treatment of 3D halide perovskites using organic spacer cations in non-interacting solvents can lead to the formation of very thin (<10nm) low-dimensional 2D halide perovskite layers on top of the 3D halide perovskite, effectively passivating the dangling

bonds and grain boundaries (**Figure 22c**). This 2D passivation strategy can simultaneously improve the stability of the 3D perovskite and the device's charge transport behavior. However, producing thicker layers of 2D on top of 3D is challenging because of the similar solubilities of 2D and 3D halide perovskites in conventional solvents (**Figure 22d**). In this part of the review, we will discuss all possible methodologies to harness the synergy between 3D and 2D halide perovskites, highlighting the advantages and limitations of each approach.

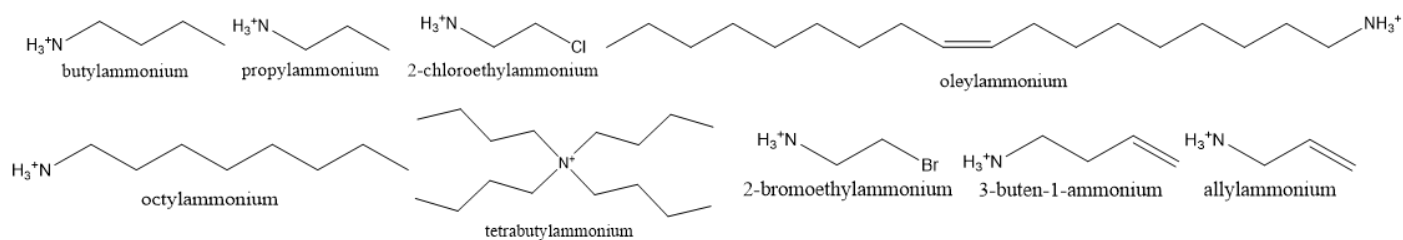
## 5. Doping 3D halide perovskites with 2D halide perovskites

Spacer cations used in 2D halide perovskites are generally comprised of an organic chain or ring type molecule with an ammonium cation at one or both ends. The type of spacer cation determines the type of 2D halide perovskite formed, like Ruddlesden popper (RP), Dion-Jacobson (DJ) or alternating cation (ACI). The incorporation of 2D halide perovskites as spacer cations in 3D halide perovskites has emerged as a promising strategy to enhance the optoelectronic properties and stability of halide perovskite solar cells. The bulky nature of 2D halide perovskite spacer cations has been shown to create large  $n$  value 2D-layered structure within the 3D bulk. This type of 3D-2D composite halide perovskites are very appealing because they can produce 3D halide perovskite like optoelectronic behavior (low bandgaps, high absorption coefficients, lower exciton energies) while the bulky spacer cations can protect the halide perovskite layer from degradation effects like ion migration, halide segregation, humidity, photo-illumination, and thermal stressors. However, achieving optimal doping concentrations of 2D spacer cations is crucial

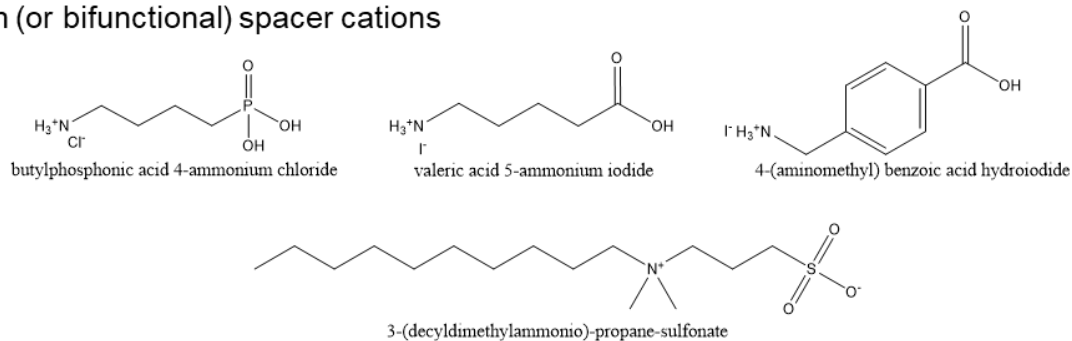
to avoiding insulating channels and maintaining effective charge transport in the halide perovskite layer. Higher concentrations of 2D halide perovskite cations can lead to a blueshift in the bandgap of the 3D halide perovskite, leading to lower absorption and current and may also increase the exciton binding energy leading to inferior charge separation and charge diffusion lengths.

To address these challenges, researchers have explored a variety of 2D spacer cations with different organic chains to stabilize or enhance the 3D halide perovskite properties (**Figure 23**). Although this list is not exhaustive, we try to categorize these cations into 5 different types of 2D spacer cations as long chain monoammonium cations, zwitterion (or Bifunctional) cations, aromatic ring monoammonium cations, diammonium cations and ACI type cations, based on the type of organic chain and their functionalization. We will also investigate how different cations influence the overall performance and durability of halide perovskite solar cells.

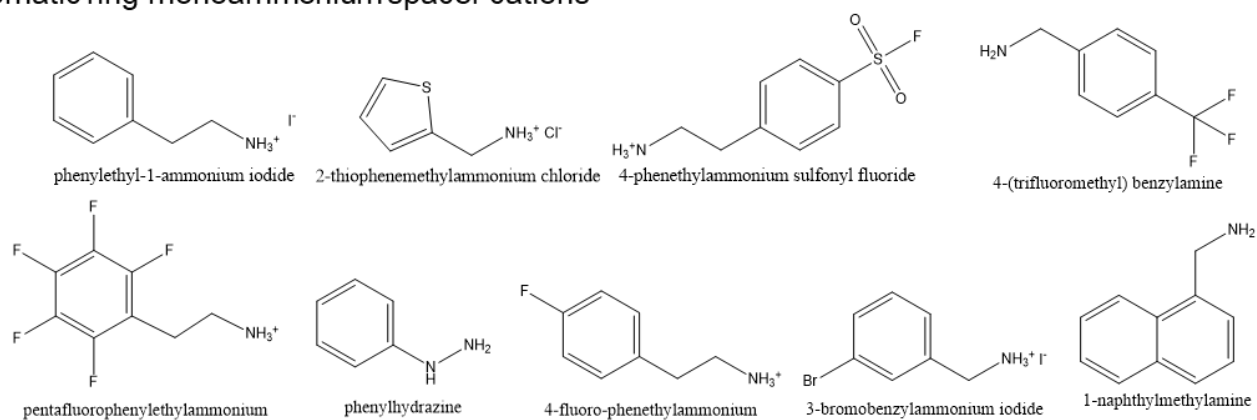
## Long chain Monoammonium spacer cations



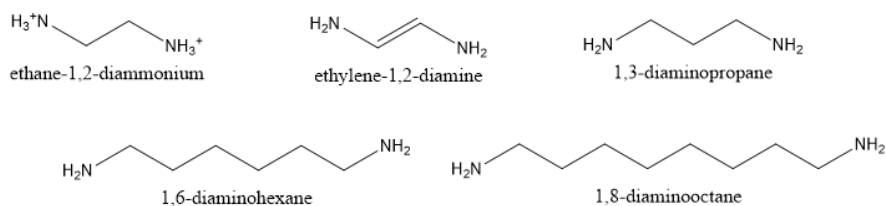
## Zwitterion (or bifunctional) spacer cations



## Aromatic ring monoammonium spacer cations



## Diammonium spacer cations



## ACI type cations

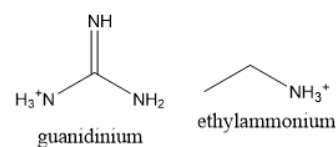


**Figure 23. Some examples of organic spacer cations found in the literature.** These cations can be categorized into 5 major sets, long chain monoammonium cations, bifunctional (or zwitterion) monoammonium cations, aromatic ring monoammonium cations, diammonium spacer cations and, ACI type cations.

### 5.1. Long chain monoammonium cations

Earliest iterations of 2D RP halide perovskite solar cells used aromatic ring and long chain ammonium spacer cations like PEA and BA.<sup>48</sup> The ammonium ends of the spacer cation interact with the halide ions while the organic ends orient towards the other organic end of the other cation to stabilize the layered structure. RP halide perovskite films made by Cao et al. and Sidhik et al. using BA as a spacer cation tend to orient preferentially in the (110) plane, which is perpendicular to the halide perovskite stacking axis, thereby improving the charge transfer across the film.<sup>323</sup> Wang et al. carefully replaced 9% FA/Cs atoms with BA cations in  $\text{FA}_{0.83}\text{Cs}_{0.17}\text{Pb}(\text{I}_y\text{Br}_{1-y})_3$  and observed the formation of 2D platelets distributed between a highly-oriented 3D halide perovskite grain.<sup>540</sup> SEM and GIWAXS measurements for different molar ratios of BA cations reveal the formation of plate-like 2D grains scattered across the grain boundaries of the 3D halide perovskite that became progressively larger at higher concentrations (**Figure 24a,c**). The 3D (100) peak intensity also increased by a factor of 10 while the other peaks became weaker, implying the preferential orientation of the 3D halide perovskite. Improved crystallinity also led to longer here (**Figure 24e,f**).<sup>541</sup>

TRPL lifetimes, indicating suppression of non-radiative recombination in 3D-2D halide perovskites. Devices made with 9% substitution of FA/Cs with BA atoms had a lower hysteresis and a higher stabilized efficiency of 19.5% ( $E_g \sim 1.6\text{V}$ ) and 17.3% ( $E_g \sim 1.72\text{V}$ ) (**Figure 24b**). Unencapsulated devices under illumination and ambient humidity ( $\sim 45\%$ ) in open circuit conditions showed a  $T_{80}$  of 1005 hr, 50% higher than the control samples. A similar study was later conducted by Zheng et al. to understand the effect of using long chain monoammonium cations to template the growth of  $\text{Cs}_{0.05}(\text{FA}_{0.92}\text{MA}_{0.08})_{0.95}\text{Pb}(\text{I}_{0.92}\text{Br}_{0.08})_3$ . The authors added oleylammonium ( $\text{OIA}^+$ ), octylammonium ( $\text{OA}^+$ ), PEA<sup>+</sup>, and BA<sup>+</sup> cations in trace quantities ( $<0.3\text{ wt}\%$ ) and noticed an enhanced crystallization of the (100) orientation and restriction of other crystal orientations, thus reducing the defect density due to random crystallization (**Figure 24d**). During annealing, the spacer cations migrated to the top surface, passivating any defects and providing moisture resistance. p-i-n devices made with 0.1wt% OIA yielded a champion PCE of 23.0% with no loss in PCE for over 1000 hr when tested under MPPT in  $\text{N}_2$  atmosphere.

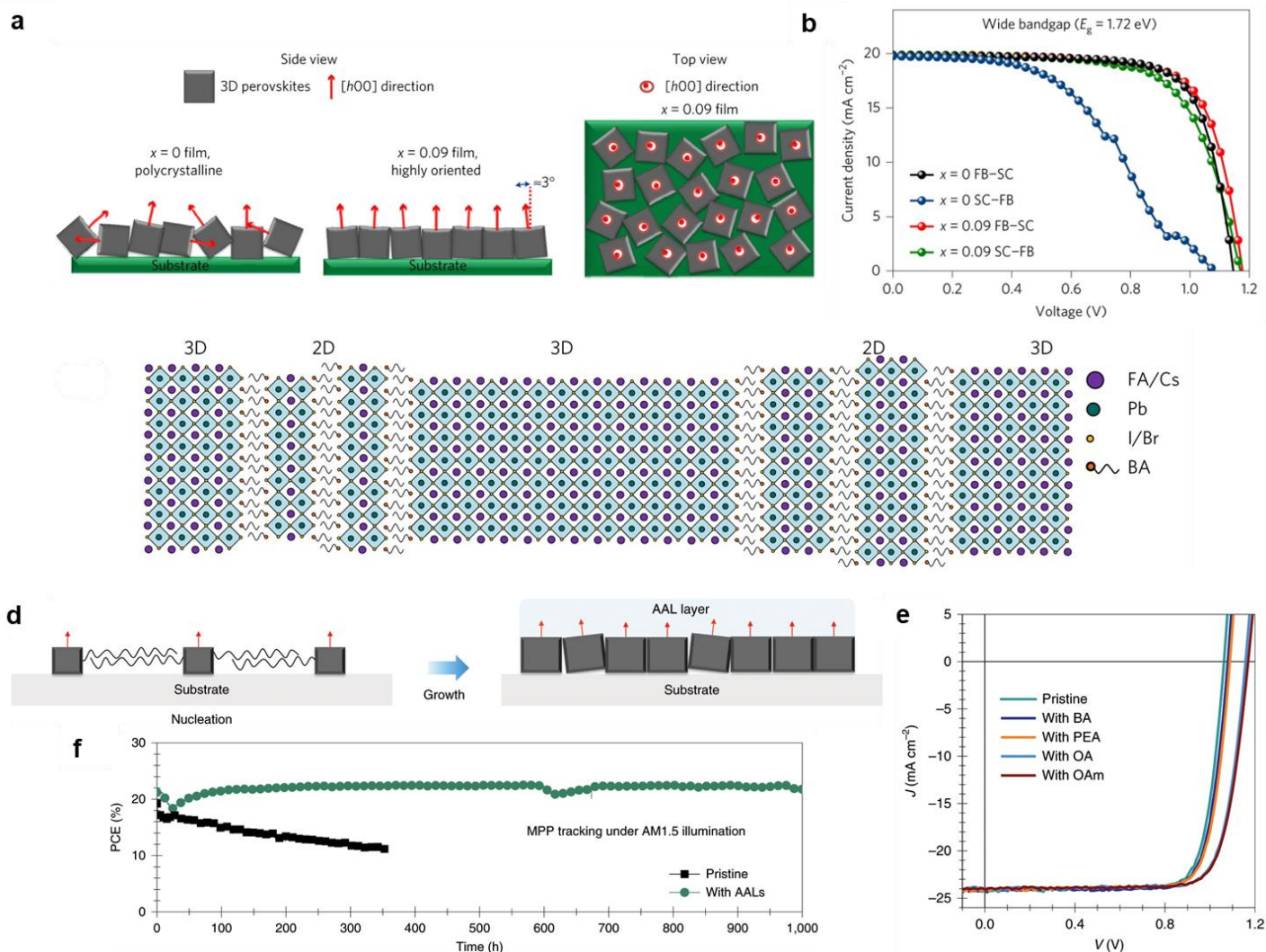


**Figure 24. Alkylammonium cations for templating 3D halide perovskite.** a) Schematic depicting that BA cation ( $x=0.09$ ) doping can lead to preferential orientation of the 3D-2D halide perovskite in the (h00) direction forming highly oriented defect-free crystalline films. b) J-V curves for wide bandgap FA/Cs ( $E_g \sim 1.72$  eV) halide perovskite solar cells with and without BA doping. c) Proposed schematic for self-assembled 3D-2D halide perovskite films. (a-c) reproduced with permission from ref.<sup>540</sup> Copyright 2017 Springer Nature. d) Proposed mechanism of templating induced by addition of long chain monoammonium cations. e) J-V curves of  $\text{Cs}_{0.05}(\text{FA}_{0.92}\text{MA}_{0.08})_{0.95}\text{Pb}(\text{I}_{0.92}\text{Br}_{0.08})_3$  solar cells with 0.1 wt% addition of different spacer cations. f) Plot showing MPPT under continuous light illumination for control and 0.1wt% doped OIA devices. (d-f) reproduced with permission from ref.<sup>541</sup> Copyright 2020 Springer Nature.

Fei et al. did a systematic study to test the effect on performance and stability of using iodide salts of different aliphatic chain monoammonium cations like ethylammonium (EAI), propylammonium (PAI) and butylammonium (BAI) as additives for 3D-2D halide perovskites. Due to the self-assembly nature of 2D spacer cations, the crystallinity for 3% PAI doped  $\text{Cs}_{0.05}\text{FA}_{0.80}\text{MA}_{0.15}\text{Pb}(\text{I}_{0.85}\text{Br}_{0.15})_3$  was improved significantly with a reduction in the FWHM of the (001) peak and a grain size of up to 1  $\mu\text{m}$ . The authors used femtosecond transient absorption (TA)

and transient reflectance spectroscopy (TR) to understand the charge transfer dynamics in the bulk and the surface. Since the TR signal decayed much faster than the TA signal, the surface trap density was determined to be higher than the bulk trap density in the halide perovskite films. The addition of large spacer cations improved the TR decay times, indicating that the cations can accumulate at the surface and passivate these surface traps. PL lifetimes also increased with the addition of bulky cations, implying improved crystallinity and reduced

recombination. Devices made with 3% PAI doping showed the best photovoltaic efficiency of 20.3% with a  $T_{97}$  of 600 hr under shelf storage conditions.<sup>542</sup>

Organic spacer cations with electronegative atoms (like O, F, Cl, Br, I) substituting the H positions can induce hydrogen bonding and halogen-halogen interactions that can lead to better templating of halide perovskites. Sourisseau et al.<sup>543</sup> substituted one of the end H atoms with a Cl or Br atom in ethylammonium, resulting in hydrogen bonding between the ammonium group and the halide atom. This interaction led to negligible hydrogen bonding between the  $-NH_3$  group and I-Pb groups, giving a Pb-I-Pb bond angle close to  $180^\circ$ . Larger bond angle implies a better overlap between the Pb s-orbital and I p-orbital, raising the antibonding VBM and leading to lower bandgaps in the 2D halide perovskites.<sup>108</sup> Liu et al. mixed 2-chloroethylammonium ( $CEA^+$ ) and 2-bromoethylammonium ( $BEA^+$ ) spacer cations into

$Cs_{0.1}FA_{0.9}Pb(I_{0.9}Br_{0.1})_3$  and noticed a formation of 3D-2D composite halide perovskite with reduction in FWHM of the (110) peak to  $0.13^\circ$ , accompanied with improvement in the absorption and PL intensity. At concentrations  $> 5\%$ , lower angle peaks corresponding to quasi-2D halide perovskites start to shift due to lattice expansion (**Figure 25a**). Similarly, at higher concentrations, absorption of the halide perovskite decreases, and the PL spectra intensity decreases and is blue shifted, indicating that larger amount of quasi-2D halide perovskite can hinder charge transfer. Devices J-V curves are shown in **Figure 25b**, showing the initial increase in efficiency and then decrease as the concentration is increased. While the unencapsulated control device could only maintain 73% of initial PCE in 2400 hr, CEA and BEA 3D-2D composite halide perovskite devices retained 92% and 87% of their initial PCE under 50% Relative Humidity.<sup>544</sup>



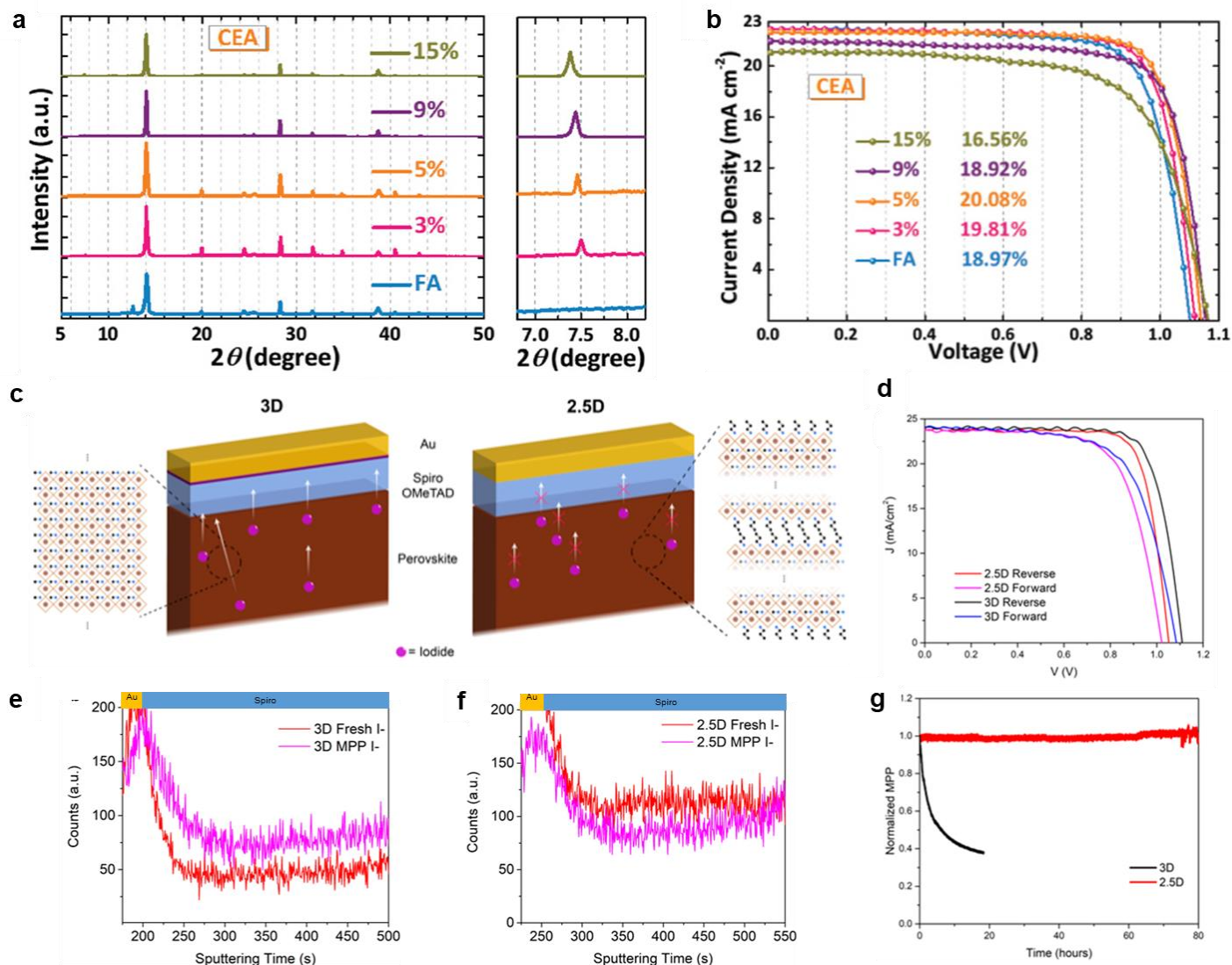


**Figure 25. 3D-2D composite halide perovskites with long chain monoammonium spacer cations.** a) XRD patterns of 3D and 3D-2D composite halide perovskite with different CEA concentrations. Even 3% incorporation leads to formation of low angle peaks corresponding to quasi-2D halide perovskite. b) J-V curves for different concentrations of CEA in 3D-2D composite halide perovskites showing a max PCE = 20.08% for 5% CEA doping. (a-b) reproduced with permission from ref.<sup>544</sup> Copyright 2019 Wiley-VCH. c) Schematic illustrating ion migration in 3D halide perovskite and a suppressed ion migration in 3D-2D composite halide perovskite device during operation. d) J-V curves for 3D and 3D-2D composite halide perovskites with forward and reverse curves showing similar performance metrics. Enlarged TOF-SIMS depth profiles for fresh and aged e) 3D halide perovskite and f) 3D-2D composite halide perovskite, showing reduced migration of Iodine ion through the spiro-OMeTAD layer during MPP operation. g) Stability plot showing MPPT under continuous light illumination under  $\text{N}_2$  atmosphere for 3D and 3D-2D composite halide perovskite solar cells. (c-g) reproduced with permission from ref.<sup>545</sup> Copyright 2019 American Chemical Society.

Conjugation in the spacer cation can improve the charge transport between the organic layers. Double bond and triple bond counterparts of the butylammonium cation (3-buten-1-ammonium ( $\text{BdA}^+$ ) or 3-butyn-1-ammonium ( $\text{BtA}^+$ )) have been used to fabricate quasi-2D ( $n=3,4$ ) solar cells with improved performance. This can be attributed to a

decrease in the molecule size leading to a reduced barrier for charge transport.<sup>546</sup> Huang et al. substituted 5% of the A site cations with allylammonium ( $\text{ALA}^+$ ) cations in  $\text{Cs}_{0.05}\text{FA}_{0.8}\text{MA}_{0.15}\text{PbI}_{2.88}\text{Br}_{0.04}\text{Cl}_{0.08}$  to fabricate a 3D-2D composite ( $n=40$ ) halide perovskite with a 19% PCE (Figure 25d). MPP tracking for 60 hr in inert



conditions resulted in a 20% increase in the  $\text{PbI}_2$ :halide perovskite XRD peak ratio for the control samples but no change for the 3D-2D ALA halide perovskite samples. TOF-SIMS measurements on 60 hr MPP aged devices revealed a 4x effective suppression of Iodine migration in doped samples (**Figure 25 e,f**). Presence of Au-I complexes in the control 3D halide perovskite were further verified by sputtering-XPS, implying Iodine migrates to the Au surface during photo-illumination (**Figure 25c**). The 5% ALA 3D-2D composite halide perovskite devices also retained 100% PCE in 80 hr of MPP whereas the control samples lost about 50% performance in 24 hr (**Figure 25g**).<sup>545</sup>

## 5.2. Zwitterion type spacer cations (bifunctional spacer cations)

halide perovskite solar cell performance and stability depends very strongly on the crystalline morphology of the thin films, 1) the size of the crystalline domains and 2) the compactness (or tightness) of the neighboring halide perovskite grains. Non-compact films can lead to formation of a large density of grain boundaries and pinholes that can act as recombination centers and serve as the starting point of degradation.<sup>379</sup> Long chain zwitterion type molecules (molecules that have a cationic and an anionic end) with ammonium ends can be used for a variety of benefits: 1) These cations can go to the grain boundaries and act as crosslinking anchors between grains, leading to a much more compact film, and 2) their hydrophobic chains can passivate the grain boundaries and top surface to reduce trap assisted recombination, boosting the solar cell performance.  $^1\text{H}$  NMR conducted on a 4% addition of butylphosphonic acid 4-ammonium chloride (4-ABPACl) to  $\text{MAPbI}_3$  revealed strong  $\text{P}-\text{OH}\cdots\text{I}^-$  hydrogen bonding signatures, implying that the phosphonic acid end binds to the Iodine anion in the halide perovskite octahedra.<sup>547</sup> The ammonium ( $-\text{NH}_3^+$ ) group on the other end can occupy the grain boundary vacant A-site, thus crosslinking two neighboring halide perovskite grains (**Figure 26a**). 4APBA- $\text{MAPbI}_3$  deposited on a mesoporous  $\text{TiO}_2$  scaffold also resulted in a more uniform coverage of halide perovskite grains compared to the control samples, as shown by SEM in **Figure 26b**. Solar cells fabricated with 4-ABPA additive improved PCE

from 8.1% to 16.58% with a reduced hysteresis index. Unencapsulated 4ABPA- $\text{MAPbI}_3$  devices lost 28.5% of their performance in 1000 hr when stored in ~55% humidity compared to the control  $\text{MAPbI}_3$  films that completely degraded in 100 hr.

A similar large zwitterion spacer cation salt, 5-Ammonium Valeric acid ( $\text{AVA}^+$ ) iodide, has been used to crosslink halide perovskite octahedral units, improving the crystallinity and passivating the defects in the film.<sup>548-551</sup> Grancini et al. demonstrated 1-year-stable halide perovskite solar cells using the ultra-stable 3D-2D AVAI- $\text{MAPbI}_3$  composite layer. Photoluminescence measured on 3% AVAI- $\text{MAPbI}_3$  films made on  $\text{ZrO}_2$  scaffold revealed that excitation from the oxide side leads to a weak emission from the  $\text{AVA}_2\text{PbI}_4$  ( $n=1$ ) halide perovskite phase, suggesting that the 2D phase can act as a template to grow the 3D halide perovskite. Excitation from the front results in a peak at 760nm while excitation from the back reveals a shoulder at 730nm, suggesting a wider bandgap 3D-2D composite halide perovskite. The AVAI- $\text{MAPbI}_3$  also showed improved charge transfer dynamics, as seen by longer decay curves in TRPL measurements. AVAI- $\text{MAPbI}_3$  solar cells with Spiro-OMETAD hole transport layer retained 60% of their performance in 300 hr under MPP tracking in Ar atmosphere.  $10 \times 10 \text{ cm}^2$  modules fabricated with carbon electrodes produced a PCE of 11.2%, one of the first to be reported in the field (**Figure 26c**).<sup>552</sup> AVAI has recently been used to stabilize the  $\alpha$ - $\text{FAPbI}_3$  halide perovskite. Multinuclear and two-dimensional solid-state NMR revealed that  $\text{AVA}^+$  molecules can form a periodic RP type halide perovskite structure with the  $\text{NH}_3^-$  end hydrogen bonding with the halide perovskite octahedra (vacant A site) and the  $-\text{COOH}$  end dynamically bonding with other  $-\text{COOH}$  species. This crosslinking of halide perovskite grains can stabilize the  $\alpha$ - $\text{FAPbI}_3$  and protect it from converting to the photoinactive  $\delta$ -phase (**Figure 26e**). Transient Absorption also showed a slower decay rate (286ps vs 76ps) in ground-state bleaching. AVAI- $\text{FAPbI}_3$  solar cells achieved a maximum PCE of 18.94% with negligible hysteresis and a 90% performance retention after 300 hr under MPP tracking in  $\text{N}_2$  (**Figure 26d,f**).<sup>553</sup>

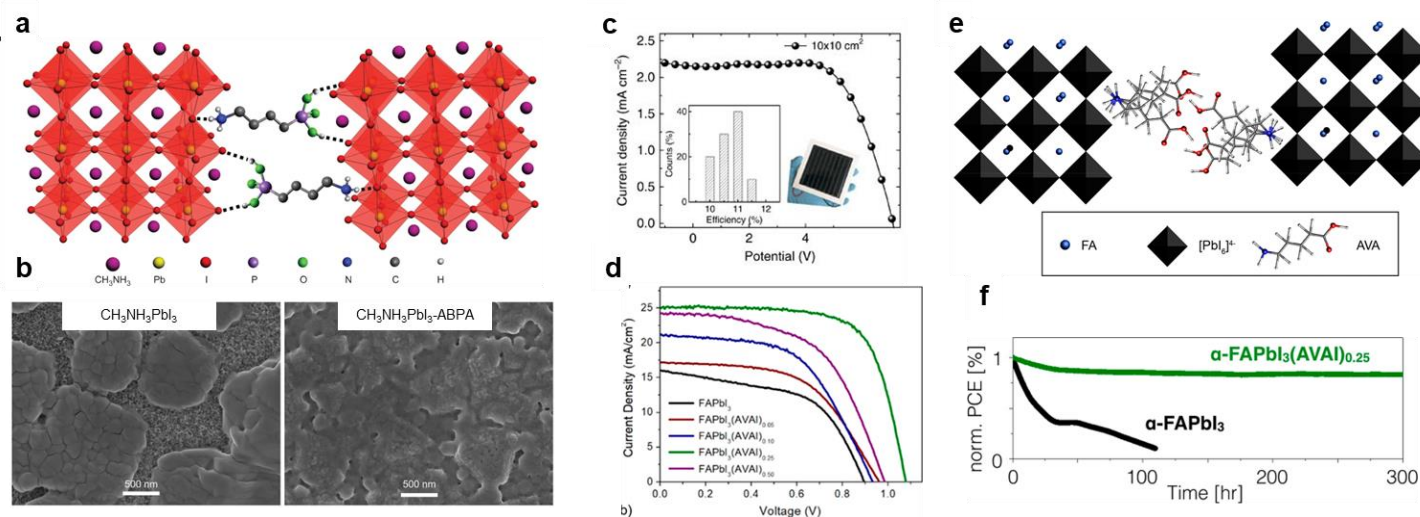


**Figure 26. Long chain zwitterion monoammonium cations.** a) Schematic showing two neighboring perovskite grains crosslinked by butylphosphonic acid 4-ammonium ions. The Phosphonic end can hydrogen bond with the iodine of the  $\text{PbI}_6^{4-}$  ( $\text{O}-\text{H}\dots\text{I}$ ) and the  $\text{NH}_3^+$  end can occupy the vacant A site cation at the grain boundary. b) Surface SEM images showing  $\text{MAPbI}_3$  and  $\text{MAPbI}_3$ -ABPA films deposited on mesoporous  $\text{TiO}_2$  scaffold.  $\text{MAPbI}_3$ -ABPA films show superior coverage due to the crosslinking nature of the ABPA<sup>+</sup> molecules with  $\text{TiO}_2$ . (a-b) reproduced with permission from ref.<sup>547</sup> Copyright 2015 Springer Nature. c) J-V curves for a  $10 \times 10 \text{ cm}^2$  HTM free module with 3% AVAI demonstrating a PCE of 11.2%. Reproduced with permission from ref.<sup>552</sup> Copyright 2017 Springer Nature. d) J-V curves for different concentration of AVAI in FAPbI<sub>3</sub> solar cells. Large concentrations of AVAI molecules (>25%) can hinder charge transport within the lattice due to its large organic framework. e) Proposed model for stabilizing  $\alpha$ -FAPbI<sub>3</sub> using AVAI molecules. The ammonium end can interact with the grain boundary and the COOH side can dynamically create hydrogen bonds with other COOH groups. f) Stability plot showing MPPT with continuous light illumination for AVAI-FAPbI<sub>3</sub> and control samples. (d-f) reproduced with permission from ref.<sup>553</sup> Copyright 2019 American Chemical Society.

Although aliphatic bifunctional cations have been used widely to fabricate quasi-2D and 3D-2D composite halide perovskites with long term durability, their long alkyl chains can hinder charge transport that can limit the FF in solar cells. Hu et al. synthesized a bifunctional aromatic spacer cation, 4-(aminomethyl) benzoic acid hydroiodide (AB), to make HTM-free printable solar cells with 15.6% PCE and improved stability compared to  $\text{MAPbI}_3$  (Figure 27b).<sup>554</sup> Similar to AVAI, -COOH groups in AB can selectively bind to the oxide transport layer, improving the deposition of the halide perovskite in the mesoporous scaffold. DFT calculations also showed that there is a large distance between the HOMO and LUMO orbitals in the AVAI compared to that in AB, which can be a reason why charge transport is hindered in the AVAI molecules (Figure 27a). Conductive AFM measurements at 1.0V bias also revealed a 4x improvement in the AB- $\text{MAPbI}_3$  film conductivity compared to AVAI- $\text{MAPbI}_3$ .

Molecules like DMSO have sulfonyl groups that act as a Lewis base and can form an adduct with the Lewis acid of  $\text{PbI}_2$ . The DMSO: $\text{PbI}_2$  adducts (complex) in the halide perovskite precursor can slow halide perovskite film crystallization during the spin-coating process and increase the average film grain size.<sup>186,187</sup> Zheng et al. discussed the possibility of using a sulfonic zwitterion 3-(decyldimethylammonio)-propane-sulfonate inner salt (DPSI) containing a positive charge ammonium group and a negative charge sulfonic acid group. The S=O group here can donate its lone electron to the empty  $\text{Pb}^{2+}$  orbitals creating a strong complex, that can slow down the crystallization and suppress formation of morphological defects in the film (Figure 27c). Like other zwitterions discussed here, the positively charged  $-\text{NH}_3^+$  group can interact with the A site vacancy in the halide perovskite, whereas the negatively charged sulfonyl group can interact with the iodide vacancy to passivate charged defects. The authors conduct TRPL and TPV to understand

the charge carrier dynamics, revealing that DPSI molecules improve the charge carrier lifetimes by 4-6x compared to the control MAPbI<sub>3</sub>. The authors also demonstrate blade coated FA<sub>0.85</sub>MA<sub>0.15</sub>Pb(Br<sub>0.15</sub>I<sub>0.85</sub>)<sub>3</sub> (0.04% DPSI) 1 cm<sup>2</sup> devices with a PCE of 18.3% (**Figure 27d**) and a T<sub>90</sub> of 480 hr for encapsulated device stability under continuous light illumination.<sup>555</sup> Sulfonyl fluoride functionalization in PEA<sup>+</sup> (SF-PEA<sup>+</sup>) can also work as a bifunctional aromatic spacer cation where the O=S⋯PbI<sub>2</sub> complex can slow down the FAPbI<sub>3</sub> crystallization during thermal annealing.<sup>556</sup> A lower concentration of SF-PEA<sup>+</sup> in FAPbI<sub>3</sub> does not form 3D-2D composites and does not significantly change the optical bandgap of the α-FAPbI<sub>3</sub>. Addition of SF-PEA<sup>+</sup> also showed a sharper absorption edge, suggesting a passivation of shallow defects. SF-PEA<sup>+</sup> additive devices achieved a champion PCE of 21.25% (**Figure 27e**) and the unencapsulated devices retained 91% of their original performance in 1000 hr under ambient storage conditions. The films also demonstrated a 20x improvement in α to δ phase transition protection under 40% RH (**Figure 27f**).

Wide bandgap (WBG) perovskite solar cells use a mixed iodine-bromine X-site anion with 20-40% Br concentration. Under continuous light WBG perovskites can spatially segregate into I-rich and Br-rich regions, leaving halide vacancies at the original sites.<sup>410,557</sup> This happens due to the low activation

energy for halide ion migration (0.1eV) compared to the A site (0.5eV) and B site (0.8eV) cations.<sup>558</sup> Bulk incorporation of large spacer cations can lead to the formation of quasi-2D perovskites at the grain boundaries that can suppress this halide segregation across grains. Spacer cation incorporation can also suppress halide segregation by improving crystallinity and chemical uniformity in the 3D film. Zheng et al. introduced the multifunctional spacer cation salt 4-(2-aminoethyl)-benzenesulfonyl fluoride hydrochloride (ABF) to the precursor solution for a 1.68eV bandgap mixed-halide perovskite. The ABF molecule with terminal groups of fluoro-sulfonate (–SOOF) and ammonium (–NH<sub>3</sub><sup>+</sup>) could bind to the PbI<sub>6</sub> and PbBr<sub>6</sub> octahedra molecules and increase the size of the colloid particles in the precursor solution. The fluoro-sulfonate group was chosen so that the electronegativity of the fluorine could fix perovskite ions in place and the sulfonyl (in addition to the ammonium group) could passivate charged defects, together suppressing the halide segregation process. The linker molecules improved the crystallinity of the perovskite film and homogenized the halide distribution as seen by SEM and PL measurements. p-i-n perovskite solar cells with 1 wt% ABF improved the PCE from 18.7% to 21.8%, and simultaneously increased the T<sub>95</sub> to 1200 hr under ambient air shelf storage and the T<sub>86</sub> to 240 hr under continuous 1-sun illumination.<sup>558</sup>

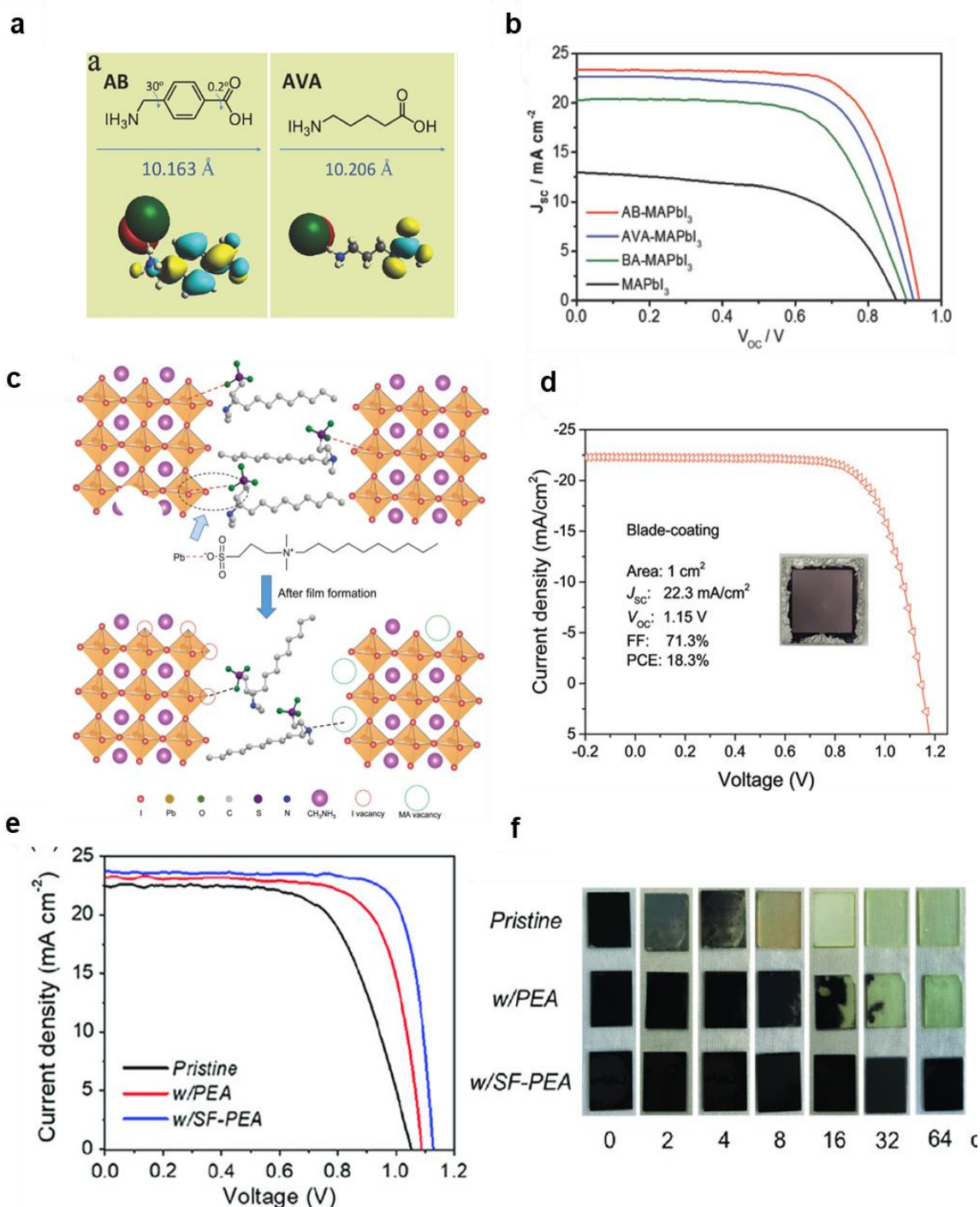


**Figure 27. Functionalized Zwitterion monoammonium cations.** a) The structures of AB<sup>+</sup> and AVA<sup>+</sup> with their molecular length and dihedral angles. The HOMO, LUMO orbitals are shown in red/green and blue/yellow respectively. The HOMO of AB<sup>+</sup> and AVA<sup>+</sup> lies near the -NH<sub>3</sub> group but the LUMO of AB<sup>+</sup> is scattered throughout the molecule while the LUMO of AVA<sup>+</sup> is towards the -COOH group. This spatial arrangement of HOMO/LUMO is proposed to improve the charge transfer in AB<sup>+</sup>. b) J-V curves of champion devices with AB<sup>+</sup>, AVA<sup>+</sup>, BA<sup>+</sup> and no additive. AB-MAPbI<sub>3</sub> exhibits a higher current density and voltage due to its charge transfer capabilities. (a-b) reproduced with permission from ref.<sup>554</sup> Copyright 2018 Wiley-VCH. c) Proposed mechanism of DPSI assisted halide perovskite growth. DPSI initiates uniform crystal growth and then migrates to the grain boundaries to passivate defects through hydrogen bonding of S=O...Pb. d) J-V curve of a blade coated 1cm<sup>2</sup> DPSI-FA<sub>0.85</sub>MA<sub>0.15</sub>Pb(I<sub>0.85</sub>Br<sub>0.15</sub>)<sub>3</sub> solar cell with a PCE of 18.3%. (c-d) reproduced with permission from ref.<sup>555</sup> Copyright 2018 Wiley-VCH. e) J-V curves of champion solar cells with PEA, SF-PEA and no additive. f) Optical images of films with different additives under 40% RH. SF-PEA

improves the stability of the films by almost 20x compared to control films. (e-f) reproduced with permission from ref.<sup>556</sup> Copyright 2020 Wiley-VCH.

### 5.3. Aromatic ring monoammonium spacer cations

Like conjugated alkylammonium spacers, aromatic spacers can be better for charge transport due to charge delocalization across the aromatic rings bridging the  $\text{PbI}_6$  octahedra. The  $\text{PEA}^+$  cation is the most used aromatic spacer cation for 3D-2D composite halide perovskites.  $\text{PEA}^+$  cations can also lower the exciton binding energies in 3D-2D halide perovskites due to their  $\pi$ - $\pi$  interactions with the halide anions. DFT calculations done by Quan et al. revealed that it required 0.36eV more energy to remove the PEAI molecule from the halide perovskite lattice compared to MAI. As seen in **Figure 28a** bottom panel, 3D-2D halide perovskite films ( $\langle n \rangle = 40, 60$ ) exhibit substantially better stability than  $\text{MAPbI}_3$  when stored under 90% relative humidity, while also demonstrating improved overall charge dynamics compared to pure 2D halide perovskites. For lower order ( $\langle n \rangle = 10$ ) halide perovskite films, high bandgap and weak absorption limits the photovoltaic application.  $\text{MAPbI}_3$ -PEAI solar cells retained ~80% of their PCE compared to the control samples that could only retain 20% of their PCE over 8 weeks of  $\text{N}_2$  shelf storage.<sup>485</sup>

PEAI at high concentrations is suggested to grow into crystallite nanoplates between the grains in the halide perovskite films that passivate the pinholes and the grain boundaries, suppressing trap-assisted recombination mechanisms. Long chain  $\text{PEA}^+$  molecules can anchor the halide perovskite grains and prevent moisture ingress through the grain boundaries (**Figure 28b**). However, PEAI at higher concentrations can start accumulating at the grain boundaries and due to the large bandgap of  $n=1$   $\text{PEA}_2\text{PbI}_4$ , the devices with higher PEAI concentration can form a barrier for charge transport at the grain boundaries and exhibit a worse performance than the control devices. Lee et al. conducted KPFM measurements to understand the effect of PEAI concentration with halide perovskite crystal film morphology and its electrical properties. At 1-4.5% PEAI concentration, there is an increasing trend in contact potential difference between the grain boundary and the grain interior, which is a

result of reduced carrier recombination. 4.5% PEAI- $(\text{FAPbI}_3)_{0.85}(\text{MAPbBr}_3)_{0.15}$  devices showed an improved open circuit voltage of 1.10 but due to the excess PEAI, the current decreased to  $17\text{mA cm}^{-2}$ . PEAI doped devices retained >50% performance while the control device completely died in 1200 hr of 70%RH storage (**Figure 28d**). Zhu et al. added 0.1 mol/L PEAI (7 mol%) into  $\text{FA}_{0.95}\text{Cs}_{0.05}\text{PbI}_3$  and observed discrete Bragg spots with a higher scattering intensity for peaks in the out-of-plane direction. Although there are no separate 2D phase PL emission peaks for 7mol% PEA-FACs, the intensity of the peak increases by almost one order of magnitude, indicating a longer lifetime of charge carriers due to reduced recombination at grain boundaries. Champion devices yielded a PCE of 20.34% and the devices retained 85.5% of their initial performance in 200 hr under 85% humidity storage (**Figure 28c**).

Lee et al. optimized the PEAI concentration to 1.67 mol% in  $\text{FAPbI}_3$  to demonstrate solar cells with a stabilized PCE of 20.64% with an impressive open circuit voltage of 1.13V. At low concentrations of the 2D  $\text{PEA}_2\text{PbI}_4$  halide perovskite, there is a small shift in the XRD peak positions indicating a compressive strain that suppresses the formation of the  $\text{FAPbI}_3$   $\delta$ -phase (**Figure 28e**). Conductive AFM under ambient light conditions and a 100mV bias showed a higher current flow at the grain boundaries for the PEA- $\text{FAPbI}_3$  films, which may suggest a better charge separation and transport across the grain boundaries. Due to the high potential barrier created by the 2D  $\text{PEA}_2\text{PbI}_4$  for the holes, charge recombination is reduced, leading to a superior device performance from 16.4% to 21.06% PCE. The encapsulated 3D-2D devices also perform better than the 3D controls under continuous light illumination and humidity (**Figure 28f**). Wang et al. also used a low concentration of the PEAI additive in  $\text{CsPbI}_3$  precursor solution to the form 3D-2D composite halide perovskite (large  $\langle n \rangle$ ), stabilizing the  $\gamma$ - $\text{CsPbI}_3$  phase. Although the  $\langle n \rangle = 40$  stoichiometry devices (13.65%) perform worse than the control  $\text{CsPbI}_3$  (15.3%), unencapsulated 3D-2D composite

halide perovskite film solar cells retained 89% of their PCE in 12 days under 30% humidity.<sup>559</sup>

Silicon used as the narrow-bandgap bottom layer in Si-perovskite tandem cells requires texturing to achieve high performance, which complicates the deposition of conformal perovskite layers on top of it. Depositing high-quality WBG perovskite films with long carrier diffusion lengths on textured silicon is critical to achieve high-efficiency tandem solar cells. Yang et al. added tribromide salts of tetrabutylammonium (TBA<sup>+</sup>) and trimethylphenylammonium (TPA<sup>+</sup>) in the precursor formulation of the WBG perovskite and blade coated 1 $\mu$ m thick perovskite films with a PCE of 21.9% and a small open-circuit V<sub>OC</sub> deficit of 0.4V.<sup>560</sup> The Br<sub>3</sub><sup>-</sup> molecule was shown to occupy the halide vacancy site and the two terminal Br ions could suppress the formation of iodide vacancies. 0.2mol% of TPABr<sub>3</sub> in Cs<sub>0.1</sub>FA<sub>0.2</sub>MA<sub>0.7</sub>Pb(I<sub>0.85</sub>Br<sub>0.15</sub>)<sub>3</sub> (E<sub>g</sub>~1.65eV) improved the film morphology for thick perovskite films and reduced non-radiative recombination losses. While these cations do not form a 2D perovskite in the bulk of the film, the bulky spacer cations can anchor grains and thus create a barrier for halide segregation.

HuO et al. added bromide salts of phenylammonium (PhA), phenmethylammonium (PMA) and phenethylammonium (PEA) into a 1.74eV WBG perovskite precursor to study their role in passivating defects and suppressing halide segregation.<sup>561</sup> Control films had a PL peak at 710nm with a

shoulder at 740nm, indicating an Iodine-rich region. Films doped with 0.5mol% PMABr suppressed halide segregation with an improved carrier lifetime that yielded devices with a PCE of 17.3% and a V<sub>OC</sub> of 1.19V. Ye et al. partially replaced PEA<sup>+</sup> based n=1 with a fluorine-doped PEA<sup>+</sup> (F5PEA) based n=1 perovskite and observed a 5x improvement in the out-of-plane charge transport and a 3x improvement in the in-plane charge transport for the 2D perovskite. When the authors added F5PEA<sup>+</sup>-PEA<sup>+</sup> n=1 to a 1.68eV WBP 3D perovskite, the resulting film showed a longer charge carrier lifetime, a reduced trap density and an improved conductivity. Adding 0.75% F5PEA<sup>+</sup>-PEA<sup>+</sup> 2D n=1 in the precursor solution led to devices with a 21.1% PCE and an enhanced unencapsulated shelf stability (T<sub>83</sub>~720 hr) in 45-60% RH.<sup>562</sup>

Kim et al. used a co-additive of PEA(I<sub>0.25</sub>SCN<sub>0.75</sub>) in a 1.68eV WBG perovskite precursor solution to form mixed 2D-3D composite perovskite solar cells. TEM images showed the formation of 2D n=1 perovskite at the grain boundaries of the 3D perovskite. The 2D n=1 perovskite passivated the grain boundaries and defects, improving the V<sub>OC</sub> for the devices. Transient photoconductivity measurements showed a more uniform distribution of photocurrent through intragrain regions for the PEA(I<sub>0.25</sub>SCN<sub>0.75</sub>) compared to a control PEAI additive, improving the device performance from 17.5% to 20.7% and achieving a T<sub>80</sub> of 1000 hr under continuous light illumination.<sup>563</sup>



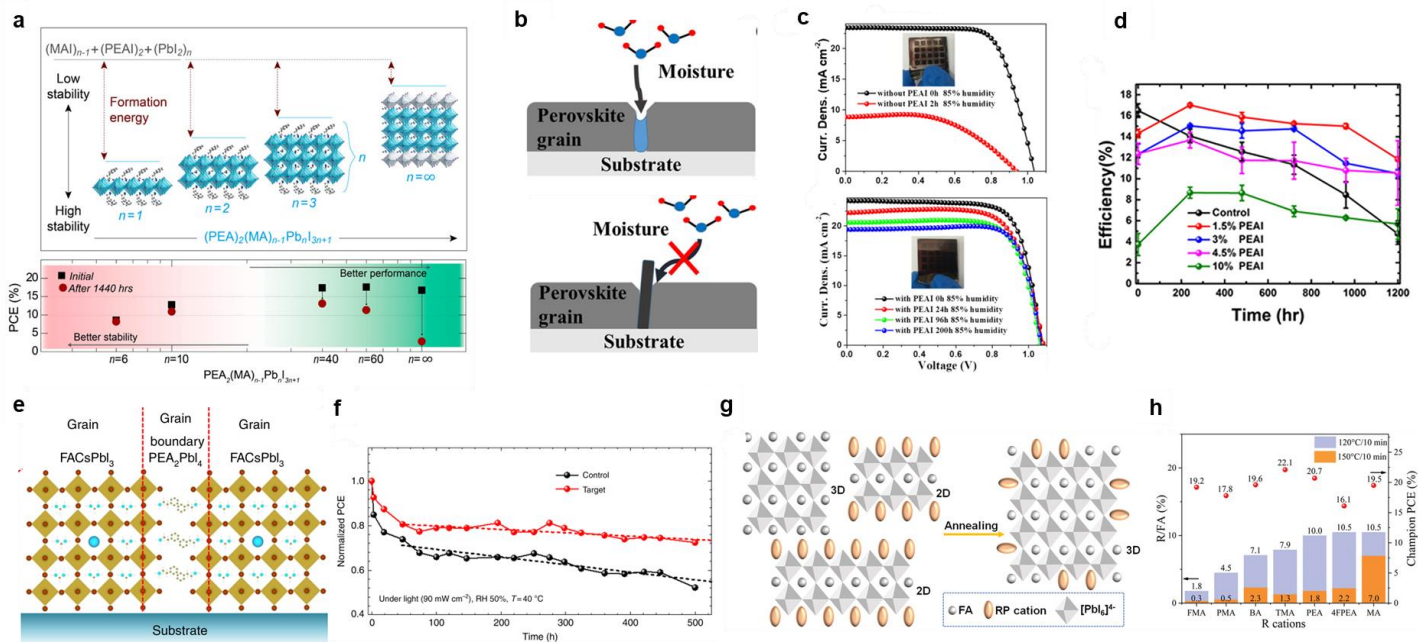


**Figure 28.** a) Formation energy comparison and relative stability of different  $n$  values of  $\text{PEA}_2\text{MA}_{n-1}\text{Pb}_n\text{I}_{3n+1}$ . While low  $n$  perovskites have better stability, they lack the performance of 3D counterparts. Stoichiometry for  $\langle n \rangle = 60$  yields 3D-2D perovskites with optimum performance and stability. Reproduced with permission from ref.<sup>485</sup> Copyright 2016 American Chemical Society. b) Schematic illustration of PEA molecules passivating the 3D halide perovskite grain boundaries, protecting the films from moisture degradation. c) J-V curves of 3D and 3D-2D halide perovskite devices at different times during an 85% humidity stability test. 3D halide perovskite PCE halved in 2 hr while 3D-2D halide perovskite retained 85% of its original PCE. (b-c) reproduced with permission from ref.<sup>564</sup> Copyright 2018 American Chemical Society. d) Average efficiency of 4 unencapsulated devices with different concentration of PEA, stored in 70% RH in dark for 1200 hr. While the PEA devices retained >50% of their initial efficiency, the control samples degraded almost completely. Reproduced with permission from ref.<sup>565</sup> Copyright 2018 American Chemical Society. e) Schematic illustration showing the proposed stabilization method of FA based 3D halide perovskite with  $\text{PEA}_2\text{PbI}_4$  incorporating at the grain boundaries. f) Device stability plot for encapsulated control and PEA-FAPbI<sub>3</sub> devices under 0.9 sun illumination and 50% RH. (e-f) reproduced with permission from ref.<sup>566</sup> Copyright 2018 Springer Nature. g) Schematic illustration of interaction of 3D and 2D halide perovskite in the solution and the volatilization of the spacer cations during annealing to stabilize the  $\alpha$ -FAPbI<sub>3</sub> phase. h) The ratio  $R/\text{FA}$  denotes the relative amount of cation left in the films after annealing at 120 (blue) and 150 deg (orange). The red circle shows the champion PCE obtained from the respective spacer cation. (g-h) reproduced with permission from ref.<sup>567</sup> Copyright 2022 Wiley-VCH.

Sn based perovskites suffer from the oxidation of the  $\text{Sn}^{2+}$  to  $\text{Sn}^{4+}$  and this reaction can be initiated at the perovskite grain boundaries that generally have a high concentration of vacancies. Although  $\text{SnF}_2$  is commonly used as a reducing agent to suppress Sn oxidation, excess amounts of  $\text{SnF}_2$  can form aggregates in the film and act as recombination centers.<sup>568</sup> As discussed above, PEA can be used to passivate the grain boundaries and it can be a potential way to stabilize the Sn based perovskites.<sup>569</sup> Shao et al. successfully introduced 0.08M of PEA based 2D halide perovskite into  $\text{FASnI}_3$ , fabricating a near-single-crystalline  $\text{FASnI}_3$

films with a PCE of 9.0% in p-i-n architecture.<sup>570</sup> 3D-2D composite films show Bragg spots for the (h00) planes in GIWAXS measurements indicating a preferential crystallization that is beneficial to charge transport (**Figure 29**). TRPL measurements also reveal a higher charge carrier lifetime for the 3D-2D composite films (6.29 ns) compared to the control films (4.32 ns), suggesting a lower trap density due to improved crystallization and reduced number of grain boundaries. 3D-2D composite devices also retained 59% of their original PCE in 76 hr of unencapsulated air exposure.



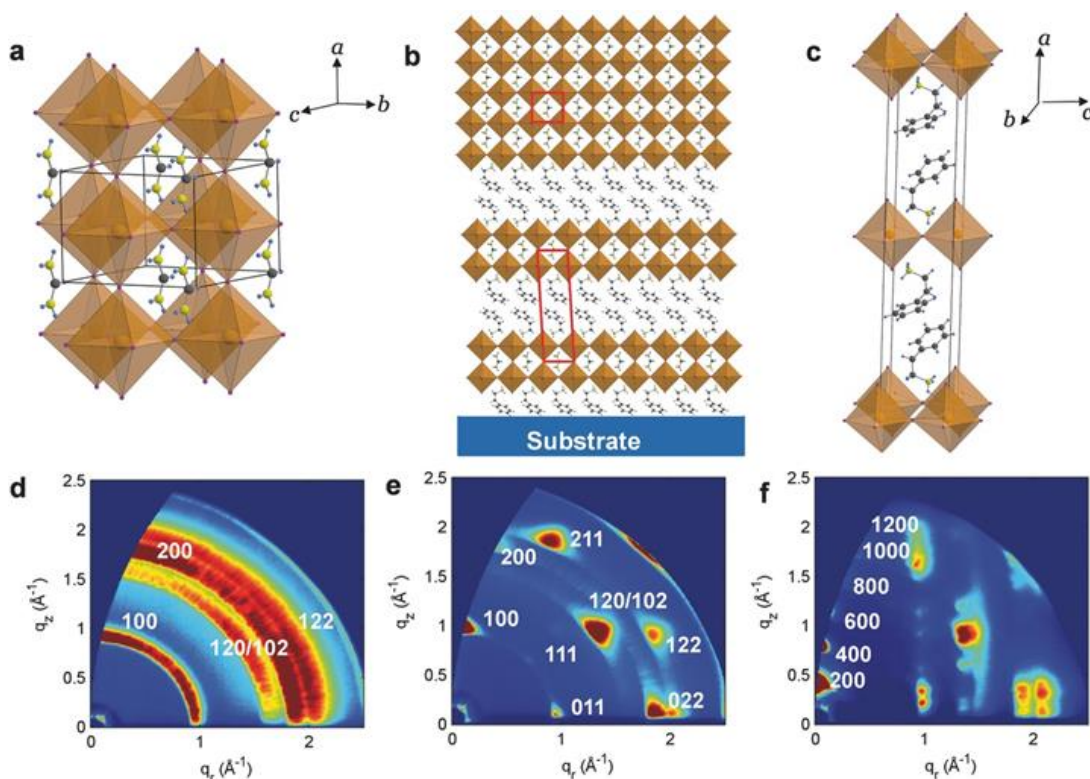


**Figure 29.** Schematic representation of a) 3D FASnI<sub>3</sub>, b) 3D-2D composite FASnI<sub>3</sub> and, c) 2D PEA<sub>2</sub>PbI<sub>4</sub> halide perovskite crystal structures. GIWAXS plots of d) 3D FASnI<sub>3</sub>, e) 3D-2D composite FASnI<sub>3</sub> and, f) 2D PEA<sub>2</sub>PbI<sub>4</sub> halide perovskite crystal structures. GIWAXS image for 3D-FASnI<sub>3</sub> shows Debye-Scherrer like rings which is indicative of a random orientation in the film. Adding PEA in FASnI<sub>3</sub> leads to a preferred crystallization of the (h00) peak, evident by the Bragg spot like features of (100) and (200) planes. This is also observed in the 2D PEA<sub>2</sub>PbI<sub>4</sub> halide perovskite XRD. Reproduced with permission from ref.<sup>570</sup> Copyright 2017 Wiley-VCH.

Liang et al. conducted a systematic study of using different RP cations to stabilize the  $\alpha$ -FAPbI<sub>3</sub> halide perovskite phase. MACl is a widely used additive to stabilize  $\alpha$ -FAPbI<sub>3</sub> and although it is claimed that majority of the MACl volatilized from the film during the annealing process, the residual MA cations in the film can catalyze degradation due to their hygroscopic nature. The authors compared several types of RP cations including BA<sup>+</sup>, PEA<sup>+</sup>, PMA<sup>+</sup>, 4FPEA<sup>+</sup>, FMA<sup>+</sup>, and TMA<sup>+</sup> with MACl as additives in the FAPbI<sub>3</sub> precursor. Formation of the 2D halide perovskite in the film can be observed initially but annealing at higher temperatures usually led to volatilization of the 2D spacer cations. Photoluminescence measurements with front and back side illumination verified the presence of quasi-2D ( $\langle n \rangle = 1-5$ ) halide perovskite signature that disappeared after annealing at 150°C. <sup>1</sup>H NMR measurements revealed that TMA volatilized faster

than MA and the ratio of TMA/FA (1.3%) is much lower than MA/FA (7.0%) (**Figure 28h**). The residual cations left in the film (0.3-2.3%) can get inserted between the grain boundaries and anchor the grains (**Figure 28g**). Additionally, the sulfur ion in TMA binds with the Pb to passivate the iodine vacancy sites, reducing defect assisted recombination. n-i-p devices made with TMA cations demonstrated a PCE of 22.1% with 2.3% hysteresis index and retained 93% of their PCE in 1440 hr during shelf storage in 25% RH.<sup>567</sup>

One of the challenges with MA based halide perovskites is the risk of volatilization of MA cations at higher temperature. As discussed in section V.(i), replacing the C-H bond in the organic spacer cation with C-F can induce strong hydrogen bonding interactions between the cage cations (MA, FA) and spacer cation, that can suppress the A site cation volatilization to give a better thermal stability.

Addition of low surface energy molecules like 4-(trifluoromethyl) benzylammonium (4TFBZA<sup>+</sup>) in MAPbI<sub>3</sub> can lead to a top-down growth of 3D-2D composite ( $n > 20$ ) halide perovskites, with a surface passivation layer of low dimensional 2D halide perovskite. EDS mapping on the surface of  $n = 20, 40, 60, 80$  and 3D-MAPbI<sub>3</sub> films showed a progressive decrease of fluorine atom concentration on the surface as the value of  $n$  is increased. Due to the strong hydrogen bonding character of fluorine in 4TFBZA<sup>+</sup> with the -NH<sub>3</sub> group of the MA cation, 4TFBZA based  $n = 60$  films were much more stable compared to the Benzylammonium (BZA<sup>+</sup>) based  $n = 60$  and 3D-MAPbI<sub>3</sub> films (**Figure 30a**). Unencapsulated devices with 4TFBZA kept 84% of its initial performance of 17% PCE in 1000 hr, while the 3D-MAPbI<sub>3</sub> dropped to 5% of its initial PCE. This may be due to the high hydrophobic character of the 4TFBZA spacer cation that will effectively block any moisture from interacting with the halide perovskite underneath.<sup>571</sup>

Other fluorophenyl molecules like FPEABr have also been used to fabricate stable 3D-2D Sn halide perovskite microstructures. Yu et al. substituted FAI with FPEABr, that can induce growth of 2D halide perovskite phase near the grain boundaries and the surface, creating a local reducing environment to suppress the oxidation of Sn<sup>2+</sup> to Sn<sup>4+</sup>.<sup>572</sup> They conducted GIWAXS measurements to confirm the presence of 2D halide perovskite for different concentrations of FPEABr in 3D-2D composite halide perovskites. Angle dependent GIWAXS and cross-section EDX maps also revealed a uniform distribution of the 2D phase in the bulk of the 3D halide perovskite. The authors fabricated p-i-n devices with a certified PCE of 14.03% and a T<sub>80</sub> of 432 hr in N<sub>2</sub> storage conditions. A similar approach was used Wang et al. by introducing different ratios of phenylhydrazine hydrochloride (PHCl) into FASnI<sub>3</sub> to fabricate p-i-n solar cells with 11.4% PCE and a T<sub>90</sub> of 120 h under MPP in inert atmosphere.<sup>573</sup> The reducing behavior of hydrazine group and the hydrophobic phenyl group help in self-repairing the Sn<sup>4+</sup> to Sn<sup>2+</sup> while simultaneously passivating the defects in the film.

Similar to PEA, naphthalene-based aromatic spacer cations have also been used to synthesize

2D halide perovskites. Strong  $\pi$ - $\pi$  interactions between 1-naphthyl-methylammonium (NMA<sup>+</sup>) molecules can facilitate the formation of RP type 2D halide perovskites, that have been used for solar cells and LEDs.<sup>317,574</sup> This conjugated structure also enhances charge transport in the out-of-plane direction, improving conductivity in the halide perovskites. Changing NMA concentration in MAPbI<sub>3</sub> can lead to different  $n = 20, 40, 60$  3D-2D composite halide perovskites with improved crystallinity and excellent thermal stability. At high NMA concentrations XRD shows a new Bragg peak at 6.1 deg for higher NMA concentrations, indicating formation of  $n < 10$  quasi-2D halide perovskites.  $n = 40, 60$  3D-2D composite films kept under 85°C in inert atmosphere revealed a substantial reduction in crack and pinhole formation compared to 3D-MAPbI<sub>3</sub> (**Figure 30b**). This may indicate that the NMA cations can affect the crystal growth in the film and make more compact defect-free films. ATR-FTIR spectroscopy measurements were done to monitor the relative change in vibrational modes of C-H, C-N, and N-H bonds before and after the thermal ageing measurements.  $n = 40, 60$  3D-2D composite halide perovskites showed relatively lower change in C-N stretching mode compared to 3D-MAPbI<sub>3</sub>, suggesting that the large aromatic NMA molecules can effectively prevent the diffusion of MA ions. This passivation strategy also led to a reduction in trap-assisted recombination, improving the charge carrier lifetimes, evident in TRPL measurements.  $n = 40, 60$  3D-2D halide perovskite solar cells also retained better performance compared to the 3D-MAPbI<sub>3</sub> solar cells after 360 hr of 85°C thermal ageing.<sup>575</sup>

Even small concentrations of NMA can improve the crystallinity of the halide perovskite film without forming 3D-2D composite halide perovskites. At lower concentrations, the NMA spacer cations (0-1 vol%) are incorporated into the grain boundaries or near the surface, passivating the defects and pinholes in the film. XPS measurements conducted by Lin et al. revealed a significant increase in C-C intensity in the NMA-MAPbI<sub>3</sub> films, implying the presence of NMA on the surface. They also performed Low Energy Ion Scattering (LEIS) measurements, in which the surface is bombarded with very low energy ions and the backscattered ion signature is collected. LEIS measurements also

showed a 40% decrease in the Pb and I backscattered peaks in NMA-MAPbI<sub>3</sub>, implying the presence of a capping layer on top of the halide perovskite surface (**Figure 30c**). NMA at grain boundaries can suppress nonradiative recombination by suppressing charge trapping in defects, as shown in photoluminescence measurements, but excess NMA (>0.025%) can start to hinder charge transport causing a reduction in the J<sub>sc</sub> and FF.<sup>576</sup>

Yang et al. proposed a self-assembled bottom-up crystallization of 3D-2D composite halide perovskites with 3-bromobenzylammonium iodide (3-BBAI) as the organic spacer cation. 3-BBAI facilitated the growth of low-n 2D halide perovskite

( $n < 3$ ) with a preferred out of plane crystallization (**Figure 30d Schematic**). This low dimensional 2D halide perovskite then templates the growth of large-n halide perovskites with improved crystallinity and a smooth film surface (**Figure 30d GIWAXS**). Compared to BAI, 3-BBAI additive can improve the charge transport in the devices due to its conjugated structure, as seen in solar cell performance. 3-BBAI 3D-2D halide perovskite devices retained 82% of their initial performance after 2400 hr under a 40% humidity. Due to suppressed recombination, the 3-BBAI halide perovskite device was also operated as a LED with a EQE of 3.85% and demonstrated a device stability of 96 hr at 200 mA cm<sup>-2</sup>.<sup>556,564,565,577</sup>

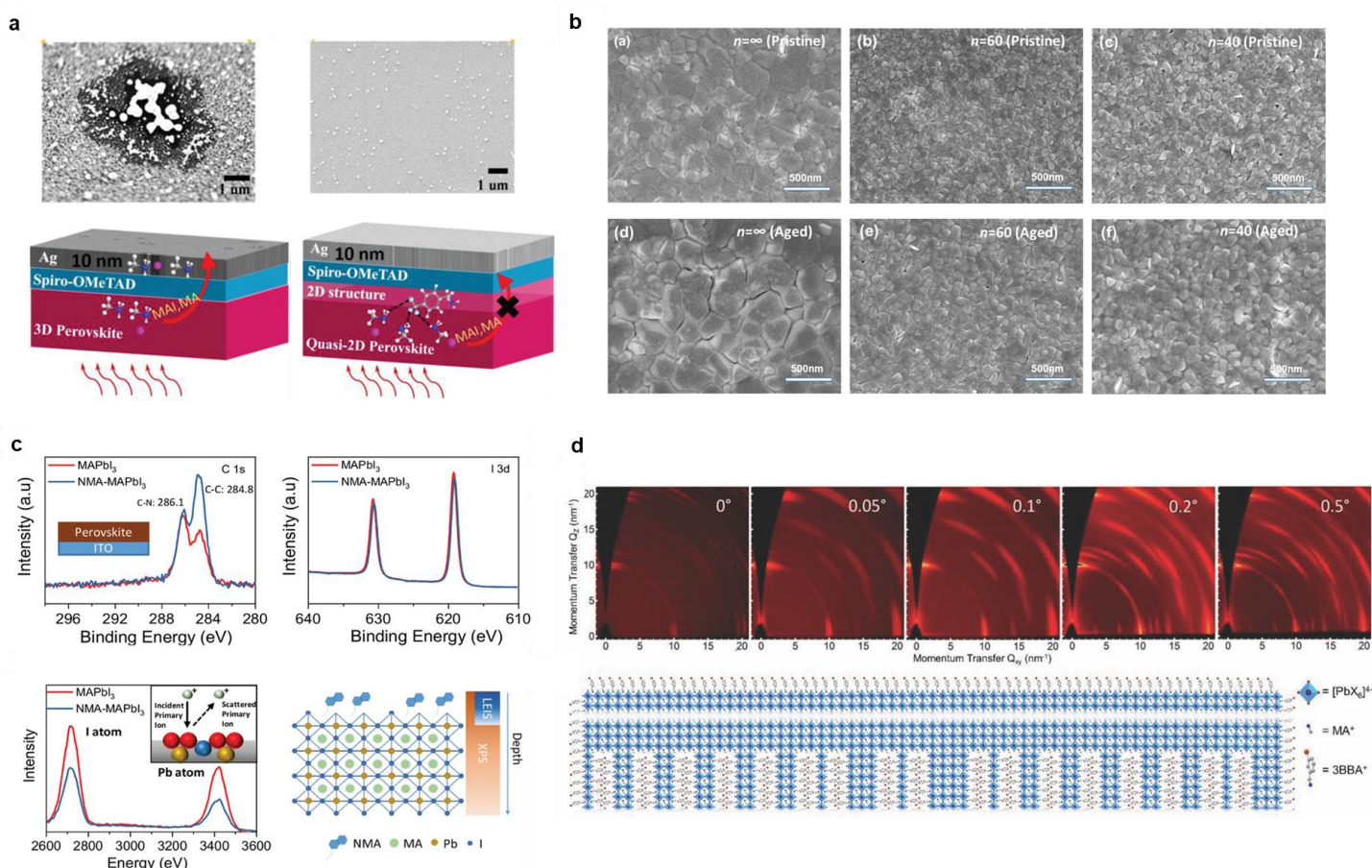


**Figure 30.** a) SEM images of the top surface of the (3D halide perovskite or 3D-2D halide perovskite) | Spiro-OMeTAD | Ag films kept at 85°C in N<sub>2</sub> atmosphere for 8 days. Corresponding schematic illustrations depict the suppression of MA volatilization in presence of 4TFBZA. Reproduced with permission from ref.<sup>571</sup> Copyright 2021 Wiley-VCH. b) SEM images of before/after thermal ageing at 85°C for 4 hr for different concentration of NMA in MAPbI<sub>3</sub>. Control MAPbI<sub>3</sub> films show grain boundary widening and formation of new pinholes under thermal ageing. 3D-2D halide perovskite with  $\langle n \rangle = 40, 60$  stoichiometry show much better thermal stability due to the strong bonding character of NMA that prevents the degradation of halide perovskite crystal structure. Reproduced with permission from ref.<sup>575</sup> Copyright 2020 Springer Nature. c) XPS spectra of C 1s (top left) and I 3d (top right) showing presence of NMA (through C 1s signal increase in NMA-MAPbI<sub>3</sub>). Bottom

right: Schematic showing the probing sensitivity of Low energy ion scattering (LEIS) and XPS on the perovskite surface. Bottom left: LEIS spectra of 3D and 3D-2D halide perovskite. The drop in the LEIS intensity of Pb and I suggests that the bulky molecules may have created a layer on the top surface. Reproduced with permission from ref.<sup>576</sup> Copyright 2019 Wiley-VCH. d) GIWAXS plots at 5 different incident angles for 3-BBAI templated 3D-2D composite halide perovskites. While lower incident angles (surface) do not show any quasi-2D halide perovskite peaks, higher incident angles (deeper into bulk), there are small Bragg peaks at low  $q^{-1}$  values, indicating the presence of 2D peaks. Bottom: Proposed Schematic illustrating the self-assembly of 3D-2D composite halide perovskites. Reproduced with permission from ref.<sup>577</sup> Copyright 2018 Wiley-VCH.

#### 5.4. Diammonium spacer cations

Similar to bifunctional cations with -NH and -COOH ends, diammonium ( $H_3N-R-NH_3$ ) spacer cations can also facilitate large grain formation and defect passivation. The -NH<sub>3</sub> ends can serve the dual purpose of forming bonds with the uncoordinated Pb ions and occupying the A site cations at the grain boundaries. These bonds can thus simultaneously anchor the grains and the long alkyl chain can create a hydrophobic passivation layer. Lu et al. studied the effect of incorporating C2, C3 and C6 chain diammonium spacer cations in MAPbI<sub>3</sub> film morphology and device performance. Although addition of ethanediammonium cations (EDA<sup>2+</sup>) do not induce the formation of 3D-2D composites, the spacer cation acts as a grain boundary anchor, creating much compact halide perovskite films with smaller grain sizes (**Figure 31a**). Longer chain spacers (C3, C6) do not improve the film morphology considerably and may induce the formation of uncontrolled 3D-2D halide perovskite structures at larger concentrations, which may hinder the charge transport. Champion devices made with 0.8mol% EDA-MAPbI<sub>3</sub> achieved a PCE of 18.6% (**Figure 31b**). Encapsulated devices retained 75% of original performance in 72 hr under MPP conditions in 50°C and 50% RH (**Figure 31c**).<sup>578</sup>

Wu et al. bulk-incorporated a diammonium spacer cation 1,3-diaminopropane (DAP<sup>2+</sup>) in MAPbI<sub>3</sub> to achieve a PCE of 21.5% (**Figure 31e**) with a record open circuit voltage deficit of 0.35V.<sup>579</sup> Although addition of DAP<sup>2+</sup> in MAPbI<sub>3</sub> decreases the grain size to 100-300nm from 300-500nm, the films have a lower RMS of 24.9nm from 31.1nm and improved resistance to mechanical stress. DAP<sup>2+</sup> also improved the adhesion between the hole

transport layer and the halide perovskite, reducing the chance of film delamination due to thermal and mechanical stressors. DAP<sup>2+</sup> also passivates the grain boundaries as corroborated by an improved PL lifetime of 689ns for DAP-MAPbI<sub>3</sub>, 2.5 times higher than the control MAPbI<sub>3</sub> (278ns) (**Figure 31d**). Reduced recombination is also evident by light-intensity-dependent  $V_{OC}$  measurements that showed an ideality factor of 1.43 for DAP-MAPbI<sub>3</sub> compared to 2.72 of MAPbI<sub>3</sub>. Devices made with DAP-MAPbI<sub>3</sub> displayed a  $T_{90}$  of 1000 hr in ambient shelf storage conditions (50% humidity) without encapsulation, demonstrating the moisture barrier properties of the bilateral alkylamines (**Figure 31f**).

The bilateral cations can also be used to stabilize all inorganic halide perovskites like CsPbI<sub>3</sub>. CsPbI<sub>3</sub> has a bandgap of 1.73eV, which is ideal for many perovskite-perovskite tandem photovoltaics. Unfortunately, the  $\alpha$ -CsPbI<sub>3</sub> is structurally unstable and reverts to the photo-inactive  $\delta$ -CsPbI<sub>3</sub> under ambient conditions.<sup>580</sup> Zhao et al were successful in stabilizing the  $\alpha$ -CsPbI<sub>3</sub> at room temperature by incorporating ethylenediammonium cations (EyDA<sup>2+</sup>) in CsPbI<sub>3</sub>. The terminal -NH<sub>3</sub><sup>+</sup> can cross link the CsPbI<sub>3</sub> grains, reducing the grain size but creating more compact (pinhole free) films. Layered (110) 2D EDA<sub>2</sub>PbI<sub>4</sub> can act as an interface to template the CsPbI<sub>3</sub> crystallites, thus creating the anchors in the grain boundaries. The reduced density of pinholes also suggests a suppression of non-radiative recombination, as seen by improved PL lifetimes. A 0.025 mole ratio of EDA<sub>2</sub>PbI<sub>4</sub> mixed with CsPbI<sub>3</sub> resulted in the best PV devices with a PCE of 11.8% (**Figure 31g**) and a dry-box shelf stability of over a month (**Figure 31h**).<sup>581</sup>



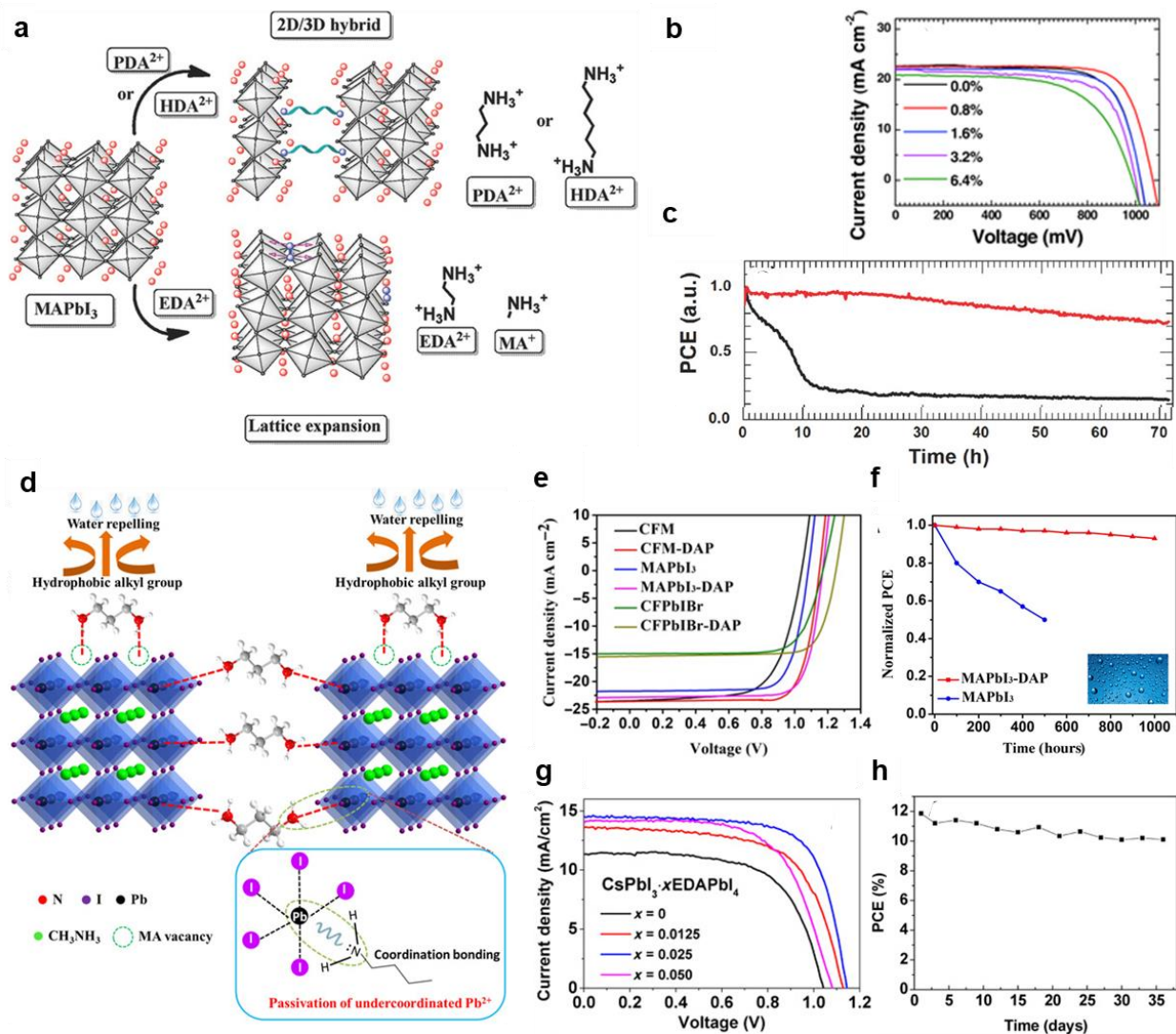


**Figure 31.** a) Possible structures of MAPbI<sub>3</sub> with spacer cations of different lengths and ammonium centers. Smaller spacer cations can get intercalated into the 3D lattice and expand it, while the larger cations will create 3D-2D composite structures. b) J-V curves of 3D-2D halide perovskite devices with different concentrations of EDA. c) PCE evolution with time for MAPbI<sub>3</sub> and 3D-2D halide perovskite (EDA = 0.008) tested under 1 sun irradiation, at 50 °C and RH 50%. (a-c) reproduced with permission from ref.<sup>578</sup> Copyright 2017 Wiley-VCH. d) Schematic illustration of diammonium cation incorporation into the 3D halide perovskite to anchor the grains and passivate defects. e) J-V curves of different 3D halide perovskite with DAP. f) Stability plot of unencapsulated solar cells stored under 50% RH. (d-f) reproduced with permission from ref.<sup>579</sup> Copyright 2019 American Association for the Advancement of Science. g) J-V curves of CsPbI<sub>3</sub> solar cells with different ethylenediammonium cation concentration. h) Stability plot of an unencapsulated device stored in a dry box for over one month. (g-h) reproduced with permission from ref.<sup>581</sup> Copyright 2017 American Association for the Advancement of Science.

## 5.5. ACI-type spacer cations

As discussed in earlier sections, the Goldschmidt tolerance factor decides if a perovskite structure is possible or not for a combination of A and X site ions. Guanidinium (GA, ionic radius  $\sim 278\text{pm}$ )<sup>582</sup> is just large enough to not be incorporated into a perovskite lattice by itself, but when incorporated with  $\text{MAPbI}_3$ , it can lead to a lattice expansion, that can weaken the Pb-I bond overlap and increase the bandgap of the resulting perovskite (**Figure 32a**). Jodlowski et al. substituted GA for MA cations in  $\text{MAPbI}_3$  to make  $\text{GA}_x\text{MA}_{1-x}\text{PbI}_2$  and noticed a gradual increase in the lattice parameter  $a$  from  $8.838\text{\AA}$  to  $8.902\text{\AA}$  while a constant  $c$  at  $12.625\text{\AA}$ , suggesting the incorporation of a larger molecule stretching the tetragonal  $\text{MAPbI}_3$  structure (**Figure 32a**)<sup>583</sup>. 14% GA incorporation yielded solar cells with a champion PCE of 20.15% (**Figure 32b**) and a  $T_{60}\sim 1100$  hr under MPP tracking in Ar atmosphere (**Figure 32c**). Gao et al. also studied the incorporation limits of GA in  $\text{MAPbI}_3$  to form  $\text{GA}_x\text{MA}_{1-x}\text{PbI}_3$ <sup>584</sup>. Single crystal Xray diffraction revealed that the Pb-I bond is elongated at 5,10% GA doping (**Figure 32d**). At higher concentrations ( $>24\%$ ), ACI type 2D perovskite Bragg peaks appear near  $2\theta = 14$  deg. They notice a gradual but nominal increase in the bandgap with GA addition, with an improvement in PL lifetimes from  $154.4\text{ns}$  to  $266.3\text{ns}$ , suggesting a suppression of nonradiative recombination. Devices with 5.26% GA incorporation led to a PCE of 20.38% and an improved

unencapsulated device shelf stability  $T_{90}$  of 900 hr (**Figure 32e**). Wu et al. added GA to  $\text{Cs}_{0.1}(\text{FA}_{0.83}\text{MA}_{0.17})_{0.9}\text{Pb}(\text{I}_{0.83}\text{Br}_{0.17})_3$  and achieved a high  $V_{\text{OC}}$  of 1.19 yielding a PCE of 21.1% (**Figure 32g**)<sup>585</sup>. They attributed the increase of  $V_{\text{OC}}$  to a reduction of defects in the film leading to a much sharper Urbach tail and a remarkable PL lifetime of  $2.66\mu\text{s}$ . They also see a small shift in the Valence and the conduction band levels, aligning the transport layers better for charge transport (**Figure 32f**).

Wang et al. made a semitransparent  $\text{FA}_{0.8}\text{Cs}_{0.2}\text{Pb}(\text{I}_{0.6}\text{Br}_{0.4})_3$  ( $E_g\sim 1.77$  eV) perovskite film for an all-perovskite tandem cell and observed a poor fill factor and  $V_{\text{OC}}$ , which they attributed to deep level traps caused by regions of high Br concentration that increased nonradiative recombination.<sup>586</sup> To avoid the lattice distortion caused by larger cations like  $\text{PEA}^+$ , they incorporated Guanidine tetrafluoroborate ( $\text{GuaBF}_4$ ) which proved more effective in suppressing halide vacancy defect formation and ion migration.  $\text{BF}_4^-$  anions have been used by several groups in the past to fill I<sup>-</sup> vacancies, exploiting their similar ionic radii ( $\text{I}^- = 220\text{pm}$ ,  $\text{BF}_4^- = 218\text{pm}$ ).<sup>587,588</sup> With an optimized  $\text{GuaBF}_4$  doping concentration of 1.5 mol% (with respect to  $\text{Pb}^{2+}$ ), the champion device showed a PCE of 17.3% compared to the control PCE of 15.8%. Encapsulated tandem devices made with  $\text{GuaBF}_4$  doped WBG perovskite retained 100% of their PCE after 600h of continuous light illumination with MPP tracking.

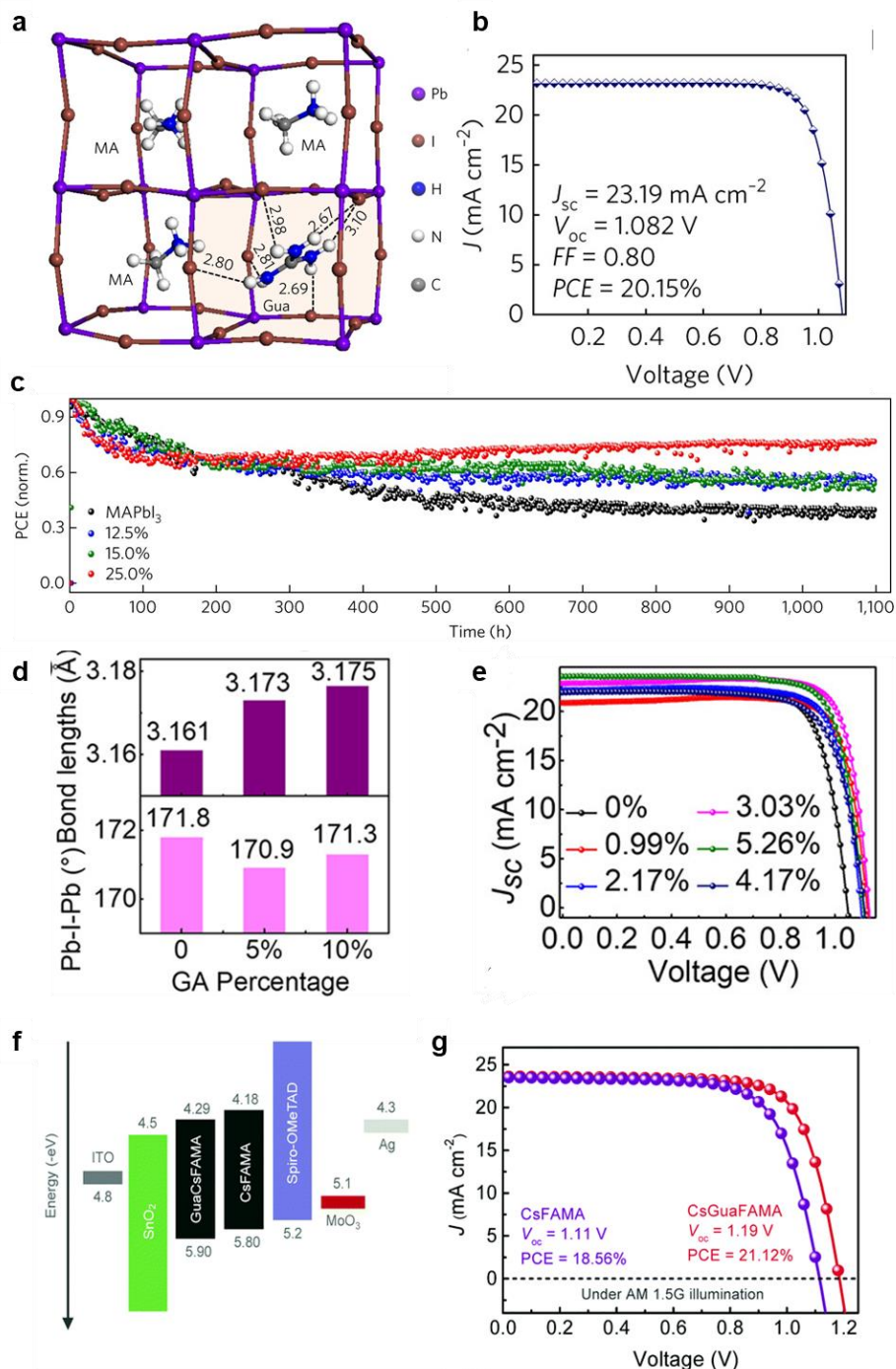


**Figure 32.** a) Simulated structure of  $\text{Ma}_{0.75}\text{Ga}_{0.25}\text{PbI}_3$  where the GA cation can intercalate into the 3D-MAPbI<sub>3</sub> lattice, thereby expanding it. Higher concentration of GA leads to a separation of a quasi-2D perovskite that can hinder charge transport. b) J-V curve of the champion solar cell, exhibiting a high  $V_{\text{oc}}$  of 1.082V. c) Improved solar cell stability of GA doped MAPbI<sub>3</sub> under continuous light illumination MPPT and 60°C in inert atmosphere. (a-c) reproduced with permission from ref.<sup>583</sup> Copyright 2017 Springer Nature. d) Increase in the Pb-I bond length with change in GA suggests that the lattice is expanding and therefore leading to a decreased overlap of Pb-I orbitals, thus decreasing the bond angle. e) Solar cell device performance for different concentrations of GA incorporated inside MAPbI<sub>3</sub>. (d-e) reproduced with permission from ref.<sup>584</sup> Copyright 2020 American Chemical Society. f) Band-edge positions of GA-CsFAMA and CsFAMA halide perovskite with respect to the different hole and electron transport layers in a device stack. A slight shift in the CBM may improve the electron transfer to the SnO<sub>2</sub> in GA-CsFAMA. g) J-V curves of CsFAMA and GA-



CsFAMA under AM1.5G illumination, showing a high  $V_{oc}$  of 1.19V from the GA-CsFAMA device. (f-g) reproduced with permission from ref.<sup>585</sup> Copyright 2019 Royal Society of Chemistry.

**Table 13: 3D-2D composite halide perovskite solar cells with long chain monoammonium cations**

| A' cation  | 3D halide perovskite                                     | V <sub>oc</sub> (V) | J <sub>sc</sub> (mA/cm <sup>2</sup> ) | FF (%) | PCE (%) | Stability (hr)         | Conditions   | Ref |
|--|--|---------------------|---------------------------------------|--------|---------|------------------------|--|-----|
| BAPb(I <sub>0.8</sub> Br <sub>0.2</sub> ) <sub>3</sub> precursor | FACsPb(I <sub>0.8</sub> Br <sub>0.2</sub> ) <sub>3</sub> | 1.14                | 22.7                                  | 80     | 20.6    | T <sub>80</sub> = 1005 | Unencapsulated (~45% RH, air), AM1.5G, 0.76 suns, OC, periodic J-V               | 540 |
| Propylammonium   | CsFAMA   | 1.06                | 21.9                                  | 74.4   | 17.3    | T <sub>50</sub> =2000  | Unencapsulated (45% RH, air), Dark, OC, periodic J-V                             | 589 |
| Propylammonium   | CsFAMA   | 1.13                | 22.6                                  | 78     | 20.25   | T <sub>97</sub> = 600  | Unencapsulated (~15-45% RH, air), Dark, OC, periodic J-V                         | 542 |
| Propylammonium   | FASnI <sub>3</sub>                                       | 0.73                | 22.8                                  | 72     | 11.8    | T <sub>95</sub> ~ 1000 | Encapsulated (in N <sub>2</sub> ), MPP tracking in continuous 1-sun illumination | 590 |
| 2-chloroethylammonium  | FACsPbI <sub>3</sub>                                     | 1.1                 | 22.7                                  | 79.9   | 20.1    | T <sub>92</sub> = 2400 | Unencapsulated (~15-45% RH, air), Dark, OC, periodic J-V                         | 544 |
| Tetrabutylammonium   | FAMAPbIBr <sub>3</sub>                                   | 1.12                | 23.41                                 | 76.9   | 20.1    | T <sub>95</sub> ~ 700  | Unencapsulated (N <sub>2</sub> ), Dark, OC, periodic J-V                         | 591 |
| Allylammonium  | CsFAMA   | 1.05                | 23.9                                  | 79     | 19.1    | T <sub>99</sub> = 80   | Unencapsulated (N <sub>2</sub> ), MPP tracking in continuous light illumination  | 545 |
| Oleylammonium  | CsFAMA   | 1.17                | 24.1                                  | 81.6   | 23      | T <sub>99</sub> ~ 1000 | Encapsulated (N <sub>2</sub> ), MPP tracking in continuous 1-sun illumination    | 541 |
| Hexaneammonium   | FA <sub>x</sub> MA <sub>1-x</sub> PbI <sub>3</sub>       | 1.18                | 24.91                                 | 81.8   | 24.07   | T <sub>81</sub> = 288  | Unencapsulated (N <sub>2</sub> ), 1 sun illumination, OC, periodic J-V           | 592 |

**Table 14: 3D-2D composite halide perovskite solar cells with zwitterion monoammonium cations**

| A' cation                       | 3D halide perovskite | V <sub>oc</sub> (V) | J <sub>sc</sub> (mA/cm <sup>2</sup> ) | FF (%) | PCE (%) | Stability (hr)         | Conditions   | Ref |
|---------------------------------|----------------------|---------------------|---------------------------------------|--------|---------|------------------------|--|-----|
| Butylphosphonic acid 4-ammonium | MAPbI <sub>3</sub>   | 1                   | 22.11                                 | 75     | 16.58   | T <sub>72</sub> =1000  | Unencapsulated (~55% RH, air), Dark, OC, periodic J-V measurement under AM 1.5G, 0.1 sun | 547 |
| 5-aminovaleric acid             | FAPbI <sub>3</sub>   | 1.08                | 25.1                                  | 0.7    | 18.94   | T <sub>90</sub> =300   | Unencapsulated (N <sub>2</sub> ), MPP tracking in continuous 1-sun illumination          | 553 |
| 5-aminovaleric acid             | MAPbI <sub>3</sub>   | 1.025               | 18.84                                 | 75.5   | 14.6    | T <sub>60</sub> =300   | Unencapsulated (Ar), MPP tracking in continuous 1-sun illumination                       | 552 |
| 5-aminovaleric acid             | MAPbI <sub>3</sub>   | 0.85                | 22.7                                  | 66     | 12.9    | T <sub>99</sub> ~ 1000 | Unencapsulated (Ar), MPP tracking  | 550 |

|   |                                  |      |       |      |       |                        |   |     |
|---|----------------------------------|------|-------|------|-------|------------------------|---|-----|
|   |                                  |      |       |      |       |                        | in continuous 1-sun illumination                                    |     |
| 5-aminovaleric acid                                   | MAPbI <sub>3</sub>               | 0.85 | 22.8  | 66   | 12.85 | T <sub>99</sub> ~ 1000 | Unencapsulated (air), MPP tracking in continuous 1-sun illumination | 551 |
| 4-(aminomethyl) benzoic acid hydroiodide              | MAPbI <sub>3</sub>               | 0.94 | 23.4  | 0.71 | 15.6  | T <sub>90</sub> =100   | MPP tracking in continuous 1-sun illumination                       | 554 |
| 3-(decyldimethylammonio)-propane-sulfonate inner salt | FAMAPb(I Br) <sub>3</sub>        | 1.13 | 23.3  | 80   | 21.1  | T <sub>88</sub> =480   | Encapsulated (air), MPP tracking in continuous 1-sun illumination   | 555 |
| Sulfonyl-Phenylethylammonium                          | FAPbI <sub>3</sub>               | 1.12 | 23.7  | 79.6 | 21.25 | T <sub>91</sub> = 1000 | Unencapsulated (~50% RH, air), Dark, OC, periodic J-V               | 556 |
| 4-(2-aminoethyl)-benzenesulfonyl fluoride             | Mixed-cation I-Br (Wide-Bandgap) | 1.18 | 22.56 | 81.8 | 21.8  | T <sub>93</sub> = 1200 | Unencapsulated (~35% RH, air), Dark, OC, periodic J-V               | 558 |

**Table 15: 3D-2D composite halide perovskite solar cells with aromatic monoammonium cations**

| A' cation                    | 3D halide perovskite                   | V <sub>oc</sub> (V) | J <sub>sc</sub> (mA/cm <sup>2</sup> ) | FF (%) | PCE (%) | Stability (hr)         | Conditions  | Ref |
|------------------------------|--|---------------------|---------------------------------------|--------|---------|------------------------|---|-----|
| Phenylethylammonium          | MAPbI <sub>3</sub>                     | 1.095               | 19                                    | 73.7   | 15.3    | T <sub>80</sub> ~ 1400 | Unencapsulated (N <sub>2</sub> ), Dark, OC, periodic J-V      | 485 |
| Phenylethylammonium          | FAPbI <sub>3</sub>                     | 1.12                | 24.4                                  | 76.5   | 21.06   | T <sub>70</sub> = 500  | Encapsulated (45% RH, air), AM 1.5G 0.9 sun, OC, periodic J-V | 566 |
| Phenylethylammonium          | FAPbI <sub>3</sub> -MAPbI <sub>3</sub> | 1.07                | 21.7                                  | 74.2   | 17.2    | T <sub>83</sub> = 1200 | Unencapsulated (~15-45% RH, air), Dark, OC, periodic J-V      | 565 |
| Phenylethylammonium          | CsPbI <sub>3</sub>                     | 0.993               | 19.5                                  | 70.46  | 13.65   | T <sub>89</sub> ~ 300  | Unencapsulated (~30% RH, air), Dark, OC, periodic J-V         | 559 |
| Phenylethylammonium          | FACsPbI <sub>3</sub>                   | 1.07                | 24.66                                 | 77     | 20.34   | T <sub>85</sub> = 200  | Unencapsulated (~85% RH, air), Dark, OC, periodic J-V         | 564 |
| Phenylethylammonium          | FASnI <sub>3</sub>                     | 0.61                | 22.1                                  | 70     | 9.41    | T <sub>90</sub> ~ 600  | Unencapsulated (N <sub>2</sub> ), Dark, OC, periodic J-V      | 569 |
| Phenylethylammonium          | FASnI <sub>3</sub>                     | 0.525               | 24.1                                  | 71     | 9       | T <sub>59</sub> ~ 76   | Unencapsulated (~15% RH, air), OC, periodic J-V under AM 1.5G | 593 |
| 3-phenyl-2-propen-1-ammonium | FASnI <sub>3</sub>                     | 0.56                | 23.34                                 | 73.3   | 9.61    | T <sub>92</sub> ~ 1440 | Unencapsulated (N <sub>2</sub> ), Dark, OC, periodic J-V      | 594 |
| 2-Thiophenemethylammonium    | FAPbI <sub>3</sub>                     | 1.13                | 24.43                                 | 80     | 22.1    | T <sub>93</sub> = 1440 | Unencapsulated (~25% RH, air), Dark, OC, periodic J-V         | 567 |

Accepted manuscript

|   |   |      |       |       |       |                        |   |     |
|---|---|------|-------|-------|-------|------------------------|---|-----|
| 4-(trifluoromethyl) benzylammonium                    | MAPbI <sub>3</sub>  | 1.1  | 21.66 | 71.42 | 17.07 | T <sub>84</sub> = 1000 | Unencapsulated (N <sub>2</sub> ), Dark, OC, periodic J-V                        | 571 |
| 4-fluoro-phenethylammonium                            | FASnI <sub>3</sub>  | 0.82 | 25.15 | 71.6  | 14.79 | T <sub>80</sub> ~ 432  | Encapsulated (N <sub>2</sub> ), Dark, OC, periodic J-V                          | 572 |
| phenylhydrazine hydrochloride                         | FASnI <sub>3</sub>  | 0.76 | 23.5  | 64    | 11.4  | T <sub>98</sub> ~ 110  | Unencapsulated (N <sub>2</sub> ), MPP tracking in continuous 1-sun illumination | 573 |
| 1-naphthylmethylammonium                              | MAPbI <sub>3</sub>  | 1.03 | 20.9  | 78.2  | 16.9  | T <sub>70</sub> = 360  | Encapsulated (85°C), OC, periodic J-V   | 575 |
| 1-naphthylmethylammonium                              | MAPbI <sub>3</sub>  | 1.15 | 21.1  | 80    | 19.3  | N/A                    | N/A   | 576 |
| 3-bromobenzylammonium                                 | MAPbI <sub>3</sub>  | 1.23 | 18.2  | 81.2  | 18.2  | T <sub>82</sub> = 2400 | Unencapsulated (~40% RH, air), Dark, OC, periodic J-V                           | 577 |
| trimethylphenylammonium tribromide                    | CsFAMA  | 1.23 | 21.2  | 83.8  | 21.9  | T <sub>90</sub> ~500   | Encapsulated, MPP tracking in continuous 1-sun illumination                     | 560 |
| F5PEA <sup>+</sup> -PEA <sup>+</sup> 2D n=1 precursor | CsFAMA  | 1.19 | 21.65 | 81.5  | 21.1  | T <sub>83</sub> ~ 720  | Unencapsulated (~60% RH, air), Dark, OC, periodic J-V                           | 562 |
| phenmethylammonium bromide                            | FA <sub>0.75</sub> MA <sub>0.15</sub> Cs <sub>0.1</sub> PbI <sub>2</sub> Br                                     | 1.19 | 18.69 | 78.2  | 17.3  | T <sub>90</sub> ~ 24   | Unencapsulated (N <sub>2</sub> ), MPP tracking in continuous 1-sun illumination | 561 |
| PEA(I <sub>0.25</sub> SCN <sub>0.75</sub> )           | (FA <sub>0.65</sub> MA <sub>0.2</sub> Cs <sub>0.15</sub> )Pb(I <sub>0.8</sub> Br <sub>0.2</sub> ) <sub>3</sub>  | 1.21 | 21.0  | 81.4  | 20.7  | T <sub>80</sub> = 1000 | Unencapsulated (N <sub>2</sub> ), periodic J-V in continuous 1-sun illumination | 563 |
| PEAI + PEASCN   | (FA <sub>0.65</sub> MA <sub>0.20</sub> Cs <sub>0.15</sub> )Pb(I <sub>0.8</sub> Br <sub>0.2</sub> ) <sub>3</sub> | 1.17 | 21.2  | 79.8  | 19.8  | T <sub>96</sub> ~ 4000 | Encapsulated (N <sub>2</sub> ), Dark, OC, periodic J-V                          | 595 |
| Benzylammonium  | FAPbI <sub>3</sub>  | 1.1  | 25    | 73    | 20.2  | T <sub>85</sub> = 140  | Unencapsulated (N <sub>2</sub> ), MPP tracking in continuous 1-sun illumination | 596 |

**Table 16: 3D-2D composite halide perovskite solar cells with Diammonium spacer cations**

| A' cation          | 3D halide perovskite | V <sub>oc</sub> (V) | J <sub>sc</sub> (mA/cm <sup>2</sup> ) | FF (%) | PCE (%) | Stability (hr)         | Conditions  | Ref |
|--------------------|----------------------|---------------------|---------------------------------------|--------|---------|------------------------|---|-----|
| Ethanediammonium   | MAPbI <sub>3</sub>   | 1.07                | 22.6                                  | 0.77   | 18.6    | T <sub>75</sub> ~ 72   | Encapsulated (50% RH in air), MPP tracking in continuous 1-sun illumination, 50°C | 578 |
| Ethylenediammonium | CsPbI <sub>3</sub>   | 1.15                | 14.5                                  | 71     | 11.86   | T <sub>85</sub> ~ 700  | Unencapsulated (N <sub>2</sub> ), Dark, OC, periodic J-V                          | 581 |
| 1,3-diaminopropane | MAPbI <sub>3</sub>   | 1.18                | 22.5                                  | 81.7   | 21.7    | T <sub>90</sub> ~ 1000 | Unencapsulated (~50% RH, air),  | 579 |

Table 17: 3D-2D composite halide perovskite solar cells with ACI type cations

| A' cation                   | 3D halide perovskite   | V <sub>oc</sub> (V) | J <sub>sc</sub> (mA/cm <sup>2</sup> ) | FF (%) | PCE (%) | Stability (hr)         | Conditions  | Ref |
|-----------------------------|--|---------------------|---------------------------------------|--------|---------|------------------------|---|-----|
| Guanidinium                 | MAPbI <sub>3</sub>   | 1.028               | 23.1                                  | 80     | 20.15   | T <sub>60</sub> ~ 1100 | Unencapsulated (N <sub>2</sub> ), MPP tracking in continuous 1-sun illumination | 583 |
| Guanidinium                 | MAPbI <sub>3</sub>   | 1.11                | 23.55                                 | 0.78   | 20.38   | T <sub>90</sub> = 900  | Unencapsulated (~15% RH, air), OC, periodic J-V under AM 1.5G                   | 584 |
| Guanidinium                 | CsFAMA   | 1.19                | 23.66                                 | 75     | 21.12   | N/A                    | N/A   | 585 |
| Guanidine tetrafluoroborate | FA <sub>0.8</sub> Cs <sub>0.2</sub> Pb(I <sub>0.6</sub> Br <sub>0.4</sub> ) <sub>3</sub> | 1.265               | 16.7                                  | 81.9   | 17.3    | T <sub>100</sub> = 600 | Encapsulated, MPP tracking in continuous 1-sun illumination                     | 586 |
| Ammonium tetrafluoroborate  | MAPbI <sub>3</sub>   | 1.15                | 23.38                                 | 75     | 20.16   | T <sub>86</sub> = 300  | Periodic J-V in continuous 1-sun illumination                                   | 587 |

## 6. Capping 3D halide perovskite with 2D halide perovskite

### 6.1. Processing methods for capped 3D-2D halide perovskites

#### 6.1.1. Interdiffusion method

3D-2D bilayer stacks (thick 2D) and passivation layers (thin 2D) are commonly made through the in-situ growth of a 2D halide perovskite layer on top of a 3D halide perovskite thin film. Halide salts of bulky alkyl chain or aromatic cations with one (RP) or two (DJ) ammonia groups (e.g., BAI, PEAI) are dissolved in isopropyl alcohol (IPA),<sup>597-600</sup> chloroform,<sup>229</sup> tetrahydrofuran (THF),<sup>601</sup> or chlorobenzene (CBZ)<sup>602,603</sup> and dripped on a 3D halide perovskite layer where they react with the excess or unreacted  $\text{PbI}_2$  near the surface of the 3D halide perovskite to form a 2D halide perovskite layer. Various thicknesses of the 2D halide perovskite layer on the 3D halide perovskite can be achieved by varying the concentration of the organic spacer cation in the respective solvents.

A 2D layer can be introduced either through dip-coating or spin-coating. Using the dip coating process, the already fabricated 3D halide perovskite is dipped inside a solution of IPA containing dissolved organic spacer cation to synthesize a 2D capping layer.<sup>604,605</sup> In the spin-coating process the spacer cation solution is dynamically spin-coated onto the surface of the 3D film. A schematic diagram depicting the in-situ growth of the 2D halide perovskite film on the 3D underlying layer using the spin coating and dip coating technique is shown in **Figure 33a**. In some cases when the 3D halide perovskite film does not have excess lead iodide, a flash annealing technique can be utilized to remove the organic component from the surface of the 3D film. In this process the 3D halide perovskite film is exposed to a high temperature of 300°C for less than 10 s. In the case of  $\text{MAPbI}_3$  films MAI is released from the surface leaving excess  $\text{PbI}_2$  which can react with a deposited A' cation to form a 2D phase at the interface.<sup>606</sup>

In some cases, a mixture of the AX and A'X or A'X<sub>2</sub> precursor salts results in the formation of higher n-value 2D or a 3D/quasi-2D halide perovskite heterostructure. There are some attempts where a mixture of bulky organic cation salts (BAI or PEAI) and small organic cation salts (MAI or FAI) with different stoichiometric ratios are first dissolved in

IPA followed by spin coating on the 3D halide perovskite layer to form a higher-n quasi 2D halide perovskite, for example  $\text{BA}_2\text{FA}_{n-1}\text{Pb}_n\text{I}_{3n+1}$  from BAI and FAI,<sup>607</sup> or  $\text{PEA}_2\text{FA}_{n-1}\text{Pb}_n\text{I}_{3n+1}$  (n=1-2) from PEAI and FAI.<sup>608</sup>

#### 6.1.2. Antisolvent method

Antisolvents (such as CB, ether, ethyl acetate, and toluene) are conventionally used in halide perovskite solution processing to precipitate a homogeneous film of a halide perovskite-Lewis base adduct complex and form a high-quality 3D or 2D halide perovskite thin film.<sup>609</sup> The in-situ 2D halide perovskite growth method can be combined with the antisolvent growth process by using the antisolvent as a solvent for the A'X or A'X<sub>2</sub> spacer cation salt (**Figure 33b**). The antisolvent containing the organic spacer cation is dropped onto the spinning substrate with a wet 3D halide perovskite precursor solution. After spin-coating, the films are annealed which results in the 1-step formation of 3D and 2D halide perovskite layers together. Bai et al. used this approach with a toluene antisolvent and a PEAI A' cation salt to fabricate a 3D/2D bilayer structure.<sup>610</sup> The presence of the 2D layer was verified by a ToF-SIMS depth profile which showed an increase in the A' cation concentration at the surface.<sup>610</sup>

#### 6.1.3. Vapor based method

It is logical to believe that the aforementioned solution processing techniques for growing a 2D halide perovskite layer might affect the underlying 3D halide perovskite layer. In addition these solvent processes could also result in diffusion of the organic cation within the grain boundaries, and do not give control over the distribution of the 2D layer on the underlying 3D.<sup>540,597</sup> As a result, researchers have sometimes resorted to vapor-based techniques to deposit 2D layers on top of 3D halide perovskites. A general approach to obtain a 3D/2D bilayer structure using vapor-based techniques involves exposing the 3D halide perovskite film to an A' organoamine gas. An organoamine liquid or solid is heated and the vapors are directed to the surface of a 3D film.<sup>611,612</sup> Chen et al., fabricated a 3D/2D bilayer by exposing the 3D halide perovskite to the vapors from

volatilizing butylamine liquid inside a sealed chamber.<sup>611</sup> On the other hand, Xu et al., fabricated the full 3D/2D structure using vapor based techniques.<sup>612</sup> They evaporated  $\text{PbI}_2$  onto a  $\text{TiO}_2$  ETL in a thermal evaporator followed by the evaporation of MAI in a vacuum oven at a temperature of  $180^\circ\text{C}$  for 30 minutes for full conversion of the  $\text{PbI}_2$  to  $\text{MAPbI}_3$ . Following this the 3D halide perovskite layer was exposed to BAI vapors in a vacuum oven at  $120^\circ\text{C}$  for a period of 5 to 60 min to form a capping layer of 2D halide perovskite. It was observed that the coverage and the conversion of the 2D halide perovskite was fully controlled by the time of exposure to the organoamine vapors. In another experiment, Bolink et al. fabricated a 3D film through the coevaporation of MAI and  $\text{PbI}_2$  in a thermal evaporator, and added a 2D layer through the co-evaporation of PEAI and  $\text{PbI}_2$  (**Figure 33c**).<sup>613</sup> One of the advantages of using a thermal evaporator is that the evaporation rate and the thickness of the layers can be measured simultaneously with the help of a quartz crystal. This technique also allows for the fabrication of complex multilayer structures (e.g., 2D/3D/2D) with clean interfaces.<sup>613</sup>

There have been several attempts to fabricate high-efficiency 3D halide perovskite solar cells with enhanced stability using a 2D capping layer. However, solution processing techniques for 3D-2D stacks or passivation layers leads to the formation of unintended quasi-2D phases which can negatively impact charge extraction. These techniques form a heterogeneous 2D phase distribution with the presence of lower n-value 2D halide perovskites ( $n < 3$ ) which not only have a Type I band alignment with the 3D halide perovskite but also hinder the charge transport and carrier extraction because of the preferential in-plane orientation, hence limiting the 2D layer thickness to less than 5-10 nm in a PV device for tunneling to occur. Recent work has focused on growing both vertically-oriented and phase-pure 2D halide perovskite layers on top of the 3D halide perovskite which can eliminate the deleterious effects of a 2D layer and achieve synergistic effects for simultaneously improved efficiency and stability<sup>221,241</sup>.

#### **6.1.4. Solid phase in-plane growth**

In an attempt to obtain a high purity 2D halide perovskite with arbitrary thickness on top of the 3D halide perovskite layer, Jang et al, devised a solid-state in-plane growth (SIG) method in which a combination of pressure and temperature was applied to a physically-contacted stack of a 3D film and a 2D  $n=1$  film (**Figure 33d**).<sup>221</sup> With this technique they were able to grow a phase-pure  $\text{BA}_2\text{PbI}_4$  ( $n=1$ ) 2D halide perovskite layer on top of the 3D layer without any unintended phases, and obtained arbitrary thicknesses (up to 80 nm) by controlling the time of growth. By controlling the thickness of the 2D capping layer, they were able to tune the built-in potential at the junction, hence obtaining an optimized solar cell performance. A huge increase in the stability was also observed with the presence of an intact phase-pure 2D halide perovskite layer on top of the 3D film. In spite of all these advantages, the SIG technique requires a precise control of temperature and pressure to grow the 2D capping layer which is difficult to scale for commercialization. As a result, there is a need for a simple solution processing technique which could grow any arbitrary phase of 2D halide perovskites with arbitrary thickness on the 3D film to take the full advantage of the 2D halide perovskites not only in passivation but also for absorption and charge transport with appropriate band alignments.

#### **6.1.5. Solvent selective technique for solution processed phase-pure 2D halide perovskites**

Recently, our group developed a design principle utilizing the basic solvent characteristics of dielectric constant ( $\epsilon_r$ ) and Gutmann donor number ( $D_N$ ) to control the coordination between the precursor ions and the solvent for fabricating a fully solution-processed 3D-2D stack with arbitrary film thickness and high phase purity of 2D halide perovskite (**Figure 33e**).<sup>241</sup> We found that the solvents with  $\epsilon_r > 30$  and  $5 < D_N < 18$  kcal/mol, such as acetonitrile (MeCN), tetramethyl sulfone, propylene carbonate, and ethylene carbonate, can effectively dissolve the RP 2D halide perovskite without dissolving the underlying 3D layer. Considering the low boiling point of the MeCN, it was selected to fabricate the 3D/2D bilayer stack at low temperature. We were also able to control the thickness of the 2D layer



from sub-10nm to sub- $\mu\text{m}$  scales by changing the concentration of the 2D precursor solution. The phase purity of the 3D/2D bilayer stack was confirmed using XRD, optical absorbance, and PL. The 2D halide perovskite with high n-value ( $n = 3$ ) achieved a near-perfect type II energy-level alignment, benefiting hole transport and collection. Furthermore, we demonstrated an n-i-p solar cell (FTO/SnO<sub>2</sub>/3D/2D [n=3] halide perovskite/spiro-OMeTAD/Au) with an optimized thickness of 2D halide perovskite (50-60 nm) and a champion PCE of 24.5%. After 2,000 h of continuous illumination, the devices with 2D/3D halide perovskite as light absorber showed negligible degradation with T99 > 2,000 h, much better than those of the 3D based PSCs and traditional 2D-passivated 3D PSCs.

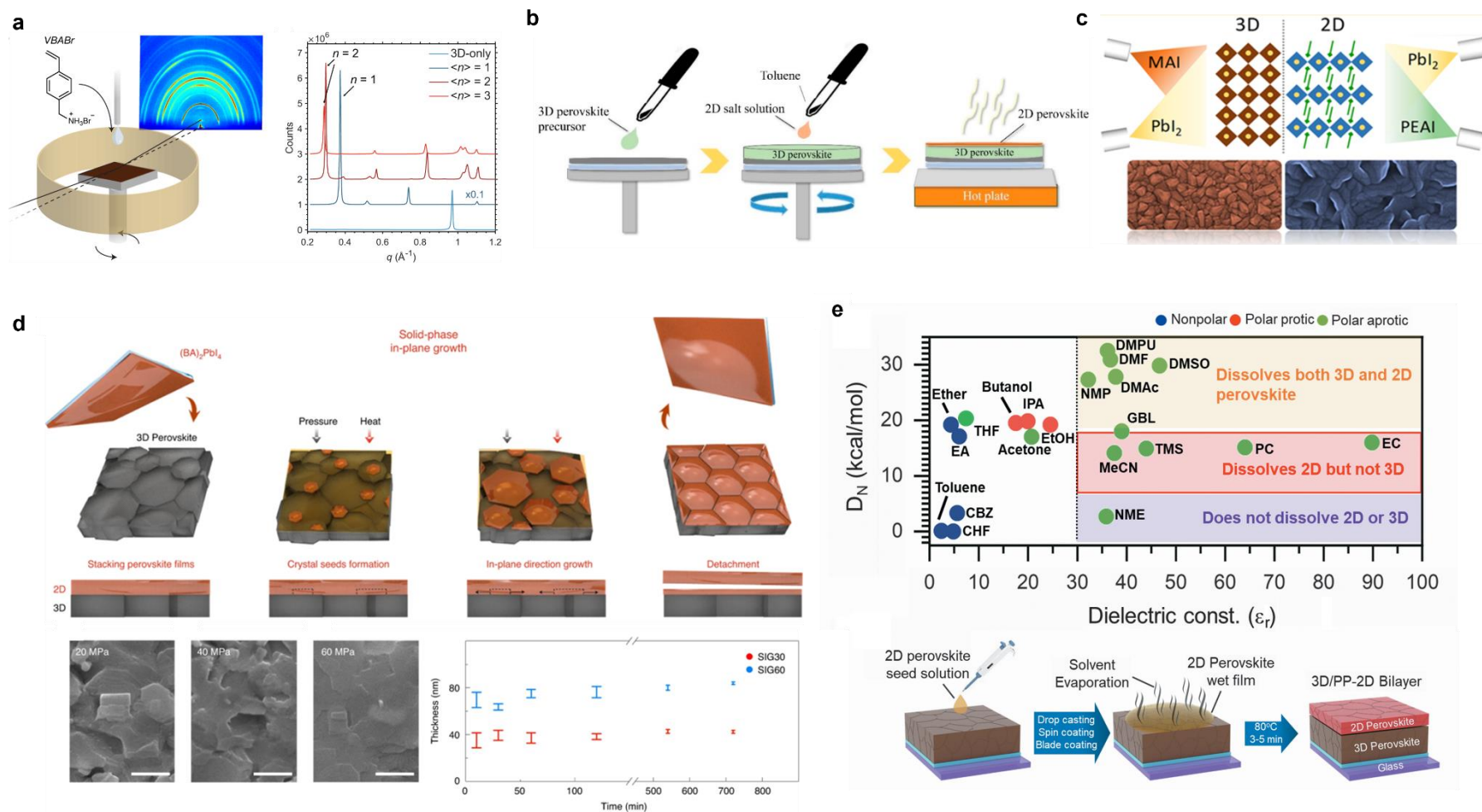


**Figure 33: Processing methods for capped 3D-2D halide perovskites.** a) Schematic of spin-coating process for making 3D/2D stacks (left) and example XRD of 2D deposited on top of 3D (right). Reproduced with permission from ref.<sup>614</sup> Copyright 2021 Springer Nature. b) Schematic of growing 2D layer by dissolving A' cation salt in antisolvent. Reproduced with permission from ref.<sup>615</sup> Copyright 2020 Multidisciplinary Digital Publishing Institute. c) Schematic of vacuum deposition for 3D/2D stack. Reproduced with permission from ref.<sup>613</sup> Copyright 2019 American Chemical Society. d) Schematic of manufacturing of a  $(\text{BA})_2\text{PbI}_4$  film on a 3D perovskite substrate via the solid-phase in-plane growth method (top), 3D film morphology after pressing for 10 min at 20MPa, 40MPa, and 60MPa (bottom left, left to right), and the thickness distribution of the  $(\text{BA})_2\text{PbI}_4$  layer over time at 30°C (red) and 60°C (blue) (bottom right). Reproduced with permission from ref.<sup>221</sup> Springer Nature. e) A collection of common solvents plotted on a dielectric constant - donor number plot with regions demarcated showing for which solvents 2D halide perovskites, 2D and 3D halide perovskites, and neither are dissolved (top), and a schematic of the 3D-2D stack formation process from a 2D seed solution (bottom). Reproduced with permission from ref.<sup>241</sup> Copyright 2022 American Association for the Advancement of Science.

## 6.2. Orientation of 2D halide perovskites on 3D halide perovskites

As mentioned above, 2D halide perovskites alone perform poorly in single junctions due to out-of-plane carrier transport being suppressed by the insulating organic cations. Thus, devices having a horizontal orientation with respect to the substrate will have a lower  $J_{sc}$ .<sup>322,616</sup> A vertical orientation relative to the substrate is preferred as it allows for continuous charge transport through the inorganic layers without traveling through the electrically insulating cations.<sup>322,617</sup>

The orientation of the 2D halide perovskite can be determined through GIWAXS measurements on the film. GIWAXS uses a grazing-incidence X-ray beam to probe into the depth or the surface of the film depending on the incident angle,  $\alpha_i$ . In a 3D-2D

film where 2D is very thin,  $\alpha_i$  of  $0.08\text{--}0.1^\circ$  is more surface sensitive and provides information of the 2D layer while  $\alpha$  of  $0.2\text{--}0.5^\circ$  is more bulk sensitive and will measure 3D halide perovskite.<sup>241,605</sup> A typical GIWAXS pattern of a 3D halide perovskite exhibits Debye Scherrer rings at  $q_z = 1.0 \text{ \AA}^{-1}$  corresponding to the (001) plane; GIWAXS patterns of 2D halide perovskites show a characteristic series of low- $q$  diffraction peaks corresponding to their very large interlayer spacing. Rings within GIWAXS patterns indicate disorganized and mixed orientations whereas spots of high intensities indicate a preferred alignment of lattices. For oriented films, there will be localized diffraction peaks centered along  $q_z = 0$  (horizontal axis) or  $q_r = 0$  (vertical axis) indicating vertical or horizontal orientation, respectively.

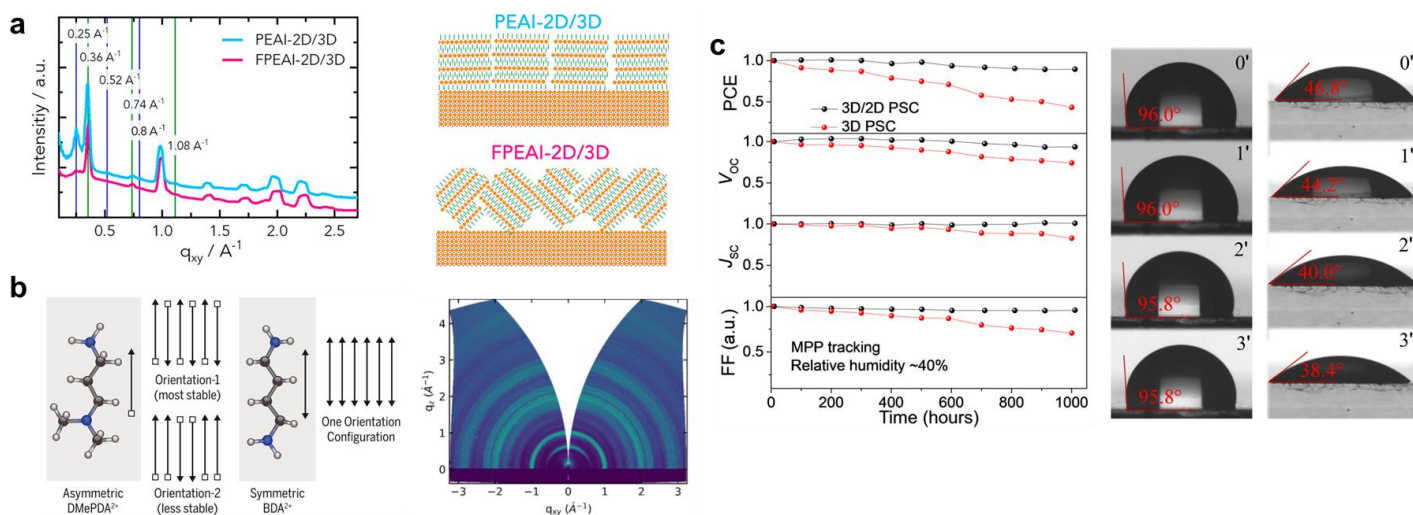


**Figure 34: Orientation of 2D halide perovskite on 3D halide perovskite.** a) Orientational mixing of 2D halide perovskite capping layer induced by FPEAI cation on top of  $\text{Cs}_{0.10}\text{FA}_{0.77}\text{MA}_{0.13}\text{PbI}_{2.59}\text{Br}_{0.41}$ . While PEAI-treated films show more domination n-value mixing, FPEAI-treated 3D-2D devices perform better overall due to their highly oriented nature. Reproduced with permission from ref.<sup>618</sup> Copyright 2019 American Chemical Society. b) Asymmetry of N,N-dimethyl-1,3-propane diammonium ( $\text{DMePDA}^{2+}$ ) cation compared to the symmetry of 1,4-butane diammonium ( $\text{BDA}^{2+}$ ) make it possible to form metastable DJ 2D halide perovskites (left). GIWAXS pattern shows that  $\text{DMePDA}^{2+}$  is able to form vertical metastable 2D halide perovskite structures on 3D halide perovskite (right). Reproduced with permission from ref.<sup>605</sup> Copyright 2019 American Association for the Advancement of Science. c) Stability testing of vertically aligned pFPEA 3D-2D unencapsulated devices under illumination and ambient conditions (left). Due to the hydrophobic fluorine atoms, pFPEA 2D halide perovskite retains high contact angles with water droplets over the course of 3 min (right). Reproduced with permission from ref.<sup>245</sup> Copyright 2021 American Association for the Advancement of Science.

While there is preference towards vertically-oriented films in terms of charge transport, there are

benefits to having horizontally-oriented films.<sup>221,229,245,605,614,618–622</sup> Mixed orientation within the

2D halide perovskite capping layer can actually reduce PCE relative to horizontal orientation, since the latter more effectively blocks back-recombination between holes from the HTL and electrons from the 3D halide perovskite. Bouduban et al. synthesized a 2D capping layer on top of triple-cation double-halide halide perovskite using the iodide salts of fluorophenethylammonium (FPEA<sup>+</sup>) and PEA<sup>+</sup> cations. The GIWAXS patterns of PEAI-treated 3D-2D films exhibited higher intensities around the  $q_z$  axis indicating horizontal orientation, whereas FPEAI-treated films showed diffraction rings indicating mixed orientation (**Figure 34a**). PEAI-films additionally grew higher ratios of mixed  $n=1,2$  films than FPEAI, but they owed differences in charge carrier lifetimes and band alignments to orientation. The carrier lifetime of FPEAI 3D-2D devices slightly increased compared to pure 3D devices, but PEAI 3D-2D devices decay times increased by over an order of magnitude. This was attributed to the slower back-recombination kinetics of PEAI-treated films due to the horizontal orientation serving as a barrier to electron transport. This synergistic improvement in carrier dynamics is reflected in device performance, with a significant increase in  $V_{OC}$  from 1.104V (3D), to 1.127V (FPEAI) or 1.138V (PEAI).<sup>618</sup> Moreover, the bulky cation-coordinated surface of a horizontally-oriented 2D halide perovskite can better protect the underlying halide perovskite against moisture and thermal effects. Liu et al. passivated triple-cation 3D halide perovskite with pentafluorophenylethylammonium iodide (PFEAI) which formed a horizontally-oriented 2D layer such that the surface of the 3D-2D halide perovskite was a plane of hydrophobic fluorine atoms. This orientation, combined with the fluorine-based cation, increased its resistance to moisture as evident from the  $T_{90}$  of 1000 hr under combined sunlight and humid air, and a high contact angle of  $\sim 96^\circ$  with droplets of water, as shown in **Figure 34c**.<sup>605</sup>

Zhang et al. was able to create a horizontally oriented DJ 2D capping layer with enhanced transport by changing the symmetry of the bulky spacer cations. To maximize transport through the DJ capping layer, they decreased the interlayer distance of  $[PbI_6]^{2-}$  octahedra by using short, divalent organoammonium cations to improve the carrier mobility through the 2D structure. They additionally

reduced the band offset between the lead-iodide planes and bulky cation layers by weakening the spacer cation's NH-I hydrogen bonds, which has the effect of shifting the bonding states of the organic layers closer to the valence band energy of the  $[PbI_6]^{2-}$  octahedra. A smaller band offset improves out-of-plane hole transport at the expense of structural stability. Weakened interlayer bonding was achieved with a metastable DJ structure using the asymmetric diammonium cation N,N-dimethyl-1,3-propane diammonium (DMePDA<sup>2+</sup>), with a primary ammonium on one end of its propyl chain and a dimethyl-substituted tertiary ammonium on the other end (**Figure 34b**). The different H-bonding strengths at either end of the spacer cation create an orientation-dependent structural stability for the crystal, with the antiparallel alignment of spacer cations the ground-state structure. A metastable structure without perfect antiparallel alignment could be realized through fast crystallization of the DJ phase. The authors confirmed the improved charge transport with DFT calculations and time-resolved microwave conductivity (TRMC), where they saw that vertical charge transport in the metastable 2D phase was 4 to 5 times faster than in BDAPbI<sub>4</sub> with a symmetric spacer (BDA=1,4-butanediammonium) and magnitudes faster than in RP structures. Improved charged transport qualities led to enhanced PL intensities, longer TRPL lifetimes, and improved device performance. Treatment of a triple-cation mixed-halide 3D halide perovskite, a double-cation mixed-halide 3D halide perovskite, and MAPbI<sub>3</sub> with DMePDA enhanced  $V_{OC}$  in all devices. Metastable films consistently showed 10% relative efficiency decrease over the course of 1000 hr under full illumination and in an inert atmosphere.<sup>245</sup>

Few reports have shown vertically oriented 2D halide perovskite capping films. Our group recently synthesized vertically oriented 2D films using epitaxial growth of BA 2D seeds. Their orientation was confirmed with GIWAXS showing diffraction peaks along the  $q_r$  axis, and their enhanced charge transport was seen in an increased  $V_{OC}$  and  $J_{sc}$ . The increased  $V_{OC}$  may be due to less nonradiative recombination processes occurring within the organic compounds, and the slightly better  $J_{sc}$  may be due to a better charge extraction within the films.<sup>241</sup>

### 6.3. Dimensional (n-value) control of 2D halide perovskite layer on 3D halide perovskite

Achieving high phase purity with a phase-selective method is essential for optimized device performance since 2D halide perovskite thin films with mixed phases might result in stacking faults and dangling bonds between two adjacent layers of different thicknesses. These defects can then act as recombination centers. The variations in n-values and composition alter optical and electronic properties that can be tuned to best fit device structure and 3D halide perovskite VBM/CBM positions.

There are cases where researchers purposefully use 2D mixed phases as capping support.<sup>229,621,623,624</sup> De Wolf utilized a mixture of n=1 and n=2 oleylammonium (OLA<sup>+</sup>)-based RP phases formed at room temperature as a capping layer for better band alignment in a p-i-n device structure. They were able to tune the phase purity by

performing post-treatment at different temperatures from mixed-phase n1-n2 (no annealing) to pure n1 (annealing at 100°C), as the formation energy for n=2 was lower than for n=1. Cross-sectional elemental mapping shows a decrease in lead and iodide contents approaching the surface and an increase in carbon content in distinct layers, indicating the formation of higher n=2 phase near the 3D-2D interface and lower n=1 phase at the surface. PL mapping of the films supports n=2 uniform coverage of room-temperature films. The mixed-phase 2D passivation resulted in minimal device energy loss by better aligning the CBM of the 3D halide perovskite with that of the C<sub>60</sub> ETL. The OLAI treatment caused the secondary electron cutoff to shift to a higher binding energy, indicating the ion exchange-induced 3D-to-2D halide perovskite phase transition could change the Fermi level to more n-type. This n-type behavior shifts the bands downwards such that the 2D conduction band is near that of C<sub>60</sub>, aiding in charge transfer.<sup>229</sup>

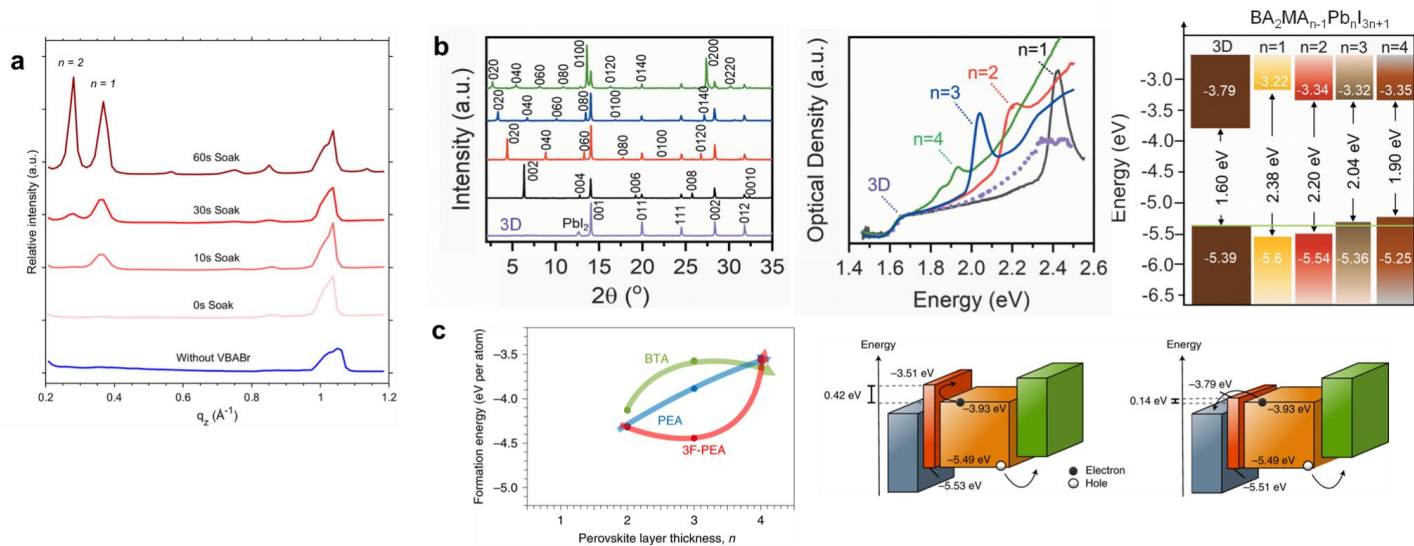


**Figure 35: Dimensional (n-value) Control of 2D halide perovskite Layer on 3D halide perovskite.** a) GIWAXS experiments measure the increase in mixed n-values with increased solution exposure time. By tuning the ratio of n=1 and n=2, it provides an opportunity for better band alignment. Reproduced with permission from ref.<sup>623</sup> Copyright 2022 Springer Nature. b) Dissolving a single crystal of known n-value allows for phase purity within the 2D halide perovskite layer; this control over phase purity enables more control towards favorable band alignments. BA-based 2D halide perovskite was grown above triple-cation mixed-halide 3D halide perovskite; different phases were confirmed with XRD (left) and PL (right) measurements. Reproduced with permission from ref.<sup>241</sup> Copyright 2022 American Association for the Advancement of Science. c) Leveraging formation energies of specific cations, bulky cations can be combined with MAI to synthesize large n-values. The n=3 phase of 3F-PEA has the lowest formation energy and can therefore preferentially be created from solution with the addition of MA precursor (left). Band alignment of a 2D-only capping layer



(center) shows a barrier to electron extraction compared to band alignment of a 2D-MAI layer (right). Reproduced with permission from ref.<sup>621</sup> Copyright 2020 American Chemical Society.

Teale et al. developed a method to achieve mixed n-values by varying the amount of time the 3D bulk was exposed to the 2D cation solution. Their 2D solution consisted of vinylbenzylammonium bromide (VBABr) in 97% volume chloroform and 3% volume IPA on top of (FAPbI<sub>3</sub>)<sub>0.95</sub> (MAPbBr<sub>3</sub>)<sub>0.05</sub>. In depositing the 2D layer, they varied the solution exposure time from 0s to 60s and measured the change in GIWAXS intensity of the n=1 and n=2 diffraction peaks. They observed an increase in n=2 percentage with longer exposure times from 3% n=2 (10s) to 51% n=2 (60s). The ratios of n=1 and n=2 formed can be seen in **Figure 35a**. It is intuitive to speculate that the IPA solvent is partially dissolving the 3D bulk at longer soaking times, thus generating higher n-values, but Teale and coworkers argue that 3% volume IPA is not enough to dissolve a substantial amount of 3D. The best-performing device of 21.7% PCE was obtained from 30s soaking (18% n=2), compared to 19.4% PCE for the control device. In particular, the capping layer improves V<sub>OC</sub> from 1.09V to 1.14V. Simulations of these devices attribute the increase in V<sub>OC</sub> to lower surface trap state density, but also suggest that a misaligned VBM of the 2D layer would significantly reduce V<sub>OC</sub>. The authors hypothesize that such a misalignment is responsible for the comparatively worse performance of the 60s exposure 3D-2D film, suggesting that tuning the mixture of n=1 and n=2 can optimize band alignment and device performance.<sup>621</sup>

Many groups have resorted to mixed 2D phases for desirable band alignments since there is very little control over phase purity using the interdiffusion method of 2D layer formation. There have been attempts to control the dimensionality through specific spacer cations, concentration ratios, and deposition techniques.

A multitude of studies have grown n=1 in their 3D-2D devices using a spacer-cation solution.<sup>597,602,605,610,614,625,626</sup> Some control over phase purity can be achieved through engineering of the 2D precursor solution. Lin et al. have demonstrated that changing the ammonium group of BA<sup>+</sup> to an amine (BA<sup>0</sup>) can create a phase-pure n=1 capping film, as compared to BAI which creates

some amount of n=2. BA<sup>0</sup> is expected to react with excess MAI and MAPbI<sub>3</sub> at surfaces, forming BA n=1 by taking a proton from MA<sup>+</sup>, which allows MA<sup>0</sup> to volatilize and leave the lattice. In contrast, BAI does not act as a reducing agent and will not cause MA to volatilize as MA<sup>0</sup>, allowing it to react with multiple MAPbI<sub>3</sub> structures to create multiple n-phases. The authors confirm this mechanism with XRD and absorption, which show phase-pure n=1 for BA<sup>0</sup>-treated films and a mixture of n1 to n4 for BAI-treated films. While both devices using BAI (18.51% PCE) and BA<sup>0</sup> (19.29% PCE) were found to improve efficiency compared to control devices (17.28% PCE), the higher performance of BA<sup>0</sup> was attributed to better film quality. Moreover, phase-pure n1 capping layers from BA<sup>0</sup> improved device thermal stability at 95°C compared to BAI, which was attributed to the higher concentration of bulky BA in the n=1 phase suppressing volatilization of thermal degradation products.<sup>602</sup> There has also been phase control for n=1 values in using the solid-state in-plane growth (SIG) mentioned earlier from using a larger phase-pure 2D halide perovskite crystal to grow the capping layer.<sup>221</sup>

Phase-pure higher n-values for favorable band alignments have rarely been grown on bulk materials due to the limitations of deposition methods. Despite this, there have been n=2 values reported using this method.<sup>619,627</sup> Liu et al. formed an iso-butylammonium (IBA<sup>+</sup>)-based n=2 capping layer on top FAPbI<sub>3</sub> by converting FA-sites in the  $\delta$ -phase to higher n-value 2D. Using GIWAXS and XRR measurements, they confirmed the conversion of  $\delta$ -FAPbI<sub>3</sub> to 2D n=2, with a simultaneous decrease in PbI<sub>2</sub> and FAPbI<sub>3</sub>  $\delta$ -phase. TRPL showed longer carrier lifetimes upon the introduction of the 2D, with over an order of magnitude slower decay within the first 10 ns. DFT calculations confirm this effect is from effective passivation of surface defects. 2D-capped devices showed a distinct increase in V<sub>OC</sub> from 1.053V (20.4% PCE) in 3D FAPbI<sub>3</sub> to 1.113V (22.7% PCE) in 3D-2D FAPbI<sub>3</sub>/IBA<sub>2</sub>FAPb<sub>2</sub>I<sub>7</sub>. 3D-2D devices exhibit enhanced photostability at RT (T<sub>95</sub> = 700 hours) and 80°C (T<sub>84</sub> = 500 hours) in inert atmosphere.<sup>619</sup>



Chen et al. was able to create a higher  $n$ -value 2D capping layer by controlling the ratio between MAI and 2D ligands in the capping solution. They used DMF:IPA solvents in a 1:200 volume ratio with cations to form a predominantly  $n=3$  halide perovskite capping layer. The introduction of a small amount of DMF into the solvent facilitated the dissolution of  $\text{PbI}_2$  at the film surface, producing higher  $n$ -value films when combined with MAI and bulky cations. The DMF concentration was kept low enough to prevent interaction with the 3D bulk. PEA and 3-fluorophenylethylammonium ( $3\text{F-PEA}^+$ ) were used as  $\text{A}'$ -site cations. For PEA films,  $n=2,3$  formed simultaneously, whereas  $3\text{F-PEA}$  formed  $n=3$  first followed by trace amounts of  $n=2$ . The lack of the  $n=1$  phase was attributed to its high formation energy, a result of the structure's isolated  $[\text{PbI}_6]^{2-}$  planes (**Figure 35c**). From inverse photoelectron spectroscopy (IPES), Kelvin probe force microscopy (KPFM), and surface sensitive UPS, deeper conduction bands for  $3\text{F-PEA}$  3D-2D devices were confirmed and further supported with an increase in  $V_{\text{OC}}$  from 1.06V (3D) to 1.14V (for just  $3\text{F-PEA}$  treatment) and 1.16V (for  $3\text{F-PEA}$  and MAI treatment).<sup>623</sup>

One can also dissolve 2D halide perovskite crystals directly into a solution to deposit on top of a 3D layer to improve phase purity. Our group recently demonstrated the effectiveness of this strategy, first synthesizing phase pure 2D halide perovskite crystals via slow crystal growth from HI solution and then dissolving these crystals in MeCN solution to create partially solvated 200nm "seeds" which were spin-coated identically to a conventional precursor solution. These seeds were observed to serve as nucleation sites which facilitated the growth of homogeneous films that preserved the  $n$ -value of the parent crystals. We demonstrated the effective transfer of  $n$ -value from seeds to films for BA  $n=1, 2, 3,$  and  $4$ , as confirmed with absorbance, PL, and XRD (**Figure 35b**). Importantly, 2D formation in this method is completely independent of the 3D absorber underneath, facilitating the formation of 3D/2D stacks with disparate A-, B-, and X- cations. The precise control over phase purity allowed us to tune the band alignment of the 3D/2D/HTL stack to enhance charge transport and suppress recombination, for example by using phase-pure BA

$n=3$  as a 2D layer with VBM intermediate between the 3D halide perovskite and Spiro-OMeTAD.<sup>620</sup>

#### 6.4. Thickness control of 2D halide perovskite layer on 3D halide perovskite

The 2D layer in 3D/2D perovskites is often kept very thin, such that the material behaves less as a semiconductor and more as a source of passivating ammonium cations. Solution-processing of 3D halide perovskites creates defect states at grain boundaries and interfaces which are more deleterious to performance than point defects in the bulk. Interfacial defects, arising from dangling bonds at film surfaces and grain boundaries, pose as trap states and nonradiative recombination centers which quench PL and reduce  $V_{\text{OC}}$ .<sup>628</sup> 2D halide perovskites can act as excellent passivation layers at these interfaces due to their intrinsic stability against  $\text{H}_2\text{O}$ , their suppression of defect and degradation product mobility, and the spacer cation's propensity to coordinate and neutralize the surface defect sites of 3D grains. For this purpose very little 2D halide perovskite is needed; typically 5-10 nm will suffice to effectively mitigate defects and improve PCE and stability.<sup>597,602,605,613,619,620,624,625,627</sup>

In using an alkyl chain cation, longer chain length leads to less visible grain boundaries and reduced surface roughness as visualized from SEM and AFM respectively, showcasing the effectiveness of 2D halide perovskites with longer-chain spacers at passivating the 3D halide perovskite surface.<sup>620,629</sup> Bawedani et al. varied the length of the alkyl chain in their ammonium-based cation from BA to  $n$ -hexylammonium ( $\text{HA}^+$ ) and  $n$ -octylammonium ( $\text{OA}^+$ ) and found an increase in  $V_{\text{OC}}$  from 1.10V for pure 3D, to 1.14V for BA-2D passivation, to 1.15V for HA-2D and OA-2D passivation.<sup>620</sup>

halide perovskites' instability in ambient conditions can be suppressed by the incorporation of 2D cations, which confer heat and light resistance to the lattice by reducing ion migration and improve  $\text{O}_2$  and  $\text{H}_2\text{O}$  stability by covering surfaces with their outward-facing hydrophobic groups. Gratzel et al. introduced an 8 nm capping layer of  $\text{pFPEA}_2\text{PbI}_4$  ( $\text{pFPEA}$  = pentafluorophenylethylammonium) onto triple-cation 3D halide perovskite. Due to the strong interaction between the ammonium tail with  $\text{PbI}_2$ ,  $\text{pFPEAI}$  could be adsorbed on the surface and into

the grain boundaries by replacing A-site cations. The preferential orientation of the fluorine ends outwards created a moisture-resilient barrier. pFPEA<sup>+</sup> ions were shown to bind specifically to FAPbI<sub>3</sub>  $\delta$ -phases and excess PbI<sub>2</sub> at the surface, as evidenced by the decrease in XRD intensities of these phases. Longer carrier lifetimes and increased PL quenching efficiencies confirm the optoelectronic benefits of 2D treatment. These 3D-2D stack devices retained 90% of their 22.2% efficiency after over 1000 hours in 40% humidity (unencapsulated), which was attributed to the ultrahydrophobic nature of the 2D capping layer that could further be observed in contact angle measurements<sup>605,630</sup>.

The prevalence of thin 2D passivation layers in 3D/2D halide perovskite literature in part reflects the difficulty of engineering thicker 2D layers. Unwanted or mixed n-values and improper orientation of 2D can impede charge transport if the 2D layer is too thick to tunnel through. Nevertheless, some reports have developed thicker 3D-2D stack devices with some control over 2D n-value distribution, for example through interdiffusion by changing the concentration of bulky cation solution or varying ratios of treatment solvent and antisolvent.<sup>614</sup>

There have been few studies conducted on controlling the thickness of the 2D halide perovskite layer to create 3D-2D stacks.<sup>221,241,613</sup> One of the first reported 2D halide perovskite depth-dependent studies on 3D halide perovskite absorbers was the fabrication by La-Placa et al. of a 3D-2D halide perovskite heterojunction by dual-source vacuum deposition. The report's aim was to study interactions between 3D and 2D phases and charge transport properties near 3D-2D interfaces. With their vacuum deposition method La-Placa et al. could deposit any combination of 2D and 3D; in their devices they combined PEA<sub>2</sub>PbI<sub>4</sub>/MAPbI<sub>3</sub>, MAPbI<sub>3</sub>/PEA<sub>2</sub>PbI<sub>4</sub>, and PEA<sub>2</sub>PbI<sub>4</sub>/MAPbI<sub>3</sub>/PEA<sub>2</sub>PbI<sub>4</sub>. 2D halide perovskites were sublimed onto 3D absorbers at different thicknesses of 2.5, 5, and 10 nm. There was a monotonic loss in J<sub>SC</sub> with increased 2D thickness, but a maximum V<sub>OC</sub> for some nonzero thickness. It is important to note the vacuum-deposited 3D-2D halide perovskite devices all had worse overall device performance compared to 3D spin-coated control devices. Nevertheless, while the 2D halide perovskites served as passivation layers and not as a stacking layer, this study demonstrated that control over 2D halide perovskite thickness is achievable.<sup>613</sup>

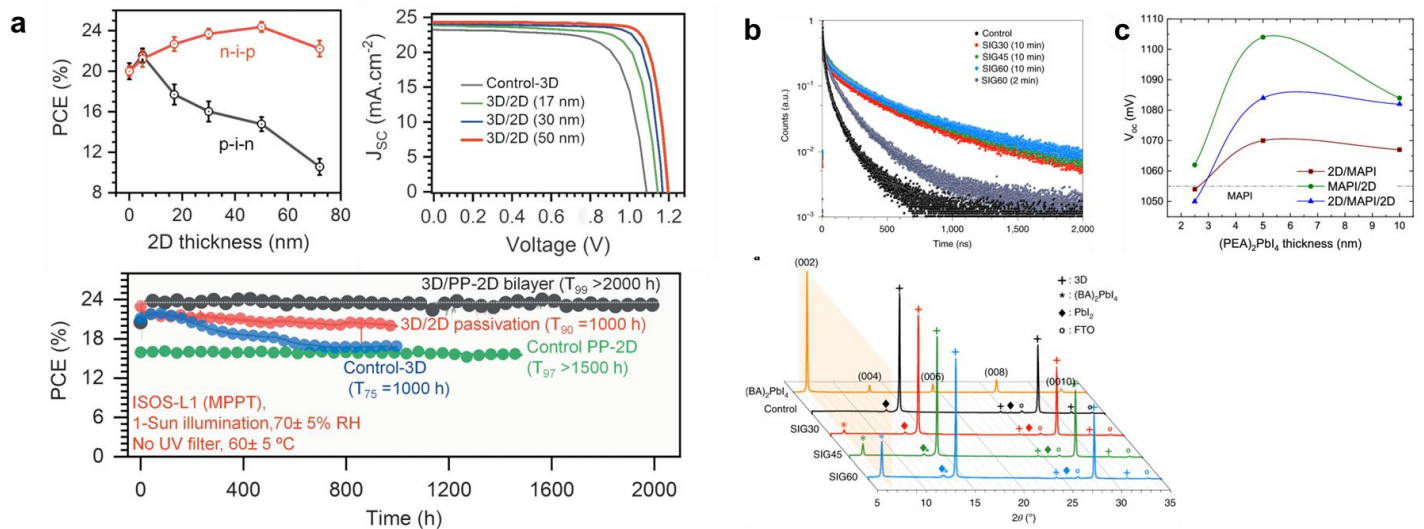


**Figure 36: Thickness control of 2D halide perovskite layer on 3D halide perovskite.** a) Using BA-2D halide perovskite n=3 memory seeds to crystallize different thicknesses on top of 3D halide perovskite. (Top left) The optimal 2D layer thickness is 50nm for an n-i-p device because of BA n3's effective band alignment; in a p-i-n device it is <10 nm since it must be tunneled through. (Top right) The J-V curve of n-i-p devices demonstrates all 2D halide perovskite thicknesses were able to passivate 3D absorbers for improved efficiencies and V<sub>OC</sub>. (Bottom) 3D/2D devices with 50nm of n=3 2D exhibit outstanding stabilities of T<sub>99</sub> > 2000 hours. Reproduced with permission from ref.<sup>241</sup> Copyright 2022 American Association for the Advancement of

Science. b) Using the solid-state in-plane growth (SIG) method to grow  $\text{BA}_2\text{PbI}_4$  from a physically-contacted single crystal. (Top) Thicker layers of 2D halide perovskite shows longer carrier lifetimes. (Bottom) Thicker 2D layers can be grown by increasing the annealing temperature from SIG30 (30°C) to SIG60 (60°C). Reproduced with permission from ref.<sup>221</sup> Copyright 2021 Springer Nature. c) Vacuum-deposited 3D-2D devices showing a maximum  $V_{\text{OC}}$  at some nonzero 2D thickness. This method was one of the first to show control over passivation thickness. Reproduced with permission from ref.<sup>613</sup> Copyright 2019 American Chemical Society.

The solid-state in-plane growth method of Noh et al. offers a degree of control over 2D layer thickness. Applying 60MPa of pressure to the physically contacted 3D-2D stack facilitated the growth of an 80nm  $\text{BA}_2\text{PbI}_4$  layer at 60°C and a 40 nm layer at 30°C. The formation of 2D halide perovskite was confirmed with XRD as seen in **Figure 36a**. Based on SEM images, there are fewer defined grain boundaries throughout the film, indicating full coverage of 2D stack. The charge carrier lifetime increased five-fold with the introduction of the 2D layer, from 0.2 $\mu\text{s}$  to 1 $\mu\text{s}$ , showing the  $\text{BA}_2\text{PbI}_4$  is able to limit trap-assisted non-radiative recombination. There is an increase in device performance when compared to control and to the solution-processed 2D stack, specifically an increase in  $V_{\text{OC}}$ .<sup>221</sup>

Our group's 2D seeds approach can also tune stack thickness by varying precursor seed concentration.<sup>324</sup> Because our this method does not rely on interdiffusion of 3D ions to form the 2D layer, there is less limitation on 2D thickness. By varying 2D seed concentration the 2D layer thickness could be tuned from <10 nm to >500 nm, which allowed us to optimize thickness for device performance (**Figure 36b**). Using 50 nm of  $n=3$  2D stack, there was a significant increase in  $V_{\text{OC}}$  from 1.09 to 1.20V, owing to the excellent band alignment of  $\text{BA } n=3$  with both the 3D halide perovskite and the HTL.<sup>241</sup>

## 6.5. Semiconductor Heterojunctions

In combining oppositely doped materials in a device, carriers diffuse into the opposite charged

region due to differences in Fermi energy levels at the interfacial junction. These carriers continue to disperse until the same Fermi energy level is maintained throughout both materials. The interface at which carrier diffusion occurs is called the depletion region. From the exchange of carriers, an electric field is generated and induces band bending of the vacuum level and of the conduction and valence band. Based on the continuity of energies within the junctions, the flow and/or accumulation of charged carriers can be predicted. If there is favorable alignment between the junctions, then effective charge extraction will occur to fabricate a high-performance device<sup>631,632</sup>.

A heterojunction can be defined as the interface region where two semiconductor materials of different bandgaps are in contact. Their union will facilitate band bending and a built-in electric field. When using nano-scale thicknesses to create a heterojunction, this creates a nano-heterojunction, which is distinct from the heterojunction as its chemical and physical properties deviate in comparison to bulk materials from differences in size, surface, interface, and quantum effects. In most heterojunction structures, 100 nm is the differentiating thickness between a nano and bulk heterojunction. However, due to halide perovskites' feature dimensions of Forster resonance energy transfer (FRET), carrier hopping/tunneling, surface reconstruction, and defects, the characteristic thickness can be ~20 nm.<sup>633,634</sup>

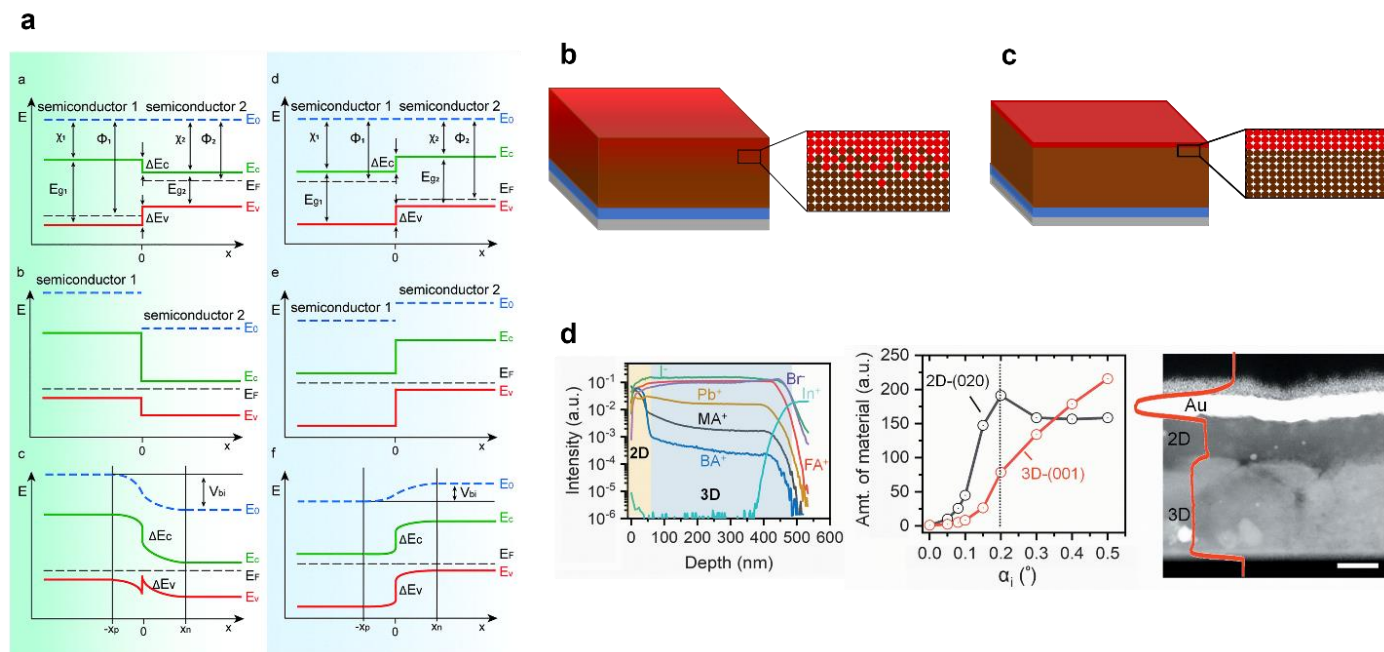


**Figure 37: Semiconductor Heterojunctions.** a) Type 1 alignment (left) and Type 2 alignment (right) at a semiconductor interface. With the two semiconductor's union, band shifting occurs to equalize the Fermi level and band bending occurs due to the formation of a depletion region. Based on the energy levels and positions, one can predict the effectiveness of charge extraction, accumulation, and recombination. Reproduced with permission from ref.<sup>631</sup> Copyright 2021 Royal Society of Chemistry. b) The graded heterojunction that typically forms with 3D-2D heterojunctions is from a concentration gradient of the A'-site cation from the surface to the bulk. Unlike a conventional semiconductor heterojunction, this leads to a semi-continuous shifting of band edges from 3D to 2D. c) Atomically abrupt heterojunctions, as shown here, are more favorable for charge transport because of improved continuity and suppression of dangling bonds. d) The formation of a sharp heterojunction through our 2D seed method, made possible by removing the need for ion interdiffusion. A sharp transition is measured through ToF-SIMS (left), GIWAXS probing angle (middle), and SEM imaging (right). The abruptness of the interface is measured to be within the length scale of 3D surface roughness. Reproduced with permission from ref.<sup>241</sup> Copyright 2022 American Association for the Advancement of Science.

Depositing a capping layer with  $\geq 20$  nm thickness requires heterojunction design considerations. Tuning band alignments of the 3D-2D interface will allow more control over carrier energy levels and transport throughout the device. Band alignments provide information on how charged carriers move throughout valence and conduction bands. There are two main types of band alignments: straddling bands (type 1) and staggered bands (type 2). These types are shown in **Figure 37a**. In type 1 alignment, the VBM of the capping material is below the VBM of the substrate material and the CBM is above the CBM of the substrate material. The difference in energies of the two bands prevents excited electrons and holes from entering the wide bandgap material in the barrier, and

confines the excitons within the halide perovskite layer in the context of 2D halide perovskites. This type of behavior within the halide perovskite can yield enhanced PL intensity and stability, making this alignment ideal for LEDs<sup>633</sup>. In type 2 alignment the VBM and CBM of the capping layer are either both above or both below the VBM and CBM of the substrate, respectively. This staggered alignment is charge selective, allowing either the diffusion of only holes (2D bands higher than 3D) or only electrons (2D bands lower than 3D) from the 3D through the 2D layer and blocking the other carrier. This can facilitate efficient photocarrier separation at internal interfaces without recombination losses, making this alignment useful for solar cell devices if it can be effectively engineered.<sup>631,635</sup>

### 6.5.1. Graded heterojunctions

The typical method in making 3D-2D heterojunctions is to coat films with a large bulky cation solution for the cation to react with  $\text{PbI}_2$  at the surface to create 2D halide perovskite. This method relies heavily on the diffusion of cations into the lattice; this in turn creates a concentration gradient of 2D to 3D as we probe from the surface to the bulk. In particular, A cation interdiffusion means that the A:A' cation ratio often is lowest at the 2D top surface and increases towards the interface, leading to the formation of a gradient n-value distribution from high-n at the interface to low-n at the surface. In **Figure 37b**, the schematic shows the transition of the 2D grains to 3D grains as depth increases. The transition of lattices from 3D to 2D generates a gradient of energies within the interface of the halide perovskite known as a graded heterojunction. Graded heterojunctions have been known to alter charge carrier dynamics between the 3D halide perovskite layer and charge transport layers via manipulation of band energies at the interfaces, demonstrating a smooth transition in band energies from the 3D to the bulk n-value 2D in the z-direction. Graded 3D/2D heterojunctions are difficult to avoid when 2D is deposited using traditional methods, but they can be engineered to facilitate efficient charge extraction<sup>631,632</sup>.

Wu et al. coated  $\text{FASnI}_3$  with 4-(trifluoromethyl)benzylammonium ( $\text{TFBA}^+$ ) cations dissolved in chloroform to create a graded heterojunction. They speculated that  $\text{TFBA}^+$  cations are exchanged with  $\text{FA}^+$  upon annealing but are limited to the film's surface due to the large steric effect of the bulky cation. This was confirmed with ToF-SIMS, which showed increasing iodide content at the surface correlating to  $\text{TFBA}_2\text{SnI}_4$ , and decreasing  $\text{TFBA}^+$  content with increased probe depth. Using UV-Vis absorption spectroscopy and UV photoelectron emission spectroscopy, they measured band alignments at the halide perovskite-ETL ( $\text{C}_{60}$ ) interface for both 3D and 3D/2D films. Both films showed type-2 band alignment but the graded 3D-to-n1 heterojunction of the 3D/2D film bent the VBM at the surface of the 3D downward, moving holes away from the interface and suppressing back recombination. Reduced interfacial recombination

was confirmed with the observation of higher carrier lifetimes, from 3.25 ns in 3D to 6.61 ns in 3D/2D. A significant increase in  $V_{\text{OC}}$  from 0.58V (3D) to 0.70V (3D/2D) was observed in the resulting devices. This improvement was attributed partially to the suppression of recombination by band bending from the graded heterojunction at the halide perovskite/ETL interface, and also to the passivation of trap defects by  $\text{TFBA}^+$  cations, improved film morphology upon cation treatment, and suppressed Sn oxidation.<sup>626</sup>

Bai et al. created a graded heterojunction with  $\text{MAPbI}_3$  and PEAI to improve the performance of p-i-n devices. They confirmed a gradient in A' cation with ToF-SIMS, suggesting a smooth transition from a 3D bulk to a 2D surface. UV photoelectron spectroscopy revealed upward band bending at the halide perovskite-ETL (PCBM) interface facilitated by this 3D-2D gradient. 3D  $\text{MAPbI}_3$  has the same CBM level as PCBM, and as a result the  $\text{MAPbI}_3$  – PCBM interface lacks an energetic barrier to the backflow of electrons. Upward band bending facilitated by the 2D layer creates a CBM offset at the halide perovskite-ETL interface which suppresses backflow. As a result, the graded heterojunction enhanced  $V_{\text{OC}}$  from 1.10 V (3D) to 1.17 V (3D/2D). These 3D-2D devices exhibited higher efficiencies compared to their pure 3D counterparts (19.89% to 18.75%), although they showed lower  $J_{\text{sc}}$  (21.8 to 22.5  $\text{mA cm}^{-2}$ ) due to poor charge transport in the 2D layer and the effect of upward band bending.<sup>610</sup>

### 6.5.2. Sharp heterojunctions

Even though graded heterojunctions have demonstrated superior  $V_{\text{OC}}$  in devices, the interdiffusion process can introduce new recombination centers near the interface through vacancies left behind from ion migration. With this in mind, atomically sharp heterojunctions can dramatically reduce the number of surface defects by transitioning from one material to the other within a few atomic distances (**Figure 37c**).<sup>636</sup> Sharp 3D/2D heterojunctions necessitate new 2D deposition techniques that do not rely on interdiffusion of ions from the 3D layer (particularly the B-site) into the 2D layer.<sup>631–634</sup> This is made challenging because of the similar chemistries of 2D and 3D halide perovskites, such that solvents which can dissolve both the

organic and inorganic precursors of a 2D halide perovskite will also interact strongly with the 3D halide perovskite and potentially wash it away completely when deposited on top. Some reports such as by Azmi et al. have created semi-abrupt heterojunctions from A'X salts in benign solvents through process engineering, for example by tuning thermal annealing, but not for 2D layers with  $n > 1$ .<sup>229</sup>

Even discounting the complications of solvent selection, achieving a 3D-2D sharp heterojunction poses a major challenge as surfaces of halide perovskite are not atomically smooth. Despite this, in changing the 2D halide perovskite crystallization method, there is an opportunity to move towards sharp heterojunctions, where the transition occurs within the roughness of the 3D bulk. One of the first groups to create an independent 2D capping layer on 3D to form an abrupt 3D-2D heterojunction was Jang et al. using their SIG method to induce 2D seeds on top of the 3D absorber without the need for interdiffusion. While this report only demonstrated this process for  $n=1$ , unlike with the interdiffusion method there is no inherent limitation to making higher- $n$  heterojunctions. The formation of an abrupt 3D/2D interface using this method was confirmed with TEM and SEM.<sup>221</sup>

More recently, our group has demonstrated abrupt 3D/2D heterojunctions with arbitrary 2D  $n$ -value and chemistry using our 2D seed solution approach. By using a solvent which targets the unique van der Waals interlayer interactions in 2D RP halide perovskites, we could dissolve full 2D crystals and precipitate them onto 3D films without damaging the 3D layer. This overcomes the limitations of interdiffusion-based processing techniques and allows for the formation of an abrupt 3D/2D interface. Using this technique, we were able to grow BA  $n=3$  on 3D  $(\text{Cs}_{0.05}\text{MA}_{0.10}\text{FA}_{0.85})\text{Pb}(\text{I}_{0.90}\text{Br}_{0.10})_3$ , creating an atomically sharp interface as confirmed with ToF-SIMS, depth-dependent GIWAXS, and cross-sectional SEM (**Figure 37d**). This yielded a device with an increased voltage of 1.2V, compared to 1.1V for the control 3D. Even in comparison to BA-treated 3D-2D devices, devices made via our seed method yielded higher efficiencies and stabilities. The efficiencies for the control, passivated, and sharp-layered devices were 21%, 22.93%, and 23.75%

respectively. Furthermore, our sharp-layered device retained >99%PCE after 2000 hr of operation under 1-Sun illumination, compared to 90% after 1000 hr for a conventional BAI-passivated device.<sup>241</sup>



**Table 18: 3D-2D stacks where 2D halide perovskite thickness is not defined, 2D deposited through IPA solvent post-treatment**

| 2D halide perovskite/<br>A' cation             | n-<br>value | Orientation | n-i-p/<br>p-i-n | 3D halide perovskite  | PCE<br>(%) | Stability<br>(hr)      | Stability testing conditions   | Ref |
|--|-------------|-------------|-----------------|---|------------|------------------------|--|-----|
| phenylethylammonium<br>iodide                  | N/A         | N/A         | n-i-p           | MAPbI <sub>3</sub>  | 14.94      | T <sub>75</sub> = 456  | Unencapsulated (~75% RH, air), Dark, OC,<br>periodic J-V   | 637 |
| butylammonium iodide                           | N/A         | N/A         | n-i-p           |   | 11.49      | N/A                    |  |     |
| phenylethylammonium<br>iodide                  | 1           | N/A         | n-i-p           | CsFAMAPbBrI   | 20.75      | T <sub>80</sub> = 800  | Encapsulated (air), MPP tracking in continuous<br>1-sun illumination                                       | 597 |
| guanidinium bromide                            | N/A         | N/A         | p-i-n           | (FA <sub>0.95</sub> PbI <sub>2.95</sub> ) <sub>0.85</sub><br>(MAPbBr <sub>3</sub> ) <sub>0.15</sub>   | 20.91      | T <sub>95</sub> = 500  | Unencapsulated (N <sub>2</sub> ), 85°C Thermal Testing   | 638 |
| 2-(4-fluorophenyl)ethyl<br>ammonium iodide     | 1+2         | N/A         | n-i-p           | Cs <sub>0.1</sub> (FA <sub>0.83</sub> MA <sub>0.17</sub> ) <sub>0.9</sub><br>Pb(I <sub>0.83</sub> Br <sub>0.17</sub> ) <sub>3</sub>         | 20.54      | T <sub>99</sub> = 864  | Unencapsulated (air), Dark, OC, periodic J-V   | 639 |
| phenylethylammonium<br>iodide                  | 1           | N/A         | n-i-p           | FAPbI <sub>3</sub>  | 23.56      | T <sub>90</sub> = 500  | Unencapsulated (N <sub>2</sub> ), 85°C Thermal Testing,<br>OC, periodic J-V                                | 640 |
| butylammonium bromide                          | 2           | N/A         | n-i-p           | Cs <sub>0.17</sub> FA <sub>0.83</sub> Pb<br>(I <sub>0.6</sub> Br <sub>0.4</sub> ) <sub>3</sub>  | 20         | N/A                    | N/A  | 627 |
| N,N-dimethylethylene-<br>1,2-diammonium iodide | 1           | N/A         | n-i-p           | MAPbI <sub>3</sub>  | 20.18      | T <sub>74</sub> = 720  | Unencapsulated (~60% RH, air), Dark, OC,<br>periodic J-V   | 625 |
| iso-butylammonium<br>iodide                    | 2           | horizontal  | n-i-p           | FAPbI <sub>3</sub>  | 22.7       | T <sub>95</sub> = 700  | Unencapsulated (N <sub>2</sub> ), MPP tracking in<br>continuous 1-sun illumination,<br>(1) RT and (2) 80°C | 619 |
|  |             |             |                 |   |            | T <sub>90</sub> = 500  |  |     |
| 2-<br>thiophenemethylammoni<br>um iodide       | 1           | N/A         |                 | [(FAPbI <sub>3</sub> ) <sub>0.87</sub><br>(MAPbBr <sub>3</sub> ) <sub>0.13</sub> ] <sub>0.92</sub><br>(CsPbI <sub>3</sub> ) <sub>0.08</sub> | 18.9       | T <sub>97</sub> = 2    | Unencapsulated (N <sub>2</sub> ), 50°C, OC, periodic J-V   | 641 |
| phenylethylammonium<br>iodide                  | 1           | N/A         |                 |   | 19.1       | T <sub>97</sub> = 2    |  |     |
| 2,2-<br>(ethylenedioxy)bis(ethyl-<br>ammonium) | 1           | vertical    | n-i-p           | Cs <sub>0.05</sub> (FA <sub>0.85</sub> MA <sub>0.15</sub> ) <sub>0.95</sub><br>PbI <sub>3</sub>   | 22.6       | T <sub>80</sub> = 960  | Unencapsulated (air), dark, periodic J-V   | 642 |
|  |             |             |                 |   |            | T <sub>65</sub> = 500  | 85°C (N <sub>2</sub> ), dark, periodic J-V   |     |
|  |             |             |                 |   |            | T <sub>85</sub> = 500  | Unencapsulated (N <sub>2</sub> ), 1-sun illumination,<br>periodic J-V                                      |     |
| N,N-dimethyl-1,3-                              | 1           | horizontal  | n-i-p           | (FAPbI <sub>3</sub> ) <sub>0.85</sub>   | 24         | T <sub>99</sub> = 1000 | Unencapsulated (in N <sub>2</sub> ), MPP tracking in   | 245 |

|   |            |            |       |  |       |                        |  |     |
|---|------------|------------|-------|--|-------|------------------------|--|-----|
| propane diammonium                                  |            |            |       | (MAPbI <sub>2</sub> Br) <sub>0.1</sub><br>(CsPbI <sub>3</sub> ) <sub>0.05</sub>  |       |                        | continuous 1-sun illumination  |     |
| 4-methoxyphenethylammonium bromide                  | 1          | N/A        | n-i-p | CsPbI <sub>(2.85)Br(0.15)</sub>  | 20.31 | T <sub>92</sub> = 800  | Unencapsulated (air), dark, periodic J-V   | 643 |
|   |            |            |       |  |       | T <sub>95</sub> = 100  | Unencapsulated (N <sub>2</sub> ), 65°C, periodic J-V   |     |
| Cyclohexylammonium iodide                           | 1          | N/A        | n-i-p | FAPbI <sub>3</sub>   | 23.1  | N/A                    | N/A  | 644 |
| Cyclohexylmethylammonium iodide                     | 1          | N/a        | n-i-p | FAPbI <sub>3</sub>   | 23.91 |                        |  |     |
| 3-fluorophenethylammonium and methylammonium iodide | 3+ trace 2 | N/A        | p-i-n | Cs <sub>0.05</sub> FA <sub>0.85</sub> MA <sub>0.1</sub> PbI <sub>3</sub>   | 23.91 | T <sub>99</sub> = 1000 | Unencapsulated (50% RH air), MPP tracking in continuous 1-sun illumination (1) RT and (2) 65°C | 623 |
|   |            |            |       |  |       | T <sub>95</sub> = 500  |  |     |
| R- $\alpha$ -methyl-4-bromobenzylammonium           | 1+2        | N/A        | n-i-p | Rb <sub>0.05</sub> Cs <sub>0.05</sub><br>(FAPbI <sub>3</sub> ) <sub>0.083</sub><br>(MAPbB <sub>3</sub> ) <sub>0.17</sub> | 21.48 | T <sub>92</sub> = 1000 | Unencapsulated (35% RH, air), periodic J-V   | 645 |
|   |            |            |       |  |       | T <sub>85</sub> = 200  | Unencapsulated (N <sub>2</sub> ), 60°C, periodic J-V   |     |
| diethylammonium iodide                              | 1          | disordered | n-i-p | (Cs <sub>0.05</sub> FA <sub>0.85</sub> MA <sub>0.1</sub> PbI <sub>3</sub> )  | 23.5  | T <sub>97</sub> = 500  | Unencapsulated (~10% RH, air), Dark, OC, periodic J-V  | 646 |

**Table 18: 3D-2D stacks where 2D halide perovskite thickness is not defined, 2D deposited through non-IPA post-treatment or with antisolvent**

| 2D halide perovskite/<br>A' cation | n-value | Orientation | n-i-p/<br>p-i-n | Solvent               | 3D halide perovskite  | PCE (%) | Stability (h)                                  | Stability testing conditions   | Ref |
|------------------------------------|---------|-------------|-----------------|-----------------------|---|---------|--|--|-----|
| Phenylethylammonium iodide         | 1       | N/A         | p-i-n           | Toluene (antisolvent) | MAPbI <sub>3</sub>  | 19.89   | T <sub>75</sub> = 240                          | Unencapsulated (~25% RH, air), Dark, OC, periodic J-V                  | 610 |
| 4-vinylbenzylammonium bromide      | 1+2     | horizontal  | n-i-p           | 1:1 IPA:CB            | (MAPbBr <sub>3</sub> ) <sub>0.15</sub><br>(FAPbI <sub>3</sub> ) <sub>0.85</sub><br>(5%Cs) | 19.8    | T <sub>90</sub> = 2300                         | Unencapsulated (~30% RH, air), Dark, OC, periodic J-V                  | 622 |
| butylammonium iodide               | 2       | N/A         | n-i-p           | CB with 1%DMSO        | CsPbI <sub>2</sub> Br   | 14.5    | T <sub>95</sub> = 240<br>T <sub>80</sub> = 600 | Unencapsulated, ((1) ~15% and (2) 25% RH, air), Dark, OC, periodic J-V | 647 |
| n-hexylammonium bromide            | 1       | horizontal  | n-i-p           | Chloroform (CF)       | (FAPbI <sub>3</sub> ) <sub>0.92</sub><br>(MAPbBr <sub>3</sub> ) <sub>0.08</sub>           | 22.4    | T <sub>85</sub> =500                           | Encapsulated (air), MPP tracking in continuous 1-sun illumination      | 620 |

|   |       |            |       |                       |                      |       |                       |   |     |
|---|-------|------------|-------|-----------------------|----------------------|-------|-----------------------|---|-----|
| n-butylammonium bromide                   | 1     | horizontal | n-i-p |                       |                      | 22.2  | N/A                   | N/A   |     |
| n-octylammonium bromide                   | 1     | horizontal | n-i-p |                       |                      | 22.1  |                       |   |     |
| 4-(trifluoromethyl)-benzylammonium iodide | 1     | N/A        | p-i-n | CF                    | FASnI <sub>3</sub>   | 10.96 | T <sub>95</sub> = 500 | Encapsulated (air), MPP tracking in continuous 1-sun illumination | 626 |
| anilinium                                 | quasi | N/A        | p-i-n | Hexafluoro-2-propanol | FAGASnI <sub>3</sub> | 10.4  | T <sub>80</sub> = 250 | Unencapsulated (~40% RH, air), Dark, OC, periodic J-V             | 624 |

Table 19: 3D-2D stacks with defined 2D halide perovskite thickness

| 2D halide perovskite/<br>A' cation                                  | n-<br>value | Orientation | Thickness<br>(nm) | n-i-p/<br>p-i-n | Solvent              | 3D halide<br>perovskite   | PCE<br>(%) | Stability<br>(hr)                                | Stability testing conditions  | Ref |
|---|-------------|-------------|-------------------|-----------------|----------------------|---|------------|--|---|-----|
| pentafluorophenyl<br>ethylammonium<br>iodide                        | 1           | horizontal  | 8                 | n-i-p           | IPA                  | FAMACsPbI <sub>3</sub>  | 22.2       | T <sub>90</sub> = 1000                           | Unencapsulated (~40% RH air),<br>MPP tracking in continuous 1-sun<br>illumination   | 605 |
| pentylammonium<br>iodide  | 1           | N/A         | 10                | p-i-n           | Vacuum<br>Deposition | MAPbI <sub>3</sub>  | 18.3       | N/A  | N/A   | 613 |
| Fluorophenethyl-<br>ammonium  | 1+2         | disordered  | 20-60             | n-i-p           | IPA                  | Cs <sub>0.10</sub> FA <sub>0.77</sub> MA <sub>0.13</sub><br>PbI <sub>2.59</sub> Br <sub>0.41</sub>                    | 20.5       | N/A  | N/A   | 618 |
| Phenylethyl-<br>ammonium iodide                                     | 1+2         | horizontal  | 20-60             | n-i-p           | IPA                  | Cs <sub>0.10</sub> FA <sub>0.77</sub> MA <sub>0.13</sub><br>PbI <sub>2.59</sub> Br <sub>0.41</sub>                    | 20.6       | N/A  | N/A   | 618 |
| Vinylbenzyl-<br>ammonium<br>bromide                                 | 1+2         | horizontal  | 10                | n-i-p           | CF:IPA<br>(97:3)     | (FAPbI <sub>3</sub> ) <sub>0.95</sub><br>(MAPbBr <sub>3</sub> ) <sub>0.05</sub>                                       | 21.7       | N/A  | N/A   | 621 |
| Butylammonium<br>lead iodide<br>(BA <sub>2</sub> PbI <sub>4</sub> ) | 1           | horizontal  | 80                | n-i-p           | Solid-state          | (FAPbI <sub>3</sub> ) <sub>0.95</sub><br>(MAPbBr <sub>3</sub> ) <sub>0.05</sub>                                       | 24.5       | T <sub>99</sub> = 1056<br>T <sub>98</sub> = 1620 | Unencapsulated (85% RH, air)<br>periodic J-V measurement<br>Encapsulated MPP tracking in<br>continuous 1-sun illumination | 221 |
| 4-vinylbenzyl-<br>ammonium<br>bromide                               | 1           | horizontal  | 35                | n-i-p           | IPA                  | (FAPbI <sub>3</sub> ) <sub>0.95</sub><br>(MAPbBr <sub>3</sub> ) <sub>0.05</sub>                                       | 21.9       | N/A  | N/A   | 614 |
| oleylammonium<br>iodide   | 2+3         | horizontal  | ~50               | p-i-n           | chloroform           | Cs <sub>0.03</sub> (FA <sub>0.9</sub> MA <sub>0.1</sub> ) <sub>0.97</sub><br>PbI <sub>3</sub>                         | 24.3       | T <sub>96</sub> = 1200                           | Encapsulated (85°C 85% RH),<br>periodic J-V measurement   | 229 |
| butylammonium   | 3           | vertical    | 50                | n-i-p           | ACN                  | Cs <sub>0.05</sub> (MA <sub>0.10</sub> FA <sub>0.85</sub> )<br>Pb(I <sub>0.90</sub> Br <sub>0.10</sub> ) <sub>3</sub> | 24.5       | T <sub>99</sub> = 2000                           | Encapsulated (air), MPP tracking<br>in continuous 1-sun illumination  | 241 |

## 7. Synergistic applications of mixed 3D-2D halide perovskites

3D/2D halide perovskites have gained a lot of attention in recent years due to their unique electronic and optical properties, as well as their ease of synthesis and processing. While much of the research on halide perovskites has focused on their applications in solar cells, there are many other potential applications for these materials.

Here are some potential applications of 3D/2D heterostructure halide perovskites other than solar cells:

**1. Light-Emitting Diodes (LEDs):** 3D/2D heterostructure halide perovskites have shown promise as materials for LEDs due to their high luminescence efficiency and tunable emission color. Researchers have been exploring the use of these materials for display and lighting applications.

**2. Photodetectors:** halide perovskite photodetectors have high sensitivity, fast response times, and can detect a wide range of wavelengths. 3D/2D heterostructure halide perovskites can further improve the performance of these photodetectors, making them useful for applications such as imaging and sensing.

**3. Transistors:** halide perovskite transistors have shown promise for use in electronic devices due to their high carrier mobility and low trap density. 3D/2D heterostructure halide perovskites could potentially improve the performance of these transistors by controlling the charge transport properties.

**4. Lasers:** 3D/2D heterostructure halide perovskites have also shown promise in the development of lasers, which are important for a variety of applications, including telecommunications, data storage, and medical devices. 3D/2D heterostructure halide perovskites can be engineered for tunable emission, high quantum efficiency, and low lasing threshold, making them energy-efficient and useful for applications such as spectroscopy, bioimaging, and precision machining.

**5. Catalysts:** halide perovskites have also been explored for use as catalysts, particularly for energy conversion and storage applications. 3D/2D

heterostructure halide perovskites can improve the catalytic activity and stability of these materials, making them useful for applications such as fuel cells and electrolyzers.

These are just a few examples of the many potential applications for 3D and 2D halide perovskites beyond solar cells. As research in this area continues, it is likely that additional applications will be discovered.

### 7.1. Two-dimensional halide perovskites as selective contacts

The relatively low efficiency of 2D or quasi 2D halide perovskite solar cells in most cases can be attributed to the poor out-of-plane charge transport due to the presence of insulating organic cations present between the conducting inorganic octahedral slabs. A solution for this is designing organic cations with high charge carrier mobilities, that can solve the efficiency issues of 2D halide perovskite solar cells once and for all. Not much work has been carried out to replace the insulating organic spacer cations with conductive ones, which will require a smart design for maintaining the stability of the 2D halide perovskite, along with enhancing the conductivity. The development of these would also enable the replacement of expensive, hygroscopic and unstable hole transport layers being widely used in the n-i-p architectures of the halide perovskite solar cell.

Wang et al., reported a bifunctional organic cation (TA-PMA<sup>+</sup>) which consists of two subunits: (i) a phenylmethylammonium (PMA<sup>+</sup>) cation group that forms a RP structure with (ii) a triarylamine (TA) group that helps in hole extraction from RP halide perovskite to the hole-transporting layer (HTL).<sup>616</sup> This designed organic cation has dual functionality, as it can not only improve the stability of the solar cells against humid environment due to the hydrophobic nature of the formed RP halide perovskite but also enables hole-transport between RP halide perovskite slabs and the HTL. Using these, they fabricated n-i-p planar heterojunction device which gave a champion efficiency of 20.71% with excellent operational stability maintaining 92% of initial efficiency after 500 h of continuous illumination without encapsulation. In another approach,

Malouangou et al, deposited a thin 2D halide perovskite by spin-coating PEABr cation on the top of 3D halide perovskite to obtain an efficiency of 20.5% with high stability compared to the 3D counterpart.<sup>617</sup> They have shown that the thin 2D halide perovskite layer formed on top of 3D layer passivates the halide and cationic vacancies and also facilitates hole transport. In a similar work reported by Ghoreishi et al., the presence of benzylammonium lead iodide (BZA<sub>2</sub>PbI<sub>4</sub>) enables solar cells with an efficiency of 15.04% using dopant free hole transport layers indicating the charge carrier extraction properties of the 2D halide perovskite along with the ability to passivate defects at the interface.<sup>628</sup>

## 7.2. 3D/2D halide perovskites for light emitting diodes

The light-emitting diode basically works on the principle of radiative recombination of electrons and holes that are injected into the semiconductor material.<sup>648</sup> Important characteristics of a light emitting diode includes the photoluminescence quantum yield (PLQY) for the semiconductor material, external quantum efficiency (EQE), and turn-on voltage<sup>630</sup>. There have been several reports of using the 2D and 3D halide perovskites individually for light emitting applications. Yuan et al., used PEA as the organic cation to fabricate PEA<sub>2</sub>(CH<sub>3</sub>NH<sub>3</sub>)<sub>n-1</sub>Pb<sub>n</sub>I<sub>3n+1</sub> 2D halide perovskite, which provided an EQE of 8.8%, with a luminous efficiency of 80 W sr<sup>-1</sup> m<sup>-2</sup> at low voltages<sup>632</sup>. These 2D halide perovskite materials allowed efficient carrier funneling to the active zone leading to increase in efficiency. The 2D halide perovskite materials have resonant excitonic features at RT making them in principle effective emitting layers to obtain high efficiency halide perovskite LED. However, the structure of 2D nanosheets (<n>=1) is unfavorable for high luminescence efficiency, because of the possible thermal quenching of excitons at room temperature. A simple strategy was developed by Yang et al., to stop the growth of NMA<sub>2</sub>PbBr<sub>4</sub>'s nanosheets by intentionally adjusting the ratio of FABr in the precursor solution<sup>331</sup>. They observed the presence of 3D halide perovskite and NMA<sub>2</sub>PbBr<sub>4</sub> in the 2D material, and if the NMA<sub>2</sub>PbBr<sub>4</sub> component increases, the electroluminescence efficiency tends

to go down. However, they observed that the addition of FABr plays a dual role by inhibiting the n=1 halide perovskite, and improving the quality of halide perovskite film leading to a PLQY of 61% with a current efficiency, and EQE of 46.8 cd A<sup>-1</sup> and 14.9%. Shang et al., reported the synthesis of a composite with PEA<sub>2</sub>Cs<sub>n-1</sub>Pb<sub>n</sub>Br<sub>3n+1</sub> and Cs<sub>4</sub>PbBr<sub>6</sub>.<sup>634</sup> The formation of a composite reduces the carrier diffusion length, and forms cascaded band alignment leading to much improved PLQY. The light emitting diodes fabricated with 20% of Cs<sub>4</sub>PbBr<sub>6</sub> gave an EQE of 4.5% with a luminance of 3,259 Cd/m<sup>2</sup>. In a similar effort, Wu et al., added NABr to CsPbBr<sub>3</sub> to obtain 2D-3D halide perovskites achieving an EQE of 15.9%, with high stability. They showed that the addition of 15% NABr increases the PLQY to 51%<sup>649</sup>. Further increase in the NABr decreases the PLQY due to the dominant presence of Na<sub>2</sub>Cs<sub>n-1</sub>Pb<sub>n</sub>Br<sub>3n+1</sub> (n < 2) phase in the film. As a general comparison, the 2D or 2D/3D halide perovskites have better advantages for light emitting applications compared to their 3D counterpart, because of large exciton binding energy, high PLQY, and increased recombination rate. However, it is interesting to note that most of the experiments show that the 2D/3D halide perovskites are better performing than the 2D halide perovskites due to high luminous efficiency. In addition, the presence of low n 2D halide perovskites results in a decrease of the PLQY due to thermal quenching. As a result, it becomes imperative to control the amount of 2D in the 2D/3D halide perovskite in order to make an efficient light emitting diode.

## 7.3. 3D/2D halide perovskites for Photodetectors

Photodetectors are devices that convert light into electrical signals, with applications related to optical communication, imaging, environmental monitoring, and biosensing.<sup>650-658</sup> There are three processes involved in a photodetector operation 1) absorption of incident light to produce charge carriers; 2) migration of charge carriers; and 3) the collection of the carriers to produce a current. The important parameters to measure the performance of the device are detectivity, responsivity, EQE, response time, on/off ratio, and photoconductive gain (G)<sup>659,660</sup>. The 2D halide perovskite materials have attracted a lot of attention compared to the 3D counterparts



because of its organic composition which provides a large structural diversity. In addition, the inherent instability of the 3D halide perovskites has limited their use in photodetectors. Looking forward to the advances made in the field of PV devices and LEDs using 2D halide perovskites, it was expected to make an impact in the field of photodetectors.

Zhou et al., fabricated photodetectors using  $\text{BA}_2\text{MA}_{n-1}\text{Pb}_n\text{I}_{3n+1}$  ( $n=1, 2, 3$ ), Ruddlesden-popper 2D halide perovskite materials<sup>64</sup>. The change in the  $n$  value leads to different bandgaps, and hence giving different optical responses with response times in the order of milliseconds. The responsivity measured for the  $n=1, 2$  and  $3$  devices were 3.0, 7.3 and 12.8 mA/W, respectively under white light with a bias voltage of 30 V. In the same time, Liu et al., fabricated a single crystal photodetector using  $\text{BA}_2\text{PbBr}_4$  with interdigitated graphene as the electrode in a lateral device<sup>661</sup>. The device gave a dark current of  $10^{-10}$ , responsivity of 2100 A/W, and on/off ratio of  $10^3$ . Further, Liu et al., grew 2D  $\text{CH}_3\text{NH}_3\text{PbI}_3$  nanodisk array on a Si/SiO<sub>2</sub> substrate with boron nitride as a buffer layer to fabricate a phototransistor<sup>662</sup>. They measured a responsivity of 22 and 12 A W<sup>-1</sup> at a wavelength of 405 and 532 nm when biased at 1V. In addition, they measured the rise and fall time to be tens of millisecond with the on/off ratio of  $10^2$ . Song et al., observed some interesting results with a 2D  $\text{CsPbBr}_3$  nanosheet as a photo detector, giving a responsivity of 0.25 A W<sup>-1</sup> with an on/off ratio of  $10^4$  which is better than the commercially available silicon based optoelectronics<sup>663</sup>. They also showed a stability much better than the 3D  $\text{MAPbI}_3$  halide perovskite. Wang et al. incorporated PEAI into  $\text{MAPbI}_3$  to build a photodetector, which improved the crystallinity, and environment stability of the halide perovskites<sup>664</sup>. They observed a responsivity of 0.53 A/W, dark current of  $1.76 \times 10^{-7}$  A/cm, and detectivity of  $2.20 \times 10^{12}$  Jones. The devices show good stability which maintains 76% of the initial current after 80 days of storage under ambient conditions. Presently, 2D/3D halide perovskites are much less studied in the field of photodetectors. Exploring other 2D halide perovskite materials having excellent photoelectric performance and easy processing can be the direction in the future.

#### 7.4. 3D/2D halide perovskites in lasing applications

One key requirement for electrically pumped lasers is efficient carrier injection toward the active emitting zone, which can be achieved through multiple layer heterostructures. III-V semiconductor lasers have been the mainstay for optical communication, but recent research highlights the potential of high-performance halide perovskite materials, which exhibit a high concentration of excited states due to the presence of inhomogeneous energy landscapes.<sup>665-667</sup> Thin films of quasi-2D halide perovskites exhibit a random distribution of quantum wells, leading to the formation of a type I heterostructure where all excited carriers funnel to lower energy states.

In 2020, Qin and colleagues reported the first successful demonstration of continuous wave (CW) lasing at room temperature using quasi-two-dimensional (quasi-2D) halide perovskites.<sup>668</sup> Specifically, they studied thin films of quasi-2D halide perovskite with PEABr and NMABr as the organic spacer cation, and observed the presence of long-lived triplet excitons that impeded population inversion during amplified spontaneous emission and optically pumped pulsed and CW lasing. To overcome this challenge and achieve stable green quasi-2D halide perovskite lasers under CW optical pumping in air at room temperature, the researchers used a distributed-feedback cavity with high quality factor and triplet management strategies. Additionally, another team also observed low-temperature ( $T \sim 100\text{K}$ ) CW lasing in the orthorhombic phase of 3D halide perovskite  $\text{MAPbI}_3$ , where randomly distributed low bandgap tetragonal-phase inclusions were generated by local heating of the pump laser<sup>669</sup>. These examples suggest that to achieve continuous wave (CW) lasing in halide perovskites, it may be crucial to utilize type I heterostructures, which can effectively inject carriers in a smaller volume of the film. Traditional "bulk heterostructure type" halide perovskites are randomly mixed-phase systems, which will help to investigate the potential of planar and ordered multilayer halide perovskite heterostructures with type I band alignment. By doing so, we can control

the energy transfer and facilitate lasing applications in these materials.

Sun et al., discovered a new phenomenon where 0D  $\text{Cs}_4\text{PbBr}_6$  can be converted into 2D/3D  $\text{CsPb}_2\text{Br}_5/\text{CsPbBr}_3$  halide perovskite heterostructures by exposing it to water at room temperature<sup>670</sup>. The derived 2D/3D composite maintained a narrow-band green light-emitting feature at 518 nm which is characteristic of the band-edge transition of  $\text{CsPbBr}_3$  (as shown in Fig. 1c). They were able to achieve random lasing with incoherent feedback in the developed 2D/3D halide perovskite heterostructure, whereas 0D  $\text{Cs}_4\text{PbBr}_6$  showed no signature of light amplification even when optically pumped much harder. The resultant random lasing demonstrated high water resistance, suggesting the potential of the developed 2D/3D heterostructures to function in harsh environments. Recently, Li et al., showed a planar heterostructures which was fabricated by

thermally laminating a wider-bandgap  $\text{CsPbBr}_3(\text{BABr})_x$  layer onto a lower-bandgap  $\text{CsPbBr}_3$  layer at 100°C and 80 MPa<sup>671</sup>. The resulting heterostructure exhibited a type I band alignment that supported excited-state transfer. They observed amplified spontaneous emission (ASE) as a function of the thickness of the  $\text{CsPbBr}_3$  layer, which supported the hypothesis of energy transfer. Despite the non-optimal energy transfer in these heterostructures, a VCSEL based on the planar heterostructure demonstrated a respectable threshold of  $46 (\pm 15) \mu\text{J cm}^{-2}$ .

Overall, 3D/2D heterostructures have shown great promise for lasing applications and are an active area of research. The development of new materials and fabrication techniques for 3D/2D heterostructures is expected to lead to further advances in this field.

## 8. Conclusions

As investigated in this review, the past few years of research have demonstrated exciting results on 3D-2D halide perovskite systems as semiconductor materials, particularly in solar cells. However, key areas of further research in 3D-2D systems could unlock exciting new technologies both for solar cells and for other optoelectronic applications with commercially viable long-term durability. Here, we attempt to summarize these research frontiers and comment on technologies they can enable. Our idea is that this summary inspires new researchers to 3D-2D halide perovskites to help push the boundaries of the field and provides a starting point for diving into solving key scientific and engineering challenges without being distracted by the large body of halide perovskite research.

### 8.1. Future work for 3D-2D stacks

#### 1. Orientation control of 2D layers

Control over orientation of the 2D layer in a 3D-2D stack is a persistent challenge, as commented on above. This goal is more pertinent given the extreme anisotropy in materials properties which 2D halide perovskites exhibit in the in-plane compared to out-of-plane directions, particularly regarding electronic transport. Scalable, repeatable processing methods

that can realize vertically oriented layers must be developed for all the different structural phases (RP, DJ and ACI) of the 2D perovskites.

#### 2. Interface sharpness, chemistry control, and n-value control of 2D layers

The sharpness of the 3D-2D interface needs to be improved to enable higher-performance solar cells and novel optoelectronic applications. Reducing the interface thickness requires no longer relying on ion diffusion from the 3D layer to form the 2D halide perovskite, as some recent work including by our group has achieved. Removing interdiffusion also allows for the use of disparate A, B, and X-site ions for the 3D and 2D layers, which significantly expands the design space for 3D-2D stacks. Related to interface sharpness and degree of ion interdiffusion is the presence of a gradient in n-value from high-n at the 3D-2D surface to low-n in the 2D bulk. Removing or suppressing interdiffusion should grant greater control over 2D bulk n-value and n-value purity, which can likewise expand the design space of 3D-2D stacks and unlock new optoelectronic applications.

#### 3. 2D band tuning and electrical doping

2D halide perovskites have a greater degree of band tunability than 3D halide perovskites, both because their A'-site cation and n-value introduce additional degrees of freedom for tuning electronic structure and because their lattice should be more accommodating towards electrical doping. Although band tuning is already often employed in 3D-2D stacks, with better control over n-value, a deeper understanding of the effect of A'-site engineering on band structure, and a rigorous investigation of 2D doping, the precision with which the band offset between the 3D and 2D layers is controlled could be significantly improved. The potential for 2D doping further raises the possibility of using a p-doped or n-doped 2D layer as a selective HTL or ETL, respectively.

#### **4. 2D-3D and 2D-3D-2D stacks**

halide perovskite stacks with a 3D layer deposited above a 2D layer have up until now not been demonstrated through solution processing techniques, in particular because of a lack of suitable orthogonal solvent for 3D halide perovskites that does not damage or dissolve a 2D layer. The realization of solution-processable 2D-3D and 2D-3D-2D stacks could have important implications for solar cells, allowing for interfacial 2D layers at both 3D halide perovskite-CTL surfaces in a device. It could also create quantum well structures with implications for, among other things, lasing and photodetection.

#### **5. Functionalizing 2D layers**

Most 3D-2D halide perovskite stacks use the 2D layer as a conventional semiconductor or buffer layer. However, the unique materials properties of 2D halide perovskites and the design space of the A'-site cation opens the possibility of functionalizing the 2D layer and introducing novel behavior. For example, incorporating A'-site cations with a functional group to bind to a particular surface or molecule could allow for charge transfer from the 3D-2D halide perovskite to that molecule. Alternately, exploiting unique properties of 2D halide perovskites, for example ferroelectricity, can introduce unique behavior at the interface.

#### **Key technological goals for 3D-2D stacks**

**2+3+5** → A 3D-2D stack with a water-stable 2D layer for photocatalysis

**2+3+4** → 3+layered quantum well structures for electronics and photonics

**1+2+3** → A halide perovskite solar cell with a 2D HTL and/or ETL

**1+2+3+4** → A 3D-2D halide perovskite High-Electron-Mobility Transistor (HEMT)

**1+2+3+5** → A perovskite device that interfaces with a substrate or environment through 2D spacer ligands

### **8.2. Future work for 3D-2D composites**

#### ***1. Improving hydrophobicity and stability of 3D-2D composites***

The stability of 3D-2D composite systems can still be increased. In particular, engineering the A'-site cation and promoting the diffusion of 2D phases to surfaces and grain boundaries could improve the hydrophobicity of 3D-2D composites. The durability towards heat and light can also be improved through the suppression of ion migration and the localization of degradation products, which is of particular importance for commercial devices. This will require simultaneous research on A'-site cation interactions with reactive species and research on 3D-2D film formation.

#### ***2. Multifunctional A'-site cations for defect passivation***

The design space of A'-site cations can accommodate functional groups to passivate defects in 3D halide perovskites, particularly those common at surfaces. Interrogating this design space and rationally constructing spacer cations to target common defects could both reduce nonradiative recombination and improve stability in a variety of environmental conditions.

#### ***3. Lattice matching and strain control***

The quasi-perovskite structure of 2D halide perovskites can serve as a template for 3D growth in composite systems. Since the degree of octahedral tilt and lattice spacing varies between 3D and 2D halide perovskites depending on the A'-site, 2D halide perovskites could introduce either expansive or compressive strain into a 3D lattice by coordinating at grain boundaries. 2D-induced strain could be employed to improve the optoelectronic

properties of a 3D halide perovskite by increasing its Pb-I-Pb angle towards 180°, to increase the barrier to ion migration or the diffusion of reactive species, or to stabilize the perovskite phase of phase-unstable perovskites such as FAPbI<sub>3</sub> and CsPbI<sub>3</sub>.

#### **4. Imbuing 3D bulk with 2D materials properties**

2D halide perovskites have unique materials properties beyond improved stability over 3D halide perovskites. The extent to which these properties can be transferred to a 3D-2D composite should be explored. For instance, ferroelectric 2D halide perovskites could confer a static ferroelectric response to a 3D lattice. Likewise, chiral 2D halide perovskites could give a composite the behavior of a chiral optoelectronic material. 3D-2D composites could be used to merge the unique functionality of 2D halide perovskites with the improved optoelectronic properties and narrow bandgaps of 3D halide perovskites.

#### **5. Characterization of 3D-2D microstructure**

New characterization techniques need to be developed to identify and study the 2D phase within 3D-2D composites. In particular, the location of the 2D phase should be resolved. Examination of grain boundaries for the presence and behavior of 2D interfacial layers, either directly through imaging or indirectly, will help to develop more effective methods of passivating such grain boundaries or varying their behavior. In-situ characterization of the 2D component of composites, both its location and its phase, can help to understand and improve the formation and degradation mechanisms of composite films.

#### **Key technological goals for 3D-2D composites**

**1+3+5** → A water-stable 3D-2D composite film and device

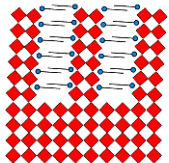
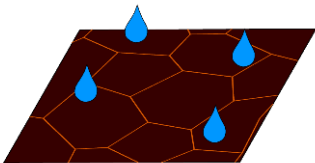
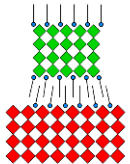
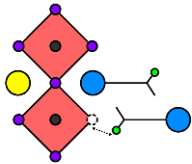
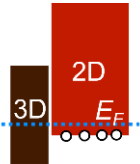
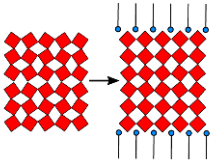
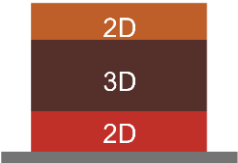
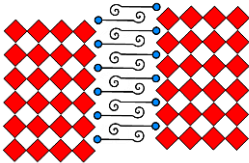
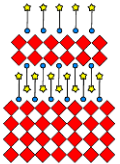
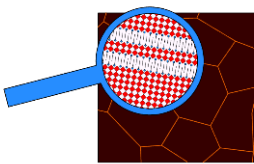
**1+2+3+5** → A MA/Cs-free 3D-2D composite device with commercial stability and efficiency

**1+2+3+5** → A Pb-free 3D-2D composite device with commercial stability and efficiency

**4+5** → A 3D-chiral 2D composite device for light polarization detection

**4+5** → A 3D-FE 2D composite ferroelectric solar cell

In conclusion, 3D/2D halide perovskite heterostructure solar cells that incorporate both 2D and 3D halide perovskite materials have demonstrated great potential for achieving high efficiency and long-term stability. The use of 2D halide perovskites as interlayers or as a component of the halide perovskite structure has been shown to improve the device stability and reduce defects. Additionally, 2D halide perovskites exhibit unique electronic properties that can be utilized to tune the band alignment and optical properties of the solar cell, resulting in enhanced light absorption and charge transport. On the other hand, 3D halide perovskites have high absorption coefficients, suitable bandgap, and high carrier mobility, which are necessary for efficient solar cell operation. By combining the unique properties of both 2D and 3D halide perovskites, 3D/2D halide perovskite heterostructures can achieve high efficiency and long-term stability, making them a promising candidate for a wide range of optoelectronic applications. However, there are still challenges that need to be addressed, such as the optimization of interfacial properties, reduction of hysteresis, and long-term stability. Additionally, the large-scale production and commercialization of 3D/2D halide perovskite heterostructure solar cells will require further development and standardization of fabrication methods. Overall, 3D/2D halide perovskite heterostructure solar cells with both 2D and 3D halide perovskite properties show great potential for achieving high-efficiency, low-cost, and long-term stable solar cell technology. Further research and development in this area will pave the way for the widespread adoption of halide perovskite solar cells in the near future.

| 3D-2D stacks  |  | 3D-2D composites  |  |
|---|--|---|--|
| Open challenge  | Graphical representation   | Open challenge  | Graphical representation   |
| 1. Orientation control                                |   | 1. Improving hydrophobicity and stability of 3D-2D        |   |
| 2. Interface sharpness, chemistry and n-value control |   | 2. Multifunctional A'-site cations for defect passivation |   |
| 3. 2D band tuning and electrical doping               |   | 3. Lattice matching and strain control                    |   |
| 4. 2D-3D and 2D-3D-2D stacks                          |   | 4. Imbuing 3D bulk with 2D properties                     |   |
| 5. Functionalizing 2D layers                          |  | 5. Characterization of 3D-2D microstructure               |  |

**Figure 38: Key future research directions for 3D-2D halide perovskite systems.** Research directions are separated into those pertaining to 3D-2D stacks (left) and 3D-2D composites (right).

## Declarations

**Acknowledgments:** I.M. acknowledges the financial support from the Hertz Foundation. J.H. acknowledges the financial support from the China Scholarship Council (No. 202107990007). I.M. and J.P. acknowledge the National Science Foundation Graduate Research Fellowship Program (This material is based upon work supported by the National Science Foundation Graduate Research

Fellowship Program under grant no. NSF 20-587. Any opinions, findings and conclusions or recommendations expressed in this material are those of the author and do not necessarily reflect the views of the National Science Foundation). J.E. acknowledges the financial support from the Institut Universitaire de France.

**Competing interests:** The authors declare no competing interests.

## References

1. Renewable Capacity Statistics 2022.  
<https://www.irena.org/publications/2022/Apr/Renewable-Capacity-Statistics-2022> (2022).
2. Organization (WMO), W. M. & World Meteorological Organization (WMO). 2022 *State of Climate Services: Energy (WMO-No. 1301)*. (WMO, 2022).
3. Net Zero by 2050 – Analysis. *IEA*  
<https://www.iea.org/reports/net-zero-by-2050>.
4. Song, Z. *et al.* A technoeconomic analysis of perovskite solar module manufacturing with low-cost materials and techniques. *Energy & Environmental Science* **10**, 1297–1305 (2017).
5. Best Research-Cell Efficiency Chart | Photovoltaic Research | NREL.  
<https://www.nrel.gov/pv/cell-efficiency.html>.
6. Kojima, A., Teshima, K., Shirai, Y. & Miyasaka, T. Organometal halide perovskites as visible-light sensitizers for photovoltaic cells. *Journal of the american chemical society* **131**, 6050–6051 (2009).
7. Brivio, F., Butler, K. T., Walsh, A. & Van Schilfgaarde, M. Relativistic quasiparticle self-consistent electronic structure of hybrid halide perovskite photovoltaic absorbers. *Physical Review B* **89**, 155204 (2014).
8. Stoumpos, C. C., Malliakas, C. D. & Kanatzidis, M. G. Semiconducting Tin and Lead Iodide Perovskites with Organic Cations: Phase Transitions, High Mobilities, and Near-Infrared Photoluminescent Properties. *Inorg. Chem.* **52**, 9019–9038 (2013).
9. Goldschmidt, V. M. Die Gesetze der Krystallochemie. *Naturwissenschaften* **14**, 477–485 (1926).
10. Li, Z. *et al.* Stabilizing perovskite structures by tuning tolerance factor: formation of formamidinium and cesium lead iodide solid-state alloys. *Chemistry of Materials* **28**, 284–292 (2016).
11. Li, C. *et al.* Formability of  $ABX_3$  ( $X = F, Cl, Br, I$ ) halide perovskites. *Acta Crystallographica Section B: Structural Science* **64**, 702–707 (2008).
12. Kieslich, G., Sun, S. & Cheetham, A. K. An extended tolerance factor approach for organic–inorganic perovskites. *Chemical science* **6**, 3430–3433 (2015).
13. Poglitsch, A. & Weber, D. Dynamic disorder in methylammoniumtrihalogenoplumbates (II) observed by millimeter-wave spectroscopy. *The Journal of Chemical Physics* **87**, 6373–6378 (1987).



14. Møller, C. K. Crystal structure and photoconductivity of caesium plumbahalides. *Nature* **182**, 1436–1436 (1958).
15. Stoumpos, C. C. & Kanatzidis, M. G. The renaissance of halide perovskites and their evolution as emerging semiconductors. *Accounts of chemical research* **48**, 2791–2802 (2015).
16. Schueller, E. C. *et al.* Crystal structure evolution and notable thermal expansion in hybrid perovskites formamidinium tin iodide and formamidinium lead bromide. *Inorganic chemistry* **57**, 695–701 (2018).
17. Saliba, M. *et al.* Cesium-containing triple cation perovskite solar cells: improved stability, reproducibility and high efficiency. *Energy & environmental science* **9**, 1989–1997 (2016).
18. Hao, F., Stoumpos, C. C., Chang, R. P. H. & Kanatzidis, M. G. Anomalous Band Gap Behavior in Mixed Sn and Pb Perovskites Enables Broadening of Absorption Spectrum in Solar Cells. *J. Am. Chem. Soc.* **136**, 8094–8099 (2014).
19. Noh, J. H., Im, S. H., Heo, J. H., Mandal, T. N. & Seok, S. I. Chemical Management for Colorful, Efficient, and Stable Inorganic–Organic Hybrid Nanostructured Solar Cells. *Nano Lett.* **13**, 1764–1769 (2013).
20. Green, M. A., Ho-Baillie, A. & Snaith, H. J. The emergence of perovskite solar cells. *Nature Photon* **8**, 506–514 (2014).
21. Korshunova, K., Winterfeld, L., Beenken, W. J. & Runge, E. Thermodynamic stability of mixed Pb: Sn methyl-ammonium halide perovskites. *physica status solidi (b)* **253**, 1907–1915 (2016).
22. Gratia, P. *et al.* The many faces of mixed ion perovskites: unraveling and understanding the crystallization process. *ACS Energy Letters* **2**, 2686–2693 (2017).
23. Ke, W., Spanopoulos, I., Stoumpos, C. C. & Kanatzidis, M. G. Myths and reality of HPbI<sub>3</sub> in halide perovskite solar cells. *Nature communications* **9**, 4785 (2018).
24. Shannon, R. D. Revised effective ionic radii and systematic studies of interatomic distances in halides and chalcogenides. *Acta Cryst A* **32**, 751–767 (1976).
25. El-Mellouhi, F. *et al.* Hydrogen bonding and stability of hybrid organic–inorganic perovskites. *ChemSusChem* **9**, 2648–2655 (2016).
26. Mannino, G. *et al.* Temperature-dependent optical band gap in CsPbBr<sub>3</sub>, MAPbBr<sub>3</sub>, and FAPbBr<sub>3</sub> single crystals. *The journal of physical chemistry letters* **11**, 2490–2496 (2020).
27. Yamada, K. *et al.* Phase transition and electric conductivity of ASnCl<sub>3</sub> (A= Cs and CH<sub>3</sub>NH<sub>3</sub>).

- Bulletin of the Chemical Society of Japan* **71**, 127–134 (1998).
28. Yamada, K., Nakada, K., Takeuchi, Y., Nawa, K. & Yamane, Y. Tunable perovskite semiconductor  $\text{CH}_3\text{NH}_3\text{SnX}_3$  (X: Cl, Br, or I) characterized by X-ray and DTA. *Bulletin of the Chemical Society of Japan* **84**, 926–932 (2011).
  29. Sharma, V. K. *et al.* Influence of the Halide Ion on the A-Site Dynamics in  $\text{FAPbX}_3$  (X= Br and Cl). *The Journal of Physical Chemistry C* **126**, 7158–7168 (2022).
  30. Zhumekenov, A. A. *et al.* Formamidinium lead halide perovskite crystals with unprecedented long carrier dynamics and diffusion length. *ACS Energy Letters* **1**, 32–37 (2016).
  31. Nagabhushana, G. P., Shivaramaiah, R. & Navrotsky, A. Direct calorimetric verification of thermodynamic instability of lead halide hybrid perovskites. *Proceedings of the National Academy of Sciences* **113**, 7717–7721 (2016).
  32. Tao, S. *et al.* Absolute energy level positions in tin- and lead-based halide perovskites. *Nature communications* **10**, 2560 (2019).
  33. Yamada, K., Fujise, K., Hino, S., Yamane, Y. & Nakagama, T. Characterization of Sn (II)-based perovskites by XRD, DTA, NQR and  $^{119}\text{Sn}$  NMR for photovoltaic applications. *Chemistry Letters* **48**, 749–752 (2019).
  34. Mitzi, D. B. & Liang, K. Synthesis, resistivity, and thermal properties of the cubic perovskite  $\text{NH}_2\text{CH}=\text{NH}_2\text{SnI}_3$  and related systems. *Journal of Solid State Chemistry* **134**, 376–381 (1997).
  35. Berastegui, P., Hull, S. & Eriksson, S. G. A low-temperature structural phase transition in  $\text{CsPbF}_3$ . *Journal of Physics: Condensed Matter* **13**, 5077 (2001).
  36. Fujii, Y., Hoshino, S., Yamada, Y. & Shirane, G. Neutron-scattering study on phase transitions of  $\text{CsPb}\{\text{Cl}\}_3$ . *Phys. Rev. B* **9**, 4549–4559 (1974).
  37. Hirotsu, S., Harada, J., Iizumi, M. & Gesi, K. Structural Phase Transitions in  $\text{CsPbBr}_3$ . *J. Phys. Soc. Jpn.* **37**, 1393–1398 (1974).
  38. Trots, D. M. & Myagkota, S. V. High-temperature structural evolution of caesium and rubidium triiodoplumbates. *Journal of Physics and Chemistry of Solids* **69**, 2520–2526 (2008).
  39. Thao Tran, T. & Shiv Halasyamani, P. Synthesis and characterization of  $\text{ASnF}_3$  (A= $\text{Na}^+$ ,  $\text{K}^+$ ,  $\text{Rb}^+$ ,  $\text{Cs}^+$ ). *Journal of Solid State Chemistry* **210**, 213–218 (2014).
  40. Barrett, J., Bird, S. R. A., Donaldson, J. D. & Silver, J. The Mössbauer effect in tin(II) compounds. Part XI. The spectra of cubic trihalogenostannates(II). *J. Chem. Soc. A* 3105–3108 (1971) doi:10.1039/J19710003105.

41. Fabini, D. H. *et al.* Dynamic Stereochemical Activity of the Sn<sup>2+</sup> Lone Pair in Perovskite CsSnBr<sub>3</sub>. *J. Am. Chem. Soc.* **138**, 11820–11832 (2016).
42. Chung, I. *et al.* CsSnI<sub>3</sub>: Semiconductor or Metal? High Electrical Conductivity and Strong Near-Infrared Photoluminescence from a Single Material. High Hole Mobility and Phase-Transitions. *J. Am. Chem. Soc.* **134**, 8579–8587 (2012).
43. Katan, C., Mercier, N. & Even, J. Quantum and dielectric confinement effects in lower-dimensional hybrid perovskite semiconductors. *Chemical reviews* **119**, 3140–3192 (2019).
44. Papavassiliou, G. C. Three- and low-dimensional inorganic semiconductors. *Progress in Solid State Chemistry* **25**, 125–270 (1997).
45. Mitzi, D. B. Synthesis, structure, and properties of organic-inorganic perovskites and related materials. *Progress in inorganic chemistry* 1–121 (1999).
46. Ishihara, T., Takahashi, J. & Goto, T. Exciton state in two-dimensional perovskite semiconductor (C<sub>10</sub>H<sub>21</sub>NH<sub>3</sub>)<sub>2</sub>PbI<sub>4</sub>. *Solid state communications* **69**, 933–936 (1989).
47. Stoumpos, C. C. *et al.* Ruddlesden–Popper Hybrid Lead Iodide Perovskite 2D Homologous Semiconductors. *Chem. Mater.* **28**, 2852–2867 (2016).
48. Cao, D. H., Stoumpos, C. C., Farha, O. K., Hupp, J. T. & Kanatzidis, M. G. 2D homologous perovskites as light-absorbing materials for solar cell applications. *Journal of the American Chemical Society* **137**, 7843–7850 (2015).
49. Smith, I. C., Hoke, E. T., Solis-Ibarra, D., McGehee, M. D. & Karunadasa, H. I. A layered hybrid perovskite solar-cell absorber with enhanced moisture stability. *Angewandte Chemie International Edition* **53**, 11232–11235 (2014).
50. Blancon, J.-C., Even, J., Stoumpos, C. C., Kanatzidis, M. G. & Mohite, A. D. Semiconductor physics of organic–inorganic 2D halide perovskites. *Nat. Nanotechnol.* **15**, 969–985 (2020).
51. Mao, L. *et al.* Hybrid Dion–Jacobson 2D Lead Iodide Perovskites. *J. Am. Chem. Soc.* **140**, 3775–3783 (2018).
52. Soe, C. M. M. *et al.* New Type of 2D Perovskites with Alternating Cations in the Interlayer Space, (C(NH<sub>2</sub>)<sub>3</sub>)(CH<sub>3</sub>NH<sub>3</sub>)<sub>n</sub>Pb<sub>n</sub>I<sub>3n+1</sub>: Structure, Properties, and Photovoltaic Performance. *J. Am. Chem. Soc.* **139**, 16297–16309 (2017).

53. Billing, D. G. & Lemmerer, A. Synthesis, characterization and phase transitions of the inorganic–organic layered perovskite-type hybrids [(C<sub>n</sub>H<sub>2n+1</sub>NH<sub>3</sub>)<sub>2</sub>PbI<sub>4</sub>](n= 12, 14, 16 and 18). *New Journal of Chemistry* **32**, 1736–1746 (2008).
54. Mączka, M., Ptak, M., Gağor, A., Stefańska, D. & Sieradzki, A. Layered lead iodide of [Methylhydrazinium] 2PbI<sub>4</sub> with a reduced band gap: thermochromic luminescence and switchable dielectric properties triggered by structural phase transitions. *Chemistry of Materials* **31**, 8563–8575 (2019).
55. Billing, D. G. & Lemmerer, A. Inorganic–organic hybrid materials incorporating primary cyclic ammonium cations: The lead iodide series. *CrystEngComm* **9**, 236–244 (2007).
56. Billing, D. G. & Lemmerer, A. Inorganic–organic hybrid materials incorporating primary cyclic ammonium cations: the lead bromide and chloride series. *CrystEngComm* **11**, 1549–1562 (2009).
57. Li, X., Hoffman, J. M. & Kanatzidis, M. G. The 2D Halide Perovskite Rulebook: How the Spacer Influences Everything from the Structure to Optoelectronic Device Efficiency. *Chem. Rev.* **121**, 2230–2291 (2021).
58. Hong, X., Ishihara, T. & Nurmikko, A. V. Dielectric confinement effect on excitons in PbI<sub>4</sub>-based layered semiconductors. *Physical Review B* **45**, 6961 (1992).
59. Papavassiliou, G. C., Patsis, A. P., Lagouvardos, D. J. & Koutselas, I. B. Spectroscopic studies of (C<sub>10</sub>H<sub>21</sub>NH<sub>3</sub>)<sub>2</sub>PbI<sub>4</sub>, (CH<sub>3</sub>NH<sub>3</sub>)(C<sub>10</sub>H<sub>21</sub>NH<sub>3</sub>)<sub>2</sub>Pb<sub>2</sub>I<sub>7</sub>, (CH<sub>3</sub>NH<sub>3</sub>)<sub>3</sub>PbI<sub>3</sub>, and similar compounds. *Synthetic metals* **57**, 3889–3894 (1993).
60. Calabrese, J. *et al.* Preparation and characterization of layered lead halide compounds. *J. Am. Chem. Soc.* **113**, 2328–2330 (1991).
61. Oswald, I. W., Koegel, A. A. & Neilson, J. R. General Synthesis Principles for Ruddlesden–Popper Hybrid Perovskite Halides from a Dynamic Equilibrium. *Chemistry of Materials* **30**, 8606–8614 (2018).
62. Liu, C. *et al.* Imidazolium ionic liquid as organic spacer for tuning the excitonic structure of 2D perovskite materials. *ACS Energy Letters* **5**, 3617–3627 (2020).
63. Cao, D. H. *et al.* Thin films and solar cells based on semiconducting two-dimensional ruddlesden–popper (CH<sub>3</sub>(CH<sub>2</sub>)<sub>3</sub>NH<sub>3</sub>)<sub>2</sub>

- (CH<sub>3</sub>NH<sub>3</sub>)<sup>n-</sup>1Sn<sup>n</sup>I<sub>3</sub><sup>n+</sup>1 perovskites. *ACS Energy Letters* **2**, 982–990 (2017).
64. Yao, K., Wang, X., Xu, Y., Li, F. & Zhou, L. Multilayered perovskite materials based on polymeric-ammonium cations for stable large-area solar cell. *Chemistry of Materials* **28**, 3131–3138 (2016).
65. Blancon, J.-C. *et al.* Scaling law for excitons in 2D perovskite quantum wells. *Nat Commun* **9**, 2254 (2018).
66. Soe, C. M. M. *et al.* Structural and thermodynamic limits of layer thickness in 2D halide perovskites. *Proc. Natl. Acad. Sci. U.S.A.* **116**, 58–66 (2019).
67. Kepenekian, M. *et al.* Concept of lattice mismatch and emergence of surface states in two-dimensional hybrid perovskite quantum wells. *Nano letters* **18**, 5603–5609 (2018).
68. Li, X. *et al.* Negative pressure engineering with large cage cations in 2D halide perovskites causes lattice softening. *Journal of the American Chemical Society* **142**, 11486–11496 (2020).
69. Liu, X. *et al.* Polarization-Driven Self-Powered Photodetection in a Single-Phase Biaxial Hybrid Perovskite Ferroelectric. *Angewandte Chemie International Edition* **58**, 14504–14508 (2019).
70. Mao, L. *et al.* Tunable White-Light Emission in Single-Cation-Templated Three-Layered 2D Perovskites (CH<sub>3</sub>CH<sub>2</sub>NH<sub>3</sub>)<sub>4</sub>Pb<sub>3</sub>Br<sub>10-x</sub>Cl<sub>x</sub>. *J. Am. Chem. Soc.* **139**, 11956–11963 (2017).
71. Geselle, M. & Fuess, H. Crystal structure of tetrakis(ethylammonium) decachlorotriplumbate(II), (C<sub>2</sub>H<sub>5</sub>NH<sub>3</sub>)<sub>4</sub>Pb<sub>3</sub>Cl<sub>10</sub>. *Zeitschrift für Kristallographie - New Crystal Structures* **212**, 241–242 (1997).
72. Hoffman, J. M. *et al.* From 2D to 1D Electronic Dimensionality in Halide Perovskites with Stepped and Flat Layers Using Propylammonium as a Spacer. *J. Am. Chem. Soc.* **141**, 10661–10676 (2019).
73. Li, L. *et al.* Tailored engineering of an unusual (C<sub>4</sub>H<sub>9</sub>NH<sub>3</sub>)<sub>2</sub>(CH<sub>3</sub>NH<sub>3</sub>)<sub>2</sub>Pb<sub>3</sub>Br<sub>10</sub> two-dimensional multilayered perovskite ferroelectric for a high-performance photodetector. *Angewandte Chemie* **129**, 12318–12322 (2017).
74. Mitzi, D. B., Feild, C. A., Harrison, W. T. A. & Guloy, A. M. Conducting tin halides with a layered organic-based perovskite structure. *Nature* **369**, 467–469 (1994).
75. Li, L. *et al.* A Potential Sn-Based Hybrid Perovskite Ferroelectric Semiconductor. *J. Am. Chem. Soc.* **142**, 1159–1163 (2020).

76. Fu, Y. *et al.* Cation Engineering in Two-Dimensional Ruddlesden–Popper Lead Iodide Perovskites with Mixed Large A-Site Cations in the Cages. *J. Am. Chem. Soc.* **142**, 4008–4021 (2020).
77. Han, S. *et al.* High-temperature antiferroelectric of lead iodide hybrid perovskites. *Journal of the American Chemical Society* **141**, 12470–12474 (2019).
78. Chen, H. *et al.* Structural and spectral dynamics of single-crystalline Ruddlesden–Popper phase halide perovskite blue light-emitting diodes. *Science advances* **6**, eaay4045 (2020).
79. Vasileiadou, E. S. *et al.* Insight on the stability of thick layers in 2D Ruddlesden–Popper and Dion–Jacobson lead iodide perovskites. *Journal of the American Chemical Society* **143**, 2523–2536 (2021).
80. Spanopoulos, I. *et al.* Uniaxial expansion of the 2D Ruddlesden–Popper perovskite family for improved environmental stability. *Journal of the American Chemical Society* **141**, 5518–5534 (2019).
81. Jung, M.-H. Hydrophobic perovskites based on an alkylamine compound for high efficiency solar cells with improved environmental stability. *J. Mater. Chem. A* **7**, 14689–14704 (2019).
82. Vasileiadou, E. S. *et al.* Thick-Layer Lead Iodide Perovskites with Bifunctional Organic Spacers Allylammonium and Iodopropylammonium Exhibiting Trap-State Emission. *J. Am. Chem. Soc.* **144**, 6390–6409 (2022).
83. Peng, Y. *et al.* Exploiting the Bulk Photovoltaic Effect in a 2D Trilayered Hybrid Ferroelectric for Highly Sensitive Polarized Light Detection. *Angewandte Chemie International Edition* **59**, 3933–3937 (2020).
84. Xi, J. *et al.* Alternative Organic Spacers for More Efficient Perovskite Solar Cells Containing Ruddlesden–Popper Phases. *J. Am. Chem. Soc.* **142**, 19705–19714 (2020).
85. Wang, J. *et al.* Unusual ferroelectric-dependent birefringence in 2D trilayered perovskite-type ferroelectric exploited by dimensional tailoring. *Matter* **5**, 194–205 (2022).
86. Ma, Y. *et al.* The First Improper Ferroelectric of 2D Multilayered Hybrid Perovskite Enabling Strong Tunable Polarization-Directed Second Harmonic Generation Effect. *Advanced Functional Materials* **31**, 2103012 (2021).
87. Li, D. *et al.* Unprecedented Self-Powered Visible–Infrared Dual-Modal Photodetection Induced by a Bulk Photovoltaic Effect in a Polar



- Perovskite. *ACS Appl. Mater. Interfaces* **14**, 5608–5614 (2022).
88. Li, D. *et al.* A reduced-dimensional polar hybrid perovskite for self-powered broad-spectrum photodetection. *Chem. Sci.* **12**, 3050–3054 (2021).
89. Slavney, A. H. *et al.* Chemical approaches to addressing the instability and toxicity of lead–halide perovskite absorbers. *Inorganic chemistry* **56**, 46–55 (2017).
90. Lai, H. *et al.* Two-dimensional Ruddlesden–Popper perovskite with nanorod-like morphology for solar cells with efficiency exceeding 15%. *Journal of the American Chemical Society* **140**, 11639–11646 (2018).
91. Liu, Y. *et al.* Spacer Cation Alloying of a Homoconformational Carboxylate trans Isomer to Boost in-Plane Ferroelectricity in a 2D Hybrid Perovskite. *J. Am. Chem. Soc.* **143**, 2130–2137 (2021).
92. Li, X. *et al.* Two-Dimensional Halide Perovskites Incorporating Straight Chain Symmetric Diammonium Ions,  $(\text{NH}_3\text{C}_m\text{H}_{2m}\text{NH}_3)(\text{CH}_3\text{NH}_3)_n\text{-1PbI}_{3n+1}$  ( $m = 4\text{--}9$ ;  $n = 1\text{--}4$ ). *J. Am. Chem. Soc.* **140**, 12226–12238 (2018).
93. Li, P. *et al.* Low-Dimensional Dion–Jacobson-Phase Lead-Free Perovskites for High-Performance Photovoltaics with Improved Stability. *Angewandte Chemie International Edition* **59**, 6909–6914 (2020).
94. Mao, L. *et al.* Seven-Layered 2D Hybrid Lead Iodide Perovskites. *Chem* **5**, 2593–2604 (2019).
95. Li, X. *et al.* Two-Dimensional Dion–Jacobson Hybrid Lead Iodide Perovskites with Aromatic Diammonium Cations. *J. Am. Chem. Soc.* **141**, 12880–12890 (2019).
96. Gao, L. *et al.* m-Phenylenediammonium as a New Spacer for Dion–Jacobson Two-Dimensional Perovskites. *J. Am. Chem. Soc.* **143**, 12063–12073 (2021).
97. Daub, M. & Hillebrecht, H. From 1D to 3D: Perovskites within the System  $\text{HSC}(\text{NH}_2)_2/\text{CH}_3\text{NH}_3/\text{PbI}_2$  with Maintenance of the Cubic Closest Packing. *Inorg. Chem.* **60**, 3082–3093 (2021).
98. *Theoretical Modeling of Organohalide Perovskites for Photovoltaic Applications.* (CRC Press, 2017). doi:10.4324/9781315152424.
99. Tang, G., Ghosez, P. & Hong, J. Band-edge orbital engineering of perovskite semiconductors for optoelectronic applications. *The Journal of Physical Chemistry Letters* **12**, 4227–4239 (2021).
100. Quarti, C., Katan, C. & Even, J. Physical properties of bulk, defective, 2D and 0D metal

- halide perovskite semiconductors from a symmetry perspective. *Journal of Physics: Materials* **3**, 042001 (2020).
101. Liu, S.-C. *et al.* An antibonding valence band maximum enables defect-tolerant and stable GeSe photovoltaics. *Nature communications* **12**, 670 (2021).
102. Li, T., Luo, S., Wang, X. & Zhang, L. Alternative Lone-Pair ns<sup>2</sup>-Cation-Based Semiconductors beyond Lead Halide Perovskites for Optoelectronic Applications. *Advanced Materials* **33**, 2008574 (2021).
103. Xiao, Z., Meng, W., Wang, J., Mitzi, D. B. & Yan, Y. Searching for promising new perovskite-based photovoltaic absorbers: the importance of electronic dimensionality. *Materials Horizons* **4**, 206–216 (2017).
104. Even, J., Pedesseau, L., Jancu, J.-M. & Katan, C. Importance of spin–orbit coupling in hybrid organic/inorganic perovskites for photovoltaic applications. *The Journal of Physical Chemistry Letters* **4**, 2999–3005 (2013).
105. Even, J., Pedesseau, L. & Katan, C. Analysis of multivalley and multibandgap absorption and enhancement of free carriers related to exciton screening in hybrid perovskites. *The Journal of Physical Chemistry C* **118**, 11566–11572 (2014).
106. Miyata, A. *et al.* Direct measurement of the exciton binding energy and effective masses for charge carriers in organic–inorganic tri-halide perovskites. *Nature Phys* **11**, 582–587 (2015).
107. Poncé, S., Schlipf, M. & Giustino, F. Origin of low carrier mobilities in halide perovskites. *ACS Energy Letters* **4**, 456–463 (2019).
108. Prasanna, R. *et al.* Band gap tuning via lattice contraction and octahedral tilting in perovskite materials for photovoltaics. *Journal of the American Chemical Society* **139**, 11117–11124 (2017).
109. Filip, M. R., Eperon, G. E., Snaith, H. J. & Giustino, F. Steric engineering of metal-halide perovskites with tunable optical band gaps. *Nature communications* **5**, 5757 (2014).
110. Lee, J.-W., Seol, D.-J., Cho, A.-N. & Park, N.-G. High-Efficiency Perovskite Solar Cells Based on the Black Polymorph of HC(NH<sub>2</sub>)<sub>2</sub>PbI<sub>3</sub>. *Advanced Materials* **26**, 4991–4998 (2014).
111. Eperon, G. E. *et al.* Formamidinium lead trihalide: a broadly tunable perovskite for efficient planar heterojunction solar cells. *Energy & Environmental Science* **7**, 982–988 (2014).
112. Hao, F., Stoumpos, C. C., Cao, D. H., Chang, R. P. H. & Kanatzidis, M. G. Lead-free solid-state

- organic–inorganic halide perovskite solar cells. *Nature Photon* **8**, 489–494 (2014).
113. Edri, E., Kirmayer, S., Cahen, D. & Hodes, G. High Open-Circuit Voltage Solar Cells Based on Organic–Inorganic Lead Bromide Perovskite. *J. Phys. Chem. Lett.* **4**, 897–902 (2013).
114. Rajagopal, A., Stoddard, R. J., Hillhouse, H. W. & Jen, A. K.-Y. On understanding bandgap bowing and optoelectronic quality in Pb–Sn alloy hybrid perovskites. *Journal of Materials Chemistry A* **7**, 16285–16293 (2019).
115. Saxena, R. *et al.* Contrasting temperature dependence of the band gap in  $\text{CH}_3\text{NH}_3\text{PbX}_3$  ( $X = \text{I}, \text{Br}, \text{Cl}$ ): Insight from lattice dilation and electron-phonon coupling. *Phys. Rev. B* **102**, 081201 (2020).
116. Yagyu, H. & Katagami, S. Effect of Cs partial substitution on crystal systems and bandgap values of  $\text{MASnCl}_3$ . *Physica B: Condensed Matter* **633**, 413784 (2022).
117. Wang, L. *et al.* Pressure-induced structural evolution, optical and electronic transitions of nontoxic organometal halide perovskite-based methylammonium tin chloride. *Appl. Phys. Lett.* **111**, 233901 (2017).
118. Chiarella, F. *et al.* Combined experimental and theoretical investigation of optical, structural, and electronic properties of  $\text{CH}_3\text{NH}_3\text{PbX}_3$  thin films ( $X = \text{Cl}, \text{Br}$ ). *Phys. Rev. B* **77**, 045129 (2008).
119. Li, B., Long, R., Xia, Y. & Mi, Q. All-Inorganic Perovskite  $\text{CsSnBr}_3$  as a Thermally Stable, Free-Carrier Semiconductor. *Angewandte Chemie International Edition* **57**, 13154–13158 (2018).
120. Dang, Y. *et al.* Formation of Hybrid Perovskite Tin Iodide Single Crystals by Top-Seeded Solution Growth. *Angewandte Chemie International Edition* **55**, 3447–3450 (2016).
121. Saidaminov, M. I., Abdelhady, A. L., Maculan, G. & Bakr, O. M. Retrograde solubility of formamidinium and methylammonium lead halide perovskites enabling rapid single crystal growth. *Chem. Commun.* **51**, 17658–17661 (2015).
122. Alharbi, O. K. Experimental and Theoretical Investigation on the Temperature-dependent Optical Properties of Hybrid Halide Perovskites. (2022). doi:10.25781/KAUST-94BU7.
123. Igual-Muñoz, A. M., Ávila, J., Boix, P. P. & Bolink, H. J.  $\text{FAPb}_0.5\text{Sn}_0.5\text{I}_3$ : A Narrow

- Bandgap Perovskite Synthesized through Evaporation Methods for Solar Cell Applications. *Solar RRL* **4**, 1900283 (2020).
124. Koh, T. M. *et al.* Formamidinium tin-based perovskite with low  $E_g$  for photovoltaic applications. *J. Mater. Chem. A* **3**, 14996–15000 (2015).
125. Heidrich, K. *et al.* Electronic structure, photoemission spectra, and vacuum-ultraviolet optical spectra of  $\text{CsPb}(\text{Cl})_3$  and  $\text{CsPb}(\text{Br})_3$ . *Phys. Rev. B* **24**, 5642–5649 (1981).
126. Sebastian, M. *et al.* Excitonic emissions and above-band-gap luminescence in the single-crystal perovskite semiconductors  $\text{CsPbB}(\text{r})_3$  and  $\text{CsPbC}(\text{l})_3$ . *Phys. Rev. B* **92**, 235210 (2015).
127. Liu, Z. *et al.* Heavy metal ternary halides for room-temperature x-ray and gamma-ray detection. in *Hard X-Ray, Gamma-Ray, and Neutron Detector Physics XV* vol. 8852 17–23 (SPIE, 2013).
128. Peedikakkandy, L. & Bhargava, P. Composition dependent optical, structural and photoluminescence characteristics of cesium tin halide perovskites. *RSC Adv.* **6**, 19857–19860 (2016).
129. Shahjahan Ali, M., Das, S., Fatha Abed, Y. & A. Basith, M. Lead-free  $\text{CsSnCl}_3$  perovskite nanocrystals: rapid synthesis, experimental characterization and DFT simulations. *Physical Chemistry Chemical Physics* **23**, 22184–22198 (2021).
130. Siddik, A. *et al.* Nonvolatile resistive switching and synaptic characteristics of lead-free all-inorganic perovskite-based flexible memristive devices for neuromorphic systems. *Nanoscale* **13**, 8864–8874 (2021).
131. Chen, W. *et al.* Bifunctional additive 2-amino-3-hydroxypyridine for stable and high-efficiency tin–lead perovskite solar cells. *Journal of Materials Chemistry C* **11**, 151–160 (2023).
132. Jeon, N. J. *et al.* Compositional engineering of perovskite materials for high-performance solar cells. *Nature* **517**, 476–480 (2015).
133. Zhang, F. *et al.* Comparative studies of optoelectrical properties of prominent PV materials: Halide perovskite, CdTe, and GaAs. *Materials Today* **36**, 18–29 (2020).
134. Lei, Y., Xu, Y., Wang, M., Zhu, G. & Jin, Z. Origin, Influence, and Countermeasures of Defects in Perovskite Solar Cells. *Small* **17**, 2005495 (2021).
135. Yuan, Y., Yan, G., Hong, R., Liang, Z. & Kirchartz, T. Quantifying Efficiency Limitations

- in All-Inorganic Halide Perovskite Solar Cells. *Advanced Materials* **34**, 2108132 (2022).
136. Zhang, X., Turiansky, M. E. & Van de Walle, C. G. Correctly Assessing Defect Tolerance in Halide Perovskites. *J. Phys. Chem. C* **124**, 6022–6027 (2020).
137. Huang, H., Bodnarchuk, M. I., Kershaw, S. V., Kovalenko, M. V. & Rogach, A. L. Lead Halide Perovskite Nanocrystals in the Research Spotlight: Stability and Defect Tolerance. *ACS Energy Lett.* **2**, 2071–2083 (2017).
138. Ferreira, A. C. *et al.* Elastic softness of hybrid lead halide perovskites. *Physical Review Letters* **121**, 085502 (2018).
139. Siekmann, J., Ravishankar, S. & Kirchartz, T. Apparent defect densities in halide perovskite thin films and single crystals. *ACS Energy Letters* **6**, 3244–3251 (2021).
140. Cahen, D., Kronik, L. & Hodes, G. Are defects in lead-halide perovskites healed, tolerated, or both? *ACS energy letters* **6**, 4108–4114 (2021).
141. Kurchin, R. C., Gorai, P., Buonassisi, T. & Stevanović, V. Structural and Chemical Features Giving Rise to Defect Tolerance of Binary Semiconductors. *Chem. Mater.* **30**, 5583–5592 (2018).
142. Dunfield, S. P. *et al.* From Defects to Degradation: A Mechanistic Understanding of Degradation in Perovskite Solar Cell Devices and Modules. *Advanced Energy Materials* **10**, 1904054 (2020).
143. Luo, D., Su, R., Zhang, W., Gong, Q. & Zhu, R. Minimizing non-radiative recombination losses in perovskite solar cells. *Nat Rev Mater* **5**, 44–60 (2020).
144. Wilson, J. N., Frost, J. M., Wallace, S. K. & Walsh, A. Dielectric and ferroic properties of metal halide perovskites. *APL Materials* **7**, 010901 (2019).
145. Rakita, Y., Lubomirsky, I. & Cahen, D. When defects become ‘dynamic’: halide perovskites: a new window on materials? *Materials Horizons* **6**, 1297–1305 (2019).
146. Stranks, S. D. *et al.* Electron-Hole Diffusion Lengths Exceeding 1 Micrometer in an Organometal Trihalide Perovskite Absorber. *Science* **342**, 341–344 (2013).
147. Rehman, W. *et al.* Photovoltaic mixed-cation lead mixed-halide perovskites: links between crystallinity, photo-stability and electronic properties. *Energy Environ. Sci.* **10**, 361–369 (2017).
148. Fu, Y., Jin, S. & Zhu, X.-Y. Stereochemical expression of ns<sup>2</sup> electron pairs in metal halide perovskites. *Nat Rev Chem* **5**, 838–852 (2021).

149. Frohna, K. *et al.* Inversion symmetry and bulk Rashba effect in methylammonium lead iodide perovskite single crystals. *Nat Commun* **9**, 1829 (2018).
150. Roma, G., Marronnier, A. & Even, J. From latent ferroelectricity to hyperferroelectricity in alkali lead halide perovskites. *Physical Review Materials* **4**, 092402 (2020).
151. Akkerman, Q. A., Rainò, G., Kovalenko, M. V. & Manna, L. Genesis, challenges and opportunities for colloidal lead halide perovskite nanocrystals. *Nature materials* **17**, 394–405 (2018).
152. Shaklee, K. L. & Nahory, R. E. Valley-Orbit Splitting of Free Excitons? The Absorption Edge of Si. *Phys. Rev. Lett.* **24**, 942–945 (1970).
153. Adhyaksa, G. W. P. *et al.* Carrier Diffusion Lengths in Hybrid Perovskites: Processing, Composition, Aging, and Surface Passivation Effects. *Chem. Mater.* **28**, 5259–5263 (2016).
154. Dong, Q. *et al.* Electron-hole diffusion lengths > 175  $\mu\text{m}$  in solution-grown  $\text{CH}_3\text{NH}_3\text{PbI}_3$  single crystals. *Science* **347**, 967–970 (2015).
155. Ferreira, A. C. *et al.* Direct evidence of weakly dispersed and strongly anharmonic optical phonons in hybrid perovskites. *Communications Physics* **3**, 48 (2020).
156. Schilcher, M. J. *et al.* The Significance of Polarons and Dynamic Disorder in Halide Perovskites. *ACS Energy Lett.* **6**, 2162–2173 (2021).
157. Buizza, L. R. V. & Herz, L. M. Polarons and Charge Localization in Metal-Halide Semiconductors for Photovoltaic and Light-Emitting Devices. *Advanced Materials* **33**, 2007057 (2021).
158. Miyata, K., Atallah, T. L. & Zhu, X.-Y. Lead halide perovskites: Crystal-liquid duality, phonon glass electron crystals, and large polaron formation. *Science Advances* **3**, e1701469 (2017).
159. Meggiolaro, D., Ambrosio, F., Mosconi, E., Mahata, A. & De Angelis, F. Polarons in Metal Halide Perovskites. *Advanced Energy Materials* **10**, 1902748 (2020).
160. Wolf, C., Cho, H., Kim, Y.-H. & Lee, T.-W. Polaronic Charge Carrier–Lattice Interactions in Lead Halide Perovskites. *ChemSusChem* **10**, 3705–3711 (2017).
161. Neukirch, A. J. *et al.* Polaron Stabilization by Cooperative Lattice Distortion and Cation Rotations in Hybrid Perovskite Materials. *Nano Lett.* **16**, 3809–3816 (2016).

162. Egger, D. A. *et al.* What Remains Unexplained about the Properties of Halide Perovskites? *Advanced Materials* **30**, 1800691 (2018).
163. Hehlen, B. *et al.* Pseudospin-phonon pretransitional dynamics in lead halide hybrid perovskites. *Physical Review B* **105**, 024306 (2022).
164. Tamarat, P. *et al.* Universal scaling laws for charge-carrier interactions with quantum confinement in lead-halide perovskites. *Nature Communications* **14**, 229 (2023).
165. Neukirch, A. J. *et al.* Polaron stabilization by cooperative lattice distortion and cation rotations in hybrid perovskite materials. *Nano letters* **16**, 3809–3816 (2016).
166. Shrestha, S. *et al.* Assessing temperature dependence of drift mobility in methylammonium lead iodide perovskite single crystals. *The Journal of Physical Chemistry C* **122**, 5935–5939 (2018).
167. Yi, H. T., Wu, X., Zhu, X. & Podzorov, V. Intrinsic charge transport across phase transitions in hybrid organo-inorganic perovskites. *Advanced Materials* **28**, 6509–6514 (2016).
168. Biewald, A. *et al.* Temperature-dependent ambipolar charge carrier mobility in large-crystal hybrid halide perovskite thin films. *ACS applied materials & interfaces* **11**, 20838–20844 (2019).
169. Mayers, M. Z., Tan, L. Z., Egger, D. A., Rappe, A. M. & Reichman, D. R. How lattice and charge fluctuations control carrier dynamics in halide perovskites. *Nano letters* **18**, 8041–8046 (2018).
170. Munson, K. T., Kennehan, E. R., Doucette, G. S. & Asbury, J. B. Dynamic disorder dominates delocalization, transport, and recombination in halide perovskites. *Chem* **4**, 2826–2843 (2018).
171. Ugur, E. *et al.* Life on the Urbach Edge. *J. Phys. Chem. Lett.* **13**, 7702–7711 (2022).
172. Ledinský, M. *et al.* Impact of Cation Multiplicity on Halide Perovskite Defect Densities and Solar Cell Voltages. *The Journal of Physical Chemistry C* **124**, 27333–27339 (2020).
173. Ledinsky, M. *et al.* Temperature dependence of the urbach energy in lead iodide perovskites. *The journal of physical chemistry letters* **10**, 1368–1373 (2019).
174. Caselli, V. M. *et al.* Charge Carrier Dynamics upon Sub-bandgap Excitation in Methylammonium Lead Iodide Thin Films: Effects of Urbach Tail, Deep Defects, and Two-Photon Absorption. *ACS Energy Lett.* **5**, 3821–3827 (2020).



175. Akin, S., Akman, E. & Sonmezoglu, S. FAPbI<sub>3</sub>-Based Perovskite Solar Cells Employing Hexyl-Based Ionic Liquid with an Efficiency Over 20% and Excellent Long-Term Stability. *Advanced Functional Materials* **30**, 2002964 (2020).
176. Anion Substitution Effects on the Structural, Electronic, and Optical Properties of Inorganic CsPb(I<sub>1-x</sub>Br<sub>x</sub>)<sub>3</sub> and CsPb(Br<sub>1-x</sub>Cl<sub>x</sub>)<sub>3</sub> Perovskites: Theoretical and Experimental Approaches | The Journal of Physical Chemistry C. <https://pubs.acs.org/doi/10.1021/acs.jpcc.0c07983>.
177. Gehrman, C. & Egger, D. A. Dynamic shortening of disorder potentials in anharmonic halide perovskites. *Nat Commun* **10**, 3141 (2019).
178. Jean, J. *et al.* Radiative efficiency limit with band tailing exceeds 30% for quantum dot solar cells. *ACS Energy Letters* **2**, 2616–2624 (2017).
179. Ledinsky, M. *et al.* Temperature dependence of the Urbach energy in lead iodide perovskites. *The journal of physical chemistry letters* **10**, 1368–1373 (2019).
180. Rezaee, E., Zhang, W. & Silva, S. R. P. Solvent Engineering as a Vehicle for High Quality Thin Films of Perovskites and Their Device Fabrication. *Small* **17**, 2008145 (2021).
181. Chao, L. *et al.* Solvent Engineering of the Precursor Solution toward Large-Area Production of Perovskite Solar Cells. *Advanced Materials* **33**, 2005410 (2021).
182. Cao, X. *et al.* A Review of the Role of Solvents in Formation of High-Quality Solution-Processed Perovskite Films. *ACS Appl. Mater. Interfaces* **11**, 7639–7654 (2019).
183. Konstantakou, M., Perganti, D., Falaras, P. & Stergiopoulos, T. Anti-Solvent Crystallization Strategies for Highly Efficient Perovskite Solar Cells. *Crystals* **7**, 291 (2017).
184. Wang, P. *et al.* Solution-Processable Perovskite Solar Cells toward Commercialization: Progress and Challenges. *Advanced Functional Materials* **29**, 1807661 (2019).
185. Wang, K. *et al.* Isothermally crystallized perovskites at room-temperature. *Energy & Environmental Science* **13**, 3412–3422 (2020).
186. Jeon, N. J. *et al.* Solvent engineering for high-performance inorganic–organic hybrid perovskite solar cells. *Nature materials* **13**, 897–903 (2014).
187. Ahn, N. *et al.* Highly reproducible perovskite solar cells with average efficiency of 18.3% and best efficiency of 19.7% fabricated via Lewis base adduct of lead (II) iodide. *Journal of the*

- American Chemical Society* **137**, 8696–8699 (2015).
188. Lee, J.-W. *et al.* Tuning Molecular Interactions for Highly Reproducible and Efficient Formamidinium Perovskite Solar Cells via Adduct Approach. *J. Am. Chem. Soc.* **140**, 6317–6324 (2018).
189. Lee, J.-W., Kim, H.-S. & Park, N.-G. Lewis acid–base adduct approach for high efficiency perovskite solar cells. *Accounts of chemical research* **49**, 311–319 (2016).
190. Yang, W. S. *et al.* High-performance photovoltaic perovskite layers fabricated through intramolecular exchange. *Science* **348**, 1234–1237 (2015).
191. Kim, M. *et al.* Methylammonium Chloride Induces Intermediate Phase Stabilization for Efficient Perovskite Solar Cells. *Joule* **3**, 2179–2192 (2019).
192. Park, N.-G. & Zhu, K. Scalable fabrication and coating methods for perovskite solar cells and solar modules. *Nat Rev Mater* **5**, 333–350 (2020).
193. Li, Z. *et al.* Scalable fabrication of perovskite solar cells. *Nature Reviews Materials* **3**, 1–20 (2018).
194. Jung, Y.-S. *et al.* Progress in Scalable Coating and Roll-to-Roll Compatible Printing Processes of Perovskite Solar Cells toward Realization of Commercialization. *Advanced Optical Materials* **6**, 1701182 (2018).
195. Jung, H. S., Han, G. S., Park, N.-G. & Ko, M. J. Flexible perovskite solar cells. *Joule* **3**, 1850–1880 (2019).
196. Meng, L., You, J., Guo, T.-F. & Yang, Y. Recent advances in the inverted planar structure of perovskite solar cells. *Accounts of chemical research* **49**, 155–165 (2016).
197. Jošt, M., Kegelmann, L., Korte, L. & Albrecht, S. Monolithic perovskite tandem solar cells: a review of the present status and advanced characterization methods toward 30% efficiency. *Advanced Energy Materials* **10**, 1904102 (2020).
198. Mattoni, A., Filippetti, A. & Caddeo, C. Modeling hybrid perovskites by molecular dynamics. *J. Phys.: Condens. Matter* **29**, 043001 (2016).
199. Eames, C. *et al.* Ionic transport in hybrid lead iodide perovskite solar cells. *Nat Commun* **6**, 7497 (2015).
200. Xing, J. *et al.* Ultrafast ion migration in hybrid perovskite polycrystalline thin films under light and suppression in single crystals. *Physical Chemistry Chemical Physics* **18**, 30484–30490 (2016).
201. Yuan, Y. *et al.* Photovoltaic Switching Mechanism in Lateral Structure Hybrid

- Perovskite Solar Cells. *Advanced Energy Materials* **5**, 1500615 (2015).
202. Euvrard, J., Yan, Y. & Mitzi, D. B. Electrical doping in halide perovskites. *Nat Rev Mater* **6**, 531–549 (2021).
203. Wang, Q. *et al.* Qualifying composition dependent p and n self-doping in CH<sub>3</sub>NH<sub>3</sub>PbI<sub>3</sub>. *Applied Physics Letters* **105**, 163508 (2014).
204. Schulz, P. *et al.* Electronic level alignment in inverted organometal perovskite solar cells. *Advanced Materials Interfaces* **2**, 1400532 (2015).
205. Miller, E. M. *et al.* Substrate-controlled band positions in CH<sub>3</sub>NH<sub>3</sub>PbI<sub>3</sub> perovskite films. *Physical chemistry chemical physics* **16**, 22122–22130 (2014).
206. Rakita, Y. *et al.* Tetragonal CH<sub>3</sub>NH<sub>3</sub>PbI<sub>3</sub> is ferroelectric. *Proceedings of the National Academy of Sciences* **114**, E5504–E5512 (2017).
207. Beilsten-Edmands, J., Eperon, G. E., Johnson, R. D., Snaith, H. J. & Radaelli, P. G. Non-ferroelectric nature of the conductance hysteresis in CH<sub>3</sub>NH<sub>3</sub>PbI<sub>3</sub> perovskite-based photovoltaic devices. *Applied Physics Letters* **106**, 173502 (2015).
208. Garten, L. M. *et al.* The existence and impact of persistent ferroelectric domains in MAPbI<sub>3</sub>. *Science Advances* **5**, eaas9311 (2019).
209. Fan, Z. *et al.* Ferroelectricity of CH<sub>3</sub>NH<sub>3</sub>PbI<sub>3</sub> Perovskite. *J. Phys. Chem. Lett.* **6**, 1155–1161 (2015).
210. Kim, H.-S. *et al.* Ferroelectric Polarization in CH<sub>3</sub>NH<sub>3</sub>PbI<sub>3</sub> Perovskite. *J. Phys. Chem. Lett.* **6**, 1729–1735 (2015).
211. Rakita, Y. *et al.* CH<sub>3</sub>NH<sub>3</sub>PbBr<sub>3</sub> is not pyroelectric, excluding ferroelectric-enhanced photovoltaic performance. *APL Materials* **4**, 051101 (2016).
212. Ding, R. *et al.* Flexible Piezoelectric Nanocomposite Generators Based on Formamidinium Lead Halide Perovskite Nanoparticles. *Advanced Functional Materials* **26**, 7708–7716 (2016).
213. Ambrosio, F., De Angelis, F. & Goñi, A. R. The Ferroelectric–Ferroelastic Debate about Metal Halide Perovskites. *J. Phys. Chem. Lett.* **13**, 7731–7740 (2022).
214. Li, D. *et al.* Recent progress of inverted organic–inorganic halide perovskite solar cells. *Journal of Energy Chemistry* **79**, 168–191 (2023).
215. Huang, Y., Lei, X., He, T., Jiang, Y. & Yuan, M. Recent Progress on Formamidinium-Dominated

- Perovskite Photovoltaics. *Advanced Energy Materials* **12**, 2100690 (2022).
216. Park, J. *et al.* Controlled growth of perovskite layers with volatile alkylammonium chlorides. *Nature* 1–3 (2023) doi:10.1038/s41586-023-05825-y.
217. Yoo, J. J. *et al.* Efficient perovskite solar cells via improved carrier management. *Nature* **590**, 587–593 (2021).
218. Jeong, J. *et al.* Pseudo-halide anion engineering for  $\alpha$ -FAPbI<sub>3</sub> perovskite solar cells. *Nature* **592**, 381–385 (2021).
219. Min, H. *et al.* Perovskite solar cells with atomically coherent interlayers on SnO<sub>2</sub> electrodes. *Nature* **598**, 444–450 (2021).
220. Park, B. *et al.* Stabilization of formamidinium lead triiodide  $\alpha$ -phase with isopropylammonium chloride for perovskite solar cells. *Nat Energy* **6**, 419–428 (2021).
221. Jang, Y.-W. *et al.* Intact 2D/3D halide junction perovskite solar cells via solid-phase in-plane growth. *Nat Energy* **6**, 63–71 (2021).
222. Jeong, M. *et al.* Stable perovskite solar cells with efficiency exceeding 24.8% and 0.3-V voltage loss. *Science* **369**, 1615–1620 (2020).
223. Kim, G. *et al.* Impact of strain relaxation on performance of  $\alpha$ -formamidinium lead iodide perovskite solar cells. *Science* **370**, 108–112 (2020).
224. Kim, M. *et al.* Conformal quantum dot–SnO<sub>2</sub> layers as electron transporters for efficient perovskite solar cells. *Science* **375**, 302–306 (2022).
225. Jiang, Q. *et al.* Surface reaction for efficient and stable inverted perovskite solar cells. *Nature* **611**, 278–283 (2022).
226. Li, Z. *et al.* Organometallic-functionalized interfaces for highly efficient inverted perovskite solar cells. *Science* **376**, 416–420 (2022).
227. Zhou, X. *et al.* Integrated Ideal-Bandgap Perovskite/Bulk-Heterojunction Solar Cells with Efficiencies > 24%. *Advanced Materials* **34**, 2205809 (2022).
228. Li, X. *et al.* Constructing heterojunctions by surface sulfidation for efficient inverted perovskite solar cells. *Science* **375**, 434–437 (2022).
229. Azmi, R. *et al.* Damp heat–stable perovskite solar cells with tailored-dimensionality 2D/3D heterojunctions. *Science* **376**, 73–77 (2022).
230. Wu, S. *et al.* Manipulating Crystallographic Orientation via Cross-Linkable Ligand for Efficient and Stable Perovskite Solar Cells. *Small* **n/a**, 2207189.

231. Ma, Y. *et al.* De-doping buried interface in p-i-n perovskite solar cells by utilizing compositional heterogeneity in depth. *Nano Energy* **108**, 108250 (2023).
232. Zhu, Z. *et al.* Correlating the perovskite/polymer multi-mode reactions with deep-level traps in perovskite solar cells. *Joule* **6**, 2849–2868 (2022).
233. Li, G. *et al.* Highly efficient p-i-n perovskite solar cells that endure temperature variations. *Science* **379**, 399–403 (2023).
234. Dale, P. J. & Scarpulla, M. A. Efficiency versus effort: A better way to compare best photovoltaic research cell efficiencies? *Solar Energy Materials and Solar Cells* **251**, 112097 (2023).
235. Jeong, M. J. *et al.* Boosting radiation of stacked halide layer for perovskite solar cells with efficiency over 25%. *Joule* **7**, 112–127 (2023).
236. Jin, M. *et al.* Enhanced electrical properties in 2D perovskites via the bridging effect of SnS<sub>1-x</sub>O<sub>2x</sub> for perovskite solar cells with efficiency exceeding 24%. *Nano Energy* **109**, 108287 (2023).
237. Wang, Q. *et al.* Over 25% efficiency and stable bromine-free RbCsFAMA-based quadruple cation perovskite solar cells enabled by an aromatic zwitterion. *J. Mater. Chem. A* **11**, 1170–1179 (2023).
238. Luo, X. *et al.* Effective Passivation with Self-Organized Molecules for Perovskite Photovoltaics. *Advanced Materials* **34**, 2202100 (2022).
239. Wang, H. *et al.* Pre-annealing treatment for high-efficiency perovskite solar cells via sequential deposition. *Joule* **6**, 2869–2884 (2022).
240. Chen, J. *et al.* Solar Cell Efficiency Exceeding 25% through Rb-Based Perovskitoid Scaffold Stabilizing the Buried Perovskite Surface. *ACS Energy Lett.* **7**, 3685–3694 (2022).
241. Sidhik, S. *et al.* Deterministic fabrication of 3D/2D perovskite bilayer stacks for durable and efficient solar cells. *Science* **377**, 1425–1430 (2022).
242. Green, M. A. *et al.* Solar cell efficiency tables (Version 61). *Progress in Photovoltaics: Research and Applications* **31**, 3–16 (2023).
243. Min, H. *et al.* Perovskite solar cells with atomically coherent interlayers on SnO<sub>2</sub> electrodes. *Nature* **598**, 444–450 (2021).
244. Kim, M. *et al.* Enhanced electrical properties of Li-salts doped mesoporous TiO<sub>2</sub> in perovskite solar cells. *Joule* **5**, 659–672 (2021).

245. Zhang, F. *et al.* Metastable Dion-Jacobson 2D structure enables efficient and stable perovskite solar cells. *Science* **375**, 71–76 (2022).
246. Ju Jeong, M., Mun Yeom, K., Jin Kim, S., Hyuk Jung, E. & Hong Noh, J. Spontaneous interface engineering for dopant-free poly(3-hexylthiophene) perovskite solar cells with efficiency over 24%. *Energy & Environmental Science* **14**, 2419–2428 (2021).
247. Green, M. A. *et al.* Solar cell efficiency tables (version 59). *Progress in Photovoltaics: Research and Applications* **30**, 3–12 (2022).
248. Green, M. *et al.* Solar cell efficiency tables (version 57). *Progress in Photovoltaics: Research and Applications* **29**, 3–15 (2021).
249. Green, M. A. *et al.* Solar cell efficiency tables (Version 55). *Progress in Photovoltaics: Research and Applications* **28**, 3–15 (2020).
250. Mitzi, D. B., Feild, C. A., Schlesinger, Z. & Laibowitz, R. B. Transport, Optical, and Magnetic Properties of the Conducting Halide Perovskite  $\text{CH}_3\text{NH}_3\text{SnI}_3$ . *Journal of Solid State Chemistry* **114**, 159–163 (1995).
251. Sendner, M. *et al.* Optical phonons in methylammonium lead halide perovskites and implications for charge transport. *Mater. Horiz.* **3**, 613–620 (2016).
252. Wehrenfennig, C., Eperon, G. E., Johnston, M. B., Snaith, H. J. & Herz, L. M. High Charge Carrier Mobilities and Lifetimes in Organolead Trihalide Perovskites. *Advanced Materials* **26**, 1584–1589 (2014).
253. Kagan, C. R., Mitzi, D. B. & Dimitrakopoulos, C. D. Organic-Inorganic Hybrid Materials as Semiconducting Channels in Thin-Film Field-Effect Transistors. *Science* **286**, 945–947 (1999).
254. Matsushima, T. *et al.* Solution-Processed Organic–Inorganic Perovskite Field-Effect Transistors with High Hole Mobilities. *Advanced Materials* **28**, 10275–10281 (2016).
255. Milot, R. L. *et al.* Charge–Carrier Dynamics in 2D Hybrid Metal–Halide Perovskites. *Nano Lett.* **16**, 7001–7007 (2016).
256. Chen, Y. *et al.* Tailoring Organic Cation of 2D Air-Stable Organometal Halide Perovskites for Highly Efficient Planar Solar Cells. *Advanced Energy Materials* **7**, 1700162 (2017).
257. Tsai, H. *et al.* High-efficiency two-dimensional Ruddlesden–Popper perovskite solar cells. *Nature* **536**, 312–316 (2016).
258. Gélvez-Rueda, M. C. *et al.* Interconversion between free charges and bound excitons in 2D hybrid lead halide perovskites. *The Journal of*

- Physical Chemistry C* **121**, 26566–26574 (2017).
259. Venkatesan, N. R., Labram, J. G. & Chabinyo, M. L. Charge-Carrier Dynamics and Crystalline Texture of Layered Ruddlesden–Popper Hybrid Lead Iodide Perovskite Thin Films. *ACS Energy Lett.* **3**, 380–386 (2018).
260. Zhang, F. *et al.* Enhanced charge transport in 2D perovskites via fluorination of organic cation. *Journal of the American Chemical Society* **141**, 5972–5979 (2019).
261. Proppe, A. H. *et al.* Synthetic Control over Quantum Well Width Distribution and Carrier Migration in Low-Dimensional Perovskite Photovoltaics. *J. Am. Chem. Soc.* **140**, 2890–2896 (2018).
262. Mitzi, D. B., Dimitrakopoulos, C. D. & Kosbar, L. L. Structurally Tailored Organic–Inorganic Perovskites: Optical Properties and Solution-Processed Channel Materials for Thin-Film Transistors. *Chem. Mater.* **13**, 3728–3740 (2001).
263. Matsushima, T. *et al.* Intrinsic carrier transport properties of solution-processed organic–inorganic perovskite films. *Appl. Phys. Express* **10**, 024103 (2017).
264. Galkowski, K. *et al.* Determination of the exciton binding energy and effective masses for methylammonium and formamidinium lead trihalide perovskite semiconductors. *Energy Environ. Sci.* **9**, 962–970 (2016).
265. Tanaka, K. *et al.* Image charge effect on two-dimensional excitons in an inorganic-organic quantum-well crystal. *Phys. Rev. B* **71**, 045312 (2005).
266. Tanaka, K. & Kondo, T. Bandgap and exciton binding energies in lead-iodide-based natural quantum-well crystals. *Science and Technology of Advanced Materials* **4**, 599–604 (2003).
267. Koutselas, I. B., Ducasse, L. & Papavassiliou, G. C. Electronic properties of three- and low-dimensional semiconducting materials with Pb halide and Sn halide units. *J. Phys.: Condens. Matter* **8**, 1217 (1996).
268. Fujita, T., Sato, Y., Kuitani, T. & Ishihara, T. Tunable polariton absorption of distributed feedback microcavities at room temperature. *Phys. Rev. B* **57**, 12428–12434 (1998).
269. Delport, G. *et al.* Exciton–exciton annihilation in two-dimensional halide perovskites at room temperature. *The Journal of Physical Chemistry Letters* **10**, 5153–5159 (2019).
270. Dammak, T. *et al.* Two-Dimensional Excitons and Photoluminescence Properties of the Organic/Inorganic (4-FC6H4C2H4NH3)<sub>2</sub>[PbI<sub>4</sub>]



- Nanomaterial. *J. Phys. Chem. C* **113**, 19305–19309 (2009).
271. Ishihara, T., Takahashi, J. & Goto, T. Optical properties due to electronic transitions in two-dimensional semiconductors (C<sub>n</sub>H<sub>2n+1</sub>NH<sub>3</sub>)<sub>2</sub>PbI<sub>4</sub>. *Physical review B* **42**, 11099 (1990).
272. Mousdis, G. A., Papavassiliou, G. C., Raptopoulou, C. P. & Terzis, A. Preparation and characterization of [H<sub>3</sub>N(CH<sub>2</sub>)<sub>6</sub>NH<sub>3</sub>]<sub>2</sub>PbI<sub>4</sub> and similar compounds with a layered perovskite structure. *J. Mater. Chem.* **10**, 515–518 (2000).
273. Kinigstein, E. D. *et al.* Edge states drive exciton dissociation in ruddlesden–popper lead halide perovskite thin films. *ACS Materials Letters* **2**, 1360–1367 (2020).
274. Seitz, M. *et al.* Exciton diffusion in two-dimensional metal-halide perovskites. *Nature communications* **11**, 2035 (2020).
275. Deng, S. *et al.* Long-range exciton transport and slow annihilation in two-dimensional hybrid perovskites. *Nature communications* **11**, 664 (2020).
276. Mitzi, D. B., Chondroudis, K. & Kagan, C. R. Organic-inorganic electronics. *IBM Journal of Research and Development* **45**, 29–45 (2001).
277. Even, J., Pedesseau, L. & Katan, C. Understanding quantum confinement of charge carriers in layered 2D hybrid perovskites. *ChemPhysChem* **15**, 3733–3741 (2014).
278. Blancon, J.-C. *et al.* Extremely efficient internal exciton dissociation through edge states in layered 2D perovskites. *Science* **355**, 1288–1292 (2017).
279. Wang, G. *et al.* Colloquium: Excitons in atomically thin transition metal dichalcogenides. *Reviews of Modern Physics* **90**, 021001 (2018).
280. Guo, P. *et al.* Hyperbolic Dispersion Arising from Anisotropic Excitons in Two-Dimensional Perovskites. *Phys. Rev. Lett.* **121**, 127401 (2018).
281. DeCrescent, R. A. *et al.* Optical Constants and Effective-Medium Origins of Large Optical Anisotropies in Layered Hybrid Organic/Inorganic Perovskites. *ACS Nano* **13**, 10745–10753 (2019).
282. Song, B. *et al.* Determination of Dielectric Functions and Exciton Oscillator Strength of Two-Dimensional Hybrid Perovskites. *ACS Materials Lett.* **3**, 148–159 (2021).
283. Even, J., Pedesseau, L., Dupertuis, M.-A., Jancu, J.-M. & Katan, C. Electronic model for self-assembled hybrid organic/perovskite semiconductors: Reverse band edge electronic states ordering and spin-orbit coupling. *Physical Review B* **86**, 205301 (2012).

284. Ishihara, T., Takahashi, J. & Goto, T. Optical properties due to electronic transitions in two-dimensional semiconductors ( $C_n H_{2n+1} NH_3$ )<sub>2</sub> PbI<sub>4</sub>. *Physical review B* **42**, 11099 (1990).
285. Smith, M. D., Jaffe, A., Dohner, E. R., Lindenberg, A. M. & Karunadasa, H. I. Structural origins of broadband emission from layered Pb–Br hybrid perovskites. *Chem. Sci.* **8**, 4497–4504 (2017).
286. Shi, E. *et al.* Extrinsic and dynamic edge states of two-dimensional lead halide perovskites. *ACS nano* **13**, 1635–1644 (2019).
287. Tsai, H. *et al.* Design principles for electronic charge transport in solution-processed vertically stacked 2D perovskite quantum wells. *Nature communications* **9**, 2130 (2018).
288. Tsai, H. *et al.* Stable light-emitting diodes using phase-pure Ruddlesden–Popper layered perovskites. *Advanced Materials* **30**, 1704217 (2018).
289. Qin, Y. *et al.* Dangling octahedra enable edge states in 2D lead halide perovskites. *Advanced Materials* **34**, 2201666 (2022).
290. Shen, P., Vogt, T. & Lee, Y. Pressure-Induced Enhancement of Broad-Band White Light Emission in Butylammonium Lead Bromide. *J. Phys. Chem. Lett.* **11**, 4131–4137 (2020).
291. McClure, E. T., McCormick, A. P. & Woodward, P. M. Four Lead-free Layered Double Perovskites with the  $n = 1$  Ruddlesden–Popper Structure. *Inorg. Chem.* **59**, 6010–6017 (2020).
292. Bala, A. & Kumar, V. Role of Ligand–Ligand Interactions in the Stabilization of Thin Layers of Tin Bromide Perovskite: An Ab Initio Study of the Atomic and Electronic Structure, and Optical Properties. *J. Phys. Chem. C* **123**, 25176–25184 (2019).
293. Ishihara, T. Optical properties of PbI<sub>3</sub>-based perovskite structures. *Journal of Luminescence* **60–61**, 269–274 (1994).
294. Pandey, M., Jacobsen, K. W. & Thygesen, K. S. Band Gap Tuning and Defect Tolerance of Atomically Thin Two-Dimensional Organic–Inorganic Halide Perovskites. *J. Phys. Chem. Lett.* **7**, 4346–4352 (2016).
295. Wu, X. *et al.* Trap States in Lead Iodide Perovskites. *J. Am. Chem. Soc.* **137**, 2089–2096 (2015).
296. Song, K. S. & Williams, R. T. *Self-Trapped Excitons*. vol. 105 (Springer, 1993).
297. Liang, M. *et al.* Electronic Structure and Trap States of Two-Dimensional Ruddlesden–Popper Perovskites with the Relaxed Goldschmidt Tolerance Factor. *ACS Appl. Electron. Mater.* **2**, 1402–1412 (2020).

298. Hu, T. *et al.* Mechanism for broadband white-light emission from two-dimensional (110) hybrid perovskites. *The journal of physical chemistry letters* **7**, 2258–2263 (2016).
299. Xiao, Z., Meng, W., Wang, J. & Yan, Y. Defect properties of the two-dimensional (CH<sub>3</sub>NH<sub>3</sub>)<sub>2</sub>Pb(SCN)<sub>2</sub>I<sub>2</sub> perovskite: a density-functional theory study. *Physical Chemistry Chemical Physics* **18**, 25786–25790 (2016).
300. Zhang, L. *et al.* High-performance quasi-2D perovskite light-emitting diodes: from materials to devices. *Light Sci Appl* **10**, 61 (2021).
301. Xue, H., Chen, Z., Tao, S. & Brocks, G. Defects in Halide Perovskites: Does It Help to Switch from 3D to 2D? Preprint at <https://doi.org/10.48550/arXiv.2210.03415> (2022).
302. Peng, W. *et al.* Ultralow Self-Doping in Two-dimensional Hybrid Perovskite Single Crystals. *Nano Lett.* **17**, 4759–4767 (2017).
303. Xue, H., Chen, Z., Tao, S. & Brocks, G. Defects in Halide Perovskites: Does It Help to Switch from 3D to 2D? *arXiv preprint arXiv:2210.03415* (2022).
304. Philbin, J. P. & Rabani, E. Electron–hole correlations govern Auger recombination in nanostructures. *Nano Letters* **18**, 7889–7895 (2018).
305. Wang, F., Wu, Y., Hybertsen, M. S. & Heinz, T. F. Auger recombination of excitons in one-dimensional systems. *Physical Review B* **73**, 245424 (2006).
306. Jiang, Y. *et al.* Reducing the impact of Auger recombination in quasi-2D perovskite light-emitting diodes. *Nature Communications* **12**, 336 (2021).
307. Chen, X. *et al.* Impact of layer thickness on the charge carrier and spin coherence lifetime in two-dimensional layered perovskite single crystals. *ACS Energy Letters* **3**, 2273–2279 (2018).
308. Zou, W. *et al.* Minimising efficiency roll-off in high-brightness perovskite light-emitting diodes. *Nature communications* **9**, 608 (2018).
309. Huang, Y. *et al.* Stable Layered 2D Perovskite Solar Cells with an Efficiency of over 19% via Multifunctional Interfacial Engineering. *J. Am. Chem. Soc.* **143**, 3911–3917 (2021).
310. El-Ballouli, A. O., Bakr, O. M. & Mohammed, O. F. Structurally tunable two-dimensional layered perovskites: from confinement and enhanced charge transport to prolonged hot carrier cooling dynamics. *The journal of physical chemistry letters* **11**, 5705–5718 (2020).
311. Cheng, B. *et al.* Extremely reduced dielectric confinement in two-dimensional hybrid

- perovskites with large polar organics. *Communications Physics* **1**, 80 (2018).
312. Ren, H. *et al.* Efficient and stable Ruddlesden–Popper perovskite solar cell with tailored interlayer molecular interaction. *Nature Photonics* **14**, 154–163 (2020).
313. Yao, Y. *et al.* (C<sub>3</sub>H<sub>9</sub>Ni)<sub>4</sub>AgBiI<sub>8</sub>: a direct-bandgap layered double perovskite based on a short-chain spacer cation for light absorption. *Chemical Communications* **56**, 3206–3209 (2020).
314. Shi, P.-P. *et al.* Two-dimensional organic–inorganic perovskite ferroelectric semiconductors with fluorinated aromatic spacers. *Journal of the American Chemical Society* **141**, 18334–18340 (2019).
315. Tan, S. *et al.* Effect of high dipole moment cation on layered 2D organic–inorganic halide perovskite solar cells. *Advanced Energy Materials* **9**, 1803024 (2019).
316. Lermer, C. *et al.* Toward fluorinated spacers for MAPI-derived hybrid perovskites: synthesis, characterization, and phase transitions of (FC<sub>2</sub>H<sub>4</sub>NH<sub>3</sub>)<sub>2</sub>PbCl<sub>4</sub>. *Chemistry of Materials* **28**, 6560–6566 (2016).
317. Passarelli, J. V. *et al.* Enhanced out-of-plane conductivity and photovoltaic performance in n=1 layered perovskites through organic cation design. *Journal of the American Chemical Society* **140**, 7313–7323 (2018).
318. Yu, S. *et al.* Nonconfinement Structure Revealed in Dion–Jacobson Type Quasi-2D Perovskite Expedites Interlayer Charge Transport. *Small* **15**, 1905081 (2019).
319. Yan, L. *et al.* Charge-carrier transport in quasi-2D Ruddlesden–Popper perovskite solar cells. *Advanced Materials* **34**, 2106822 (2022).
320. Ashari-Astani, N. *et al.* Ruddlesden–Popper Phases of Methylammonium-Based Two-Dimensional Perovskites with 5-Ammonium Valeric Acid AVA<sub>2</sub>MA<sub>n</sub>–1Pb<sub>n</sub>I<sub>3n+1</sub> with n=1, 2, and 3. *The journal of physical chemistry letters* **10**, 3543–3549 (2019).
321. Knutson, J. L., Martin, J. D. & Mitzi, D. B. Tuning the band gap in hybrid tin iodide perovskite semiconductors using structural templating. *Inorganic chemistry* **44**, 4699–4705 (2005).
322. Zhao, X., Liu, T., Kaplan, A. B., Yao, C. & Loo, Y.-L. Accessing highly oriented two-dimensional perovskite films via solvent-vapor annealing for efficient and stable solar cells. *Nano Letters* **20**, 8880–8889 (2020).
323. Sidhik, S. *et al.* Memory Seeds Enable High Structural Phase Purity in 2D Perovskite Films

- for High-Efficiency Devices. *Adv. Mater.* **33**, 2007176 (2021).
324. Zhang, Y. *et al.* Optical Properties of Two-Dimensional Perovskite Films of  $(\text{C}_6\text{H}_5\text{C}_2\text{H}_4\text{NH}_3)_2[\text{PbI}_4]$  and  $(\text{C}_6\text{H}_5\text{C}_2\text{H}_4\text{NH}_3)_2(\text{CH}_3\text{NH}_3)_2[\text{Pb}_3\text{I}_{10}]$ . *J. Phys. Chem. Lett.* **10**, 13–19 (2019).
325. He, T. *et al.* Reduced-dimensional perovskite photovoltaics with homogeneous energy landscape. *Nat Commun* **11**, 1672 (2020).
326. Ni, L. *et al.* Real-time observation of exciton–phonon coupling dynamics in self-assembled hybrid perovskite quantum wells. *ACS nano* **11**, 10834–10843 (2017).
327. De Wolf, S. *et al.* Organometallic Halide Perovskites: Sharp Optical Absorption Edge and Its Relation to Photovoltaic Performance. *J. Phys. Chem. Lett.* **5**, 1035–1039 (2014).
328. Sadhanala, A. *et al.* Preparation of Single-Phase Films of  $\text{CH}_3\text{NH}_3\text{Pb}(\text{I}_{1-x}\text{Br}_x)_3$  with Sharp Optical Band Edges. *J. Phys. Chem. Lett.* **5**, 2501–2505 (2014).
329. Wu, G. *et al.* 2D hybrid halide perovskites: Structure, properties, and applications in solar cells. *Small* **17**, 2103514 (2021).
330. Koh, T. M. *et al.* Nanostructuring Mixed-Dimensional Perovskites: A Route Toward Tunable, Efficient Photovoltaics. *Advanced Materials* **28**, 3653–3661 (2016).
331. Zhang, X. *et al.* Stable high efficiency two-dimensional perovskite solar cells via cesium doping. *Energy Environ. Sci.* **10**, 2095–2102 (2017).
332. Wang, J. *et al.* Templated growth of oriented layered hybrid perovskites on 3D-like perovskites. *Nat Commun* **11**, 582 (2020).
333. Chen, A. Z. *et al.* Origin of vertical orientation in two-dimensional metal halide perovskites and its effect on photovoltaic performance. *Nat Commun* **9**, 1336 (2018).
334. Li, X. *et al.* Water-assisted Crystal Growth in Quasi-2D Perovskites with enhanced charge transport and photovoltaic performance. *Advanced Energy Materials* **10**, 2001832 (2020).
335. Truhlar, D. G., Garrett, B. C. & Klippenstein, S. J. Current status of transition-state theory. *The Journal of physical chemistry* **100**, 12771–12800 (1996).
336. Quintero-Bermudez, R. *et al.* Compositional and orientational control in metal halide perovskites of reduced dimensionality. *Nature materials* **17**, 900–907 (2018).
337. Wu, G. *et al.* Fine multi-phase Alignments in 2D perovskite solar cells with efficiency over 17%

- via slow post-annealing. *Advanced Materials* **31**, 1903889 (2019).
338. Fu, H. Dion–Jacobson halide perovskites for photovoltaic and photodetection applications. *Journal of Materials Chemistry C* **9**, 6378–6394 (2021).
339. Liu, Z., Wang, L. & Xie, X. Improving the performance of inverted two-dimensional perovskite solar cells by adding an anti-solvent into the perovskite precursor. *Journal of Materials Chemistry C* **8**, 11882–11889 (2020).
340. Liang, C. *et al.* Two-dimensional Ruddlesden–Popper layered perovskite solar cells based on phase-pure thin films. *Nature Energy* **6**, 38–45 (2021).
341. Lin, Y. *et al.* Suppressed Ion Migration in Low-Dimensional Perovskites. *ACS Energy Lett.* **2**, 1571–1572 (2017).
342. Xiao, X. *et al.* Suppressed Ion Migration along the In-Plane Direction in Layered Perovskites. *ACS Energy Lett.* **3**, 684–688 (2018).
343. Zhu, W. *et al.* Ion Migration in Organic–Inorganic Hybrid Perovskite Solar Cells: Current Understanding and Perspectives. *Small* **18**, 2105783 (2022).
344. Cho, J., DuBose, J. T., Le, A. N. T. & Kamat, P. V. Suppressed Halide Ion Migration in 2D Lead Halide Perovskites. *ACS Materials Lett.* **2**, 565–570 (2020).
345. Mathew, P. S., DuBose, J. T., Cho, J. & Kamat, P. V. Spacer Cations Dictate Photoinduced Phase Segregation in 2D Mixed Halide Perovskites. *ACS Energy Lett.* **6**, 2499–2501 (2021).
346. Wygant, B. R., Ye, A. Z., Dolocan, A. & Mullins, C. B. Effects of Alkylammonium Choice on Stability and Performance of Quasi-2D Organolead Halide Perovskites. *J. Phys. Chem. C* **124**, 10887–10897 (2020).
347. Elmelund, T., Scheidt, R. A., Seger, B. & Kamat, P. V. Bidirectional halide ion exchange in paired lead halide perovskite films with thermal activation. *ACS Energy Letters* **4**, 1961–1969 (2019).
348. Liao, W.-Q. *et al.* A lead-halide perovskite molecular ferroelectric semiconductor. *Nature communications* **6**, 7338 (2015).
349. Papavassiliou, G. C., Mousdis, G. A., Raptopoulou, C. P. & Terzis, A. Preparation and Characterization of [C<sub>6</sub>H<sub>5</sub>CH<sub>2</sub> NH<sub>3</sub>] <sub>2</sub>PbI<sub>4</sub>, [C<sub>6</sub>H<sub>5</sub>CH<sub>2</sub>CH<sub>2</sub>SC (NH<sub>2</sub>) <sub>2</sub>] <sub>3</sub>PbI<sub>5</sub> and [C<sub>10</sub>H<sub>7</sub>CH<sub>2</sub>NH<sub>3</sub>] PbI<sub>3</sub> Organic-Inorganic Hybrid Compounds. *Zeitschrift für Naturforschung B* **54**, 1405–1409 (1999).

350. Wang, S. *et al.* An unprecedented biaxial trilayered hybrid perovskite ferroelectric with directionally tunable photovoltaic effects. *Journal of the American Chemical Society* **141**, 7693–7697 (2019).
351. Braun, M. & Frey, W. Crystal structure of bis (benzylammonium) lead tetrachloride,  $(C_7H_7NH_3)_2PbCl_4$ . *Zeitschrift für Kristallographie-New Crystal Structures* **214**, 331–332 (1999).
352. Kepenekian, M. *et al.* Rashba and Dresselhaus effects in hybrid organic–inorganic perovskites: from basics to devices. *ACS nano* **9**, 11557–11567 (2015).
353. Wu, Z. *et al.* Alloying n-Butylamine into CsPbBr<sub>3</sub> To Give a Two-Dimensional Bilayered Perovskite Ferroelectric Material. *Angewandte Chemie International Edition* **57**, 8140–8143 (2018).
354. Li, L. *et al.* Two-dimensional hybrid perovskite-type ferroelectric for highly polarization-sensitive shortwave photodetection. *Journal of the American Chemical Society* **141**, 2623–2629 (2019).
355. Mao, L. *et al.* Organic cation alloying on intralayer A and interlayer A' sites in 2D hybrid dion–jacobson lead bromide perovskites (A')(A)Pb<sub>2</sub>Br<sub>7</sub>. *Journal of the American Chemical Society* **142**, 8342–8351 (2020).
356. Long, G. *et al.* Chiral-perovskite optoelectronics. *Nature Reviews Materials* **5**, 423–439 (2020).
357. Zhao, X.-H. *et al.* An enantiomeric pair of 2D organic–inorganic hybrid perovskites with circularly polarized luminescence and photoelectric effects. *Journal of Materials Chemistry C* **10**, 3440–3446 (2022).
358. Xie, Y. *et al.* Kinetically Controlled Structural Transitions in Layered Halide-Based Perovskites: An Approach to Modulate Spin Splitting. *Journal of the American Chemical Society* **144**, 15223–15235 (2022).
359. Huang, P.-J. *et al.* Chirality-Dependent Circular Photogalvanic Effect in Enantiomorphic 2D Organic–Inorganic Hybrid Perovskites. *Advanced Materials* **33**, 2008611 (2021).
360. Kim, Y.-H. *et al.* Chiral-induced spin selectivity enables a room-temperature spin light-emitting diode. *Science* **371**, 1129–1133 (2021).
361. Jana, M. K. *et al.* Organic-to-inorganic structural chirality transfer in a 2D hybrid perovskite and impact on Rashba-Dresselhaus spin-orbit coupling. *Nature communications* **11**, 4699 (2020).
362. Lu, H. *et al.* Highly distorted chiral two-dimensional tin iodide perovskites for spin



- polarized charge transport. *Journal of the American Chemical Society* **142**, 13030–13040 (2020).
363. Huang, P.-J., Taniguchi, K. & Miyasaka, H. Bulk photovoltaic effect in a pair of chiral–polar layered perovskite-type lead iodides altered by chirality of organic cations. *Journal of the American Chemical Society* **141**, 14520–14523 (2019).
364. Thouin, F. *et al.* Phonon coherences reveal the polaronic character of excitons in two-dimensional lead halide perovskites. *Nature materials* **18**, 349–356 (2019).
365. Neutzner, S. *et al.* Exciton-polaron spectral structures in two-dimensional hybrid lead-halide perovskites. *Physical Review Materials* **2**, 064605 (2018).
366. Srimath Kandada, A. R. & Silva, C. Exciton polarons in two-dimensional hybrid metal-halide perovskites. *The Journal of Physical Chemistry Letters* **11**, 3173–3184 (2020).
367. Guo, P. *et al.* Cross-plane coherent acoustic phonons in two-dimensional organic-inorganic hybrid perovskites. *Nature communications* **9**, 2019 (2018).
368. Maity, P. *et al.* Layer-dependent coherent acoustic phonons in two-dimensional Ruddlesden–Popper perovskite crystals. *The journal of physical chemistry letters* **10**, 5259–5264 (2019).
369. Quan, L. N. *et al.* Vibrational relaxation dynamics in layered perovskite quantum wells. *Proceedings of the National Academy of Sciences* **118**, e2104425118 (2021).
370. Cuthriell, S. A. *et al.* Nonequilibrium Lattice Dynamics in Photoexcited 2D Perovskites. *Advanced Materials* **34**, 2202709 (2022).
371. Zhang, H. *et al.* Ultrafast relaxation of lattice distortion in two-dimensional perovskites. *Nature Physics* 1–6 (2023).
372. Li, W. *et al.* Light-activated interlayer contraction in two-dimensional perovskites for high-efficiency solar cells. *Nat. Nanotechnol.* **17**, 45–52 (2022).
373. Zhang, Y. & Park, N.-G. Quasi-Two-Dimensional Perovskite Solar Cells with Efficiency Exceeding 22%. *ACS Energy Lett.* **7**, 757–765 (2022).
374. Li, N., Niu, X., Chen, Q. & Zhou, H. Towards commercialization: the operational stability of perovskite solar cells. *Chem. Soc. Rev.* **49**, 8235–8286 (2020).
375. Siegler, T. D. *et al.* Water-Accelerated Photooxidation of CH<sub>3</sub>NH<sub>3</sub>PbI<sub>3</sub> Perovskite. *J. Am. Chem. Soc.* **144**, 5552–5561 (2022).

376. Marronnier, A. *et al.* Anharmonicity and disorder in the black phases of cesium lead iodide used for stable inorganic perovskite solar cells. *ACS nano* **12**, 3477–3486 (2018).
377. Fang, H.-H. *et al.* Photophysics of organic–inorganic hybrid lead iodide perovskite single crystals. *Advanced Functional Materials* **25**, 2378–2385 (2015).
378. Abdelmageed, G. *et al.* Mechanisms for light induced degradation in MAPbI<sub>3</sub> perovskite thin films and solar cells. *Applied Physics Letters* **109**, 233905 (2016).
379. Song, Z. *et al.* Probing the origins of photodegradation in organic–inorganic metal halide perovskites with time-resolved mass spectrometry. *Sustainable Energy & Fuels* **2**, 2460–2467 (2018).
380. Aristidou, N. *et al.* Fast oxygen diffusion and iodide defects mediate oxygen-induced degradation of perovskite solar cells. *Nature communications* **8**, 15218 (2017).
381. Lindroos, J. & Savin, H. Review of light-induced degradation in crystalline silicon solar cells. *Solar Energy Materials and Solar Cells* **147**, 115–126 (2016).
382. Kim, G. Y. *et al.* Large tunable photoeffect on ion conduction in halide perovskites and implications for photodecomposition. *Nature materials* **17**, 445–449 (2018).
383. Senocrate, A. *et al.* Interaction of oxygen with halide perovskites. *Journal of Materials Chemistry A* **6**, 10847–10855 (2018).
384. O’Mahony, F. T. *et al.* Improved environmental stability of organic lead trihalide perovskite-based photoactive-layers in the presence of mesoporous TiO<sub>2</sub>. *Journal of Materials Chemistry A* **3**, 7219–7223 (2015).
385. Kim, N.-K. *et al.* Investigation of thermally induced degradation in CH<sub>3</sub>NH<sub>3</sub>PbI<sub>3</sub> perovskite solar cells using in-situ synchrotron radiation analysis. *Scientific reports* **7**, 4645 (2017).
386. Conings, B. *et al.* Intrinsic thermal instability of methylammonium lead trihalide perovskite. *Advanced Energy Materials* **5**, 1500477 (2015).
387. Juarez-Perez, E. J., Hawash, Z., Raga, S. R., Ono, L. K. & Qi, Y. Thermal degradation of CH<sub>3</sub>NH<sub>3</sub>PbI<sub>3</sub> perovskite into NH<sub>3</sub> and CH<sub>3</sub>I gases observed by coupled thermogravimetry–mass spectrometry analysis. *Energy & environmental science* **9**, 3406–3410 (2016).
388. Imler, G. H. *et al.* Solid state transformation of the crystalline monohydrate (CH<sub>3</sub>NH<sub>3</sub>)PbI<sub>3</sub>(H<sub>2</sub>O) to the (CH<sub>3</sub>NH<sub>3</sub>)PbI<sub>3</sub> perovskite.

- Chemical Communications* **51**, 11290–11292 (2015).
389. Leguy, A. M. *et al.* Reversible hydration of CH<sub>3</sub>NH<sub>3</sub>PbI<sub>3</sub> in films, single crystals, and solar cells. *Chemistry of Materials* **27**, 3397–3407 (2015).
390. Frost, J. M. *et al.* Atomistic origins of high-performance in hybrid halide perovskite solar cells. *Nano letters* **14**, 2584–2590 (2014).
391. Zhao, J. *et al.* Investigation of the hydrolysis of perovskite organometallic halide CH<sub>3</sub>NH<sub>3</sub>PbI<sub>3</sub> in humidity environment. *Scientific reports* **6**, 21976 (2016).
392. Fabini, D. H. *et al.* Reentrant structural and optical properties and large positive thermal expansion in perovskite formamidinium lead iodide. *Angewandte Chemie* **128**, 15618–15622 (2016).
393. Binek, A., Hanusch, F. C., Docampo, P. & Bein, T. Stabilization of the trigonal high-temperature phase of formamidinium lead iodide. *The journal of physical chemistry letters* **6**, 1249–1253 (2015).
394. Akbulatov, A. F. *et al.* Intrinsic thermal decomposition pathways of lead halide perovskites APbX<sub>3</sub>. *Solar Energy Materials and Solar Cells* **213**, 110559 (2020).
395. Pool, V. L. *et al.* Thermal engineering of FAPbI<sub>3</sub> perovskite material via radiative thermal annealing and in situ XRD. *Nature communications* **8**, 14075 (2017).
396. Liu, D. *et al.* Structural properties and stability of inorganic cspbi<sub>3</sub> perovskites. *Small Structures* **2**, 2000089 (2021).
397. Lee, J.-W. *et al.* Formamidinium and cesium hybridization for photo-and moisture-stable perovskite solar cell. *Advanced Energy Materials* **5**, 1501310 (2015).
398. Dastidar, S. *et al.* Quantitative phase-change thermodynamics and metastability of perovskite-phase cesium lead iodide. *The journal of physical chemistry letters* **8**, 1278–1282 (2017).
399. Xie, L.-Q. *et al.* Understanding the cubic phase stabilization and crystallization kinetics in mixed cations and halides perovskite single crystals. *Journal of the American Chemical Society* **139**, 3320–3323 (2017).
400. Ho, K., Wei, M., Sargent, E. H. & Walker, G. C. Grain transformation and degradation mechanism of formamidinium and cesium lead iodide perovskite under humidity and light. *ACS Energy Letters* **6**, 934–940 (2021).
401. Li, N. *et al.* Microscopic degradation in formamidinium-cesium lead iodide perovskite

- solar cells under operational stressors. *Joule* **4**, 1743–1758 (2020).
402. Tan, W., Bowring, A. R., Meng, A. C., McGehee, M. D. & McIntyre, P. C. Thermal stability of mixed cation metal halide perovskites in air. *ACS applied materials & interfaces* **10**, 5485–5491 (2018).
403. Draguta, S. *et al.* Rationalizing the light-induced phase separation of mixed halide organic–inorganic perovskites. *Nature communications* **8**, 200 (2017).
404. Chen, Z., Brocks, G., Tao, S. & Bobbert, P. A. Unified theory for light-induced halide segregation in mixed halide perovskites. *Nature communications* **12**, 2687 (2021).
405. Bischak, C. G. *et al.* Origin of reversible photoinduced phase separation in hybrid perovskites. *Nano letters* **17**, 1028–1033 (2017).
406. Zhao, Y. *et al.* Strain-activated light-induced halide segregation in mixed-halide perovskite solids. *Nature Communications* **11**, 6328 (2020).
407. Knight, A. J. *et al.* Halide segregation in mixed-halide perovskites: influence of A-site cations. *ACS Energy Letters* **6**, 799–808 (2021).
408. Knight, A. J. & Herz, L. M. Preventing phase segregation in mixed-halide perovskites: a perspective. *Energy & Environmental Science* **13**, 2024–2046 (2020).
409. Barker, A. J. *et al.* Defect-assisted photoinduced halide segregation in mixed-halide perovskite thin films. *ACS Energy Letters* **2**, 1416–1424 (2017).
410. Knight, A. J. *et al.* Electronic traps and phase segregation in lead mixed-halide perovskite. *ACS Energy Letters* **4**, 75–84 (2018).
411. Slotcavage, D. J., Karunadasa, H. I. & McGehee, M. D. Light-induced phase segregation in halide-perovskite absorbers. *ACS Energy Letters* **1**, 1199–1205 (2016).
412. Mundt, L. E. *et al.* Mixing matters: nanoscale heterogeneity and stability in metal halide perovskite solar cells. *ACS Energy Letters* **7**, 471–480 (2021).
413. Wu, F. *et al.* Bias-dependent normal and inverted J–V hysteresis in perovskite solar cells. *ACS applied materials & interfaces* **10**, 25604–25613 (2018).
414. Bertoluzzi, L. *et al.* Mobile ion concentration measurement and open-access band diagram simulation platform for halide perovskite solar cells. *Joule* **4**, 109–127 (2020).
415. Bae, S. *et al.* Electric-field-induced degradation of methylammonium lead iodide perovskite solar cells. *The journal of physical chemistry letters* **7**, 3091–3096 (2016).

416. Leijtens, T. *et al.* Overcoming ultraviolet light instability of sensitized TiO<sub>2</sub> with meso-structured organometal tri-halide perovskite solar cells. *Nature communications* **4**, 2885 (2013).
417. Roose, B. *et al.* Mesoporous SnO<sub>2</sub> electron selective contact enables UV-stable perovskite solar cells. *Nano Energy* **30**, 517–522 (2016).
418. Li, Z. *et al.* Extrinsic ion migration in perovskite solar cells. *Energy & Environmental Science* **10**, 1234–1242 (2017).
419. Domanski, K. *et al.* Not all that glitters is gold: metal-migration-induced degradation in perovskite solar cells. *ACS nano* **10**, 6306–6314 (2016).
420. Guarnera, S. *et al.* Improving the long-term stability of perovskite solar cells with a porous Al<sub>2</sub>O<sub>3</sub> buffer layer. *The journal of physical chemistry letters* **6**, 432–437 (2015).
421. Kato, Y. *et al.* Silver iodide formation in methyl ammonium lead iodide perovskite solar cells with silver top electrodes. *Advanced Materials Interfaces* **2**, 1500195 (2015).
422. Back, H. *et al.* Achieving long-term stable perovskite solar cells via ion neutralization. *Energy & Environmental Science* **9**, 1258–1263 (2016).
423. Yeo, J.-S. *et al.* Highly efficient and stable planar perovskite solar cells with reduced graphene oxide nanosheets as electrode interlayer. *Nano Energy* **12**, 96–104 (2015).
424. Bush, K. A. *et al.* Thermal and environmental stability of semi-transparent perovskite solar cells for tandems enabled by a solution-processed nanoparticle buffer layer and sputtered ITO electrode. *Advanced Materials* **28**, 3937–3943 (2016).
425. Kaltenbrunner, M. *et al.* Flexible high power-per-weight perovskite solar cells with chromium oxide–metal contacts for improved stability in air. *Nature materials* **14**, 1032–1039 (2015).
426. Liu, L. *et al.* Grain-boundary “patches” by in situ conversion to enhance perovskite solar cells stability. *Advanced Materials* **30**, 1800544 (2018).
427. Diao, E. W.-G., Jokar, E. & Rameez, M. Strategies to improve performance and stability for tin-based perovskite solar cells. *ACS Energy Letters* **4**, 1930–1937 (2019).
428. Cao, J. & Yan, F. Recent progress in tin-based perovskite solar cells. *Energy & Environmental Science* **14**, 1286–1325 (2021).
429. Wang, K., Liang, Z., Wang, X. & Cui, X. Lead replacement in CH<sub>3</sub>NH<sub>3</sub>PbI<sub>3</sub> perovskites.

- Advanced Electronic Materials* **1**, 1500089 (2015).
430. Takahashi, Y. *et al.* Charge-transport in tin-iodide perovskite  $\text{CH}_3\text{NH}_3\text{SnI}_3$ : origin of high conductivity. *Dalton Transactions* **40**, 5563–5568 (2011).
431. Ke, W. *et al.* Dopant-free tetrakis-triphenylamine hole transporting material for efficient tin-based perovskite solar cells. *Journal of the American Chemical Society* **140**, 388–393 (2018).
432. Leijtens, T., Prasanna, R., Gold-Parker, A., Toney, M. F. & McGehee, M. D. Mechanism of tin oxidation and stabilization by lead substitution in tin halide perovskites. *ACS Energy Letters* **2**, 2159–2165 (2017).
433. Lanzetta, L. *et al.* Degradation mechanism of hybrid tin-based perovskite solar cells and the critical role of tin (IV) iodide. *Nature communications* **12**, 2853 (2021).
434. Wang, F. *et al.* Organic Cation-Dependent Degradation Mechanism of Organotin Halide Perovskites. *Advanced Functional Materials* **26**, 3417–3423 (2016).
435. Shi, T. *et al.* Effects of organic cations on the defect physics of tin halide perovskites. *Journal of Materials Chemistry A* **5**, 15124–15129 (2017).
436. Jokar, E., Chien, C.-H., Tsai, C.-M., Fathi, A. & Diao, E. W.-G. Robust tin-based perovskite solar cells with hybrid organic cations to attain efficiency approaching 10%. *Advanced materials* **31**, 1804835 (2019).
437. Nakamura, T. *et al.* Sn (IV)-free tin perovskite films realized by in situ Sn (0) nanoparticle treatment of the precursor solution. *Nature Communications* **11**, 3008 (2020).
438. Gu, F. *et al.* Improving performance of lead-free formamidinium tin triiodide perovskite solar cells by tin source purification. *Solar RRL* **2**, 1800136 (2018).
439. Xiao, M. *et al.* Tin-based perovskite with improved coverage and crystallinity through tin-fluoride-assisted heterogeneous nucleation. *Advanced Optical Materials* **6**, 1700615 (2018).
440. Liu, C. *et al.* Enhanced hole transportation for inverted tin-based perovskite solar cells with high performance and stability. *Advanced Functional Materials* **29**, 1808059 (2019).
441. Yang, J., Siempelkamp, B. D., Liu, D. & Kelly, T. L. Investigation of  $\text{CH}_3\text{NH}_3\text{PbI}_3$  degradation rates and mechanisms in controlled humidity environments using in situ techniques. *ACS nano* **9**, 1955–1963 (2015).

442. Zhao, Y. *et al.* A polymer scaffold for self-healing perovskite solar cells. *Nature communications* **7**, 10228 (2016).
443. Song, Z. *et al.* Perovskite solar cell stability in humid air: partially reversible phase transitions in the Pbl<sub>2</sub>-CH<sub>3</sub>NH<sub>3</sub>I-H<sub>2</sub>O system. *Advanced Energy Materials* **6**, 1600846 (2016).
444. Manser, J. S., Saidaminov, M. I., Christians, J. A., Bakr, O. M. & Kamat, P. V. Making and breaking of lead halide perovskites. *Accounts of chemical research* **49**, 330–338 (2016).
445. Nie, W. *et al.* Light-activated photocurrent degradation and self-healing in perovskite solar cells. *Nature communications* **7**, 11574 (2016).
446. Jena, A. K., Kulkarni, A., Ikegami, M. & Miyasaka, T. Steady state performance, photo-induced performance degradation and their relation to transient hysteresis in perovskite solar cells. *Journal of Power Sources* **309**, 1–10 (2016).
447. Khenkin, M. V. *et al.* Dynamics of photoinduced degradation of perovskite photovoltaics: from reversible to irreversible processes. *ACS Applied Energy Materials* **1**, 799–806 (2018).
448. Lee, S.-W. *et al.* UV degradation and recovery of perovskite solar cells. *Scientific reports* **6**, 1–10 (2016).
449. Juarez-Perez, E. J. *et al.* Photodecomposition and thermal decomposition in methylammonium halide lead perovskites and inferred design principles to increase photovoltaic device stability. *Journal of Materials Chemistry A* **6**, 9604–9612 (2018).
450. Bag, M. *et al.* Kinetics of ion transport in perovskite active layers and its implications for active layer stability. *Journal of the American Chemical Society* **137**, 13130–13137 (2015).
451. Domanski, K. *et al.* Migration of cations induces reversible performance losses over day/night cycling in perovskite solar cells. *Energy & Environmental Science* **10**, 604–613 (2017).
452. Tress, W. *et al.* Interpretation and evolution of open-circuit voltage, recombination, ideality factor and subgap defect states during reversible light-soaking and irreversible degradation of perovskite solar cells. *Energy & Environmental Science* **11**, 151–165 (2018).
453. Ceratti, D. R. *et al.* Self-healing inside APbBr<sub>3</sub> halide perovskite crystals. *Advanced Materials* **30**, 1706273 (2018).
454. Yoon, S. J. *et al.* Tracking iodide and bromide ion segregation in mixed halide lead perovskites during photoirradiation. *ACS Energy Letters* **1**, 290–296 (2016).



455. Hoke, E. T. *et al.* Reversible photo-induced trap formation in mixed-halide hybrid perovskites for photovoltaics. *Chemical Science* **6**, 613–617 (2015).
456. Wei, H. & Huang, J. Halide lead perovskites for ionizing radiation detection. *Nature communications* **10**, 1066 (2019).
457. Lang, F. *et al.* Radiation hardness and self-healing of perovskite solar cells. *Advanced Materials* **28**, 8726–8731 (2016).
458. Khenkin, M. V. *et al.* Consensus statement for stability assessment and reporting for perovskite photovoltaics based on ISOS procedures. *Nature Energy* **5**, 35–49 (2020).
459. Khenkin, M. V. *et al.* Reconsidering figures of merit for performance and stability of perovskite photovoltaics. *Energy & Environmental Science* **11**, 739–743 (2018).
460. Howard, J. M., Tennyson, E. M., Neves, B. R. & Leite, M. S. Machine learning for perovskites' reap-rest-recovery cycle. *Joule* **3**, 325–337 (2019).
461. Zhang, F. & Zhu, K. Additive engineering for efficient and stable perovskite solar cells. *Advanced Energy Materials* **10**, 1902579 (2020).
462. Odysseas Kosmatos, K. *et al.* Methylammonium chloride: a key additive for highly efficient, stable, and up-scalable perovskite solar cells. *Energy & Environmental Materials* **2**, 79–92 (2019).
463. Fu, Q., Xiao, S., Tang, X., Chen, Y. & Hu, T. Amphiphilic fullerenes employed to improve the quality of perovskite films and the stability of perovskite solar cells. *ACS applied materials & interfaces* **11**, 24782–24788 (2019).
464. Peng, J. *et al.* A universal double-side passivation for high open-circuit voltage in perovskite solar cells: role of carbonyl groups in poly (methyl methacrylate). *Advanced Energy Materials* **8**, 1801208 (2018).
465. Wang, S. *et al.* Water-soluble triazolium ionic-liquid-induced surface self-assembly to enhance the stability and efficiency of perovskite solar cells. *Advanced Functional Materials* **29**, 1900417 (2019).
466. Liu, Z. *et al.* A holistic approach to interface stabilization for efficient perovskite solar modules with over 2,000-hour operational stability. *Nature Energy* **5**, 596–604 (2020).
467. Yang, Y. *et al.* Eliminating charge accumulation via interfacial dipole for efficient and stable perovskite solar cells. *ACS applied materials & interfaces* **11**, 34964–34972 (2019).
468. Ahn, N. *et al.* Trapped charge-driven degradation of perovskite solar cells. *Nature communications* **7**, 13422 (2016).

469. Jena, A. K., Numata, Y., Ikegami, M. & Miyasaka, T. Role of spiro-OMeTAD in performance deterioration of perovskite solar cells at high temperature and reuse of the perovskite films to avoid Pb-waste. *Journal of Materials Chemistry A* **6**, 2219–2230 (2018).
470. Sanchez, R. S. & Mas-Marza, E. Light-induced effects on Spiro-OMeTAD films and hybrid lead halide perovskite solar cells. *Solar Energy Materials and Solar Cells* **158**, 189–194 (2016).
471. Wang, S. *et al.* Morphology Control of Doped Spiro-MeOTAD Films for Air Stable Perovskite Solar Cells. *Small* **16**, 1907513 (2020).
472. Zhao, X., Kim, H.-S., Seo, J.-Y. & Park, N.-G. Effect of Selective Contacts on the Thermal Stability of Perovskite Solar Cells. *ACS Appl. Mater. Interfaces* **9**, 7148–7153 (2017).
473. Han, J. *et al.* Ultrastable Perovskite through a SiO<sub>2</sub> and PbSO<sub>4</sub> Double Protection Strategy. *ACS Appl. Energy Mater.* **5**, 13461–13469 (2022).
474. Sun, Q. *et al.* A Thiourea Competitive Crystallization Strategy for FA-Based Perovskite Solar Cells. *Advanced Functional Materials* **32**, 2208885 (2022).
475. Li, H. *et al.* Sequential vacuum-evaporated perovskite solar cells with more than 24% efficiency. *Science Advances* **8**, eabo7422 (2022).
476. Boyd, C. C., Cheacharoen, R., Leijtens, T. & McGehee, M. D. Understanding Degradation Mechanisms and Improving Stability of Perovskite Photovoltaics. *Chem. Rev.* **119**, 3418–3451 (2019).
477. Pereyra, C., Xie, H. & Lira-Cantu, M. Additive engineering for stable halide perovskite solar cells. *Journal of Energy Chemistry* **60**, 599–634 (2021).
478. Xie, H. *et al.* Decoupling the effects of defects on efficiency and stability through phosphonates in stable halide perovskite solar cells. *Joule* **5**, 1246–1266 (2021).
479. Chen, B., Wang, S., Song, Y., Li, C. & Hao, F. A critical review on the moisture stability of halide perovskite films and solar cells. *Chemical Engineering Journal* **430**, 132701 (2022).
480. Thambidurai, M., Shini, F., Harikesh, P. C., Mathews, N. & Dang, C. Highly stable and efficient planar perovskite solar cells using ternary metal oxide electron transport layers. *Journal of Power Sources* **448**, 227362 (2020).
481. Ndiaye, A. *et al.* Degradations of silicon photovoltaic modules: A literature review. *Solar Energy* **96**, 140–151 (2013).

482. Leung, T. L. *et al.* Stability of 2D and quasi-2D perovskite materials and devices. *Communications Materials* **3**, 63 (2022).
483. Gong, J., Hao, M., Zhang, Y., Liu, M. & Zhou, Y. Layered 2D Halide Perovskites beyond the Ruddlesden–Popper Phase: Tailored Interlayer Chemistries for High-Performance Solar Cells. *Angewandte Chemie International Edition* **61**, e202112022 (2022).
484. Yang, Y., Gao, F., Gao, S. & Wei, S.-H. Origin of the stability of two-dimensional perovskites: a first-principles study. *Journal of Materials Chemistry A* **6**, 14949–14955 (2018).
485. Quan, L. N. *et al.* Ligand-stabilized reduced-dimensionality perovskites. *Journal of the American Chemical Society* **138**, 2649–2655 (2016).
486. Chen, Y. *et al.* 2D Ruddlesden–Popper perovskites for optoelectronics. *Advanced Materials* **30**, 1703487 (2018).
487. Coriolano, A. *et al.* Improved photostability in fluorinated 2D perovskite single crystals. *Nanomaterials* **11**, 465 (2021).
488. Kim, B. & Seok, S. I. Molecular aspects of organic cations affecting the humidity stability of perovskites. *Energy & Environmental Science* **13**, 805–820 (2020).
489. Wygant, B. R. *et al.* Probing the degradation chemistry and enhanced stability of 2D organolead halide perovskites. *Journal of the American Chemical Society* **141**, 18170–18181 (2019).
490. Tang, J. *et al.* Imaging the moisture-induced degradation process of 2D organolead halide perovskites. *ACS omega* **7**, 10365–10371 (2022).
491. Wygant, B. R. *et al.* Moisture-driven formation and growth of quasi-2-D organolead halide perovskite crystallites. *ACS Applied Energy Materials* **3**, 6280–6290 (2020).
492. Schlipf, J. *et al.* Shedding light on the moisture stability of 3D/2D hybrid perovskite heterojunction thin films. *ACS Applied Energy Materials* **2**, 1011–1018 (2019).
493. Ahmad, S. *et al.* Dion-Jacobson phase 2D layered perovskites for solar cells with ultrahigh stability. *Joule* **3**, 794–806 (2019).
494. Milić, J. V., Zakeeruddin, S. M. & Grätzel, M. Layered hybrid formamidinium lead iodide perovskites: challenges and opportunities. *Accounts of Chemical Research* **54**, 2729–2740 (2021).
495. Saidaminov, M. I. *et al.* Suppression of atomic vacancies via incorporation of isovalent small ions to increase the stability of halide perovskite

- solar cells in ambient air. *Nature Energy* **3**, 648–654 (2018).
496. Chen, Z., Xue, H., Brocks, G., Bobbert, P. A. & Tao, S. Thermodynamic Origin of the Photostability of the Two-Dimensional Perovskite PEA<sub>2</sub>Pb(I<sub>1-x</sub>Br<sub>x</sub>)<sub>4</sub>. *ACS Energy Letters* **8**, 943–949 (2023).
497. Cho, J., Mathew, P. S., DuBose, J. T. & Kamat, P. V. Photoinduced halide segregation in Ruddlesden–Popper 2D mixed halide perovskite films. *Advanced Materials* **33**, 2105585 (2021).
498. Wang, Y.-R. *et al.* Photo De-Mixing in Dion–Jacobson 2D Mixed Halide Perovskites. *Advanced Energy Materials* **12**, 2200768 (2022).
499. Zhang, Y., Liu, Y., Xu, Z., Yang, Z. & Liu, S. 2D Perovskite Single Crystals with Suppressed Ion Migration for High-Performance Planar-Type Photodetectors. *Small* **16**, 2003145 (2020).
500. Dučinskas, A. *et al.* Unravelling the Behavior of Dion–Jacobson Layered Hybrid Perovskites in Humid Environments. *ACS Energy Letters* **6**, 337–344 (2020).
501. Hu, J., Kerner, R. A., Pelczar, I., Rand, B. P. & Schwartz, J. Organoammonium-Ion-based perovskites can degrade to Pb<sub>0</sub> via Amine–Pb(II) coordination. *ACS Energy Letters* **6**, 2262–2267 (2021).
502. Udalova, N. N. *et al.* Nonmonotonic photostability of BA<sub>2</sub>MA<sub>n-1</sub>Pb<sub>n</sub>I<sub>3n+1</sub> homologous layered perovskites. *ACS Applied Materials & Interfaces* **14**, 961–970 (2021).
503. Fang, H. *et al.* Unravelling Light-Induced Degradation of Layered Perovskite Crystals and Design of Efficient Encapsulation for Improved Photostability. *Advanced Functional Materials* **28**, 1800305 (2018).
504. Fan, Z. *et al.* Layer-by-layer degradation of methylammonium lead tri-iodide perovskite microplates. *Joule* **1**, 548–562 (2017).
505. Aharon, S. *et al.* 2D Pb-Halide Perovskites Can Self-Heal Photodamage Better than 3D Ones. *Advanced functional materials* **32**, 2113354 (2022).
506. Cohen, B.-E., Li, Y., Meng, Q. & Etgar, L. Dion–Jacobson two-dimensional perovskite solar cells based on benzene dimethan ammonium cation. *Nano letters* **19**, 2588–2597 (2019).
507. Udalova, N. N. *et al.* Nonmonotonic Photostability of BA<sub>2</sub>MA<sub>n-1</sub>Pb<sub>n</sub>I<sub>3n+1</sub> Homologous Layered Perovskites. *ACS Appl. Mater. Interfaces* **14**, 961–970 (2022).
508. Cao, D. H. *et al.* Thin Films and Solar Cells Based on Semiconducting Two-Dimensional Ruddlesden–Popper (CH<sub>3</sub>(CH<sub>2</sub>)<sub>3</sub>NH<sub>3</sub>)<sub>2</sub>(CH<sub>3</sub>NH<sub>3</sub>)<sub>n-1</sub>SnnI<sub>3n+1</sub>

- Perovskites. *ACS Energy Lett.* **2**, 982–990 (2017).
509. Zhang, T. *et al.* Controlling quantum-well width distribution and crystal orientation in two-dimensional tin halide perovskites via a strong interlayer electrostatic interaction. *ACS Applied Materials & Interfaces* **13**, 49907–49915 (2021).
510. Bala, A. & Kumar, V. Effects of Cl and F Substitution in Phenylethylammonium Spacer Cations on Stability, Structure, and Optical Properties of 2D–3D Ruddlesden–Popper Perovskite Layers. *ACS Applied Energy Materials* **4**, 1860–1867 (2021).
511. Gan, X. *et al.* Multilayered Ruddlesden–Popper perovskite hybrids with alternative organic spacers of 4- $\text{XC}_6\text{H}_4\text{C}_2\text{H}_4\text{NH}_2$  (where X= H, Br, Cl) for solar cell applications. *Journal of Materials Science* **56**, 17167–17177 (2021).
512. Wang, Z. *et al.* Spacer cation tuning enables vertically oriented and graded quasi-2D perovskites for efficient solar cells. *Advanced Functional Materials* **31**, 2008404 (2021).
513. García-Benito, I. *et al.* Fluorination of Organic Spacer Impacts on the Structural and Optical Response of 2D Perovskites. *Frontiers in chemistry* **7**, 946 (2020).
514. Park, I.-H. *et al.* Highly Stable Two-Dimensional Tin (II) Iodide Hybrid Organic–Inorganic Perovskite Based on Stilbene Derivative. *Advanced Functional Materials* **29**, 1904810 (2019).
515. Ma, C., Shen, D., Ng, T.-W., Lo, M.-F. & Lee, C.-S. 2D perovskites with short interlayer distance for high-performance solar cell application. *Advanced Materials* **30**, 1800710 (2018).
516. Shang, Y. *et al.* Highly stable hybrid perovskite light-emitting diodes based on Dion–Jacobson structure. *Science advances* **5**, eaaw8072 (2019).
517. Yang, J. *et al.*  $\pi$ -Conjugated Carbazole Cations Enable Wet-Stable Quasi-2D Perovskite Photovoltaics. *ACS Energy Lett.* **7**, 4451–4458 (2022).
518. Dalvi, V. H. & Rossky, P. J. Molecular origins of fluorocarbon hydrophobicity. *Proceedings of the National Academy of Sciences* **107**, 13603–13607 (2010).
519. Yan, G. *et al.* Selectively Fluorinated Benzylammonium-Based Spacer Cation Enables Graded Quasi-2D Perovskites for Efficient and Stable Solar Cells. *Chemistry of Materials* **34**, 3346–3356 (2022).
520. Wang, D., Chen, S.-C. & Zheng, Q. Enhancing the efficiency and stability of two-dimensional Dion–Jacobson perovskite solar cells using a

- fluorinated diammonium spacer. *Journal of Materials Chemistry A* **9**, 11778–11786 (2021).
521. Fu, W. *et al.* Tailoring the functionality of organic spacer cations for efficient and stable quasi-2D perovskite solar cells. *Advanced Functional Materials* **29**, 1900221 (2019).
522. Yukta *et al.* Thiocyanate-Passivated Diaminonaphthalene-Incorporated Dion–Jacobson Perovskite for Highly Efficient and Stable Solar Cells. *ACS Applied Materials & Interfaces* **14**, 850–860 (2022).
523. Kong, W. *et al.* Oriented Low-n Ruddlesden-Popper Formamidinium-Based Perovskite for Efficient and Air Stable Solar Cells. *Advanced Energy Materials* 2202704 (2022).
524. Zhang, Y. *et al.* Highly efficient and thermal stable guanidinium-based two-dimensional perovskite solar cells via partial substitution with hydrophobic ammonium. *Science China Chemistry* **62**, 859–865 (2019).
525. Chen, H. *et al.* Critical role of chloride in organic ammonium spacer on the performance of Low-dimensional Ruddlesden-Popper perovskite solar cells. *Nano Energy* **56**, 373–381 (2019).
526. Zheng, Y., Chen, S.-C., Ma, Y. & Zheng, Q. Furfurylammonium as a Spacer for Efficient 2D Ruddlesden–Popper Perovskite Solar Cells. *Solar Rrl* **6**, 2200221 (2022).
527. Cheng, Q. *et al.* Impact of Strain Relaxation on 2D Ruddlesden–Popper Perovskite Solar Cells. *Angewandte Chemie International Edition* **61**, e202208264 (2022).
528. Liu, C. *et al.* Multiple-Ring Aromatic Spacer Cation Tailored Interlayer Interaction for Efficient and Air-Stable Ruddlesden–Popper Perovskite Solar Cells. *Solar RRL* **5**, 2100495 (2021).
529. Yao, H. *et al.* Novel PHA Organic Spacer Increases Interlayer Interactions for High Efficiency in 2D Ruddlesden–Popper CsPbI<sub>3</sub> Solar Cells. *ACS Applied Materials & Interfaces* **14**, 35780–35788 (2022).
530. Li, Y., Cheng, H., Zhao, K. & Wang, Z.-S. 4-(Aminoethyl) pyridine as a Bifunctional Spacer Cation for Efficient and Stable 2D Ruddlesden–Popper Perovskite Solar Cells. *ACS applied materials & interfaces* **11**, 37804–37811 (2019).
531. Guo, X. *et al.* The Interplay of Organic Spacers and Small Cations for Efficient Dion–Jacobson Perovskite Solar Cells. *Solar RRL* **n/a**, 2201021.
532. Cheng, L. *et al.* Highly thermostable and efficient formamidinium-based low-dimensional perovskite solar cells. *Angewandte Chemie* **133**, 869–877 (2021).

533. Zhou, N. *et al.* Exploration of crystallization kinetics in quasi two-dimensional perovskite and high performance solar cells. *Journal of the American Chemical Society* **140**, 459–465 (2018).
534. Jiang, Y. *et al.* Intralayer A-site compositional engineering of Ruddlesden–Popper perovskites for thermostable and efficient solar cells. *ACS Energy Letters* **4**, 1216–1224 (2019).
535. Ahmad, S. *et al.* Formamidinium-incorporated Dion-Jacobson phase 2D perovskites for highly efficient and stable photovoltaics. *Journal of Energy Chemistry* **57**, 632–638 (2021).
536. Ahmad, S. *et al.* Cesium-doped Dion-Jacobson 2D perovskites for highly stable photovoltaics with an 18.3% efficiency. *Nano Energy* **103**, 107822 (2022).
537. Fu, Y. *et al.* Incorporating large A cations into lead iodide perovskite cages: Relaxed goldschmidt tolerance factor and impact on exciton–phonon interaction. *ACS central science* **5**, 1377–1386 (2019).
538. Gélvez-Rueda, M. C. *et al.* Formamidinium-based dion-jacobson layered hybrid perovskites: structural complexity and optoelectronic properties. *Advanced Functional Materials* **30**, 2003428 (2020).
539. Sidhik, S. *et al.* High-phase purity two-dimensional perovskites with 17.3% efficiency enabled by interface engineering of hole transport layer. *Cell Reports Physical Science* **2**, 100601 (2021).
540. Wang, Z. *et al.* Efficient ambient-air-stable solar cells with 2D–3D heterostructured butylammonium-caesium-formamidinium lead halide perovskites. *Nature Energy* **2**, 1–10 (2017).
541. Zheng, X. *et al.* Managing grains and interfaces via ligand anchoring enables 22.3%-efficiency inverted perovskite solar cells. *Nat Energy* **5**, 131–140 (2020).
542. Fei, C. *et al.* Self-assembled propylammonium cations at grain boundaries and the film surface to improve the efficiency and stability of perovskite solar cells. *J. Mater. Chem. A* **7**, 23739–23746 (2019).
543. Sourisseau, S. *et al.* Reduced Band Gap Hybrid Perovskites Resulting from Combined Hydrogen and Halogen Bonding at the Organic–Inorganic Interface. *Chem. Mater.* **19**, 600–607 (2007).
544. Liu, G. *et al.* Introduction of Hydrophobic Ammonium Salts with Halogen Functional Groups for High-Efficiency and Stable 2D/3D



- Perovskite Solar Cells. *Advanced Functional Materials* **29**, 1807565 (2019).
545. Huang, Z. *et al.* Suppressed Ion Migration in Reduced-Dimensional Perovskites Improves Operating Stability. *ACS Energy Lett.* **4**, 1521–1527 (2019).
546. Chao, L. *et al.* Efficient and Stable Low-Dimensional Ruddlesden–Popper Perovskite Solar Cells Enabled by Reducing Tunnel Barrier. *J. Phys. Chem. Lett.* **10**, 1173–1179 (2019).
547. Li, X. *et al.* Improved performance and stability of perovskite solar cells by crystal crosslinking with alkylphosphonic acid  $\omega$ -ammonium chlorides. *Nature chemistry* **7**, 703–711 (2015).
548. Kayesh, Md. E. *et al.* Coadditive Engineering with 5-Ammonium Valeric Acid Iodide for Efficient and Stable Sn Perovskite Solar Cells. *ACS Energy Lett.* **4**, 278–284 (2019).
549. Zhang, T. *et al.* In Situ Fabrication of Highly Luminescent Bifunctional Amino Acid Crosslinked 2D/3D  $\text{NH}_3\text{C}_4\text{H}_9\text{COO}(\text{CH}_3\text{NH}_3\text{PbBr}_3)_n$  Perovskite Films. *Advanced Functional Materials* **27**, 1603568 (2017).
550. Li, X. *et al.* Outdoor performance and stability under elevated temperatures and long-term light soaking of triple-layer mesoporous perovskite photovoltaics. *Energy Technology* **3**, 551–555 (2015).
551. Mei, A. *et al.* A hole-conductor-free, fully printable mesoscopic perovskite solar cell with high stability. *science* **345**, 295–298 (2014).
552. Grancini, G. *et al.* One-Year stable perovskite solar cells by 2D/3D interface engineering. *Nat Commun* **8**, 15684 (2017).
553. Alanazi, A. Q. *et al.* Atomic-level microstructure of efficient formamidinium-based perovskite solar cells stabilized by 5-ammonium valeric acid iodide revealed by multinuclear and two-dimensional solid-state NMR. *Journal of the American Chemical Society* **141**, 17659–17669 (2019).
554. Hu, Y. *et al.* Improved performance of printable perovskite solar cells with bifunctional conjugated organic molecule. *Advanced Materials* **30**, 1705786 (2018).
555. Zheng, X. *et al.* Dual functions of crystallization control and defect passivation enabled by sulfonic zwitterions for stable and efficient perovskite solar cells. *Advanced Materials* **30**, 1803428 (2018).
556. Shen, C. *et al.* Stabilizing Formamidinium Lead Iodide Perovskite by Sulfonyl-Functionalized Phenethylammonium Salt via Crystallization

- Control and Surface Passivation. *Solar RRL* **4**, 2000069 (2020).
557. Xu, Z., Kerner, R. A., Berry, J. J. & Rand, B. P. Iodine Electrochemistry Dictates Voltage-Induced Halide Segregation Thresholds in Mixed-Halide Perovskite Devices. *Advanced Functional Materials* **32**, 2203432 (2022).
558. Zheng, Y. *et al.* Downward Homogenized Crystallization for Inverted Wide-Bandgap Mixed-Halide Perovskite Solar Cells with 21% Efficiency and Suppressed Photo-Induced Halide Segregation. *Advanced Functional Materials* **32**, 2200431 (2022).
559. Wang, K. *et al.* Ruddlesden–Popper 2D Component to Stabilize  $\gamma$ -CsPbI<sub>3</sub> Perovskite Phase for Stable and Efficient Photovoltaics. *Advanced Energy Materials* **9**, 1902529 (2019).
560. Yang, G. *et al.* Defect engineering in wide-bandgap perovskites for efficient perovskite–silicon tandem solar cells. *Nat. Photon.* **16**, 588–594 (2022).
561. Huo, X. *et al.* Suppressed Halide Segregation and Defects in Wide Bandgap Perovskite Solar Cells Enabled by Doping Organic Bromide Salt with Moderate Chain Length. *J. Phys. Chem. C* **126**, 1711–1720 (2022).
562. Ye, J. Y. *et al.* Enhancing Charge Transport of 2D Perovskite Passivation Agent for Wide-Bandgap Perovskite Solar Cells Beyond 21%. *Solar RRL* **4**, 2000082 (2020).
563. Kim, D. *et al.* Efficient, stable silicon tandem cells enabled by anion-engineered wide-bandgap perovskites. *Science* **368**, 155–160 (2020).
564. Zhu, X. *et al.* In situ grain boundary modification via two-dimensional nanoplates to remarkably improve stability and efficiency of perovskite solar cells. *ACS applied materials & interfaces* **10**, 39802–39808 (2018).
565. Lee, D. S. *et al.* Passivation of grain boundaries by phenethylammonium in formamidinium-methylammonium lead halide perovskite solar cells. *ACS Energy Letters* **3**, 647–654 (2018).
566. Lee, J.-W. *et al.* 2D perovskite stabilized phase-pure formamidinium perovskite solar cells. *Nat Commun* **9**, 3021 (2018).
567. Liang, J. *et al.* Volatile 2D Ruddlesden-Popper Perovskite: A Gift for  $\alpha$ -Formamidinium Lead Triiodide Solar Cells. *Advanced Functional Materials* 2207177 (2022).
568. Savill, K. J. *et al.* Impact of Tin Fluoride Additive on the Properties of Mixed Tin-Lead Iodide Perovskite Semiconductors. *Advanced Functional Materials* **30**, 2005594 (2020).
569. Wang, F. *et al.* 2D-Quasi-2D-3D Hierarchy Structure for Tin Perovskite Solar Cells with

- Enhanced Efficiency and Stability. *Joule* **2**, 2732–2743 (2018).
570. Shao, S. *et al.* Highly reproducible Sn-based hybrid perovskite solar cells with 9% efficiency. *Advanced Energy Materials* **8**, 1702019 (2018).
571. Li, D. *et al.* Spontaneous Formation of Upper Gradient 2D Structure for Efficient and Stable Quasi-2D Perovskites. *Advanced Materials* **33**, 2101823 (2021).
572. Yu, B.-B. *et al.* Heterogeneous 2D/3D tin-halides perovskite solar cells with certified conversion efficiency breaking 14%. *Advanced Materials* **33**, 2102055 (2021).
573. Wang, C. *et al.* Self-repairing tin-based perovskite solar cells with a breakthrough efficiency over 11%. *Advanced Materials* **32**, 1907623 (2020).
574. Chang, J. *et al.* Enhanced performance of red perovskite light-emitting diodes through the dimensional tailoring of perovskite multiple quantum wells. *The journal of physical chemistry letters* **9**, 881–886 (2018).
575. Chaudhary, B. *et al.* Mixed-dimensional naphthylmethylammonium-methylammonium lead iodide perovskites with improved thermal stability. *Scientific reports* **10**, 429 (2020).
576. Lin, C.-T. *et al.* Origin of Open-Circuit Voltage Enhancements in Planar Perovskite Solar Cells Induced by Addition of Bulky Organic Cations. *Advanced Functional Materials* **30**, 1906763 (2020).
577. Yang, R. *et al.* Oriented quasi-2D perovskites for high performance optoelectronic devices. *Advanced Materials* **30**, 1804771 (2018).
578. Lu, J. *et al.* Diammonium and monoammonium mixed-organic-cation perovskites for high performance solar cells with improved stability. *Advanced Energy Materials* **7**, 1700444 (2017).
579. Wu, W.-Q. *et al.* Bilateral alkylamine for suppressing charge recombination and improving stability in blade-coated perovskite solar cells. *Science advances* **5**, eaav8925 (2019).
580. Wang, B., Novendra, N. & Navrotsky, A. Energetics, structures, and phase transitions of cubic and orthorhombic cesium lead iodide (CsPbI<sub>3</sub>) polymorphs. *Journal of the American Chemical Society* **141**, 14501–14504 (2019).
581. Zhang, T. *et al.* Bication lead iodide 2D perovskite component to stabilize inorganic  $\alpha$ -CsPbI<sub>3</sub> perovskite phase for high-efficiency solar cells. *Science advances* **3**, e1700841 (2017).
582. Kieslich, G., Sun, S. & Cheetham, A. K. Solid-state principles applied to organic–inorganic

- perovskites: new tricks for an old dog. *Chem. Sci.* **5**, 4712–4715 (2014).
583. Jodlowski, A. D. *et al.* Large guanidinium cation mixed with methylammonium in lead iodide perovskites for 19% efficient solar cells. *Nat Energy* **2**, 972–979 (2017).
584. Gao, L. *et al.* Incorporated Guanidinium Expands the CH<sub>3</sub>NH<sub>3</sub>PbI<sub>3</sub> Lattice and Enhances Photovoltaic Performance. *ACS Appl. Mater. Interfaces* **12**, 43885–43891 (2020).
585. Wu, S. *et al.* Efficient large guanidinium mixed perovskite solar cells with enhanced photovoltage and low energy losses. *Chem. Commun.* **55**, 4315–4318 (2019).
586. Wang, Y. *et al.* Oxidation-resistant all-perovskite tandem solar cells in substrate configuration. *Nat Commun* **14**, 1819 (2023).
587. Zhang, J., Wu, S., Liu, T., Zhu, Z. & Jen, A. K.-Y. Boosting Photovoltaic Performance for Lead Halide Perovskites Solar Cells with BF<sub>4</sub><sup>-</sup> Anion Substitutions. *Advanced Functional Materials* **29**, 1808833 (2019).
588. Wu, B. *et al.* Synergistic effect of guanidinium tetrafluoroborate boosting photovoltaic performance of perovskite solar cells. *Applied Surface Science* **603**, 154362 (2022).
589. Yao, D. *et al.* 2D–3D Mixed Organic–Inorganic Perovskite Layers for Solar Cells with Enhanced Efficiency and Stability Induced by n-Propylammonium Iodide Additives. *ACS Appl. Mater. Interfaces* **11**, 29753–29764 (2019).
590. Liu, X. *et al.* Templated growth of FASnI<sub>3</sub> crystals for efficient tin perovskite solar cells. *Energy Environ. Sci.* **13**, 2896–2902 (2020).
591. Jin, S. *et al.* Improving perovskite solar cells photovoltaic performance using tetrabutylammonium salt as additive. *Journal of Power Sources* **450**, 227623 (2020).
592. Wang, P. *et al.* 2D perovskite or organic material matter? Targeted growth for efficient perovskite solar cells with efficiency exceeding 24%. *Nano Energy* **94**, 106914 (2022).
593. Shao, S. *et al.* Highly reproducible Sn-based hybrid perovskite solar cells with 9% efficiency. *Advanced Energy Materials* **8**, 1702019 (2018).
594. Ran, C. *et al.* Conjugated Organic Cations Enable Efficient Self-Healing FASnI<sub>3</sub> Solar Cells. *Joule* **3**, 3072–3087 (2019).
595. Kim, D. H. *et al.* Bimolecular Additives Improve Wide-Band-Gap Perovskites for Efficient Tandem Solar Cells with CIGS. *Joule* **3**, 1734–1745 (2019).
596. Alanazi, A. Q. *et al.* Benzylammonium-Mediated Formamidinium Lead Iodide Perovskite Phase Stabilization for Photovoltaics. *Advanced Functional Materials* **31**, 2101163 (2021).

597. Cho, K. T. *et al.* Selective growth of layered perovskites for stable and efficient photovoltaics. *Energy & Environmental Science* **11**, 952–959 (2018).
598. Chen, P. *et al.* In situ growth of 2D perovskite capping layer for stable and efficient perovskite solar cells. *Advanced Functional Materials* **28**, 1706923 (2018).
599. Koh, T. M. *et al.* Enhancing moisture tolerance in efficient hybrid 3D/2D perovskite photovoltaics. *Journal of Materials Chemistry A* **6**, 2122–2128 (2018).
600. Lv, Y. *et al.* Hexylammonium iodide derived two-dimensional perovskite as interfacial passivation layer in efficient two-dimensional/three-dimensional perovskite solar cells. *ACS applied materials & interfaces* **12**, 698–705 (2019).
601. Zhang, H. *et al.* A universal co-solvent dilution strategy enables facile and cost-effective fabrication of perovskite photovoltaics. *Nature Communications* **13**, 89 (2022).
602. Lin, Y. *et al.* Enhanced Thermal Stability in Perovskite Solar Cells by Assembling 2D/3D Stacking Structures. *J. Phys. Chem. Lett.* **9**, 654–658 (2018).
603. Zhou, Y. *et al.* Benzylamine-treated wide-bandgap perovskite with high thermal-photostability and photovoltaic performance. *Advanced Energy Materials* **7**, 1701048 (2017).
604. Ma, C. *et al.* 2D/3D perovskite hybrids as moisture-tolerant and efficient light absorbers for solar cells. *Nanoscale* **8**, 18309–18314 (2016).
605. Liu, Y. *et al.* Ultrahydrophobic 3D/2D fluoroarene bilayer-based water-resistant perovskite solar cells with efficiencies exceeding 22%. *Science advances* **5**, eaaw2543 (2019).
606. Ye, T. *et al.* Efficient and ambient-air-stable solar cell with highly oriented 2D@ 3D perovskites. *Advanced Functional Materials* **28**, 1801654 (2018).
607. Cho, Y. *et al.* Mixed 3D–2D passivation treatment for mixed-cation lead mixed-halide perovskite solar cells for higher efficiency and better stability. *Advanced Energy Materials* **8**, 1703392 (2018).
608. Niu, T. *et al.* Interfacial engineering at the 2D/3D heterojunction for high-performance perovskite solar cells. *Nano letters* **19**, 7181–7190 (2019).
609. Xiao, M. *et al.* A fast deposition-crystallization procedure for highly efficient lead iodide perovskite thin-film solar cells. *Angewandte*

- Chemie International Edition* **53**, 9898–9903 (2014).
610. Bai, Y. *et al.* Dimensional engineering of a graded 3D–2D halide perovskite interface enables ultrahigh Voc enhanced stability in the p-i-n photovoltaics. *Advanced Energy Materials* **7**, 1701038 (2017).
611. Liu, Z. *et al.* In situ observation of vapor-assisted 2D–3D heterostructure formation for stable and efficient perovskite solar cells. *Nano Letters* **20**, 1296–1304 (2020).
612. Lin, D. *et al.* Stable and scalable 3D-2D planar heterojunction perovskite solar cells via vapor deposition. *Nano Energy* **59**, 619–625 (2019).
613. La-Placa, M.-G. *et al.* Vacuum-deposited 2D/3D perovskite heterojunctions. *ACS Energy Letters* **4**, 2893–2901 (2019).
614. Proppe, A. H. *et al.* Multication perovskite 2D/3D interfaces form via progressive dimensional reduction. *Nat Commun* **12**, 3472 (2021).
615. Choi, H.-S. & Kim, H.-S. 3D/2D Bilayered Perovskite Solar Cells with an Enhanced Stability and Performance. *Materials* **13**, 3868 (2020).
616. Wang, F. *et al.* Hole-transporting low-dimensional perovskite for enhancing photovoltaic performance. *Research* (2021).
617. Malouangou, M. D. *et al.* Facilitate hole transport with thin 2D perovskite capping layer to passivate interface defects of 3D perovskite solar cells using PEABr. *Materials Research Bulletin* **150**, 111793 (2022).
618. Bouduban, M. E. F. *et al.* Crystal Orientation Drives the Interface Physics at Two/Three-Dimensional Hybrid Perovskites. *J. Phys. Chem. Lett.* **10**, 5713–5720 (2019).
619. Liu, Y. *et al.* Stabilization of Highly Efficient and Stable Phase-Pure FAPbI<sub>3</sub> Perovskite Solar Cells by Molecularly Tailored 2D-Overlayers. *Angewandte Chemie International Edition* **59**, 15688–15694 (2020).
620. Yoo, J. J. *et al.* An interface stabilized perovskite solar cell with high stabilized efficiency and low voltage loss. *Energy Environ. Sci.* **12**, 2192–2199 (2019).
621. Teale, S. *et al.* Dimensional Mixing Increases the Efficiency of 2D/3D Perovskite Solar Cells. *J. Phys. Chem. Lett.* **11**, 5115–5119 (2020).
622. Proppe, A. H. *et al.* Photochemically Cross-Linked Quantum Well Ligands for 2D/3D Perovskite Photovoltaics with Improved Photovoltage and Stability. *J. Am. Chem. Soc.* **141**, 14180–14189 (2019).
623. Chen, H. *et al.* Quantum-size-tuned heterostructures enable efficient and stable

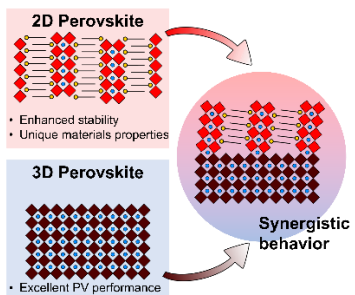
- inverted perovskite solar cells. *Nat. Photon.* **16**, 352–358 (2022).
624. Jokar, E. *et al.* Enhanced Performance and Stability of 3D/2D Tin Perovskite Solar Cells Fabricated with a Sequential Solution Deposition. *ACS Energy Lett.* **6**, 485–492 (2021).
625. He, Q. *et al.* Facile Formation of 2D–3D Heterojunctions on Perovskite Thin Film Surfaces for Efficient Solar Cells. *ACS Appl. Mater. Interfaces* **12**, 1159–1168 (2020).
626. Wu, T. *et al.* Efficient and stable tin perovskite solar cells enabled by graded heterostructure of light-absorbing layer. *Solar Rrl* **4**, 2000240 (2020).
627. Gharibzadeh, S. *et al.* Record Open-Circuit Voltage Wide-Bandgap Perovskite Solar Cells Utilizing 2D/3D Perovskite Heterostructure. *Advanced Energy Materials* **9**, 1803699 (2019).
628. Ghoreishi, F. S. *et al.* Enhanced performance of CH<sub>3</sub>NH<sub>3</sub>PbI<sub>3</sub> perovskite solar cells via interface modification using phenyl ammonium iodide derivatives. *Journal of Power Sources* **473**, 228492 (2020).
629. Zhao, T., Chueh, C.-C., Chen, Q., Rajagopal, A. & Jen, A. K.-Y. Defect Passivation of Organic–Inorganic Hybrid Perovskites by Diammonium Iodide toward High-Performance Photovoltaic Devices. *ACS Energy Lett.* **1**, 757–763 (2016).
630. Kim, J. *et al.* Efficient planar-heterojunction perovskite solar cells achieved via interfacial modification of a sol–gel ZnO electron collection layer. *Journal of Materials Chemistry A* **2**, 17291–17296 (2014).
631. Wu, X., Li, B., Zhu, Z., Chueh, C.-C. & Jen, A. K.-Y. Designs from single junctions, heterojunctions to multijunctions for high-performance perovskite solar cells. *Chemical Society Reviews* **50**, 13090–13128 (2021).
632. Yuan, M. *et al.* Perovskite energy funnels for efficient light-emitting diodes. *Nature nanotechnology* **11**, 872–877 (2016).
633. Xu, X. & Wang, X. Perovskite Nano-Heterojunctions: Synthesis, Structures, Properties, Challenges, and Prospects. *Small Structures* **1**, 2000009 (2020).
634. Shang, Y., Li, G., Liu, W. & Ning, Z. Quasi-2D Inorganic CsPbBr<sub>3</sub> Perovskite for Efficient and Stable Light-Emitting Diodes. *Advanced Functional Materials* **28**, 1801193 (2018).
635. Wang, T., Deng, W., Cao, J. & Yan, F. Recent Progress on Heterojunction Engineering in Perovskite Solar Cells. *Advanced Energy Materials* 2201436 (2022).



636. Chatterjee, A. & Marshak, A. H. Theory of abrupt heterojunctions in equilibrium. *Solid-State Electronics* **24**, 1111–1115 (1981).
637. Hu, Y. *et al.* Hybrid Perovskite/Perovskite Heterojunction Solar Cells. *ACS Nano* **10**, 5999–6007 (2016).
638. Luo, D. *et al.* Enhanced photovoltage for inverted planar heterojunction perovskite solar cells. *Science* **360**, 1442–1446 (2018).
639. Zhou, Q. *et al.* High-Performance Perovskite Solar Cells with Enhanced Environmental Stability Based on a (p-FC6H4C2H4NH3)2[PbI4] Capping Layer. *Advanced Energy Materials* **9**, 1802595 (2019).
640. Jiang, Q. *et al.* Surface passivation of perovskite film for efficient solar cells. *Nat. Photonics* **13**, 460–466 (2019).
641. Sutanto, A. A. *et al.* In Situ Analysis Reveals the Role of 2D Perovskite in Preventing Thermal-Induced Degradation in 2D/3D Perovskite Interfaces. *Nano Lett.* **20**, 3992–3998 (2020).
642. Niu, T. *et al.* Spacer Engineering of Diammonium-Based 2D Perovskites toward Efficient and Stable 2D/3D Heterostructure Perovskite Solar Cells. *Advanced Energy Materials* **12**, 2102973 (2022).
643. Zhang, S. *et al.* Spontaneous Construction of Multidimensional Heterostructure Enables Enhanced Hole Extraction for Inorganic Perovskite Solar Cells to Exceed 20% Efficiency. *Advanced Energy Materials* **12**, 2103007 (2022).
644. Jeong, S. *et al.* Cyclohexylammonium-Based 2D/3D Perovskite Heterojunction with Funnel-Like Energy Band Alignment for Efficient Solar Cells (23.91%). *Advanced Energy Materials* **11**, 2102236 (2021).
645. Jiang, J. *et al.* Mixed dimensionality of 2D/3D heterojunctions for improving charge transport and long-term stability in high-efficiency 1.63 eV bandgap perovskite solar cells. *Materials Advances* **3**, 5786–5795 (2022).
646. Yue, X. *et al.* In-Situ Surface Regulation of 3D Perovskite Using Diethylammonium Iodide for High-efficient Perovskite Solar Cells. *Physical Chemistry Chemical Physics* (2023) doi:10.1039/D2CP05535J.
647. Tai, M. *et al.* In situ formation of a 2D/3D heterostructure for efficient and stable CsPbI2Br solar cells. *J. Mater. Chem. A* **7**, 22675–22682 (2019).
648. Era, M., Morimoto, S., Tsutsui, T. & Saito, S. Organic-inorganic heterostructure electroluminescent device using a layered

- perovskite semiconductor (C<sub>6</sub>H<sub>5</sub>C<sub>2</sub>H<sub>4</sub>NH<sub>3</sub>) 2PbI<sub>4</sub>. *Applied physics letters* **65**, 676–678 (1994).
649. Wu, T. *et al.* Nanoplatelet modulation in 2D/3D perovskite targeting efficient light-emitting diodes. *Nanoscale* **10**, 19322–19329 (2018).
650. Pan, X. *et al.* Single-layer ZnO hollow hemispheres enable high-performance self-powered perovskite photodetector for optical communication. *Nano-Micro Letters* **13**, 1–12 (2021).
651. Song, Q. *et al.* Moiré Perovskite Photodetector toward High-Sensitive Digital Polarization Imaging. *Advanced Energy Materials* **11**, 2100742 (2021).
652. Loi, H.-L. *et al.* Gradient 2D/3D perovskite films prepared by hot-casting for sensitive photodetectors. *Advanced Science* **7**, 2000776 (2020).
653. Wu, D. *et al.* Welding perovskite nanowires for stable, sensitive, flexible photodetectors. *ACS nano* **14**, 2777–2787 (2020).
654. Yang, Y., You, J. & Meng, L. *Efficient and stable perovskite solar cells with all solution processed metal oxide transporting layers.* (Google Patents, 2020).
655. Hua, Y., Yang, C., Junhui, H. & Qiaowen, Y. Research progress in graphene-based infrared photodetectors. *Laser Optoelectronics Progress* **52**, 110003 (2015).
656. Chen, X., Zhou, H. & Wang, H. 2D/3D Halide Perovskites for Optoelectronic Devices. *Frontiers in Chemistry* **9**, 715157 (2021).
657. Dong, H., Zhu, H., Meng, Q., Gong, X. & Hu, W. Organic photoresponse materials and devices. *Chemical Society Reviews* **41**, 1754–1808 (2012).
658. Gong, X. *et al.* High-detectivity polymer photodetectors with spectral response from 300 nm to 1450 nm. *Science* **325**, 1665–1667 (2009).
659. Shi, L. *et al.* Research progress in organic photomultiplication photodetectors. *Nanomaterials* **8**, 713 (2018).
660. Jiaojiao, W., Zeping, Z. & Jianguo, L. Research Progress and Development Trend of Balanced Photodetectors [J]. *Laser & Optoelectronics Progress* **55**, 1–10 (2018).
661. Tan, Z. *et al.* Two-dimensional (C<sub>4</sub>H<sub>9</sub>NH<sub>3</sub>) 2PbBr<sub>4</sub> perovskite crystals for high-performance photodetector. *Journal of the American Chemical Society* **138**, 16612–16615 (2016).
662. Liu, J. *et al.* Two-dimensional CH<sub>3</sub>NH<sub>3</sub>PbI<sub>3</sub> perovskite: synthesis and optoelectronic application. *ACS nano* **10**, 3536–3542 (2016).

663. Song, J. *et al.* Monolayer and Few-Layer All-Inorganic Perovskites as a New Family of Two-Dimensional Semiconductors for Printable Optoelectronic Devices. *Advanced Materials* **28**, 4861–4869 (2016).
664. Lim, J. W. *et al.* Self-powered reduced-dimensionality perovskite photodiodes with controlled crystalline phase and improved stability. *Nano Energy* **57**, 761–770 (2019).
665. Numai, T. & Numai, T. *Fundamentals of semiconductor lasers*. (Springer, 2015).
666. Holonyak, N., Kolbas, R., Dupuis, R. & Dapkus, P. Quantum-well heterostructure lasers. *IEEE Journal of Quantum Electronics* **16**, 170–186 (1980).
667. Kroemer, H. A proposed class of hetero-junction injection lasers. *Proceedings of the IEEE* **51**, 1782–1783 (1963).
668. Qin, C. *et al.* Stable room-temperature continuous-wave lasing in quasi-2D perovskite films. *Nature* **585**, 53–57 (2020).
669. Jia, Y., Kerner, R. A., Grede, A. J., Rand, B. P. & Giebink, N. C. Continuous-wave lasing in an organic–inorganic lead halide perovskite semiconductor. *Nature Photonics* **11**, 784–788 (2017).
670. Sun, X. *et al.* 2D/3D heterostructure derived from phase transformation of 0D perovskite for random lasing applications with remarkably improved water resistance. *Nanoscale* **13**, 18647–18656 (2021).
671. Li, Y. *et al.* Lasing from Laminated Quasi-2D/3D Perovskite Planar Heterostructures. *Advanced Functional Materials* **32**, 2200772 (2022).



TOC Graphic